Doctoral Dissertation
Doctoral Program in Energetics (38^{th} cycle)

Hydrogels for ultralow-grade heat driven fresh water production

A theoretical and experimental investigation on the use of calcium alginate for adsorption-based atmospheric water harvesting and water desalination

By

Matteo Calò

******

Supervisors:
Prof. Eliodoro Chiavazzo
Prof. Matteo Fasano
Ph.D. Vincenzo Maria Gentile

Politecnico di Torino
2026

Declaration

I hereby declare that the contents and organization of this dissertation constitute my own original work and does not compromise in any way the rights of third parties, including those relating to the security of personal data.

Matteo Calò
2026

* This dissertation is presented in partial fulfillment of the requirements for **Ph.D. degree** in the Graduate School of Politecnico di Torino (ScuDo).

This study was carried out in the framework of a specific regional call for proposals (Apprendistato di Alta Formazione e Ricerca – Avviso Pubblico 2022-2024 per l'individuazione e la gestione dell'offerta formativa pubblica approvato con Determinazione 114 del 3/3/2022 e s.m.i.) and within the WADERE project – funded by the Ministero dell'Università e della Ricerca – within the PRIN 2022 program (D.D.104 - 02/02/2022). This manuscript reflects only the authors' views and opinions, and the Ministry cannot be considered responsible for them.

Questa tesi è per te, Matteo del futuro.

Acknowledgements

This doctorate thesis is the result of an intense series of passion-driven efforts, interactions and... patience. My patience, and the patience of the uncountable people that followed this research by my side, both providing scientific advice and human support.

First, I would like to thank my academic supervisors Eliodoro Chiavazzo, Vincenzo Gentile and Matteo Fasano. Each of them heavily contributed to this work, with their different views, ideas and crucial inputs. I bring home method and scientific mindset, which I believe is only obtainable by working with the best researchers.

The list of people I would like to thank extends to most of the DENERG department at Politecnico di Torino, and especially the SMaLL group. Many practical situations needed and received immediate help from researchers and technicians, including, but not only: Alberto Saija, Alessio Mondello, Matteo Morciano, Marco Simonetti, Fabrizio Bronuzzi, Emanuele Norata, Pierpaolo Nuzzo, Paolo Squillari, Alice Lorenzati, Ali Naeimi Tabasian. I bring home both human and professional connections. A huge thanks goes also to the DIATI department, and especially to Alberto Tiraferri, Fabrizio Bianco and Lorenzo Craveri for the support with the TOC and Cu content water analyses. I would like to thank the Clean Water Center for funding, spaces and equipment.

I am grateful to Sorption Technologies for co-financing this PhD course. A big thanks goes to Walter Mittelbach, company founder, both for the fruitful technical discussions and for blindly trusting me and giving me a chance in a difficult moment. I would like to also thank my company colleagues, and especially Gabriele, Cecilia, Gabriel, and Abhijeet, for their support. The time spent working in company spaces has been educational in every possible way: I bring home invaluable technical and management skills that I have acquired over the last few years.

The biggest thank goes to my family and friends, for their unconditional support. Many moments were extremely arduous for me, far beyond what I was able to manage by myself, and the constant presence of my loved ones has been **necessary**. First, I thank my wife

Beatrice for her patience and love. I thank my friend Laura for embracing my ruminations and, often, my overthinking. And, I thank my dad, mum and sisters, as well as my friends Giacomo, Alessandro, Giacomo, Edoardo, Adriano, Philippe, Manuela, Vittorio, Silvia, Lucia, Laura, Francesco, Antonio, Gianluca, Emanuele, Gianmarco, Luca, Alessia, Sara, Gabriele, Andrea, Ludovico, Federico, Riccardo, Giambattista, Matteo, Samuele, Lorenzo... for having always been there for me. May this work be both the end and the start of something important!

Abstract

Water scarcity is a serious global challenge, affecting billions of people worldwide. Limited access to safe water poses health risks and exacerbates social disparities, requiring urgent actions from policymakers and scientific communities. In this thesis, we discuss two possible approaches to alleviate this problem: Atmospheric Water Harvesting -a technology which enables the production of fresh water potentially anywhere, starting from the vapor in humid air- and Water Desalination -a technology which allows treating existing sources of water to obtain a potable liquid-.
Specifically, we explore adsorption-based solutions, where a hydrophilic material is exploited to collect, transport and condense water molecules. Conventional plants use adsorbent materials such as silica-gels and zeolites; in contrast, we propose a novel bio-derived hydrogel, Calcium Alginate (CaAlg), providing evidence that it is a competitive and cost-effective alternative for heat driven atmospheric water harvesting and water desalination applications.

First, we produced and characterized six different compositions of CaAlg. Our results show that composition Alg_1Ca_{10} has the best equilibrium capacity, of up to 1.28 g/g at a relative humidity RH = 70% and a temperature T = 30°C, a fourfold increase compared to silica-gels. Starting from the experimental type-II isotherms, we estimated an adsorption enthalpy of 2600 kJ/kg at 30°C.
Second, we tested CaAlg dynamics over adsorption-desorption transients. We found that composition $Alg_1Ca_5G_{0.1}$ has the best dynamics, and demonstrates a long-term stability over 300 cycles. We proposed an improved variation of the Linear Driving Force model (LDFDw) with which we were able to best-fit the experimental data, estimating a water vapor diffusivity of $3 \cdot 10^{-12}$ m^2/s at 30°C.
Third, we tested a surface coating of CaAlg in an atmospheric water harvesting unit. The experiments were performed in laboratory conditions as well as in arid climates, resulting in a Specific Daily Water Production of up to 1.19 m^3/day/ton and showing a stable cycle and water condensation over 2.5 days of consecutive testing, at medium-low desorption temperatures (65°C) and medium-low RH levels (45%).
Fourth, we tested a batch of CaAlg beads in an adsorption desalination unit. We achieved a desalination effect, reaching a Specific Daily Water Production of 6.04 m^3/day/ton at 60°C under optimized cycling times, and obtaining a salt rejection rate of over 99.2%. Most

importantly, we achieved a sub-optimal water production of 2.2 m^3/day/ton with a desorption temperature as low as 45°C.
Finally, we designed and tested a larger-scale adsorption device using a silica-gel composite and extrapolated the results to the use of CaAlg. Our analysis suggests that, by replacing the composite sorbent with our hydrogel, we should observe an increase in efficiency and a resulting reduction of material weight and cost of over 50%.

In general, we have proved that calcium alginate is indeed a suitable sorbent in adsorption-based atmospheric water harvesting and water desalination, outperforming existing alternatives especially at low driving temperatures. This opens a new set of opportunities: ultralow-grade heat sources can be integrated with adsorption-based solutions using CaAlg, providing water production as well as a cooling effect. Waste heat coming, for example, from power plants heat dissipation or data-centre cooling (45-60°C) is of no use for production of work, given the low exergetic content; nevertheless, it is already sufficient to drive an adsorption-based machine employing calcium alginate, providing fresh water in areas in need. These findings align with the global energy objectives established by the UN General Assembly in 2015, providing options for recycling waste heat, reducing impact on climate and increasing global access to drinkable water. Future research on CaAlg should assess experimentally its long-term stability, performance at short cycle times and bio-degradability.

Contents

List of Figures **xii**

List of Tables **xvii**

Nomenclature **xix**

1 Introduction **1**

1.1 Fresh water scarcity: a global problem needing multiple tackling 1

1.2 A broader contextualization in the global energy outlook 4

1.3 Thesis outline 7

2 Adsorption **9**

2.1 Introduction 9

2.1.1 Adsorption theory 9

2.1.2 Conventional sorbents for water vapor adsorbate 12

2.1.3 Calcium alginate and non-conventional sorbents for water vapor . . 14

2.1.4 Applications of water vapor adsorption machines 18

2.2 Adsorption models 20

2.2.1 Equilibrium models 20

2.2.2 Dynamics models 26

3 Fresh water production **42**

3.1 Introduction 42

3.2 Atmospheric water harvesting 43

3.2.1 Overview 43

3.2.2 Direct adsorption AWH . . . 45
3.3 Water desalination . . . 47
3.3.1 Overview . . . 47
3.3.2 State-of-the-art solutions . . . 51
3.4 Requirements for drinkable water . . . 61

4 Experimental characterization of calcium alginate 65
4.1 Introduction . . . 65
4.2 Main results . . . 66
4.2.1 Equilibrium uptakes . . . 66
4.2.2 Dynamics . . . 71
4.2.3 Cycling aging . . . 76
4.3 Methods . . . 78
4.3.1 Material synthesis . . . 78
4.3.2 Equilibrium experiments . . . 84
4.3.3 Assessment of dynamics and aging . . . 90
4.4 Conclusions . . . 92

5 Experimental testing of calcium alginate in lab-scale machines 94
5.1 Introduction . . . 94
5.2 Main results . . . 95
5.2.1 CaAlg for atmospheric water harvesting . . . 95
5.2.2 CaAlg for water desalination . . . 101
5.2.3 Extrapolating to large-scale ultralow-grade waste heat driven applications . . . 109
5.3 Methods . . . 116
5.3.1 AWH unit description . . . 116
5.3.2 AD unit description . . . 124
5.4 Conclusions . . . 138

6 Design and testing of a medium-scale adsorption machine 140

6.1 Introduction 140
6.2 Main results 141
6.2.1 Adsorption-based unit using a CaCl2/silica-gel composite 141
6.2.2 Extrapolation to desalination using CaAlg as sorbent and economic considerations 146
6.3 Methods 151
6.3.1 Adsorption-based unit description 151
6.3.2 Testing apparatus and procedure 157
6.4 Conclusions 160

7 Conclusions and future perspectives 162

References 165

Appendix A Models derivation 178

Appendix B MATLAB codes 184

Appendix C Models best-fitting results 187

Appendix D Experimental tests dataset 201

Appendix E Design adjustments on the desalination unit 236

Appendix F Analytical expression for steady-state SDWP maximization 239

List of Figures

1.1 Adsorption-based solutions for fresh water production. . . . 3

1.2 Contributions in air conditioning emissions. . . . 5

1.3 Schematics of the thesis structure. . . . 7

2.1 Silica-gel introduction. . . . 13

2.2 Zeolites introduction. . . . 14

2.3 Calcium alginate introduction. . . . 17

2.4 Types of adsorption equilibrium curves. . . . 21

2.5 Isotherms classification according to IUPAC and ISO 9277. . . . 23

2.6 BET model assumptions on multilayer interactions. . . . 25

2.7 Adsorption and desorption transients. . . . 27

2.8 Geometry for Fick's laws derivation. . . . 28

2.9 Adsorbate concentration in a sphere over radius and time according to FD model. . . . 30

2.10 Schematics of a layer of adsorbent (coating) covering a solid surface (wall) which is adiabatic to the vapor diffusion. . . . 33

2.11 Concentration and water uptake in a plane coating of sorbent according to the FD model. . . . 34

2.12 Dependence of FD accuracy as a function of evaluated terms in the infinite sum. . . . 37

3.1 An example of a fog harvesting system. . . . 43

3.2 AWH introduction. . . . 46

3.3 Working principle of a reverse osmosis plant. . . . 51

3.4 Schematics of a MSF plant. . . . 53

3.5 Schematics of a MED plant. . . . 54

3.6 Schematics of a MD plant. . . . 55

3.7 Schematics of an AD plant. . . . 60

3.8 Map of desalination solutions in comparison. . . . 61

4.1 Samples of CaAlg with and without graphite. . . . 68

4.2 CaAlg isotherms and best-fitting equilibrium models. 68
4.3 Comparison of CaAlg isotherm at 30°C with silica-gels and samples from the literature. 70
4.4 Time-dependent water uptake variation between adsorption and regeneration in CaAlg samples. 71
4.5 Comparing CaAlg dynamics data with FD-based and LDF-based models. 72
4.6 Dynamics models errors in comparison. 73
4.7 Effect of regeneration temperature on desorption dynamics for each tested CaAlg composition. 74
4.8 Influence of temperature on diffusivity. 75
4.9 Aging of a CaAlg sample after 0, 131 and 318 cycles in climatic chamber. 76
4.10 CaAlg adsorption isotherm aging with cycles in a desalination unit. 77
4.11 CaAlg synthesis materials and methods. 79
4.12 Dry CaAlg beads appearance and properties. 82
4.13 CaAlg bead magnifications under optical and SEM microscopy. 82
4.14 Gravimetric analysis used to produce material's isotherms. 84
4.15 Relationship between equilibrium RH and CaAlg beads diameter. 86
4.16 Effect of isotherms offset procedure. 87
4.17 Effect of the dry-mass change on the isotherm. 89
4.18 Isotherms construction: best-fitting of transient curves. 91

5.1 AWH unit. 95
5.2 A representative cycle with the AWH unit. 96
5.3 A test of 20 consecutive cycles with the AWH unit. 97
5.4 Map of AWH unit performance in comparison with plants from the literature. 101
5.5 Adsorption desalination unit. 102
5.6 A representative cycle with the AD unit. 102
5.7 One-day test showing 6 consecutive cycles with the AD unit. 104
5.8 Water production with CaAlg and silica-gel in the AD unit, as a function of temperature and time. 108
5.9 Map showing the performance of the desalination unit in comparison with adsorption-desalination plants from the literature. 109
5.10 Waste heat generation from the EU power sector. 110
5.11 Combined power production - AWH plant integrated architecture. 113
5.12 Combined data centre cooling - AD plant integrated architecture. 115
5.13 CaAlg coating materials and methods. 118
5.14 CaAlg coating realization. 118
5.15 Temperature distribution on the coated exchanger as seen through a thermal camera. 119

5.16 AWH unit control logic. . . . 120
5.17 On-site testing of the AWH unit. . . . 121
5.18 FD-based numerical simulation of the water uptake in the CaAlg coating. . . . 122
5.19 Desalination unit principle, original design (not used). . . . 125
5.20 Desalination unit description, final design. . . . 126
5.21 Geometry of the adsorber heat exchanger. . . . 129
5.22 Detail of the fine mesh used to cover the exchanger sides, keeping the material inside. . . . 132
5.23 Desorption time optimization. . . . 135
5.24 Residual solid content evaluation. . . . 138

6.1 HyperGryd concept: prototype picture and P&ID. . . . 142
6.2 Thermodynamic variables in the AC unit. . . . 143
6.3 KPIs in the AC campaign. . . . 146
6.4 Design algorithms for scaling up CaAlg production. . . . 147
6.5 Economic considerations of replacing sorbents with CaAlg. . . . 149
6.6 Commercial attractiveness of CaAlg if compared with other sorbents. . . . 150
6.7 AC unit working principle. . . . 151
6.8 AC module tilting strategy. . . . 153
6.9 Custom brass feedthrough. . . . 154
6.10 CAD of the designed adsorption machine. . . . 154
6.11 DAQ hardware and software. . . . 156
6.12 AC Testing Rig P&ID. . . . 158
6.13 AC Testing Rig appearance. . . . 159

C.1 FD-based models, best-fittings on sample S1. . . . 187
C.2 FD-based models, best-fittings on sample S2. . . . 188
C.3 FD-based models, best-fittings on sample S3. . . . 188
C.4 FD-based models, best-fittings on sample S4. . . . 189
C.5 FD-based models, best-fittings on sample S5. . . . 189
C.6 FD-based models, best-fittings on sample S6. . . . 190
C.7 LDF-based models, best-fittings on sample S1. . . . 190
C.8 LDF-based models, best-fittings on sample S2. . . . 191
C.9 LDF-based models, best-fittings on sample S3. . . . 191
C.10 LDF-based models, best-fittings on sample S4. . . . 192
C.11 LDF-based models, best-fittings on sample S5. . . . 192

C.12 LDF-based models, best-fittings on sample S6. . . . 193
C.13 LDFDw, parameters a and b with temperature, best-fittings. . . . 193
C.14 Isotherm best-fitting and error, sample 1. . . . 194
C.15 Isotherm best-fitting and error, sample 2. . . . 194
C.16 Isotherm best-fitting and error, sample 3. . . . 195
C.17 Isotherm best-fitting and error, sample 4. . . . 195
C.18 Isotherm best-fitting and error, sample 5. . . . 196
C.19 Isotherm best-fitting and error, sample 6. . . . 196
C.20 Isotherm best-fitting and error, sample 7. . . . 197
C.21 Isotherm best-fitting and error, sample 8. . . . 197
C.22 Isotherm best-fitting and error, sample 9. . . . 198
C.23 Isotherm best-fitting and error, sample 10. . . . 198
C.24 Isotherm best-fitting and error, sample 11. . . . 199
C.25 Isotherm best-fitting and error, sample 12. . . . 199
C.26 Isotherm best-fitting and error, sample 13. . . . 200
C.27 Isotherm best-fitting and error, sample 14. . . . 200

D.1 Test 1 with AWH unit. . . . 201
D.2 Test 2 with AWH unit. . . . 202
D.3 Test 3 with AWH unit. . . . 202
D.4 Test 4 with AWH unit. . . . 203
D.5 Test 5 with AWH unit. . . . 203
D.6 Test 6 with AWH unit. . . . 204
D.7 Test 7 with AWH unit. . . . 204
D.8 Test 8 with AWH unit. . . . 205
D.9 Detail of the temperatures in one cycle from test 3 with AWH unit. . . . 205
D.10 Test 1 with AD unit. . . . 206
D.11 Test 2 with AD unit. . . . 207
D.12 Test 3 with AD unit. . . . 208
D.13 Test 4 with AD unit. . . . 209
D.14 Test 5 with AD unit. . . . 210
D.15 Test 6 with AD unit. . . . 211
D.16 Test 7 with AD unit. . . . 212
D.17 Test 8 with AD unit. . . . 213

D.18 Test 9 with AD unit. . . . 214
D.19 Test 10 with AD unit. . . . 215
D.20 Test 1 with AC unit. . . . 216
D.21 Test 2 with AC unit. . . . 216
D.22 Test 3 with AC unit. . . . 217
D.23 Test 4 with AC unit. . . . 217
D.24 Test 5 with AC unit. . . . 218
D.25 Test 6 with AC unit. . . . 218
D.26 Test 7 with AC unit. . . . 219
D.27 Test 8 with AC unit. . . . 219
D.28 Test 9 with AC unit. . . . 220
D.29 Test 10 with AC unit. . . . 220
D.30 Test 11 with AC unit. . . . 221
D.31 Equilibrium pictures on sample 1. . . . 222
D.32 Equilibrium pictures on sample 2. . . . 223
D.33 Equilibrium pictures on sample 3. . . . 224
D.34 Equilibrium pictures on sample 4. . . . 225
D.35 Equilibrium pictures on sample 5. . . . 226
D.36 Equilibrium pictures on sample 6. . . . 227
D.37 Equilibrium pictures on sample 7. . . . 228
D.38 Equilibrium pictures on sample 8. . . . 229
D.39 Equilibrium pictures on sample 9. . . . 230
D.40 Equilibrium pictures on sample 10. . . . 231
D.41 Equilibrium pictures on sample 11. . . . 232
D.42 Equilibrium pictures on sample 12. . . . 233
D.43 Equilibrium pictures on sample 13. . . . 234
D.44 Equilibrium pictures on sample 14. . . . 235

E.1 Lack of reproducibility in tests with the original design of the AC unit. . . . 236
E.2 Internal surfaces of the AC unit showing unwanted condensation. . . . 237
E.3 Change in the AC unit design. . . . 238

F.1 3D plot of the analytical expression for SDWP as a function of adsorption and desorption time. 242

List of Tables

3.1 Qualitative comparison of AWH technologies. 47

3.2 Acceptable chemical contaminants amounts in drinking water, according to WHO Guidelines for drinking-water quality and EU 2020/2184. 62

3.3 Acceptable microbiological contaminants amounts in drinking water, according to WHO Guidelines for drinking-water quality, and EU 2020/2184. 63

3.4 Acceptable physical contaminants amounts in drinking water, according to WHO Guidelines for drinking-water quality and EU 2020/2184. 63

4.1 Comparison of water uptake capacities of six CaAlg compositions at RH=34%. 66

4.2 Comparison of water uptake capacities of six CaAlg compositions at RH=47%. 67

4.3 Equilibrium models best-fitting parameters for CaAlg. 69

4.4 Equilibrium models best-fitting parameters for mesoporous silica-gel. 69

4.5 LDF-based models best-fitted parameters during adsorption. 73

4.6 LDF-based models best-fitted parameters during desorption. 74

4.7 Best-fitted parameters to account for temperature dependence in LDFDw model. 76

4.8 Best-fitted diffusivities of CaAlg and silica-gel samples. 78

4.9 List of produced and tested CaAlg compositions. 83

4.10 List of samples for which we have measured an isotherm at 30°C. 85

5.1 Parameters in the condensed water during the AWH campaign with CaAlg, compared with the limits from EU 2020/2184 and WHO Guidelines for drinking-water quality regulations. 99

5.2 Results of the experimental campaign with the CaAlg coating in the AWH device. 100

5.3 Analyses results of the water produced with CaAlg in the AD unit. 105

5.4 Results of the experimental campaign in the AD unit on CaAlg (CA) and mesoporous silica-gel (SG). 106

5.5 Desalination unit components. 119

5.6 Experimental campaign with the CaAlg coating in the AWH device. 120

5.7 SMAT analyses of the water produced with CaAlg in the AWH unit. 124

5.8 Desalination unit components. 128

5.9 Experimental campaign on CaAlg (CA) and mesoporous silica-gel (SG). 131

5.10 List of analysed water samples. 137

6.1 Results of the experimental campaign with the $CaCl_2$/silica-gel in the AC device. 145

6.2 AC unit components. 155

6.3 Actuators configuration during each phase in the AC unit. 157

6.4 Experimental campaign in the AC device. 160

Nomenclature

$\bar{C}$	Spatial-average adsorbate concentration (kg/m^3)
χ	Vapor quality (g/kg)
C	Adsorbate concentration (kg/m^3)
Q	Heat (W)
R_p	Particle radius (mm)
T	Temperature (°C)
t	Time (s)
w	Water Uptake (g/g)

Subscripts

0	Initial condition
Ads	Adsorption
aux	Auxiliaries
cond (CD)	Condensation
cycle	Adsorption + desorption + preparation phases
Des (Reg)	Desorption (Regeneration)
dry	Dry sorbent
env (amb)	Environment (Ambient)
eq	Equilibrium condition
evap (EV)	Evaporation
H_2O	water
hot	Heat provision loop used to drive desorption
in	Inlet
liq	Liquid
out	Outlet

PC Pre-Cooling

sat Saturation

thermal Thermal (referring to energy driving the process)

vap Water vapor

Acronyms / Abbreviations

AAD Adsorption-based Air Dehumification

AC Adsorption Chilling

AD Adsorption Desalination

ADS Adsorption

AWH Atmospheric Water Harvesting

BET Brunauer-Emmett-Teller

CaAlg Calcium Alginate

CD Condensation

COP Coefficient Of Performance

DAQ Data Acquisition

DES (REG) Desorption (Regeneration)

DR Dubinin-Radushkevich

DWP Daily Water Production (m^3/day)

EC Electrical Conductivity ($\mu S/cm$)

ED Electrodialysis

EER Energy Efficiency Ratio

EU European Union

EV Evaporation

FD Fick-Diffusion

FDRH Fick-based model with non-constant RH

FDSW Fick-based model with stepwise integration

FO Forward Osmosis

FPV First Principle Verification

GAB Guggenheim-Anderson-deBoer

HT High-Temperature

KPI Key Performance Indicator

LDF Linear Driving Force

LDFDw Linear Driving Force with Water uptake-dependent Diffusivity

LDFm Linear Driving Force with empirical modification

LT Low-Temperature

MD Membrane Distillation

MED Multi-Effect Distillation

MOF Metal Organic Framework

MSF Multi-Stage Flash distillation

MT Medium-Temperature

NaAlg Sodium Alginate

ND Nanofiltration

P&ID Piping and Instrumentation Diagram

PC Pre-Cooling

PCB Printed Circuit Board

PLC Programmable Logic Controller

PR Performance Ratio

PWM Pulse-Width Modulation

R Rejection Ratio

RH Relative Humidity (%)

RO Reverse Osmosis

RR Recovery Ratio

SCP Specific Cooling Power (W/kg)

SDWP Specific Daily Water Production (m^3/day/ton)

SEC Specific Energy Consumption (kWh/L)

SEM Scanning Electron Microscopy

SG Silica-gel

STEC Specific Thermal Energy Consumption (kWh/L)

TDS Total Dissolved Solids (mg/L)

TEC Thermoelectric Cooling

TOC Total Organic Content (ppm)

VC (VCD) Vapor Compression Distillation

WD Water Desalination

WHO World Health Organization

Chapter 1

Introduction

1.1 Fresh water scarcity: a global problem needing multiple tackling

According to UNICEF [1], four billion people suffer from water scarcity for at least one month a year. This is expected to worsen in the following decades, due to a combination of events such as the growth of world population and the global warming-induced increase in pro-capita water demand [2]. "*By 2040, almost 1 in 4 children will live in areas of extremely high water stress.*" [3] and, again, "*The number of countries with absolute water scarcity [...] is projected to increase from 25 in 2015 to 45 by 2050*" [1]. Furthermore, even when water resources are available, their quality is often too low for human consumption: contaminated water supplies can increase the risk of diseases like cholera and typhoid [2].
Fresh water scarcity not only is a threat for human health, but also exacerbates socioeconomic disparities. In developing regions like Sub-Saharan Africa, where water is not accessible on-site, people "*must rely on an alternative: walking to water*" [4]. This often takes even more than 30 minutes, being time consuming and physically exhausting, thus not sustainable.
In order to help countries implementing and monitoring strategies which should guide humanity towards a more sustainable future, in the September 2015 the UN General Assembly defined the 17 "Sustainable Development Goals", or SDGs: they may be thought as the natural successors of the previous Millennium Development Goals (MDGs), while still different from the other top-down approaches attempted in the past [5]. The SDGs objectives are often cross-linked, and countries are guided in the implementation of strategies through the evaluation of specific performance indicators for each goal.
The SDG n. 6, "Clean water and sanitation" [6], specifically addresses the water accessibility in the world. Among its targets:

- Target 6.1: “By 2030, achieve universal and equitable access to safe and affordable drinking water for all.”.
- Target 6.3: “By 2030, improve water quality by reducing pollution, eliminating dumping and minimizing release of hazardous chemicals and materials, halving the proportion of untreated wastewater and substantially increasing recycling and safe reuse globally.”.
- Target 6.7: "By 2030, expand international cooperation and capacity-building support to developing countries in water- and sanitation-related activities and programmes, including water harvesting, desalination, water efficiency, wastewater treatment, recycling and reuse technologies.".

Targets 6.1 and 6.7 can be addressed in different ways, some already cited in the very description of the tasks. Possible approaches to tackle water scarcity include:

- Water generation - achievable, for example, through atmospheric water harvesting. In this approach, liquid water is not available at all in the first place, and an engineering effort is needed to condense vapor into a usable fresh resource. This approach is particularly useful afar from coastal regions, where no liquid source of water is available: the humid atmosphere is indeed present above the totality of Earth’s surface, and liquid water can be extracted even in desert areas.
- Water treatment - achievable, for example, through desalination. In this approach, a liquid water resource already exists, but its properties make it unusable for drinking purposes. The engineering effort here consists in treating the feedwater, removing unwanted contaminants. This approach is particularly useful near coastal regions, for instance on islands, where seawater is largely available.

The two approaches involve very different thermodynamics and, with that, also the engineering and use costs are not comparable (water treatment has intrinsically lower costs than water generation). Nevertheless, as said above, they tackle the problem from two diverse fronts, and some contexts may be suitable for only one of the two technologies.
This research perfectly fits in this context: we propose a novel material, an adsorbent hydrogel referred to as "Calcium Alginate", that is able to selectively collect large amounts of water molecules and release them on demand by providing heat. This can be used to tackle the problem of fresh water scarcity through both the approaches introduced above: it can be integrated in adsorption-based Atmospheric Water Harvesting technologies to provide fresh water afar from coastal regions (Fig. 1.1a), or it can be used in adsorption-based Water Desalination plants for the treatment of existing water resources (Fig. 1.1b). In both cases, the correspondent device can be appropriately designed and sized to answer the local water

demand according to the water availability of the area.

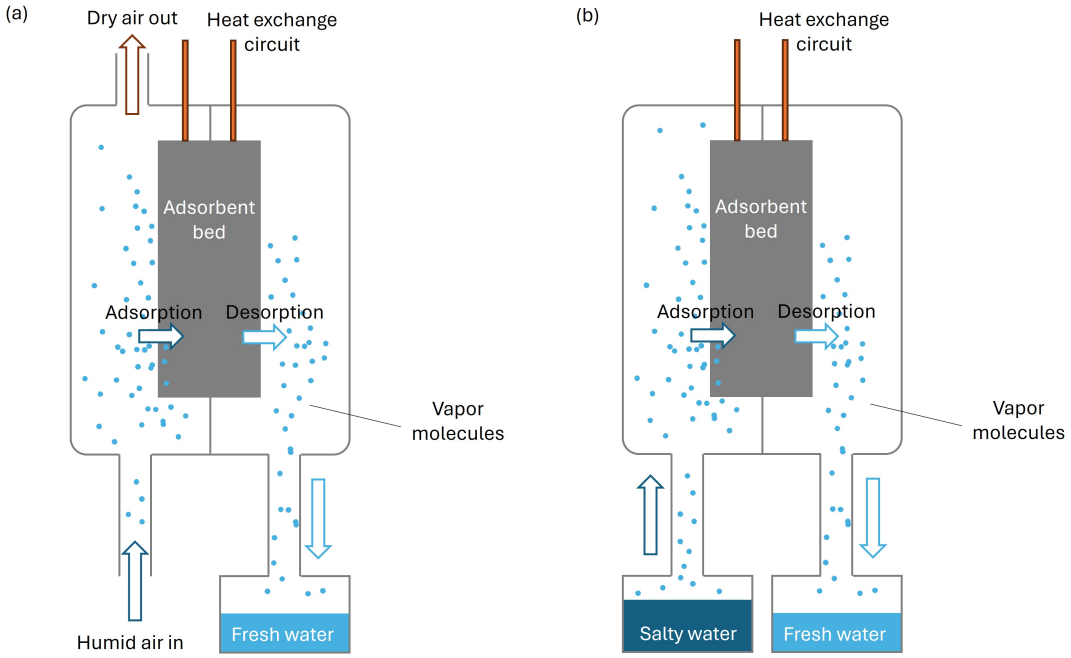

Fig. 1.1 Adsorption-based solutions for fresh water production. The diagrams are simplified: in real systems, typically, adsorption and desorption happen in separate working phases and with more complex designs, including valves and other actuators. (a) General concept of adsorption-based AWH: an open system is realized, in which humid air flows through a chamber containing adsorbent material, where vapor is collected; later, during desorption, vapor is released and condensed. (b) General concept of adsorption-based desalination: water evaporates and is collected by the adsorbent; later, during desorption, fresh water is released and condensed.

Materials such as silica-gels, zeolites and other conventional sorbents achieve similar effects. Nevertheless, unlike existing examples, calcium alginate has unique properties: its capacity to store water is relatively large, it can be used at low vapor pressures and low driving temperatures, and its production process is relatively cost-effective and scalable. Furthermore, it is bio-compatible and bio-degradable, making it an attractive alternative option to existing sorbents.

In order to achieve a water quality which is suitable for drinking uses, post-processing of the obtained water is typically required, no matter the used approach. In particular, target 6.3 can be achieved by using proper remineralization systems, together with an appropriate machine design which limits contamination. In this sense, calcium alginate provides a *good starting point* for meeting water quality requirements: it selectively adsorbs water molecules, leaving unwanted contaminants behind.

Last but not least, even if it may not be evident at a first glance, other global challenges are addressed by this work. For example, SDG n. 5, “Gender equality” is indirectly involved, too: indeed, the task of walking to water is very often accomplished by women [7]. Providing

easier access to water would help reducing gender inequality by removing the very need at the base.

1.2 A broader contextualization in the global energy outlook

Despite this research focuses on fresh water provision specifically, the achieved results can be useful to drive diverse research and improve other adsorption-based technologies (some of them are discussed in Chapter 2).
For example, adsorption-based air/water separation can be exploited for air treatment and conditioning in buildings, providing an alternative to active conditioning and helping in the objective of greenhouse emissions reduction. A study in 2022 [8] showed that air conditioning accounted for 1.95 Gtons of CO_2 released in 2020, i.e., almost the 4% of the overall global greenhouse emissions (Figure 1.2). This takes into account also the emissions associated with air conditioning technologies manufacturing (100 Mtons) and the refrigerant losses (720 Mtons). But even without considering these side contributions, the temperature and humidity controls alone account for over 1 Gton, of which 600 Mtons are related to humidity management. For this reason, scientist have already started working on raising efficiency and lowering emissions of dehumidification technologies [9, 10]. This research integrates in this context, introducing a material -calcium alginate- which has 3-4 times higher performance than common silica-gels in terms of equilibrium water uptake (i.e., amount of water collected per unit mass of material), and providing models for system design.
In Paris, 2015, over 190 countries agreed upon the idea that the human race is contributing heavily on the temperature increase: fossil fuels must be gradually left behind, because their use is introducing unsustainable amounts of greenhouse gases into the atmosphere. Unfortunately, the transition to other sources requires a significant effort. As N. Armaroli and V. Balzani efficaciously mention in “Energia per l’astronave Terra”, "*fossil fuels are a true treasure, found in the cargo hold of our spaceship*" [11]. In order to adapt to a world where energy cannot be provided anymore from such finite treasure, every possible strategy, from using different and more sustainable fuels to exploit the “hidden fuel” which is efficiency in energy management, is to be considered.

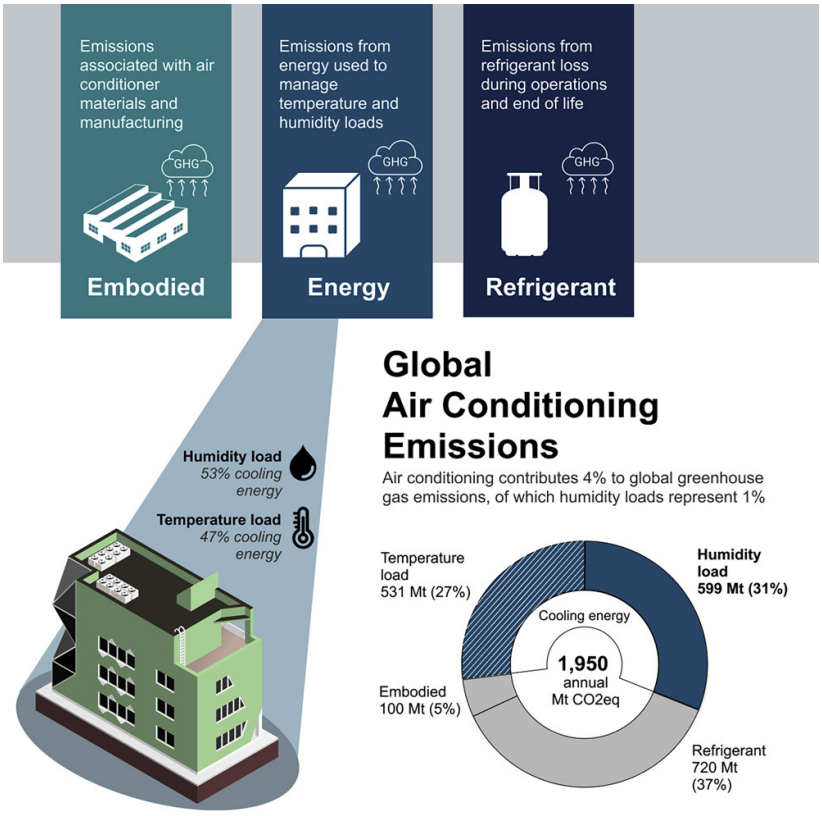

Fig. 1.2 Contributions in air conditioning emissions. Source: [8].

Different SDGs are touched when speaking of energetic efficiency in industrial and domestic contexts, like SDG n. 7 ("Affordable and clean energy") and SDG n. 11 ("Sustainable cities and communities"). But the most significant ones when speaking of technologies as the ones for air conditioning are:

- SDG n. 9, “Industry, innovation and infrastructure” [12]. It has 5 main targets, and the fourth one in particular says: “By 2030, upgrade infrastructure and retrofit industries to make them sustainable, with increased resource-use efficiency and greater adoption of clean and environmentally sound technologies and industrial processes, with all countries taking action in accordance with their respective capabilities”. It has as related indicator the amount of CO_2 emissions per unit of added value: this can be referred to a certain production area, or to the whole country.
- SDG n. 13, “Climate action” [13]. The second target, "Integrate climate change measures into policies and planning", has two indicators, one of which is “Total greenhouse gas emissions per year”: as said above, air conditioning accounts for a significant percentage of the overall gas emissions (almost 4%), so an effort should be made in order to optimize CO_2 equivalent emissions of such systems. CO_2 has a strong impact on climate change because it leads to a “chain reaction”: increase of CO_2 leads to increase in temperature due to greenhouse effect, and increase in temperature leads

to increase in CO_2 emissions due to higher release from the oceans and other effects [14]. Every possible action towards the direction of reduction of CO_2 emissions is urgent.

Both the points above can be addressed by acting upon the very technologies used for the manufacturing and air conditioning processes, and introducing more efficient ways to treat air for temperature and humidity content. In this sense, calcium alginate is a powerful resource: first, with its large water uptake capacities, it has a higher potential to control the vapor content in process air with respect to other conventional sorbents; second, it can be regenerated using low-grade waste heat from industrial processes, thus reducing the overall balance of CO_2 emissions.
A more sustainable water-air separation process is also a moral issue. If a technology requires high energy consumptions, it becomes unusable in areas where energy availability is low, like Sub-Saharan Africa [7]. In case of air conditioning, it prevents people from living in a healthy environment; in case of water availability, it becomes an even more life-threatening issue, as discussed in the previous section.

We can apply the above analysis to other technologies, like for instance adsorption-based Energy Storage. Most renewable sources are "intermittent", meaning that peaks of provision alternate with lack of energy for more or less prolonged periods of time. In this context, we need technologies able to store the excess energy and make it available when required, and adsorbent material can help in this. Showing that calcium alginate is able to durably and reversibly store large amounts of water, makes it a potential bio-compatible alternative to silica-gels or other common sorbents. Associated SDGs in this case include: SDG n. 7 ("Affordable and clean energy"), SDG n. 9 ("Industry, innovation and infrastructure"), SDG n. 11 ("Sustainable cities and communities"), SDG n. 12 ("Responsible consumption and production"), SDG n. 13 ("Climate action").

In general, the technology we propose pushes towards the directions of environmental sustainability (because of the expected reduction in CO_2 equivalent emissions) and energy equity (by lowering the energetic and social costs needed to provide domestic and industrial services such as air dehumidification and water availability). It also meets the criteria set by the EU taxonomy for being considered a sustainable investment, since an increase in energy efficiency is a "substantial contribution to climate change mitigation" [15]. In a world fearing for irreversible climate change effects, any possible action towards mitigation of the causes is useful and necessary. In this sense, research which aims at improving the existing knowledge about adsorption models and their application in air dehumidification, energy storage and water production, is a very important piece in the "big puzzle" of the future global energy panorama.

1.3 Thesis outline

A graphical representation of the thesis *fil rouge* is given in figure 1.3.

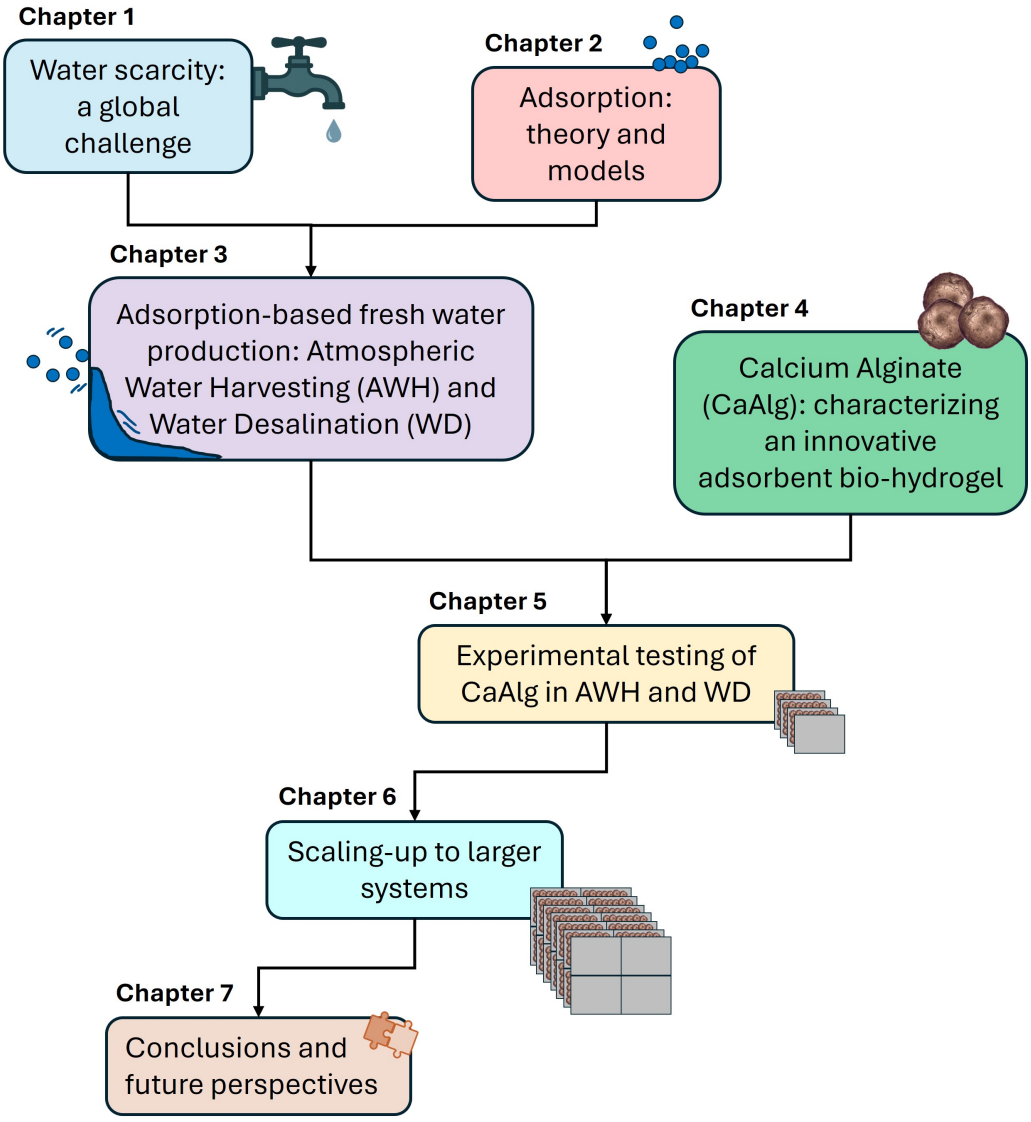

Fig. 1.3 Schematics of the thesis structure.

More in detail, this work is organized as follows:

1: The first chapter contains an introduction to water scarcity and the contextualization of this research in the global energy panorama.

2: The second chapter contains an overview of the *adsorption* process, including an introduction on the physical phenomenon and its applications. We introduce Calcium Alginate (CaAlg) as an alternative adsorbent material to other more commonly used (e.g., silica-gels). Adsorption models are then discussed, both for modeling equilibrium

behaviour of the sorbents and the dynamics of the adsorption and desorption transient phases. We introduce the theoretical models from the literature, and propose variations able to account for concentration-dependent diffusivity.

3: The third chapter contains an overview of the two analysed techniques to provide fresh water: Atmospheric Water Harvesting (AWH) and Water Desalination (WD), with specific attention to Adsorption-based Desalination (AD). State-of-the-art solutions are presented and compared. Finally, water quality standards are discussed.

4: The fourth chapter contains the experimental results on calcium alginate characterization, as achieved with this research. Diverse compositions are compared, and we select for further tests the ones with the best performance in terms of equilibrium uptake and dynamics. The isotherm curve of CaAlg is experimentally derived, best-fitted with equilibrium models and compared with sorbents from the literature. The diffusivity of CaAlg and the material aging are discussed. A *Methods* section describes the material synthesis procedure and the experiments on the compared samples.

5: The fifth chapter contains the experimental results on the use of calcium alginate in two prototypes for AWH and AD, as achieved with this research. For both technologies, the capability of CaAlg to produce fresh water is assessed: thermodynamic variables during repetitive machine cycling are commented, water productivity is discussed and compared to models' predictions, water quality is analysed and presented. Based on the observed performance, we propose a range of applications where CaAlg has higher potential than conventional sorbents. A *Methods* section describes the used prototypes and the chosen testing conditions.

6: The sixth chapter describes the work experience in the company Sorption Technologies, where an industrial-scale adsorption machine (AC unit) was designed and built, based on the testing results with CaAlg for desalination. Preliminary tests with the machine using conventional $CaCl_2$/silica-gel composite are discussed, and an extrapolation on the use of CaAlg is proposed. Preliminary economic considerations are provided.

7: The seventh chapter contains the main conclusions of this research and the future perspectives.

Chapter 2

Adsorption

2.1 Introduction

This chapter covers the fundamentals of adsorption, including materials, models and applications. First, a base overview on adsorption and adsorption theory is proposed, with specific focus on water vapor adsorbate. We list conventional and non-conventional sorbents, and introduce calcium alginate, a novel bio-derived adsorbent hydrogel that we explore in this research. We propose a list of applications based on the adsorption phenomenon.
Second, we present adsorption equilibrium models such as Langmuir, Dubinin-Radushkevich, Brunauer-Emmett-Teller, Guggenheim-Anderson-deBoer isotherms, that will be used to understand the behaviour of calcium alginate in equilibrium conditions.
Third, we present adsorption dynamics models, such as analytical and numerical Fick-diffusion based expressions, the Linear Driving Force model (LDF) and its variations, including a modified LDF model (LDFDw) that we propose as an extension of the base LDF model able to deal with larger uptake ranges. Dynamics models will be used to understand the behaviour of calcium alginate during charging and discharging transients.

2.1.1 Adsorption theory

Adsorption is a surface phenomenon in which molecules or ions from a fluid phase adhere to the surface of a solid material. The latter material is named "adsorbent" or "sorbent", while the substance being adsorbed is called "adsorbate" [16].

The pairs adsorbent-adsorbate vary according to the application. For example, notable pairs include MOF-CO_2, zeolite-oxygen, carbon-nitrogen [17, 18]. For this research, we are specifically interested in water vapor adsorption, i.e., adsorption where the adsorbate species is water vapor. Some porous materials like silica-gel offer a highly hydrophilic

surface, being able to bond with water molecules. While collecting water vapor, they increase their weight. It is convenient to introduce a performance indicator known as "water uptake", usually indicated with $w\ (g/g)$, measuring the amount of collected water per unit of sorbent [16]:

$$w = \frac{m_{H_2O}}{m_0} = \frac{m - m_0}{m_0} \tag{2.1}$$

where $m_{H_2O}\ (g)$ is the mass of water adsorbed by the material, $m_0\ (g)$ (or, sometimes in the literature, m_{dry}) is the mass of dry material (that is, the mass of the sorbent when ideally no water molecules are bound to the material), $m\ (g)$ is the total mass of the material (sum of m_0 and m_{H_2O}). The latter m is more useful for practical use with respect to m_{H2O}, since gravimetric sorption analysers normally measure directly the total mass of sorbent plus adsorbate, from which water uptake is indirectly calculated. The water uptake is typically expressed in g/g (grams of adsorbate over grams of dry adsorbent) or in percentage ($0.4\ g/g \rightarrow 40\%$).

The adsorption (ADS) process involves the creation of bonds between the water molecules and the sorbent, which is an exothermic process. On the other hand, the process of breaking the water-sorbent bonds is endothermic, and it is called "desorption" (DES), or "regeneration". Depending on the nature and strength of the attraction forces involved during adsorption, the process is generally classified, alternatively, as chemisorption or physisorption [19]:

- chemisorption, involving the formation of chemical bonds (covalent or ionic links) between adsorbent and adsorbate. It may require an activation energy (60-100 kJ per mol of adsorbate) and is associated to relatively high adsorption enthalpies (> 50 kJ per mol of adsorbate).
- physisorption, involving weaker physical forces (such as Van Der Waals interactions and hydrogen bonding). It is usually associated with relatively low heats of adsorption (< 50 kJ per mol of adsorbate).

Often, both processes contribute together to the overall adhesion of adsorbate molecules onto the sorbent species. In addition to these, further contributions are given by capillary condensation and possible changes in the material structure (happening, for instance, in case of rearrangement of polymeric chains), making modeling the phenomenon a complex task. Nevertheless, in the case of the interaction of water vapor with common sorbents like silica-gel, where multiple layers of adsorbate condensate on the surface of the sorbent, the process is predominantly classified as physisorption[1] [16]. The enthalpies of the adsorption processes focus of this research are usually in the order of the latent heat of vaporization of

[1]Even if the first layer formation might involve stronger chemical interaction, layers above the first one are characterized by an enthalpy of adsorption equal to the enthalpy of condensation of water vapor; under the hypothesis that most of the adsorption process occurs over multiple layers, where weaker condensation interactions are predominant, the contribution of chemisorption is negligible in the overall count.

water ($\approx 2430\ kJ/kg$ at 30°C, corresponding to $\approx 44\ kJ/mol$), providing further indication that these bonds are predominantly of physical nature.
At the nano-scale, the main physical interaction forces involved in physisorption can be mathematically modeled with Lennard-Jones potential [20]:

$$V(r) = 4\varepsilon \left[\left(\frac{\sigma}{r}\right)^{12} - \left(\frac{\sigma}{r}\right)^{6} \right] \tag{2.2}$$

where $V\ (K)$ is potential energy of the system made by two interacting particles, $r\ (m)$ is the distance between the centres of the particles, $\sigma\ (m)$ is a characteristic dimension of the order of the involved molecules, while $\varepsilon\ (J)$ is an indication of the amplitude of the attraction force. An equilibrium between the negative contribution (attraction) and the positive contribution (repulsion) is achieved when the resulting force is null. In particular, the final equilibrium distance r_{eq} can be evaluated as follows:

$$F(r) = -\frac{\partial V(r)}{\partial r} = 0 \qquad \rightarrow \qquad r_{eq} = 2^{\frac{1}{6}} \cdot \sigma \tag{2.3}$$

A typical order of magnitude for σ and, thus, of r_{eq}, in case of water-silica interaction, is 3 $\mathring{A}$, or 0.3 nm [20].
In practical contexts, we are interested in the effective behaviour of the material at the macroscale, rather than in the interactions at the molecular level. For this reason, larger-scale models using parameters such as diffusivity are available in the literature for modeling the charging and discharging transients, as well as the equilibrium behaviour. These are presented in sections 2.2.1 and 2.2.2, and will be used in the subsequent chapters to understand experimental results.

It can be experimentally observed that, if a sample of dry material is left in an environment with controlled temperature and relative humidity for a long time, the sorbent collects vapor (this process is properly called "adsorption") until it reaches an equilibrium condition. If the sorbent temperature increases and/or the vapor pressure decreases, the material tends towards a new equilibrium condition where less vapor is bound to the sorbent. This process ("desorption") can be used to release back the water vapor and prepare the material to the next adsorption. Desorption is typically driven by increasing the material's temperature (the provision of thermal energy helps breaking the water-sorbent bindings and the process is called "Thermal Swing Adsorption") and/or decreasing the vapor pressure around the material ("Pressure Swing Adsorption") [21]. This reversibility property is particularly useful in industrial processes, which require the material to undergo subsequent adsorption-desorption cycles in order to achieve the desired useful effect (see 2.1.4 for a list of applications).

2.1.2 Conventional sorbents for water vapor adsorbate

Several hydrophilic sorbents are known in the literature. Conventional sorbents include silica-gels, zeolites, activated carbon, activated alumina... In the following sections, silica-gel and zeolites, among the most commonly used sorbents, are discussed more in detail.

Silica-gel

Silica-gel is an amorphous form of silicon dioxide (SiO_2), which can be obtained through acid precipitation of sodium silicate [22]. It has significant vapor adsorption properties, explained with the high porosity (exposed surface area is usually in the range $600 - 900\ m^2$ per gram of material) and the presence of $-OH$ groups from silanol on the external surface, which create physical bonds with the water molecules (i.e., the adsorbate) [23]. Water uptakes capacities of up to 0.3-0.4 g/g at 30°C and Relative Humidity (RH) 70% have been observed [24].
Several variants of silica-gel exist, showing different pores sizes (from 2-3 $\mathring{A}$ to 200-300 $\mathring{A}$) and material appearance (e.g., various grain sizes, see Fig. 2.1a). The sorption properties change with the material's characteristics: mesoporous silica-gels exhibit faster adsorption rates and lower activation energy if compared to microporous ones [25]. The sorption equilibrium curves (showing the sorbent capacity at various temperature and vapor pressure conditions) change as well: different samples reach different water uptakes at fixed test conditions, possibly showing some hysteresis during the desorption process (Fig. 2.1b)
Base silica-gel and its variants are among the most used sorbents in adsorbent-based commercial applications, due to a series of advantages [23, 26]:

1. the synthesis process has a relatively low cost, and can be adapted to match different porous structures and host additives such as hygroscopic salts (see next section);
2. the material has a high thermal stability (up to 180°C, after which -OH groups detach from the sorbent surface);
3. the material has a good adsorption kinetics;
4. the material has a long-term stability to repetitive cycling, with minimal degeneration over time.

On the other hand, silica-gel has some limitations:

1. Optimal desorption temperatures are relatively high, up to 120°C [27];
2. The achieved uptake capacities are low when compared to other advanced materials.

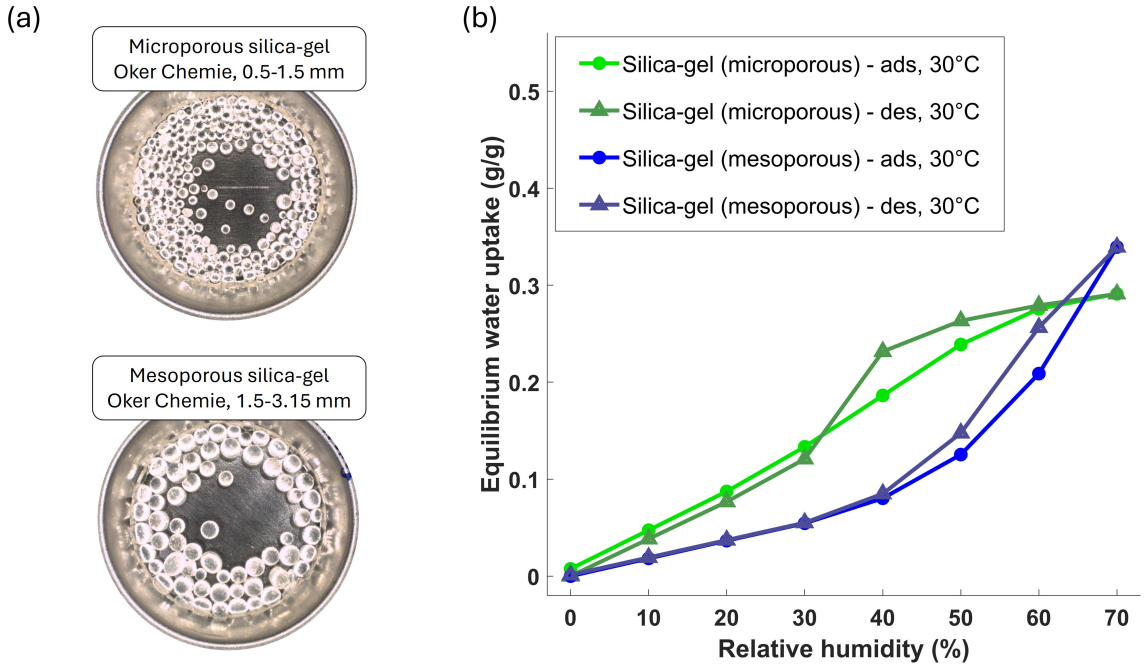

Fig. 2.1 Silica-gel introduction. (a) Microporous and mesoporous silica-gel beads from supplier Oker-Chemie. (b) Silica-gel equilibrium isotherms at 30°C, directly measured with a ProUmid vapor sorption analyser (see Chapter 4 for details).

Zeolites

Zeolites are a family of microporous crystalline aluminosilicates, including natural and artificial crystals. Some zeolites are found in nature and have been long-studied for their adsorption properties (Fig. 2.2a). They were named in the 18th century by mineralogist A. F. Cronstedt, who observed that stilbite releases water vapor when heated (from which the name "zeolite", literally "boiling stone" from ancient Greek language) [28, 29]. Zeolites are composed of tetrahedral $[SiO_4]^{4-}$ and $[AlO_4]^{5-}$ units linked by oxygen atoms and forming a rigid 3-dimensional framework, which does not collapse nor increase size when water vapor binds to the sorbent surface. In zeolites, the enthalphy of the desorption processe is typically high (e.g., 80 kJ/mol, suggesting stronger chemical binds), which make them an interesting choice for energy storage applications [30].
There exist many variants of zeolites, with the most used in industrial context being type A, type X (e.g., 3A, 4A, 5A, 13X, see Fig. 2.2b), ALPO and SAPO families (e.g., SAPO-34).

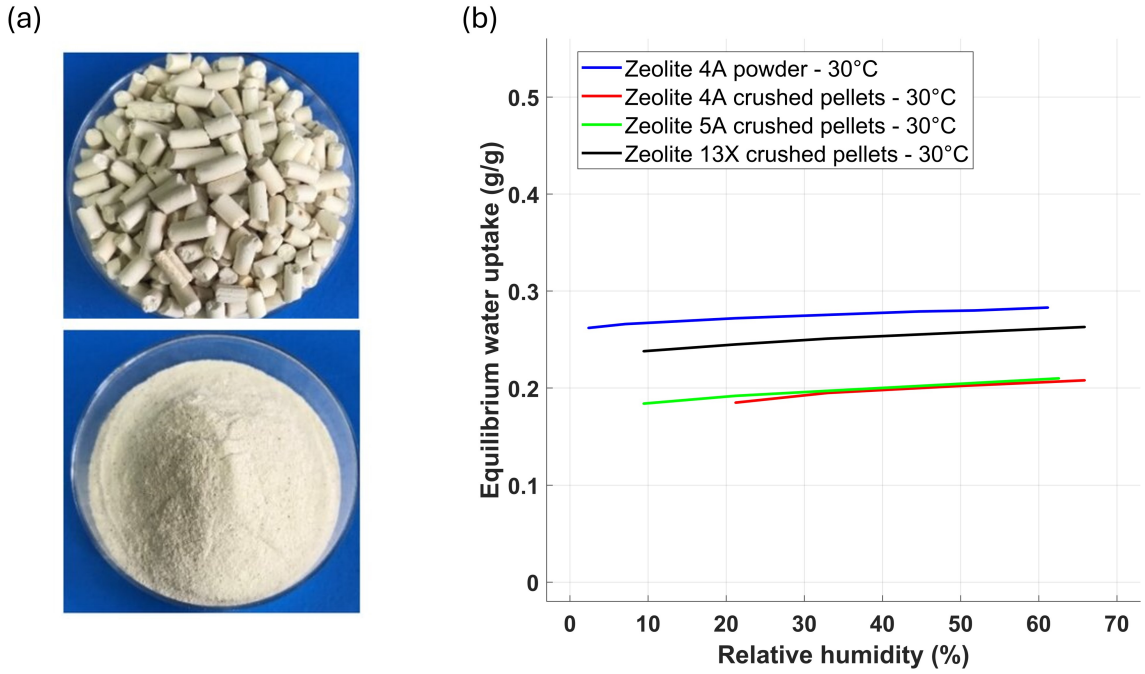

Fig. 2.2 Zeolites introduction. (a) Zeolite 13X samples, in pellets (top) and powder (bottom); the picture was extracted from [31]. (b) Zeolites isotherms at 30°C in comparison; original uptake data from [32].

Among the advantages of zeolite over silica-gels we list: high thermal stability (they can sustain over 600°C), high mechanical stability during adsorption and desorption cycles (due to the structure rigidity), fast kinetics [33]. On the other hand, zeolites show some limitations:

- their water uptake capacity is relatively low (e.g., 0.2 g/g for zeolite 5A at T=30°C and RH=60% [32]), if compared with silica-gel and other non-conventional sorbents;
- they require high desorption temperatures (up to 200°C) for the highest sorption potential to be exploited [33].

2.1.3 Calcium alginate and non-conventional sorbents for water vapor

Conventional sorbents exhibit interesting behaviour which make them suitable for many industrial applications (see next section for examples). Nevertheless, the competitiveness of a sorbent is challenged when alternative processes on the market can achieve similar results with lower cost. As an example, small water uptakes such as the ones achieved by standard silica-gel might not guarantee a sufficient level of dehumidification in industrial processes -unless using very large volumes of material-, and active chilling solutions become the best alternative options. The latter come with high-exergy sources use and carbon emissions due to the nature of traditional chilling. For these reasons, late research has focused on exploring

more complex alternative sorbents. Properties that are appreciated in a water vapor sorbent include:

- high adsorption capacity;
- fast adsorption kinetics;
- low environmental impact;
- competitive cost and scalability;
- low desorption temperature.

Composites

Water uptake capacity of base sorbents matrixes can be improved by hosting other phases. This is the case, for example, of cementitious composite materials such as PC-sepiolite, CAC-sepiolite, CSA-sepiolite (PC is the acronym for for Portland Cement, CAC for Calcium Aluminate Cement, CSA for Calcium Sulfoaluminate Cement), which have been demonstrated to be robust and cost-effective in adsorption-based energy-storage applications [34, 35].
Another common class of composites can be achieved by hosting hygroscopic salts in silica-gels. Such composites are typically synthesised via wet impregnation, where salts such as $CaCl_2$ or LiCl are dissolved in water and impregnated into silica-gel pores [36]. The sorbent is finally dried to form a homogeneous composite. The high water affinity of the salts, combined with the silica-gel sorption mechanisms, allows the composite to achieve water uptake capacities above 100% [37], resulting in a three-fourfold increase with respect to ordinary silica-gel. On the other hand, high vapor pressure can cause salt deliquescence: at large relative humidities (e.g., $> 70\%$) water molecules bind to the salt, forming a liquid solution that is lost from the matrix, irreversibly reducing the performances of the composite [38]. In general, in order for a sorbent to be industrially viable, stability over time is crucial: when working with hygroscopic salts, the cycling conditions must be controlled so that the composite does not change its structure over use.

MOFs

A Metal Organic Framework (MOF) is a porous crystalline material composed of metal ions or clusters coordinated with organic linkers [39]. MOFs were first synthesised by chemist Omar Yaghi at the end of the 20^{th} century; for such innovation, Yaghi has been recently rewarded with the Nobel Prize in Chemistry (2025), together with Susumu Kitagawa and Richard Robson [40].

MOFs have often high surface areas, even above 7000 m^2/g [41]. In general, their reticular structure is versatile, and pores sizes can be tuned to maximize the capability to selectively bind with water molecules. For instance, MOF-801 and MIL-101(Cr) have shown water uptake capacities over 1.0 g/g [42], comparable with silica-gel composites.
Advantages of MOFs compared to other conventional sorbents include high adsorption capacity and high adsorption kinetics, which can be achieved by properly tuning the parameters of the framework, such as pores volume. On the other hand, MOFs have some limitations [43]:

- high desorption temperatures are required to achieve optimal performance;
- cost and scalability: the synthesis of MOFs involve complex and expensive processes if compared with artificial zeolites and silica-gels production;
- stability concerns, with some MOFs degrading under prolonged exposure to moisture;
- health safety concerns, with some MOFs being potentially toxic to humans.

Calcium alginate

Composite polymers are advanced sorbents combining a base polymeric matrix with additives, such as hygroscopic salts, graphite and other fillers, to enhance their mechanical, thermal and adsorption properties [44]. Hydrogels are a subset of the polymers which can be used as matrix, particularly interesting for water vapor adsorption given their water-swollen networks nature. Some of them are versatile and have a high water adsorption capacity.

Among hydrogels, Calcium Alginate (CaAlg) has recently gained interest in scientific contexts. It is obtained by cross-linking Sodium Alginate (NaAlg), a polysaccharide derived from brown algae, with Calcium ions Ca^{2+} [45]. The crosslinking process is named ionotropic gelation, and generates polymer chains which propagate in the space according to the egg-box model (Fig. 2.3a,b,c) [46].
Further addivites such as graphite, bentonite, graphene oxyde can be added to the hydrogel matrix, allowing finer tuning of the sorption properties. In this sense, CaAlg is a family of possible composites, each uniquely identified by its specific composition and production procedure. More in particular, the choice of composition is made during the synthesis process of CaAlg beads, which requires to prepare and mix two jelly solutions: one containing water, Sodium Alginate (NaAlg) and possible addivites, the second one containing water and calcium chloride. As soon as the surfaces of the two solutions come in contact, Ca^{2+} ions from the second solution replace Na^{+} ions in the NaAlg structure, forming a gel, which is then dried in a oven to remove excess water. Further details on the production setup and procedure, as well as examples of production, are given in Chapter 4.

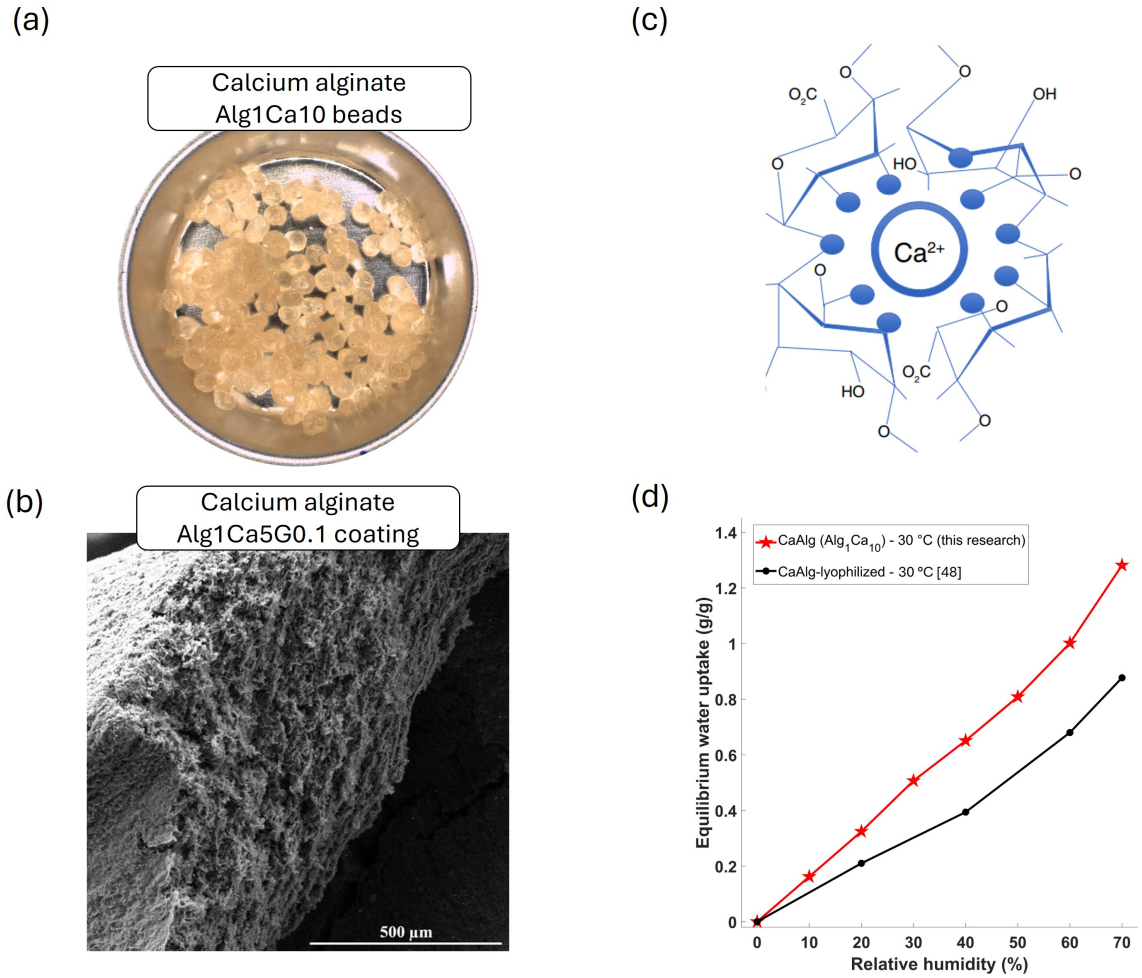

Fig. 2.3 Calcium alginate introduction. (a) Picture of CaAlg beads. (b) SEM of CaAlg+graphite coating [47]. (c) Egg-box structure. The picture was extracted from [46]. (d) CaAlg isotherms, from this research and from [48].

Calcium alginate exhibits exceptional water vapor adsorption capacities, in some cases higher than 120% at RH=70% and T=30°C, due to their porous structure and hydrophilic nature [24] (Fig. 2.3d). They exhibit reversible adsorption-desorption cycling behaviour with typically low hysteresis, making them a potential alternative for industrial applications [24]. Compared to conventional sorbents, calcium alginate has a series of unique advantages:

- biocompatibility, making it a sustainable and environmental-friendly alternative [49–52].
- the composition can be tuned to optimize adsorption properties [46];
- its reversible adsorption capacity is high if compared with other conventional and non-conventional sorbents, reaching more than a fourfold increase with respect to ordinary silica-gel;

- CaAlg regeneration can be driven using low temperatures (40-80°C), making it an option for integrating adsorption-based technologies with ultralow-grade waste heat contexts.

On the other hand, further research is necessary to understand and possibly eliminate some limitations, including: low thermomechanical stability, degradation of the material under stressful environment (such as cycling under vacuum for adsorption-based water desalination), variable production costs.
This work aims at filling some of these gaps, providing experimental evidence of the use of optimized CaAlg hydrogel in diverse contexts: under environmental pressure for atmospheric water harvesting, and under vacuum for water desalination.

2.1.4 Applications of water vapor adsorption machines

Vapor adsorption can be exploited in a series of applications, either open-cycle or closed-cycle depending on whether new vapor is introduced from the external environment during the machine operation. The most common are listed below. In this work, we also distinguish applications according to their "scale". We say that an adsorption system is a "small-scale" application when the amount of sorbent is below 2 kg, "medium-scale" when the amount of sorbent is between 2 kg and 150 kg, "large-scale" when the amount of sorbent is above 150 kg.

Atmospheric water harvesting

Given their high water affinity, sorbents like silica-gel composites and calcium alginate hydrogels are suitable for the extraction of water molecules from gas-vapor mixtures. This technique finds immediate application in Atmospheric Water Harvesting (AWH), that is the extraction of fresh water from the Earth's atmosphere, potentially allowing the provision of fresh water in areas afar from coasts, where water shortage is a serious problem. This application is explored in detail in Chapter 3.

Water desalination

The high water affinity of adsorbent materials can be leveraged to transport vapor molecules: first, water evaporates and it is adsorbed by the material; later, water is desorbed from the material and it is condensed in a separate container. This technique can be used to selectively evaporate water molecules from a salty solution (e.g., seawater, or brackish waters), leaving the salt behind and producing a desalination effect. This application is explored in detail in Chapter 3.

Air dehumidification

Adsorption-based Air Dehumidification (AAD) exploits the water affinity of sorbents to remove moisture from air. The base principle is similar to Atmospheric Water Harvesting, with the difference that the main useful effect is on the air flow decrease of vapor content and not in the water collection.
In AAD, an open-cycle configuration is typically realized, where external air is passed through a desiccant bed. The specific system configuration may vary, including rotary desiccant wheels, packed beds and coated heat exchangers. Part of the water vapor contained in the input air binds to the sorbent's pores, reducing the relative humidity of the air flow while increasing its temperature (given the exothermic nature of adsorption). In case of domestic use, the air stream is then post-humidified and heated to meet the requirements for the human well-being. Typically, to increase the system's efficiency, the heat of adsorption is recovered and used to pre-heat the returning air stream used for the desorption of the material.

Chilling

Adsorption-based chilling -or simply Adsorption Chilling (AC)- is a technology that exploits the evaporation enthalpy of water vapor to produce a cooling effect. The role of the sorbent is to facilitate the evaporation process: by adsorbing water vapor, it creates a local depression which drives the evaporation of further vapor. The adsorption phase is followed by an isosteric heating (during which the sorbent is pre-heated at constant water uptake, using an external low-grade energy source), then the desorption phase (during which water condenses back), and finally an isosteric cooling (where the sorbent is cooled-down at constant water uptake, in preparation for the subsequent cycle). The cycle is repeated, typically on at least two adsorption beds alternately, so to guarantee a continuous cooling effect: while one bed desorbs, the other adsorbs and produces a cooling effect, and viceversa.
As described above, the adsorption and desorption processes are, respectively, exothermic and endothermic: as the adsorbate molecules bind to the sorbent surface, heat is released; viceversa, as the binds break during desorption, heat is absorbed by the material. An important KPI usually defined for AC systems is the thermal Coefficient Of Performance:

$$COP_{thermal} = \frac{Q_{evap}}{Q_{hot}} \tag{2.4}$$

where Q_{hot} is the heat provided at high temperature to drive the desorption process, while Q_{evap} is the heat of evaporation (chilling effect). Since adsorption and desorption enthalpies for the water/silica-gel and water/calcium alginate pairs ($\approx$ 2600 kJ/kg at 30°C [24]) are comparable to the enthalpy of condensation of water ($\approx$ 2430 kJ/kg at 30°C), the ideal thermal efficiency of the system is close to 1. In real system, COPs are closer to 0.3-0.5 (see chapter 6), due to inefficiencies in thermal losses while driving the machine.

Note that this indicator is different from the COP in conventional compression-cycle chillers, where that is defined as the ratio between cooling effect and input electrical power. An equivalent indicator in case of adsorption chillers is instead the EER: Energy Efficiency Ratio. This is defined as the ratio between cooling power Q_{evap} and electrical power used to run auxiliaries E_{aux} [37], like pumps, valves, and control cabinet:

$$EER = \frac{Q_{evap}}{E_{aux}} \tag{2.5}$$

Energy storage

Adsorption-based Energy Storage is a solution that exploits the adsorption and desorption enthalpies of sorbent materials to store and release back low-grade thermal energy [53]. Suppose to have a thermal source (e.g., solar panels system, or cooling water exiting from a power production plant): such source can be used to drive a sorbent's desorption phase and break the bindings with water vapor. At this stage, the sorbent is ready to adsorb more vapor; thus, when energy is required by the user, the sorbent can be put in communication with a tank containing water that, evaporating, is adsorbed back by the material. The latter step is exothermic, and the released heat can be collected and used for other aims (e.g., post-heating in HVAC solutions). Energy storage densities ranges in $10^2 - 10^3\ kWh/m^3$ [53], surpassing the sensible heat storage capabilities of simple water tanks ($10 - 50\ kWh/m^3$). Furthermore, such potential energy can be stored at low temperature for long time, since the start of the adsorption process is activated on-demand by acting on proper valves in the system, making adsorption-based energy storage a viable technology in the context of a sustainable energy transition.

2.2 Adsorption models

2.2.1 Equilibrium models

If a sorbent is left under controlled temperature and relative humidities conditions for sufficiently long time[2], an equilibrium condition is met, where no net amount of water vapor binds or leaves the material surface until new energy is exchanged with the system. By repeating the experiment under different temperature and pressure conditions, it is possible to build a series of equilibrium curves such as:

[2]In principle, an infinite time would be needed to reach equilibrium in a continuous capacitive process. In real cases, equilibrium criteria are defined, where the material is considered in equilibrium if the water uptake changes by less than an arbitrary amount in a fixed time interval.

- isotherm curve: temperature is kept constant, while vapor pressure is changed step-by-step and equilibrium water uptake is registered (Fig. 2.4a);
- isobaric curve: vapor pressure is kept constant, while temperature is changed step-by-step and equilibrium water uptake is registered (Fig. 2.4b);
- isosteric curve: temperature and vapor pressure are slowly changed together, such that the equilibrium water uptake in the material stays constant (Fig. 2.4c).

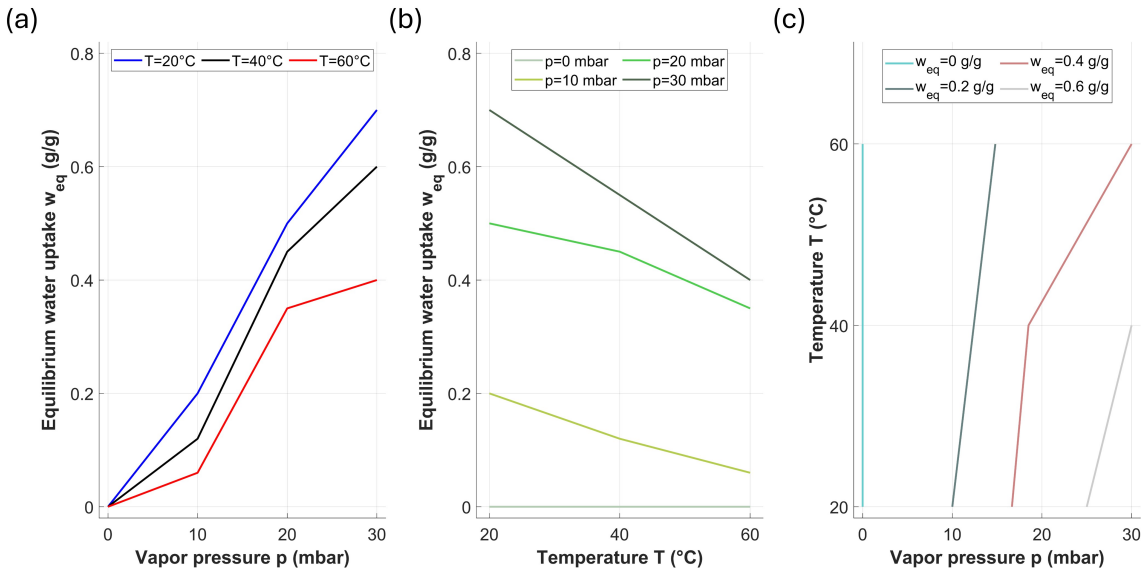

Fig. 2.4 Types of adsorption equilibrium curves. Plotted data is quantitatively fictional, but the behaviour is qualitatively correct and coherent among the three graphs. (a) Isotherm curve: temperature is constant, pressure and uptake at equilibrium are noted. (b) Isobaric curve: pressure is constant, temperature and uptake at equilibrium are noted. (c) Isosteric curve: uptake is constant, temperature and pressure at equilibrium are noted.

Note that the three equilibrium curves provide the same amount of information associated to the relationship between temperature, vapor pressure and equilibrium water uptake: in principle, it is possible to derive one from the other, if sufficient experimental data is available (including possible hysteresis) and if the results are not dependent on the nature of the method used to measure the material properties.

In this research, we chose to use isotherm curves to describe the equilibrium properties of the studied adsorbents. Due to capillary condensation causing hysteresis, an isotherm curve is not necessarily identical if measured by increasing or decreasing relative humidity. For this reason, it is often specified whether experimental curves are "adsorption" or "desorption" isotherms (respectively, in case of increasing and decreasing RH). Temperature T is kept constant during the construction of an isotherm, and so is saturation vapor pressure $p_{vap,sat}$, which is only function of temperature, e.g. according to Antoine equation [54]:

$$p_{vap,sat} = e^{A - \frac{B}{C+T}} \tag{2.6}$$

with $A = 23.4776$, $B = 3984.92$°C, $C = 233.426$°C, T expressed in °C and $p_{vap,sat}$ expressed in Pa.
For this reason, the horizontal axis in a single-isotherm plot can alternatively show vapor pressure p_{vap} or relative humidity RH without the isotherm shape being affected, since they are directly proportional by definition:

$$RH = \frac{p_{vap}}{p_{vap,sat}(T)} \tag{2.7}$$

In this work, we choose to use RH as horizontal axis for representing all isotherms.
Several models for isotherm curves have been developed over the years, and the choice of a model over another depends on the quality of information that is desired and on the hypotheses under which the adsorption process happens. For example, the base Langmuir isotherm [55] is a suitable model when a single-layer of adsorbate binds to the sorbent, but lacks in accuracy when multiple layers cumulate; on the other hand, empirical expression such as the Freundlich isotherm [55] might best-fit experimental data with minor error with respect to Langmuir under multiple-layer adsorption, but lose in physical interpretation of the isotherm parameters.
Isotherms are typically classified according to their shape (Fig. 2.5), strictly related to the characteristics of the adsorption process [56]:

- type-I: concave to the horizontal axis and approaching a limit adsorption value at very low relative pressure (often, < 0.1). The adsorption mechanism leading to this type of isotherm is the filling of sorbent pores by the adsorbate. It is often associated with microporous materials.

- type-II: presenting a sigmoid shape with a change of concavity. The first concave section models monolayer formation; then, successive layers form and the overall uptake continue to increase. It is often associated with macroporous materials.

- type-III: convex to the horizontal axis, it only models the adsorbate formation of multiple layers. It is often associated with macroporous materials which do not exhibit strong adsorbent-adsorbate interaction forces (with respect to adsorbent-adsorbent interaction forces), thus not leading to the formation of a defined monolayer.

- type-IV: analogous to type-II isotherm, but with hysteresis in the desorption trait at medium-high pressures. It models capillary condensation, where the meniscus formation on pore walls prevent vapor molecules to leave the sorbent unless sufficient energy is provided. It is often associated with mesoporous materials.

- type-V: analogous to type-III isotherm, but with hysteresis in the desorption trait at medium-high pressures. It models capillary condensation and weak adsorbent-

adsorbate interaction forces. It is often associated with microporous and mesoporous materials.

- type-VI: showing successive adsorption steps, each corresponding to one-layer formation. They are usually associated with nonporous surfaces.

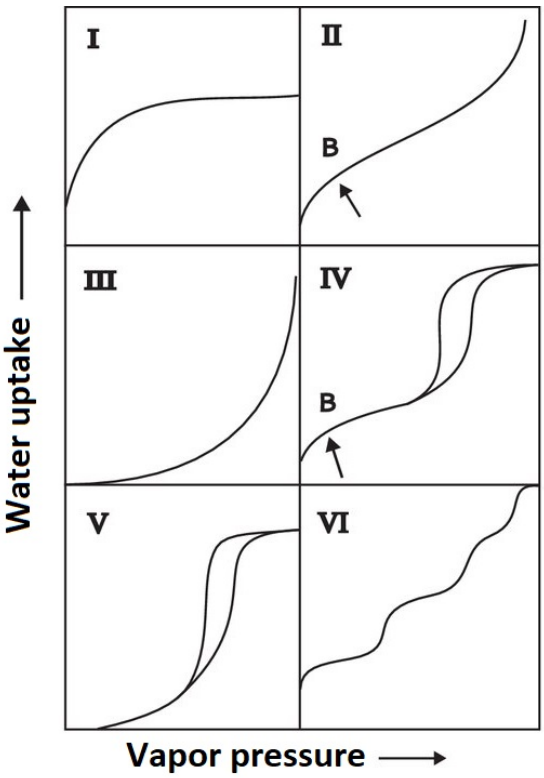

Fig. 2.5 Isotherms classification according to IUPAC and ISO 9277. The image has been adapted from [56].

In the next paragraphs, we introduce some significant models that we will use to understand the experimental results in the later chapters.

Langmuir isotherm

The Langmuir isotherm [55] is historically the first model non purely empirical, derived under the physical assumption that, under equilibrium, the adsorption rate matches the desorption rates. Further assumptions include:

1. only a single layer of adsorbate can bind to the sorbent;
2. the adsorbate-adsorbate interaction is negligible, thus the only driving force is given by the interaction with the sorbent sites;

3. the adsorption process is fully reversible (thus, the model does not account for hysteresis);

4. all adsorption sites on the sorbent surface have the same chance of being occupied.

In particular:

- Adsorption rate dw/dt is assumed proportional to the vapor pressure p_{vap} and to the amount of available sites for the adsorbate to land on:

$$\frac{dw}{dt} = k_a \cdot p_{vap} \cdot \left(1 - \frac{w}{w_{max}}\right) \tag{2.8}$$

  being k_a a proportionality constant and w_{max} the uptake corresponding to all sorbent sites occupied.

- Desorption rate is assumed as directly proportional to the amount of occupied sites, thus proportional to water uptake:

$$\frac{dw}{dt} = k_d \cdot \frac{w}{w_{max}} \tag{2.9}$$

  where k_d is a proportionality constant.

By imposing the equilibrium condition Eq. 2.8 = Eq. 2.9, the Langmuir isotherm equation is derived:

$$w = w_{max} \cdot \frac{K \cdot p_{vap}}{1 + K \cdot p_{vap}} = w_{max} \cdot \frac{K \cdot RH \cdot p_{vap,sat}}{1 + K \cdot RH \cdot p_{vap,sat}} \tag{2.10}$$

where the constant $K = \frac{k_a}{k_d}$ is a function of temperature T and can be expressed according to an Arrhenius-like form:

$$K(T) = K_0 \cdot e^{\frac{H}{RT}} \tag{2.11}$$

where R is the universal gas constant (8.314 J/kg/mol), H is an equivalent process enthalpy and K_0 is dependent on the saturation molar integral entropy of adsorption [57].

Dubinin-Radushkevich isotherm

Unlike the Langmuir isotherm, Dubinin-Radushkevich model (which is based on Polanyi potential theory [58]) accounts for the heterogeneity of micropores sizes and energies [55]. It is derived under the hypothesis that the adsorption energy follows a Gaussian distribution [59], and has the following expression:

$$w = w_{max} \cdot e^{-\beta\varepsilon^2} = w_{max} \cdot e^{-\beta \cdot \left[\frac{RT \log\left(\frac{1}{RH}\right)}{H}\right]^2} \tag{2.12}$$

being $\varepsilon = \frac{RT\log(\frac{1}{RH})}{H}$ the Polanyi potential, $\beta = \frac{1}{2E^2}$ a constant associated to the binding energy E (a value of E lower than 8 is associated with physisorption).

Brunauer–Emmett–Teller isotherm

The Brunauer-Emmett-Teller (BET) isotherm is used to model multilayer vapor adsorption [60]. It is conceived as an extension of Langmuir model, which keeps a physical meaning since it is derived under equilibrium assumptions. The model hypotheses include:

1. Lateral adsorbate-adsorbate interactions are negligible (instead, vertical interaction is taken into account, see Fig. 2.6)

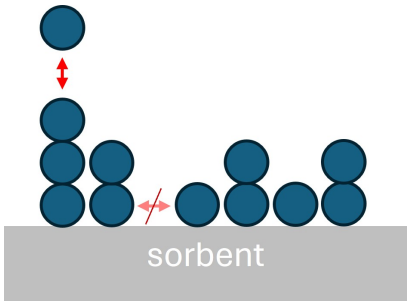

Fig. 2.6 BET model assumptions on multilayer interactions. The BET model accounts for multilayer formation, but only considers vertical interactions between adsorbate particles (blue spheres), while horizontal ones are neglected.

2. each layer of adsorbate is in equilibrium according to Langmuir model.

The BET isotherm has the following expression:

$$w = \frac{w_m \cdot c \cdot RH}{(1-RH)\cdot[1+RH\cdot(c-1)]} \tag{2.13}$$

where w_m is the monomolecular layer uptake and c is the main adimensional BET coefficient, correlated to adsorption enthalpy H_{Ads}. In particular, c can be expressed as follows:

$$c = e^{\frac{H_{Ads}-H_{vap}}{RT}} \tag{2.14}$$

where H_{vap} is the latent heat of evaporation at the considered temperature T. A c larger than 2 is typically coherent with a type-II isotherm [61].
The BET isotherm is particularly effective in modeling adsorption for $RH < 35\%$, while it lacks precision for larger RH ranges.

Guggenheim-Anderson-deBoer isotherm

A generalization of the BET isotherm is the Guggenheim-Anderson-deBoer (GAB) model. It is particularly useful to describe multilayer sorption on heterogeneous surfaces (thus keeping the advantages of the BET model) [62], but the introduction of a further parameter rescaling RH makes it a better fit for larger relative humidity ranges:

$$w = \frac{w_m \cdot c \cdot K \cdot RH}{(1 - K \cdot RH) \cdot [1 + K \cdot RH \cdot (c - 1)]} \tag{2.15}$$

The resulting semi-empirical model still keeps a physical interpretation, with the type of isotherm not being affected by a rescaling along the horizontal axis. The coefficient c can still be estimated using eq. 2.14. On the other hand, using the GAB model requires to best-fit a further parameter K, whose value must be verified to be comprised between 0 and 1 for the model validity to be confirmed. Given the "S" shape assumed by the model curve, the GAB isotherm is particularly useful to best-fit type-II and type-III isotherms.

2.2.2 Dynamics models

Equilibrium models allow to understand the sorbent's capacity under various conditions; nevertheless, they do not provide information about characteristic times of the adsorption and desorption phenomena. In general, being adsorption a capacitive phenomenon, the total amount of adsorbate molecules occupying a given sorbent mass will increase asymptotically over time: the less adsorbate in the material, the higher the potential for new molecules to bind is (with the material pores filling, the available sites decrease and it is more difficult for new adsorbate to bind). The opposite happens during desorption, where water molecules gradually leave the material: their tendency to leave is higher when the amount of adsorbate bound to the sorbent is higher. For this reason, we can expect ADS and DES dynamics curves to look like as in Fig. 2.7a.
Having short characteristic times for the adsorption phenomenon is crucial for industrial applications, where the adsorption-based machine dynamics should be fast enough for the machine to be competitive over successive cycles (Fig. 2.7b). In practice, the speed at which the vapor occupies sites in the sorbent strongly depends on the type of sorbent (e.g, pore sizes and distribution, vapor affinity, volumetric diffusivity, and so on) and the testing conditions (working under vacuum might speed up the process because less gaseous molecules are hindering the vapor movements).

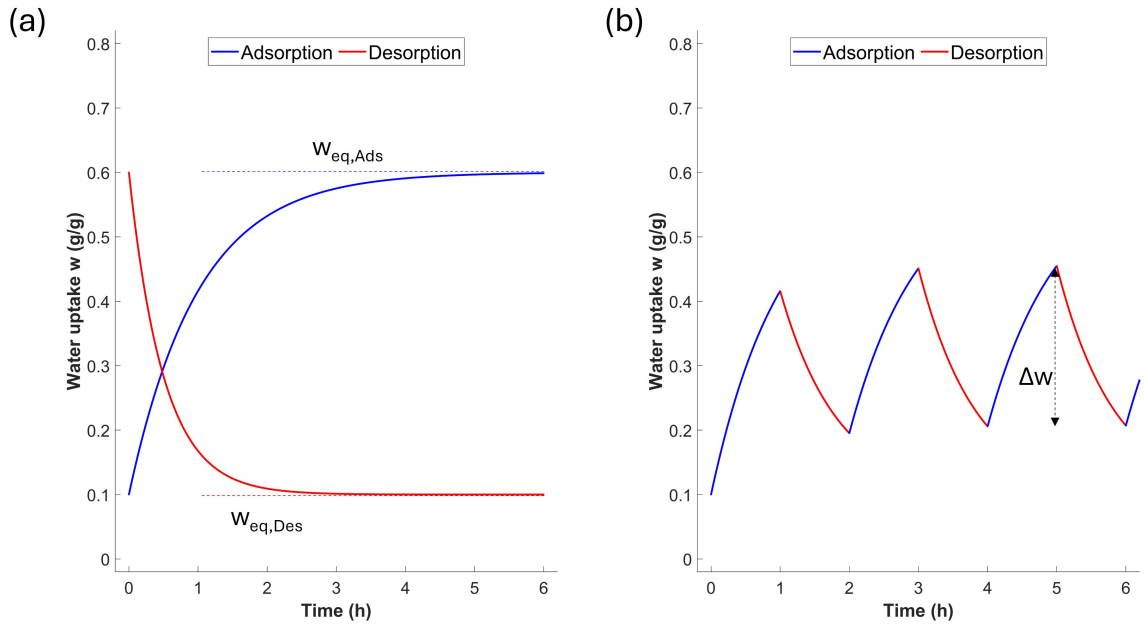

Fig. 2.7 Adsorption and desorption transients. (a) A qualitative example of adsorption and desorption curves, where the asymptote at equilibrium is shown. (b) A qualitative example of repetitive ads-des cycling, where the water uptake difference Δw between charged and discharged conditions is highlighted.

The dynamics of adsorption and desorption phenomena was modeled in multiple ways in the past literature. For this research, we will focus on two families of expressions:

A) Fick-Diffusion (FD) based models, a class of analytical and numerical expressions which model adsorption as a purely diffusive phenomenon, thus obeying Fick's laws. Their theoretical validity is justified by the accuracy of diffusion laws, but for practical applications they often result of complex use.

B) Linear Driving Force (LDF) based models, a class of simpler models which find justification in the capacitive nature of the phenomenon or, alternatively, can be derived from Fick's laws under further assumptions. Despite the semi-empirical nature, they allow a precise modeling of the adsorption and desorption dynamics while still preserving a physical interpretation.

Fick-diffusion

Fick's first law (1855) states that *the rate of transfer of diffusing substance through unit area of section is proportional to the concentration gradient measured normal to the section* [63]:

$$J = -D \cdot \frac{\partial C}{\partial n} \tag{2.16}$$

where J $(kg/m^2/s)$ is the mass rate of diffusion of substance per unit area, C (kg/m^3) is the substance concentration, n (m) is the direction normal to the reference section along which diffusion happens, and D (m^2/s) is defined as a proportionality coefficient and named "diffusivity" (or "diffusion coefficient"). The minus sign in eq. 2.16 expresses the physical fact that a decreasing concentration implies a positive transfer of mass (see Fig. 2.8a). Note: in this formulation D is a scalar and it can be in general dependent on time, space and concentration; the expression is written under the hypothesis of isotropic material, where the diffusivity is not dependent on the direction of diffusion, and the latter always happens along a direction parallel to the normal to the surface. In case of anisotropic material, the equation must instead be written redefining D as a 2nd order tensor (see [63]).

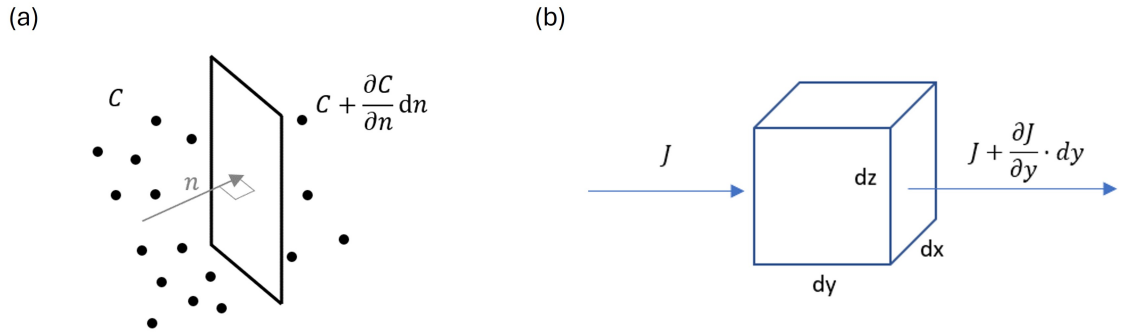

Fig. 2.8 Geometry for Fick's laws derivation. (a) Normal direction to the reference diffusion surface. (b) Elementary volume used to write a mass balance and derive the 2nd Fick's law.

By writing a substance flow mass balance around an elemental volume of material (Fig. 2.8b) and using eq. 2.16, the second Fick's law can be derived:

$$\frac{\partial C}{\partial t} = \nabla \cdot (D \nabla C) \tag{2.17}$$

where $\nabla\cdot$ and ∇ are divergence and gradient space differential operators, respectively. Under the hypothesis of a D constant with time, space and concentration, the equation becomes:

$$\frac{\partial C}{\partial t} = D \cdot \nabla^2 C \tag{2.18}$$

If the system has spherical symmetry, the Laplace operator can be written in polar coordinates, and concentration is only function of time and radial distance r from the centre of the system:

$$\frac{\partial C}{\partial t} = D \cdot \left(\frac{\partial^2 C}{\partial r^2} + \frac{2}{r} \cdot \frac{\partial C}{\partial r} \right) \tag{2.19}$$

Under proper assumptions, equation 2.19 is a good candidate for modeling adsorption and desorption of water vapor on spherical beads of sorbent. In particular, to apply most of the known solutions, the following hypotheses must be verified:

1. adsorption is approximated as a purely diffusive process (in reality, as above explained, the process is more complex and often accompanied by further mechanisms, like capillary condensation);
2. beads are approximated as homogeneous spheres of radius R_p (in reality, sorbent beads are "pseudo-spheres", with rough and irregular surfaces, and the "grain size" is the quantity specified in alternative to diameter);
3. beads are considered as single crystalline particles (in reality, they are an aggregate of portions separated by pores);
4. the material is isotropic;
5. diffusivity D is constant;
6. the external surface of the spherical beads matches the external vapor concentration immediately (no inertia due to the formation or breaking of bounds is considered);
7. the spherical radius R_p does not change with concentration.

Supposing that the environment in which the material performs is sufficiently large, such that it is not influenced by the adsorption process happening in the material ("infinite" source of adsorbate, e.g. the Earth's atmosphere), the concentration of adsorbate around the material can be considered constant over time and equal to C_∞. The same condition is realized for smaller environment's with an active control of adsorbate concentration. Thus, according to previous hypothesis 6), the concentration of adsorbate C_∞ can be found at radius $r = R_p$. Due to intraparticle diffusion, the concentration reached by the whole material at equilibrium C_{eq} will be equal to C_∞, too. The sorbent is supposed to have an initial adsorbate concentration uniformly distributed over the entire volume, with value C_0. Then, Fick's 2nd law and the necessary initial and boundary conditions can be written as:

$$\begin{cases} \frac{\partial C}{\partial t} = D \cdot \left(\frac{\partial^2 C}{\partial r^2} + \frac{2}{r} \cdot \frac{\partial C}{\partial r} \right) \\ C(r, t = 0) = C_0 \qquad \forall r \\ C(r = R_p, t) = C_{eq} \qquad \forall t \\ \left(\frac{\partial C}{\partial r} \right)_{r=0} = 0 \end{cases} \tag{2.20}$$

The latter boundary condition is written in order to preserve the spherical symmetry while still guaranteeing a continuous and derivable function for C when moving from a hemisphere to the other through the center. The problem can be proved to have analytical solution in

terms of an infinite sum (see [63]), as follows:

$$C(r,t) = C_0 + (C_{eq} - C_0) \cdot \left\{ 1 + \frac{2R_p}{\pi r} \cdot \sum_{n=1}^{\infty} \left[\frac{(-1)^n}{n} \cdot \sin\left(\frac{\pi n r}{R_p}\right) \cdot e^{-\pi^2 n^2 \left(\frac{D \cdot t}{R_p^2}\right)} \right] \right\} \quad (2.21)$$

The expression can be used to know the theoretical local concentration at any radius, at any moment. For instance, it's easy to show that the expression outputs C_{eq} if evaluated at $r = R_p$ (since the sin inside the infinite sum goes to 0 for every n), according to the second imposed condition. It is possible, but less immediate, to verify the other conditions too. Note that, for $t \to \infty$, $C \to C_{eq}$, meaning that after a sufficiently long time the whole sphere reaches a uniform equilibrium with the environment, at any radius. In figure 2.9 we show the concentration trend over the radius r of the particle, at different time instants:

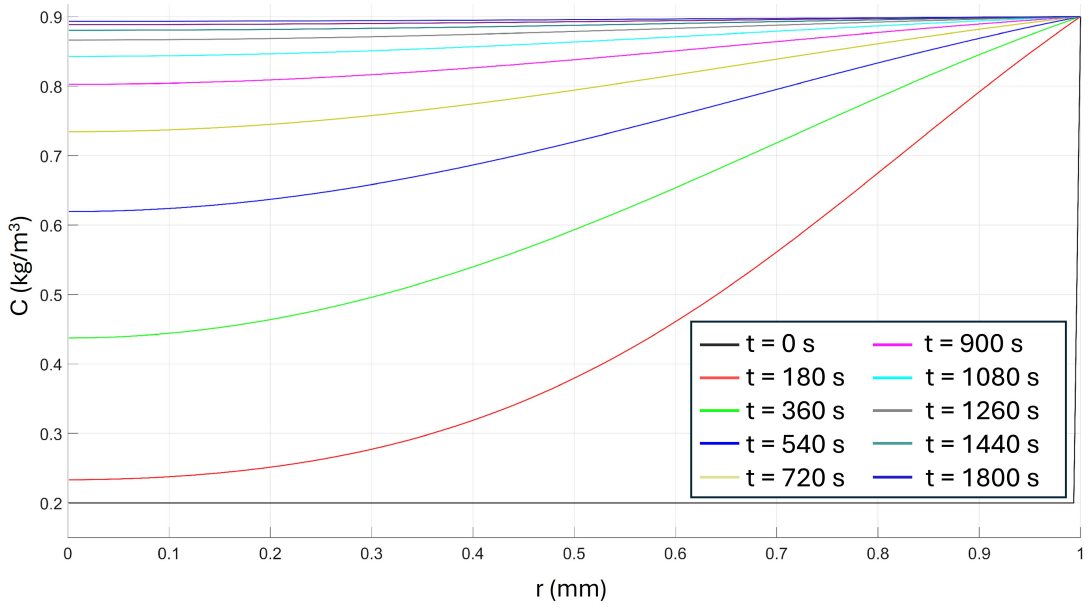

Fig. 2.9 Adsorbate concentration in a sphere over radius and time according to FD model. Concentration distribution is plotted as a function of the radial position in the particle at different times. For this specific simulation it was assumed: $C_0 = 0.2\ kg/m^3$, $C_{eq} = 0.9\ kg/m^3$, $R_p = 1 \cdot 10^{-3}\ m$, $D = 3 \cdot 10^{-10}\ m^2/s$.

Initially, the whole particle is at concentration C_0 (the sudden step just before $r = R_p$ is due to the finite number of spatial points used for numerical simulation, and the constraint of being $C(R_p) = C_{eq}$); then, the concentration grows with the radius and with time, while intraparticle diffusion happens. After a sufficiently long time, the whole particle is at concentration C_{eq}.

For practical applications, when the material is used to separate an adsorbate from the environment, what is of interest is the total amount of the latter extracted by the adsorbent, rather than its spatial local distribution. Thus, it is convenient to define a spatial average

value $\bar{C}$ for C over the volume of the particle p:

$$\begin{aligned}\bar{C}(t) =& \frac{1}{V_p} \cdot \int_p C(r,t) \cdot dV = \\ =& \frac{1}{\frac{4}{3}\pi R_p^3} \cdot \int_{r=0}^{r=R_p} \int_{\theta=0}^{\theta=2\pi} \int_{\phi=0}^{\phi=\pi} C(r,t) \cdot r^2 \sin(\phi) d\phi d\theta dr = \\ =& \frac{3}{R_p^3} \cdot \int_0^{R_p} C(r,t) \cdot r^2 dr \end{aligned} \tag{2.22}$$

Replacing eq. 2.21 into 2.22, after some algebraic passages, we get:

$$\bar{C}(t) = C_0 + \left(C_{eq} - C_0\right) \cdot \left\{ 1 - \frac{6}{\pi^2} \sum_{n=1}^{\infty} \left[\frac{e^{-\pi^2 n^2 \left(\frac{D \cdot t}{R_p^2}\right)}}{n^2} \right] \right\} \tag{2.23}$$

Note that, by hypothesis, the whole sphere at the time t=0 was at concentration C_0; so, $\bar{C}_0 = C_0$. Also, at equilibrium, $\bar{C}_{eq} = C_{eq}$. One final step is necessary to bring this result to a more useful form, i.e., one in which the "water uptake" w of the material, that is the amount of adsorbate present in the material over its dry mass, is expressed as a function of time. It can be proved that, under the assumption that the particle volume V_p is constant during the process, the ratio of concentration differences is equal to the ratio of water uptake differences:

$$\frac{\bar{C}(t) - C_0}{C_{eq} - C_0} = \frac{\frac{m_a(t)}{V_p(t)} - \frac{m_{a,0}}{V_{p,0}}}{\frac{m_{a,eq}}{V_{p,eq}} - \frac{m_{a,0}}{V_{p,0}}} \cong \frac{\frac{m_a(t)}{V_p} - \frac{m_{a,0}}{V_p}}{\frac{m_{a,eq}}{V_p} - \frac{m_{a,0}}{V_p}} = \frac{w(t) \cdot m_{dry} - w_0 \cdot m_{dry}}{w_{eq} \cdot m_{dry} - w_0 \cdot m_{dry}} = \frac{w(t) - w_0}{w_{eq} - w_0} \tag{2.24}$$

where m_a is the amount of adsorbate and m_{dry} the amount of dry sorbent, while pedixes $_{eq}$ and $_0$ represent equilibrium and initial states, respectively. Thus:

$$\frac{\bar{C}(t) - C_0}{C_{eq} - C_0} = \frac{w(t) - w_0}{w_{eq} - w_0} = 1 - \frac{6}{\pi^2} \sum_{n=1}^{\infty} \left[\frac{e^{-\pi^2 n^2 \left(\frac{D \cdot t}{R_p^2}\right)}}{n^2} \right] \tag{2.25}$$

and, finally:

$$w(t) = w_0 + \left(w_{eq} - w_0\right) \cdot \left\{ 1 - \frac{6}{\pi^2} \sum_{n=1}^{\infty} \left[\frac{e^{-\pi^2 n^2 \left(\frac{D \cdot t}{R_p^2}\right)}}{n^2} \right] \right\} \tag{2.26}$$

which is the explicit expression for water uptake as a function of time.

We also propose a step-wise variation of the model, "FDSW", where shorter transients are evaluated and, at the end of each j^{th} time interval, the external concentration $C_{eq}(t_j)$ is

updated (further details in [45]):

$$\begin{cases} C\left(r, t = t_j\right) = C_j & \forall r \\ C\left(r = R_p, t\right) = C_{eq}(t_j) & \forall t \\ \left(\frac{\partial C}{\partial r}\right)_{r=0} = 0 \end{cases} \tag{2.27}$$

The solution in the j^{th} time interval $t_j < t < t_{j+1}$ is:

$$\frac{\bar{C}(t) - C_j}{C_{eq}(t_j) - C_j} = \frac{w(t) - w_{0_j}}{w_{eq}(t_j) - w_{0_j}} = 1 - \frac{6}{\pi^2} \sum_{n=1}^{\infty} \left[\frac{e^{-\pi^2 n^2 \left(\frac{D \cdot (t - t_j)}{R_p^2}\right)}}{n^2} \right] \tag{2.28}$$

Crank provides further analytical solutions for eq. 2.19, derived under various boundary conditions. For example:

- Gas side with time-dependent concentration $C_\infty(t) = C_{\infty,eq} \cdot f(t)$ and uniform initial null concentration. We will refer to this model as "FDRH", and assume a linear $f(t)$:

$$w(t) = \left(\frac{6D \cdot w_{eq}}{R_p^2} \right) \cdot \sum_{n=1}^{\infty} \left[e^{-\pi^2 n^2 \cdot \left(\frac{D \cdot t}{R_p^2}\right)} \cdot \int_0^t f(t) \cdot e^{\pi^2 n^2 \cdot \left(\frac{D \cdot \widetilde{t}}{R_p{}^2}\right)} d\widetilde{t} \right] \tag{2.29}$$

- Gas side with finite volume V_{env} and uniform initial null sorbent concentration:

$$w(t) = w_{eq} \cdot \left\{ 1 - \sum_{n=1}^{\infty} \left[\frac{6\alpha(1+\alpha) \cdot e^{\left(-q_n^2 \cdot \frac{D \cdot t}{R_p^2}\right)}}{9 + 9\alpha + q_n^2 \alpha^2} \right] \right\} \tag{2.30}$$

where $\alpha = \frac{V_{env}}{\frac{4}{3}\pi R_p^3}$ and q_n is the n^{th} strictly positive root of $\tan(q_n) = \frac{3q_n}{3+\alpha q_n^2}$.

Adsorbents such as silica-gels and calcium alginate can be synthesised in various shapes, including spherical beads (for which equations above can be used for modeling the adsorption transients) and superficial coatings of flat surfaces [45, 47]. In the latter case, spherical coordinates are not particularly convenient to model the adsorption process. Instead, we can start from eq. 2.17 and assume to work with a plane sheet of coating adsorbent with thickness L (negligible with respect to the other dimensions) extending along direction x (Fig. 2.10)).

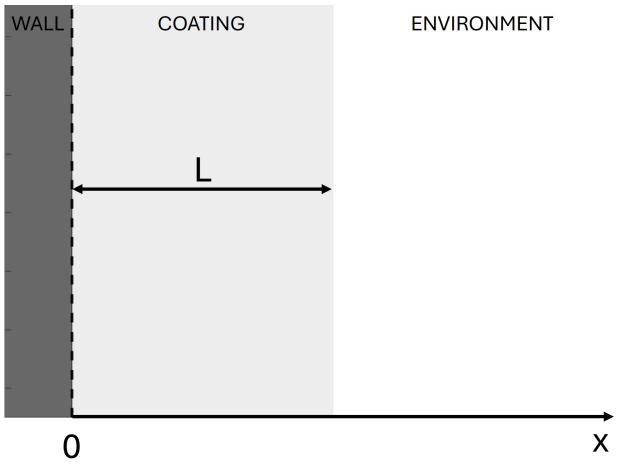

Fig. 2.10 Schematics of a layer of adsorbent (coating) covering a solid surface (wall) which is adiabatic to the vapor diffusion. Direction x normal to the wall is the only important spatial variable, as long as the coating can be assumed as infinite towards the other perpendicular spatial directions.

Concentration is thus a function of only time and position x, according to the following:

$$\frac{\partial C(x,t)}{\partial t} = \frac{\partial}{\partial x}\left[D \cdot \frac{\partial C(x,t)}{\partial x}\right] \tag{2.31}$$

In the case of a superficial coating, only one side of the sorbent is exposed to the environment, while the other is adjacent to the object whose surface is coated. On the latter surface, no vapor is diffusing, thus the surface acts as an "adiabatic wall" and a condition over the derivative of concentration over x can be written:

$$\begin{cases} \frac{\partial C(x,t)}{\partial t} = \frac{\partial}{\partial x}\left[D \cdot \frac{\partial C(x,t)}{\partial x}\right] \\ \left.\frac{\partial C(x,t)}{\partial x}\right|_{x=0,t} = 0 \\ C(x=+L,t) = C_1 \\ C(x,t=0) = C_0 \end{cases} \tag{2.32}$$

If D is constant, it can be excluded from the derivative and the Cauchy problem has analytical solution (see [63]):

$$\frac{C(x,t)-C_0}{C_1-C_0} = 1 - \frac{4}{\pi} \cdot \sum_{n=0}^{\infty}\left[\frac{(-1)^n}{2n+1} \cdot e^{-D(2n+1)^2\pi^2 \cdot \frac{t}{(2L)^2}} \cdot \cos\frac{(2n+1)\pi x}{2L}\right] \tag{2.33}$$

After averaging over the material volume, as we did above for the spherical beads, we get a solution in terms of water uptake:

$$\frac{w(t)-w_0}{w_{eq}-w_0} = 1 - \frac{8}{\pi^2}\sum_{n=0}^{\infty}\frac{1}{(2n+1)^2} \cdot e^{-(2n+1)^2 \cdot \pi^2 \cdot \frac{D \cdot t}{(2L)^2}} \tag{2.34}$$

The modeled behaviour over time is plotted in terms of concentration and water uptake in Fig. 2.11a,b for adsorption, and Fig. 2.11c,d for desorption.

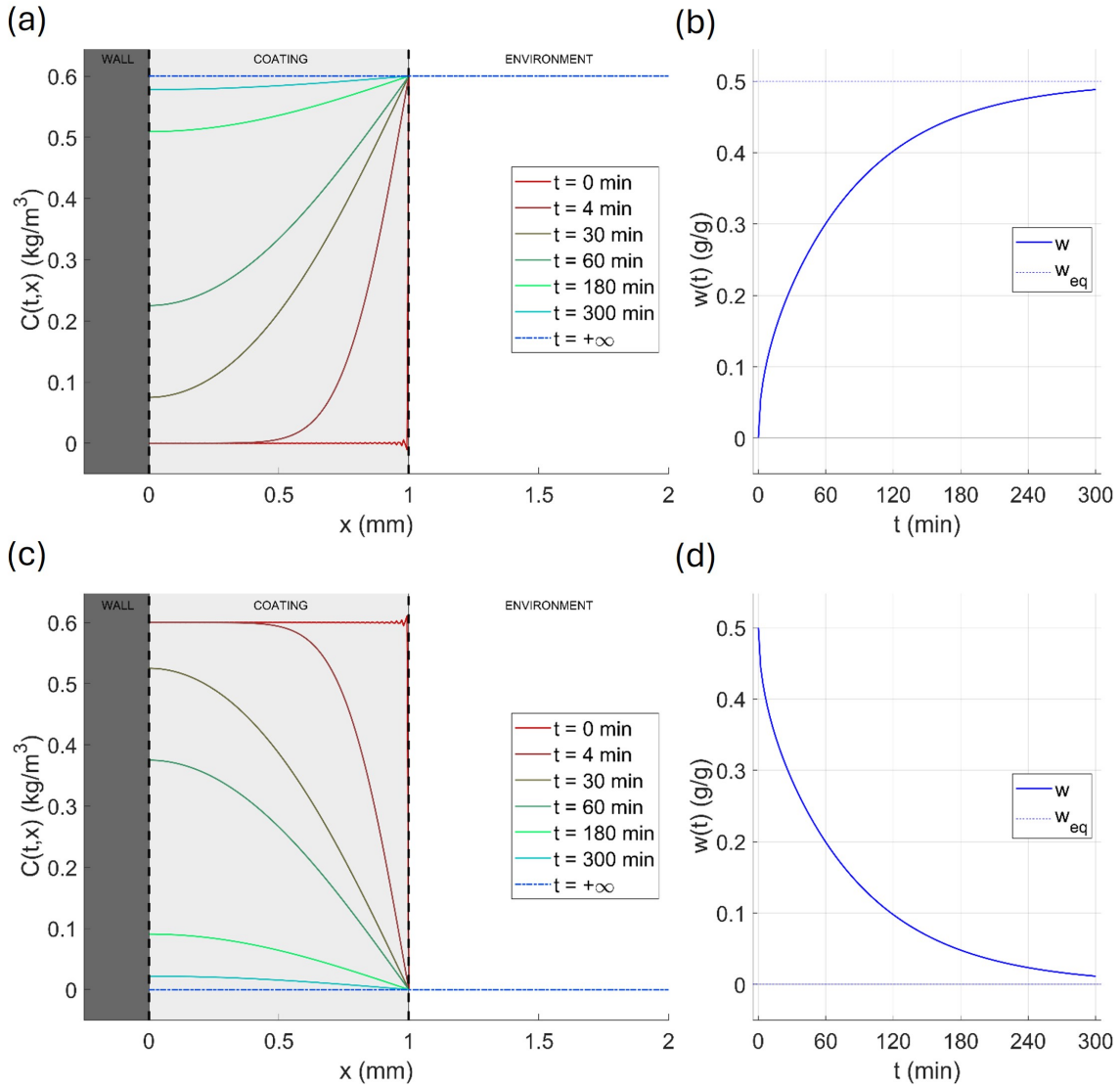

Fig. 2.11 Concentration and water uptake in a plane coating of sorbent according to the FD model. (a) Concentration C of adsorbate in the coating along space (x) and time (t); the simulation was run assuming: $L = 1\ mm$, $D = 8 \cdot 10^{-11}\ m^2/s$, $C_0 = 0\ kg/m^3$, $C_1 = 0.6\ kg/m^3$ (the value for D was chosen based on the results published in [45]). (b) Water uptake resulting from integrating C for picture (a) over the coating volume. (c) Concentration C of adsorbate in the coating along space (x) and time (t); the simulation was run assuming: $L = 1\ mm$, $D = 8 \cdot 10^{-11}\ m^2/s$, $C_0 = 0.6\ kg/m^3$, $C_1 = 0\ kg/m^3$. (d) Water uptake resulting from integrating C for picture (c) over the coating volume.

The small oscillations near the surface at $x = 1\ mm$ of the solution at time $t = 0\ min$ (red curve) are due to the fact that the infinite sum of the analytical solution was evaluated only until the term $n = N = 1000$, and for small times (close to 0) and high values of x (close to L) the influence of the cosine function in 2.33 is not attenuated except that for high N.

Fick-diffusion - A numerical model for large uptake ranges

In adsorption processes where the water uptake variation is large, diffusivity might not be considered a constant: for example, in case of polymeric hydrogels such as in calcium alginate, we can expect polymeric chains to change shape as long as the sorbent collects water molecules, thus changing internal structure and modifying the vapor capability to diffuse. For this reason, it is useful to derive a numerical model allowing a non-constant functional form for $D(C)$ - that is, diffusivity as a generic function of instantaneous adsorbate concentration.
As an example, we consider again the last problem: diffusion through a plane sheet of coating. We can start from equation 2.31, where this time $D = D(C)$; then, we approximate the spatial derivatives with a finite difference method and the time derivative with a forward-Euler or backward-Euler method [64], to achieve a fully algebraic formulation of the problem. The full step-by-step procedure is given in Appendix A.
The solution in case of Forward Euler is given in the following system of algebraic equations:

$$\begin{cases} j=0: \quad C_0^{t+1} = C_0^t + \Delta t \cdot \left[2 \cdot D\left(C_0^t\right) \cdot \frac{C_1^t - C_0^t}{h^2} \right] \\ j=1: \quad C_1^{t+1} = C_1^t + \Delta t \cdot \left[\left.\frac{\partial D(C)}{\partial C}\right|_{C_1{}^t} \cdot \frac{\left(C_2^t\right)^2 - 2 \cdot C_0^t \cdot C_2^t + \left(C_0^t\right)^2}{4h^2} + D\left(C_1^t\right) \cdot \frac{C_2^t - 2C_1^t + C_0^t}{h^2} \right] \\ j=2: \quad C_2^{t+1} = C_2^t + \Delta t \cdot \left[\left.\frac{\partial D(C)}{\partial C}\right|_{C_2{}^t} \cdot \frac{\left(C_3^t\right)^2 - 2 \cdot C_1^t \cdot C_3^t + \left(C_1^t\right)^2}{4h^2} + D\left(C_2^t\right) \cdot \frac{C_3^t - 2C_2^t + C_1^t}{h^2} \right] \\ \ldots \\ j=j: \quad C_j^{t+1} = C_j^t + \Delta t \cdot \left[\left.\frac{\partial D(C)}{\partial C}\right|_{C_j{}^t} \cdot \frac{\left(C_{j+1}^t\right)^2 - 2 \cdot C_{j-1}^t \cdot C_{j+1}^t + \left(C_{j-1}^t\right)^2}{4h^2} + D\left(C_j^t\right) \cdot \frac{C_{j+1}^t - 2C_j^t + C_{j-1}^t}{h^2} \right] \\ \ldots \\ j=N: \quad C_N^{t+1} = C_N^t + \Delta t \cdot \left[\left.\frac{\partial D(C)}{\partial C}\right|_{C_N{}^t} \cdot \frac{\left(C_{N+1}^t\right)^2 - 2 \cdot C_{N-1}^t \cdot C_{N+1}^t + \left(C_{N-1}^t\right)^2}{4h^2} + D\left(C_N^t\right) \cdot \frac{C_{N+1}^t - 2C_N^t + C_{N-1}^t}{h^2} \right] \\ j=N+1: \quad C_{N+1}^{t+1} = C_{eq}(t+1) \end{cases} \tag{2.35}$$

Solving the system of equation just above means defining the initial concentrations array $C^0 = \left[C_0^0, C_1^0, C_2^0, \ldots C_{N+1}^0\right]$ according to the initial distribution (i.e., the spatial distribution in the coating at time t=0), then easily evaluate $C^1 = \left[C_0^1, C_1^1, C_2^1, \ldots C_{N+1}^1\right]$ according to the equations above (such values are only functions on known variables, at this point), then proceed iteratively with the successive time instants: $C^2 = \left[C_0^2, C_1^2, C_2^2, \ldots C_{N+1}^2\right]$, …, $C^{M+1} = \left[C_0^{M+1}, C_1^{M+1}, C_2^{M+1}, \ldots C_{N+1}^{M+1}\right]$, being M+2 the points in which the wanted time interval of integration has been discretized (then, being M+1 the number of time intervals).

The same approach is valid if one wants to use an unconditionally stable implicit method, like backward Euler, with the difference that the quantities on the right are evaluated at time t+1. This is the resulting system:

$$\begin{cases} j=0:\ C_0^{t+1}=C_0^t+\Delta t\cdot\left[2\cdot D\left(C_0^{t+1}\right)\cdot\frac{C_1^{t+1}-C_0^{t+1}}{h^2}\right] \\ \dots \\ j=j:\ C_j^{t+1}=C_j^t+\Delta t\cdot\left[\left.\frac{\partial D(C)}{\partial C}\right|_{C_j{}^{t+1}}\cdot\frac{\left(C_{j+1}^{t+1}\right)^2-2\cdot C_{j-1}^{t+1}\cdot C_{j+1}^{t+1}+\left(C_{j-1}^{t+1}\right)^2}{4h^2}+D\left(C_j^{t+1}\right)\cdot\frac{C_{j+1}^{t+1}-2C_j^{t+1}+C_{j-1}^{t+1}}{h^2}\right] \\ \dots \\ j=N+1:\ C_{N+1}^{t+1}=C_{eq}\left(t+1\right) \end{cases} \tag{2.36}$$

In this case, though, it is required to solve each of the updates in time: it is necessary to iterate in time and, at each time, if the equations are not analytically invertible in terms of C^{t+1}, to iterate again to solve a non-linear system of implicit equations to explicit C^{t+1} (that is function of C^t and C^{t+1} itself). A MATLAB® [65] code for the aim is provided in Appendix B.
Again, it is more useful to speak in terms of water uptake w, instead of concentration:

$$\bar{C}(t)=\frac{m_{H_2O}(t)}{V_p}=\frac{w(t)\cdot m_{dry}}{V_p}=w(t)\cdot\rho_{dry} \tag{2.37}$$

where ρ_{dry} is the dry sorbent density, and $\bar{C}$ is again the average density along the coating, evaluated at every time t as the algebraic average (avg) of the components of C along j:

$$\bar{C}\left(t\right)\cong\bar{C}^t=avg\left(\left[C_0^t,C_1^t,C_2^t,\dots,C_j^t,\dots C_{N+2}^t\right]\right) \tag{2.38}$$

If the model is used to best-fit experimental data which are initially given in terms of water uptake, equation 2.37 can be used to convert the data into average concentration. With the further hypothesis that concentration is homogeneous along the coating (which is true if the initial experimental water uptake is measured with the material in equilibrium), we can use the average value of C as initial concentration at every point along x. Note that, since each equation coming from the model has common factor C, when converting back to water uptake ρ is simplified; thus, if we are only interested in best-fitting water uptake, we can use a unitary value for density: $\rho=1\ kg/m^3$.

Linear Driving Force

The above discussed models have robust theoretical justification, as they derive from Fick's laws. On the other hand, the nature of the models make them rarely chosen in practical contexts. In order to isolate the effects of pure diffusion from side phenomena, a large set of experiments is often required: for example, in order to exclude bed effects in the zero length column method, further experiments changing the sample mass or using Helium, Argon or Nitrogen must be performed [66]. Furthermore, care should be used when employing

numerical models or replacing analytical models with an approximation. For example, the number of evaluated terms in the infinite series strongly affects the approximation, as shown in Fig. 2.12 (at this resolution, only starting from N=100 the curves visually overlap):

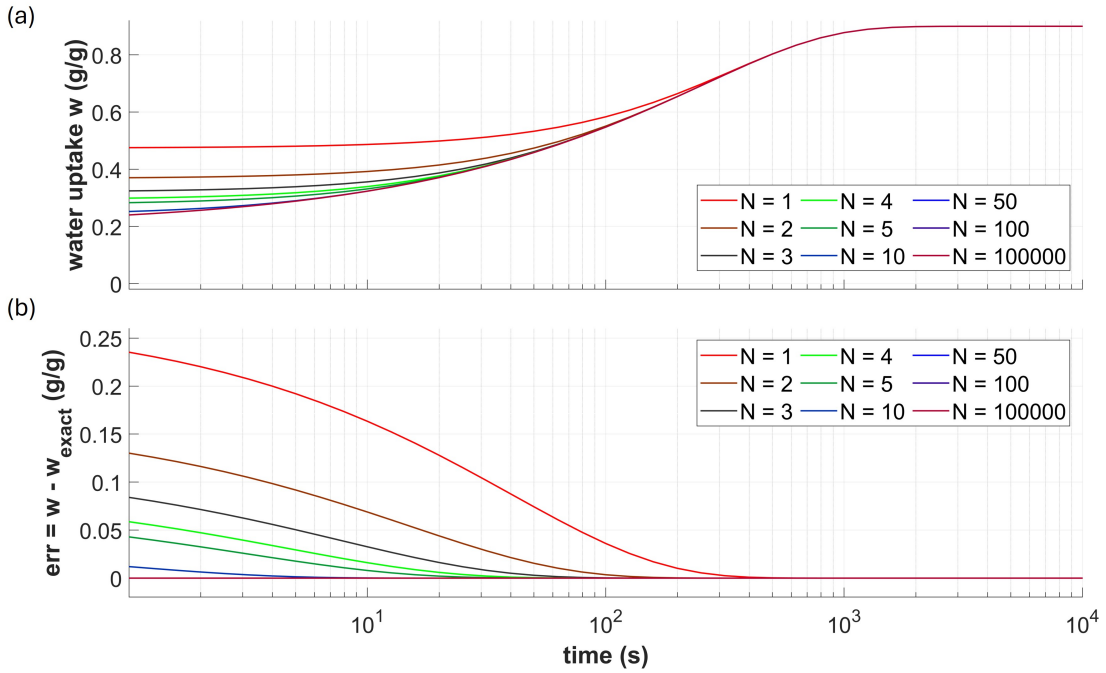

Fig. 2.12 Dependence of FD accuracy as a function of evaluated terms in the infinite sum. (a) Different approximation of uptake distribution over time (log scale) from FD expression in eq. 2.26, varying the number of evaluated terms of the infinite sum. (b) Absolute errors against the "exact" solution (i.e., $N = 100000$). We assumed: $w_0 = 0.2\ g/g$, $w_{eq} = 0.9\ g/g$, $R_p = 10^{-3}\ m$, $D = 3 \cdot 10^{-10}\ m^2/s$.

In the initial part of adsorption, the error can be of the order of 0.1 g/g. For these reasons, simplified approaches have been proposed over time, including purely empirical and semi-empirical equations. With the idea of keeping a physical interpretation for future discussions, we choose to discuss a semi-empirical largely diffused model, known as "Linear Driving Force" [16, 63]. The base idea is to model the mass flux of adsorbate towards the sorbent as linearly proportional to the available sites in the whole volume of material:

$$\frac{d\bar{C}(t)}{dt} = K \cdot \left[C_{eq}(t) - \bar{C}(t)\right] \tag{2.39}$$

where $\bar{C}$ is again the unknown average concentration in the particle, C_{eq} is the external concentration (toward which the material is tending), K is a proportionality factor taking into account diffusivity and geometry.
The latter model finds various justifications, including:

1. Adsorption is a capacitive process, and eq. 2.39 is a 1st-order ODE modeling such type of phenomenon (e.g., the equation describing the charging and discharging of a capacitor in a *RC* electrical circuit has the same structure).

2. Eq. 2.39 is the same used by Langmuir for the modeling of the first layer formation; under the hypothesis that the contribution of internal diffusion of adsorbate is negligible with respect to superficial links, the LDF can be thought as the extension of the Langmuir driving idea to the whole particle.

3. Eq. 2.39 can be derived analytically as a particular case of Fick-diffusion theory [67]. For example, in case of spherical diffusion, we can start from eq. 2.22, derive with respect to time, replace the 2nd Fick's law into the general expression for $\frac{\partial C(r,t)}{\partial t}$ and integrate by parts (using symmetry at $r = 0$), to get:

$$\bar{C} = \frac{3}{R_p^3} \cdot \int_0^{R_p} C(r,t) \cdot r^2 dr \tag{2.40}$$

$$\frac{\partial \bar{C}}{\partial t} = \frac{3}{R_p^3} \cdot \int_0^{R_p} \frac{\partial C(r,t)}{\partial t} \cdot r^2 dr \tag{2.41}$$

$$\frac{\partial \bar{C}}{\partial t} = \frac{3D}{R_p^3} \cdot \int_0^{R_p} \left(\frac{\partial^2 C}{\partial r^2} + \frac{2}{r} \cdot \frac{\partial C}{\partial r} \right) \cdot r^2 dr \tag{2.42}$$

$$\frac{\partial \bar{C}}{\partial t} = \frac{3D}{R_p} \cdot \left(\frac{\partial C}{\partial r} \right)_{r=R_p} \tag{2.43}$$

We can assume for $C(r,t)$ a parabolic profile along radius: $C(r,t) = a(t) + b(t) \cdot r + c(t) \cdot r^2$. The three constants can be found, respectively:

- by imposing symmetry at $r = 0$ -that is, null derivative-, from which $b(t) = 0$;
- applying the boundary condition $C(r = R_p) = C_{eq}$, from which we find $a(t) = C_{eq} - c \cdot R_p^2$;
- integrating the parabolic expression for $C(r,t)$ over the spherical volume to link $c(t)$ to the average $\bar{C}$, from which we find: $c(t) = \frac{5}{2} \cdot \frac{C_{eq} - \bar{C}}{R_p^2}$.

Finally, we can evaluate the concentration change rate at $r = R_p$: $\left(\frac{\partial C}{\partial r} \right)_{r=R_P} = 2cR_p = \frac{5 \cdot (C_{eq} - \bar{C})}{R_p}$. By replacing into Eq. 2.43, we finally get:

$$\frac{d\bar{C}}{dt} = \frac{3D}{R_p} \cdot \frac{5 \cdot (C_{eq} - \bar{C})}{R_p} = \frac{15 \cdot D}{R_p^2} \cdot (C_{eq} - \bar{C}) \tag{2.44}$$

which is exactly the LDF model, where $K = \frac{15 \cdot D}{R_p^2}$. The same approach can be repeated for different sorbent shapes, where we expect K to have the same structure: $K = \frac{F_0 \cdot D}{R^2}$, with F_0 being a generic shape factor (equal to 15 in case of spherical beads, as proved above), and R a geometrical reference dimension (radius of the particles in case of spherical beads).

The last justification may be considered as the most robust, but it was derived under further assumptions such as a parabolic distribution in the sorbent sphere. In general, reason n.1 already justifies the use of LDF model because it encloses the capacitive nature of the phenomenon. Thus, we think that LDF should be treated as a separate model, rather than a particular case of FD.
Equation 2.39 is a standard 1st-order ODE, having the following known solution:

$$\bar{C}(t) = C_0 + (C_{eq} - C_0) \cdot \left(1 - e^{-K \cdot t}\right) \tag{2.45}$$

As usual, recalling that $\frac{\bar{C}-C_0}{C_{eq}-C_0} = \frac{w-w_0}{w_{eq}-w_0}$, we can re-write the model in terms of water uptake instead of average concentration:

$$w(t) = w_0 + (w_{eq} - w_0) \cdot \left(1 - e^{-\frac{F_0 \cdot D}{R_p^2} t}\right) \tag{2.46}$$

with $F_0 = 15$ as long as we work with spherical particles.

Modified Linear Driving Force - A novel approach for large uptake ranges

We propose here a novel approach to model adsorption and desorption dynamics. The discussion below is based on the journal article [45].
Equation 2.46 is largely used to model the adsorption and desorption transients of conventional sorbents. Nevertheless, it lacks in accuracy when approximating large water uptake changes (some examples are provided in the next chapter "Methods" section). Empirical variations of the base LDF model have been proposed in the literature, for instance by introducing corrective exponents to adimensional groups. An example comes from a work by I. I. El-Sharkawy [68], who proposed the following variation of the LDF model:

$$w(t) = w_0 + (w_{eq} - w_0) \cdot \left(1 - e^{-F_0 \cdot \left(\frac{D \cdot t}{R_p^2}\right)^m \cdot \left(\frac{T}{T_c}\right)^n}\right) \tag{2.47}$$

where T is adsorption or desorption temperature, T_c is a reference temperature (in the original model, proposed in the context of adsorption cooling applications, it is the condenser temperature), m and n are the introduced corrective coefficients. For this research, this model will be tested against experimental data after assuming $n = 0$, thus only considering the correction on the adimensional time $\left(\frac{D \cdot t}{R_p^2}\right)$, and will be referred to as LDFm:

$$w(t) = w_0 + (w_{eq} - w_0) \cdot \left(1 - e^{-F_0 \cdot \left(\frac{D \cdot t}{R_p^2}\right)^m}\right) \tag{2.48}$$

Equation 2.48 provides an accurate method for best-fitting experimental data: given the extra degree of freedom with respect to the base LDF model, the best-fitting error is much lower [68]. Nevertheless, the increase in accuracy comes with the disadvantage of a slight increase in the expression complexity and, most importantly, the new parameter m has not an immediate physical interpretation, being an empirical corrective coefficient.
In this research, we fill this gap by proposing an alternative LDF-based model named LDFDw [45], which still involves an extra parameter, but keeps a stronger physical meaning. In particular, following the same idea as in the case of FD numerical model, we here try to generalize the LDF model to the case where D is a function of water uptake: $D = D(w)$. Among the different functional forms, we decided to model D as linearly dependent on w:

$$D = D(w) = a + b \cdot w \tag{2.49}$$

In this case, a and b have both a direct physical interpretation: the first being the diffusivity of the dry sorbent, the second being a measure of the influence on diffusivity of the vapor presence in the sorbent (in case of hydrogels such as calcium alginate, it is one way of high-level modeling the change in shape of polymeric chains).
In order to derive the expression for $w(t)$, we start from the differential formulation 2.39 along with the initial conditions of the Cauchy problem:

$$\begin{cases} \frac{dw(t)}{dt} = \frac{F_0 \cdot D(w)}{R_p^2} \cdot \left[w_{eq} - w(t) \right] \\ D(w) = a + b \cdot w \\ w(t_0) = w_0 \end{cases} \tag{2.50}$$

Upon substitution of the second equation into the first, we get a non linear ODE:

$$\frac{dw}{dt} = \frac{F_0}{R_p^2} \cdot (a + b \cdot w) \cdot \left(w_{eq} - w \right) \tag{2.51}$$

The latter can be solved by separation of variables and subsequent partial fractions decomposition. After the necessary algebraic steps (full calculations in Appendix A), we get:

$$\frac{w(t) - w_0}{w_{eq} - w_0} = \frac{e^{\frac{F_0 (a + b\ w_{eq})}{R_p^2} \cdot t} - 1}{e^{\frac{F_0 (a + b\ w_{eq})}{R_p^2} \cdot t} + b \cdot \left(\frac{w_{eq} - w_0}{a + b\ w_0} \right)} \tag{2.52}$$

where we recall that w_{eq} is the equilibrium uptake under the test conditions and w_0 is the water uptake of the sorbent sample at time $t = 0$. By appropriately choosing initial and equilibrium water uptakes, equation 2.52 can be used to model both adsorption and desorption transients.

A note on the validity of the best-fitted diffusivity coefficients

In modeling adsorption dynamics, we prefer using models where the number of parameters is limited, and these have all physical interpretation. Diffusivity "D" has indeed a physical meaning, being specifically defined within the context of Fick-Diffusion law. On the other hand, best-fitting diffusivity over experimental data when not all the model hypotheses are met, may result in a distortion of the coefficient, which loses its univocality.

Specifically, if non-negligible heat effects are associated with the adsorption or desorption processes, the temperature field on the material volume can significantly change over time, and the best-fitted diffusivity is not representative of an isothermal process anymore. Instead, all the dynamics and heat transfer effects occurring during adsorption are lumped into the diffusion coefficient, which overshadows the more complex physics of the process. Adsorption on calcium alginate makes no exception, with important heat effects suggested by the large error bars resulting from the experiments presented later in this research.

Nevertheless, in this research, we will still use the presented models in order to best-fit the adsorption and desorption experimental data. This choice is a compromise, accepted because of the difficulty in performing experiments in which the heat effects become completely negligible (the samples should be kept at constant temperature during adsorption and desorption). As a consequence, the best-fitted diffusivities will be surely a strong tool for process simulation and for initial considerations on the material dynamics, but they might have a distorted absolute value when compared with coefficients evaluated on purely-diffusive processes from the literature.

Chapter 3

Fresh water production

3.1 Introduction

In order to provide fresh water in areas where a liquid source (including rivers, lakes, springs, underground basins...) is not easily accessible, a series of non-conventional solutions have been developed over the years, including:

1. Atmospheric Water Harvesting (AWH), a promising solution to provide fresh water far away from liquid resources, relying exclusively on the available vapor in the atmosphere (this is estimated to surpass 12900 km^3 of water [69]).

2. Water Desalination (WD), which stands out as a large-scale solution to provide fresh water, especially in islands and coastal regions, where sea-water is easily accessible and other fresh water sources are not. Currently, the global desalination plants capacity is in the order of 100 million m^3/day of water [70].

3. Rainwater collection, where water precipitation is collected from rooftops or dedicated surfaces and then stored in tanks or cisterns for later use. This is especially functional in areas with high precipitation rate, like in the tropical band around the equator (central Africa, South America, India, Malesia, Indonesia) [71]. On the other hand, this approach is not reliable in areas with less uniform rainfall patterns.

4. Water transportation from surplus basins to deficit areas, by means of trucks or ships [72]. This requires an important infrastructure and elevated costs, and it is not always a suitable approach, depending on the environmental constraints.

5. Other less common approaches, like deep groundwater extraction via drilling techniques, iceberg melting, cloud seeding [73].

In this work, we focus on the first two technologies, AWH and WD, and especially on the adsorption-based variants. The chapter starts with an overview on Atmospheric Water Harvesting, including an introduction to the subject, a classification of the main state-of-the-art solutions and a list of the typical KPIs used to evaluate the performance of a AWH plant. After that, we present an overview on Water Desalination, even in this case including an introduction to the subject, a classification of the main state-of-the-art solutions and a list of the typical KPIs used to evaluate the performance of a WD plant.
We conclude with an overview on the legal requirements that must be satisfied in order for water to be considered "drinkable", suitable for human consumption.

3.2 Atmospheric water harvesting

3.2.1 Overview

Atmospheric Water Harvesting (AWH) is the process of extracting water from the moisture present in the air, leveraging on the large availability of vapor in the Earth's atmosphere. The moisture must be first condensed into liquid water, and this requires an engineering effort. Diverse classifications exist: one option is to classify AWH solutions as active (providing an energy input, either work or thermal) or passive (exploiting natural variations); another option is to classify AWH solutions depending whether they are based on "active condensation" or "sorption". We decided to use the first classification, with an extra distinction between high-exergy and low-exergy active sources, for a total of three groups:

1. Passive solutions. These rely on natural favorable conditions and require ideally no further energy input for the harvesting process. They include:
    - fog harvesting: mesh nets are employed to capture supersaturated fog droplets [74];

Fig. 3.1 An example of a fog harvesting system. Source: [74].

- dew collection via radiative cooling: advanced materials like polyethylene films are used to reject heat, until the surface cools down below the dew-point temperature (typically at night) [75];
- solar chimneys: tall structures are heated by solar energy, with warm humid air moving upwards, until it cools down enough to reach its dew-point temperature and condense on the chimney surfaces;
- underground cooling: humid air is moved through underground pipes, where the ground lower temperature leads to condensation.

These approaches have the pros of requiring no energy[1] expense and low maintenance, but the cons that the water production rate is low and subject to natural variations (for instance, low relative humidity hinders passive AWH).

2. Active solutions using high-exergy sources. These rely on active provision of work (typically electrical energy) in order to force condensation from moisture. They use:
   - Active refrigeration via compression cycle: a heat-pump cycle is used to extract heat from air and locally cool it down below the dew point temperature.
   - Thermoelectric cooling (TEC): the Peltier effect is exploited to cool down one surface of a Peltier cell, causing condensation.

   Active refrigeration allows better control on the amount of condensing water, allowing large production rates. TEC is compact and requires less maintenance, but the cooling efficiency is relatively low (typically, below 10%).

3. Active solutions using low-exergy sources. These use active provision of low-grade energy, such as waste heat, to facilitate condensation. They use:
   - Direct adsorption: an adsorbent material collects water molecules from humid air and, when heated up, it releases them at high dew-point temperatures, allowing ambient-temperature condensation [76].
   - Adsorption/absorption chilling: waste heat is used to drive an adsorption chiller or an absorption chiller, which cools down proper surfaces where vapor condensation happens [77].
   - Other less common heat driven chilling solutions, for instance heat driven ejector refrigeration (vapor is pressurized using the heat, then it is expanded through a nozzle producing a cooling effect) [78].

[1] In a sense, they do: solar energy is the initial energy source causing air to heat up and increase its capacity to store water vapor.

All AWH solutions have the objective of extracting the most possible amount of vapor using the least possible amount of energy. Thus, their performance can be compared with proper KPIs, including:

- RR: Recovery Ratio: fraction of water collected with respect to the whole water content of the treated air. Typically, a quantity named "vapor quality" is defined as the ratio of mass of vapor m_{vapor} over mass of total humid air $m_{vapor} + m_{dry-air}$:

$$x = \frac{m_{vapor}}{m_{vapor} + m_{dry-air}} \tag{3.1}$$

  The recovery ratio is then defined as follows:

$$RR = \frac{x_{in} - x_{out}}{x_{in}} \tag{3.2}$$

  with pedixes *in* and *out* indicating, respectively, the inlet humid air flow and the outlet drier air flow. The higher RR, the greater the water collection efficiency.

- SEC: Specific Energy Consumption. This is defined as the total energy (electrical plus thermal) necessary to harvest a unit of water:

$$SEC = \frac{E_{electrical} + E_{thermal}}{V_{H_2O}} \tag{3.3}$$

  where V_{H_2O} is the volume of water produced in the time period considered in the energy consumption estimation (e.g., one working day).

- STEC: Specific Thermal Energy Consumption [79]. This KPI is usually used for assessing performance of Membrane Desalination system, but we propose it as a KPI to evaluate the efficiency of a generic thermal AWH plant, in terms of thermal energy used to produce one liter of water:

$$STEC = \frac{E_{thermal}}{V_{H_2O}} \tag{3.4}$$

  where $E_{thermal}$ is the thermal energy provided to the plant to make the harvesting process in the reference time interval happen.

3.2.2 Direct adsorption AWH

In general, the three classes of solutions are not directly comparable, since they rely on very different inputs from the user: for example, active solutions cannot compete with passive solutions if we compare the SEC or STEC indicators. Nevertheless, we can still try to understand in which area each approach excels and map the contexts in which they must be

preferred [80]. To do so, we first go deeper into the technology of direct adsorption AWH. Adsorption-based AWH devices are open-cycle systems that allow humid air to exchange water molecules with an adsorbent material. Typically, such devices operate alternating two phases:

1. Adsorption: a stream of external humid air is forced through a heat exchanger, typically either coated with sorbent or containing the latter in packed-bed configurations (Fig. 3.2a) [47]. The water molecules contained in the humid air stream bind to the sorbent pores, lowering the air stream vapor quality and increasing the sorbent water uptake.

2. Desorption: the device is isolated from the external environment, and heat is provided to the heat exchanger containing the material, causing vapor to be released at ideally constant temperature[2] (Fig. 3.2b). After the desorption process, the device internal atmosphere observes high dew-point temperatures, making condensation possible even above the ambient temperatures. Condensation heat is then rejected by means of an external circuit, where no active cooling is needed, and water is collected and removed from the device.

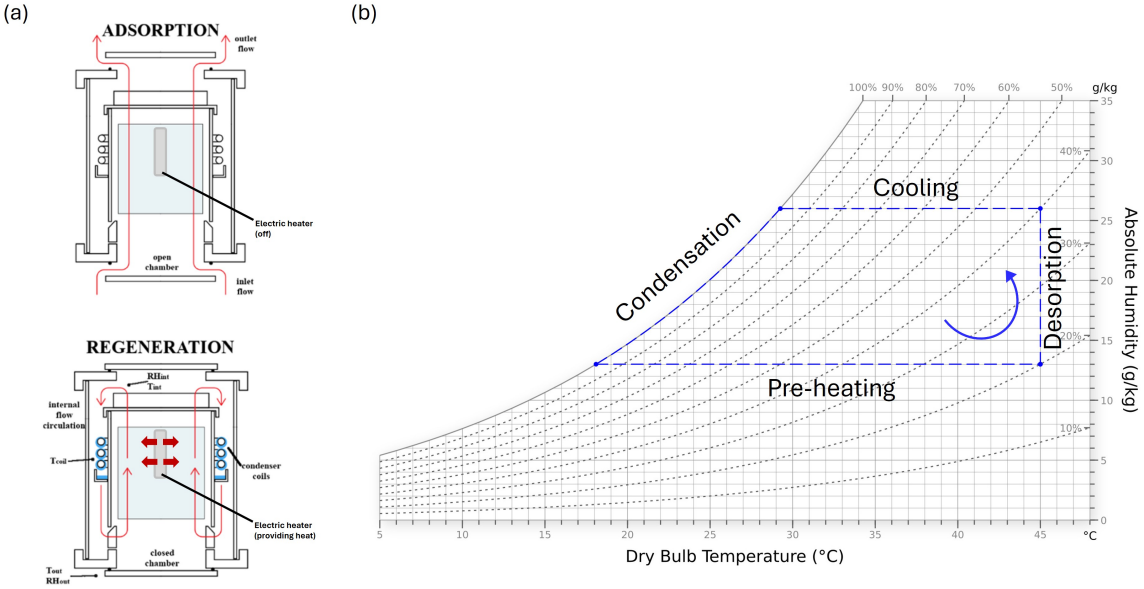

Fig. 3.2 AWH introduction. (a) Adsorption-regeneration phases in a AWH device [47]. 3) (b) Thermodynamic cycle in case of isothermal desorption. The psychrometric chart was built using the online tool from Dr. Andrew Marsh at [81].

The water production increases with the amount of sorbent used; for this reason, typically, a specific indicator is used to assess the performance of an adsorption-based AWH system:

[2]Most common applications implement a isoenthalpic desorption instead, but [76] showed that a isothermal desorption allows to span over a larger vapor quality, optimizing water productivity.

Specific Daily Water Production (SDWP). This is defined as the amount of water produced per day and per unit of sorbent material:

$$SDWP = \frac{V_{H_2O}}{m_{dry} \cdot t_{cycle}} \tag{3.5}$$

where V_{H_2O} is the volume of water produced per cycle, m_{dry} is the mass of dry sorbent in the plant, t_{cycle} is the time spent to run a full adsorption-desorption cycle. Typically, the units used are $[V_{H_2O}] = m^3$, $[m_{dry}] = ton$, $[t_{cycle}] = day$, from which: $[SDWP] = \frac{m^3}{ton \cdot day}$. In this work, we also propose and use a related KPI:

$$SCWP = \frac{V_w}{m_{dry}} \tag{3.6}$$

which is the amount of water produced during one cycle of operation (C stands for "Cycle").

When compared with the above discussed alternatives, adsorption-based AWH offers some unique advantages: it can be driven using low-grade thermal sources (like waste heat at relatively low temperatures, below 100°C), and is able to guarantee a water production even at low relative humidities. On the other hand, water productivity is typically lower than active cooling solutions, unless sorbents with very high performance are used. Qualitative pros and cons of the discussed alternative AWH technologies are summarized in table 3.1:

	Passive fog harvesting	Adsorption-based AWH	Active cooling via compression cycle
RH	Near saturation (95-100%)	Medium-low (10-80%)	Medium-high (30-100%)
Input energy from user	none	low-exergy	high-exergy
Productivity	Proportional to nets area	Medium	High

Table 3.1 Qualitative comparison of AWH technologies.

3.3 Water desalination

3.3.1 Overview

Water desalination technologies work by taking as input a salty water solution (feedwater, typically seawater or brackish water) and providing as output a water solution with solute concentration below acceptable levels for the target use (the specific case of drinkable water is

treated in the next section). This useful effect is called "solute rejection" and can be achieved in different ways:

1. Membrane-filtration, where a semipermeable membrane is used to separate water from solute.

2. Evaporation and condensation, where water vapor is created and condensed again to form fresh water.

3. Other approaches -not explored in depth in this work-, including crystallization methods (ice is produced as intermediate product, then it is melted and fresh water is collected) and chemical filtration [70].

A further classification is based on the type of energy source needed. Desalination can be driven using high-exergy sources, such as mechanical or electrical work (for instance, Reverse Osmosis), or using low-exergy sources, such as low-temperature heat extracted by solar panels [70].
The performance of a water desalination plant is typically measured using the following KPIs:

- R: rejection ratio. This is defined as the ratio between the reduction in concentration and the initial concentration of the salty solution:

$$R = \frac{C_{initial} - C_{final}}{C_{initial}} = 1 - \frac{C_{final}}{C_{initial}} \tag{3.7}$$

  where $C_{initial}$ is the solute concentration in the starting salty solution and C_{final} is the output desalinated water solute concentration.

- SEC: Specific Energy Consumption. This is defined as the total energy (electrical plus thermal) necessary to desalinate a unit of water:

$$SEC = \frac{E_{electrical} + E_{thermal}}{V_{H_2O}} \tag{3.8}$$

  where V_{H_2O} is the volume of water produced in the time period considered in the energy consumption estimation (e.g., one working day).

- STEC: Specific Thermal Energy Consumption [79, 82]. That is, the thermal energy used to produce one liter of water:

$$STEC = \frac{E_{thermal}}{V_{H_2O}} \tag{3.9}$$

where $E_{thermal}$ is the thermal energy provided to the plant to make the desalination process happen, defined as the integral of thermal power $Q_{thermal}$ over time:

$$E_{thermal} = \int_0^{t_{cycle}} Q_{thermal}\, dt \tag{3.10}$$

Another related KPI is SEEC (Specific Electrical Energy Consumption), which provides the STEC-complementary contribution to SEC.

In general, the cost of use of a desalination plant will be equal to the sum of a term proportional to the amount of water produced, plus installation and management costs. It is clear that the role of research in exploring alternatives for water desalination is crucial, in order to minimize the economic and social-environmental impact of water desalination plants while maximizing the benefit of fresh water production.

Membrane-filtration solutions include:

- Reverse Osmosis (RO), where salty feedwater is pushed through a semi-permeable membrane against the natural concentration gradient. The membrane allows water molecules to pass, leaving behind most of the solute to be removed (typical solute rejection are over 99% [83]). Among the main disadvantages we report membrane fouling -that is the accumulation of contaminants in the membrane pores clogging the passages for water molecules and requiring regular maintenance-, and concentration polarization.

- Forward Osmosis (FO), where a high-concentration solution is used to "draw" the water molecules out of the feedwater solution; then, the diluted draw solution is treated using one or more of the other conventional desalination methods. In this second phase, the fouling process is reduced, since the solution already underwent solute reduction. Fouling is still present in the first phase of the process, though.

- Electrodialysis (ED), where an electric voltage is used to force charged ions move through membranes [84]. In Italy, the plant Maggiulivedi in the island of Pantelleria uses electrodialysis as main process to provide over $3 \cdot 10^5\ m^3/year$ of water to the local population [85].

- Membrane Distillation (MD), where a hydrophobic membrane is used to separate water vapor from liquid saline water. Differently from the other membrane technologies in this list, MD is thermally driven: recent research has shown that the process can be easily integrated with renewable energy such as solar as well as within waste heat recovery systems [86].

- Nanofiltration (NF), where membranes are used to separate highly charged ions (Ca^{2+}, Mg^{2+}) and organic content. NF alone is not sufficient to reduce seawater salinity below drinking water threshold, so it is often coupled with RO [87].

Evaporation and condensation technologies include:

- Multi-Stage Flash Distillation (MSF), where seawater is heated and moved through a series of chambers under vacuum, each with lower pressure. The decrease in pressure causes the water to boil ("flash") and condense again on tubes to produce fresh water. The heat of condensation is re-used to preheat the incoming seawater, making the process more efficient. More details below.
- Multiple-Effect Distillation (MED), where heat is initially provided to seawater causing it to evaporate and condense in subsequent stages ("effects") at lower temperatures. The heat of condensation is recovered and used to evaporate further water along the stages, thus realizing a thermally efficient solution. More details below.
- Vapor Compression Distillation (VC, or VCD), where a compressor is used to increase vapor pressure and temperature [88]. In the plant at steady state, the seawater is evaporated by the heat provided by the same compressed water vapor which is about to condense.
- Adsorption-Desalination (AD), where water vapor physically binds to the pores of a hydrophilic sorbent material and it is later released and re-condensed by providing heat to the material. More details below.
- Solar still desalination, an ancient solution where seawater is heated up by direct sunlight, causing vapor to generate, move and condense in colder underground containers, where fresh water is collected.

Other methods include humidification dehumidification desalination [89], Gas-Hydrate Desalination -which promises low desalination costs ($\$0.50/m^3$ of produced water) but low solute reduction (31% for NaCl) [90]- and Chemical filtration -where ions are chemically bonded to other chemical species such as in Ion Exchange membranes technology- [70].

While some of the above technologies have a high-maturity level (e.g., RO, MSF, MED), others are still object of research and have few commercial implementations. Adsorption Desalination, object of this research, belongs to the latter family. In the next section, some of the most common desalination technologies are discussed more in depth. In particular, we will cover the three most diffused solutions: RO (currently used in the majority of the desalination plants in the world), MSF and MED. We will then discuss MD and AD, emerging technologies that allow water production while being potentially driven by low-grade waste heat.

3.3.2 State-of-the-art solutions

Reverse Osmosis (RO)

Reverse Osmosis provides a sustainable method to convert seawater into drinkable water, contributing in the alleviation of water shortage in regions in need. For its maturity, it is by far the most common seawater desalination technology: about 61% of the desalinated water globally is produced through RO plants [70, 84].
RO is based on a membrane-based separation process that utilizes a semi-permeable membrane to remove ions, molecules and large particles from water. Contrary to the natural osmotic process, where water moves from an area of low solute concentration to one of higher concentration, RO involves applying hydraulic pressure to the seawater and forcing it through the membrane, against natural concentration gradient [91].
The schematics of a RO plant is reported in 3.3.

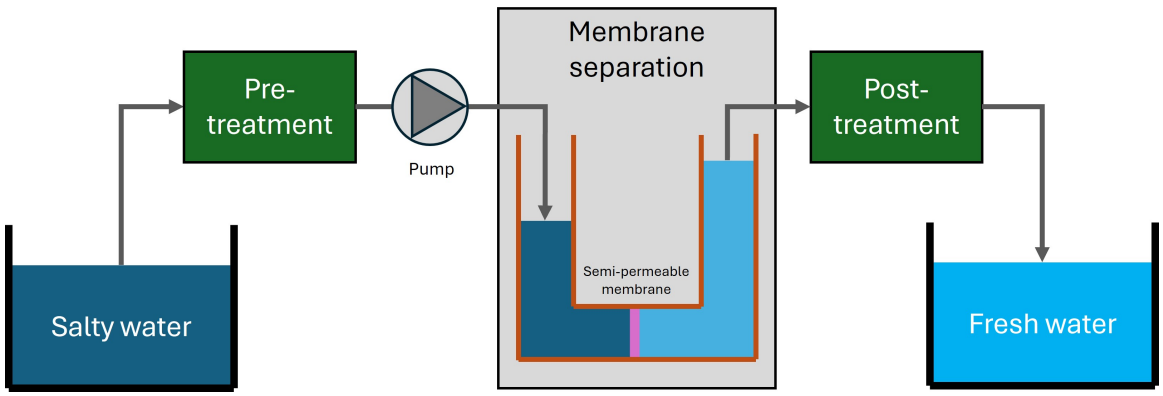

Fig. 3.3 (a) Working principle of a reverse osmosis plant. Phases include: pre-treatment, pumping of permeate, membrane separation, post-treatment. The schematics is simplified, and does not show, for example, the connections needed to remove the salts and contaminants accumulating over time on the high-concentration side of the membrane.

In addition to the KPIs introduced above, common to all desalination processes, RO performances are often evaluated in terms of enrichment factor E, defined as the ratio between the initial and final volume of the salty solution (high E means that it was possible to transport a high amount of water before the process became impossible). Another correlated KPI in RO process is the Recovery Rate RR, defined as the ratio of output flowrate and feed flowrate. Recovery Rate ranges between 30% and 80%, depending on the plant configuration [92], and can be increased by adding further membrane stages.

The worldwide diffusion of RO can be attributed to its many strong points:

- It is able to remove over $R = 99\%$ of the contaminants, including salts (especially the ones with high molecular weight and electrically charged ions), minerals, bacteria.

- It has a high technological maturity level (thus, it is reliable).
- It is efficient. State-of-the-art membrane technology allows Specific Energy Consumption as low as $2-3\ kWh/m^3$ of produced water [93].
- It is scalable. Water treatment applications range from domestic to municipal sites, from rural to industrial systems.

On the other hand, treatment of high-salinity water with RO has some disadvantages:

- Polarization concentration: as the solution flows through the semi-permeable membrane, the rejected solutes accumulate on one side of its surface. Once the local concentration reaches the saturation level, the solute precipitate and forms a layer on the membrane, making the mass flow more difficult over time [94].
- Membrane fouling: as the feedwater flows through the membrane, extraneous bodies such as microorganisms and other impurities are deposited on the membrane surface. Over time, this blocks the pores and reduces the water mass flow, requiring continuous maintenance to clean or replace the fouled components. Monitoring of pressure difference along the membrane and Silt Density Index (SDI) evaluation can help to program maintenance [95].
- Necessity of high-exergy sources: Reverse Osmosis uses as energy source mechanical work (usually created using electrical energy to run pumps), that is converted to hydraulic power and used to push the water against natural gradient. Thus, the integration with renewable energy is only possible if the latter is a high-exergy source, such as photovoltaic or wave energy [96]. On the other hand, it is not possible to effectively integrate RO with thermal solar plants or waste heat.

Multi-Stage Flash Distillation (MSF)

Multi-Stage Flash Distillation is a mature evaporation-condensation solution developed in the late 1950's and currently the second most diffused desalination technology in the world. It accounts for about 26% [70] of the global desalination capacity, being second to only Reverse Osmosis. A schematics of a MSF plant is provided in 3.4.

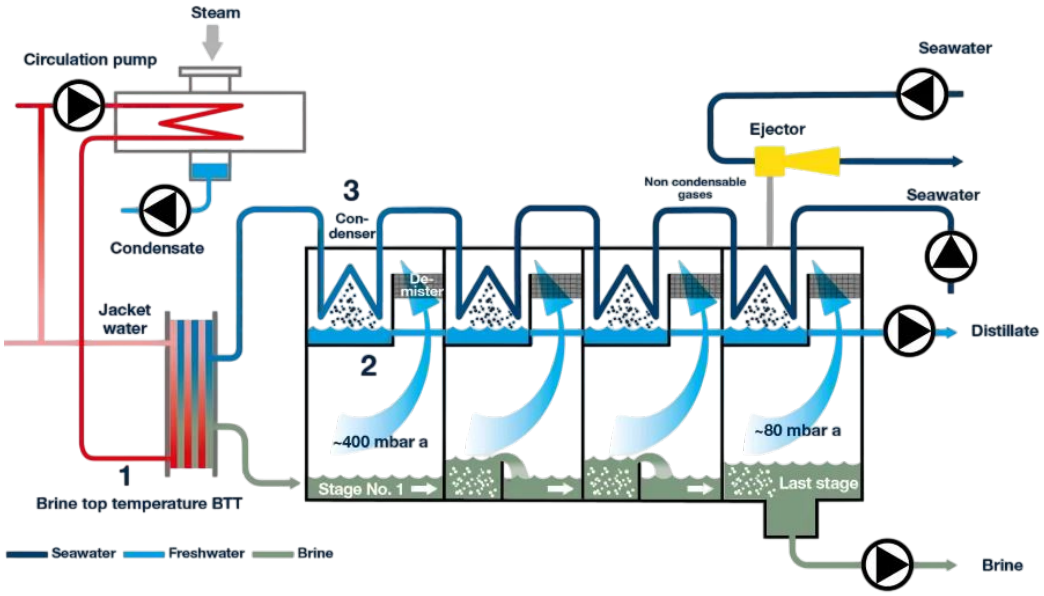

Fig. 3.4 Schematics of a MSF plant. (1): brine heater. (2): flash chamber. (3): first-stage condenser. Source of the picture: [97].

The input feedwater is first pretreated so to reduce the risks of scaling and fouling in the plant; then, heat is provided to water via an external source, bringing water temperature above 80°C [91]. The heated water (called *brine* from this point on) is introduced into a series of stages (up to 30 in large plants [91]) where it meets heat exchangers in which the colder input feedwater is running. This provides two useful effects: first, the vapor condenses and desalinated water is collected; second, in steady-state conditions, the heat of condensation is provided to the input water which is about to enter the heater, providing pre-heating and reducing the overall energy cost. The stages are kept under vacuum, at progressively decreasing pressures, so that the flashing (boiling) of water happens at the desired temperatures along the stages. The solute concentration in the brine increases gradually along the stages, before being disposed back into the sea.
Among the strong points of MSF, we report [91]:

1. high reliability and lower sensitivity to fouling with respect to RO, even in case of heavily polluted seawater, given that no membranes are used;
2. high water quality;
3. use of a low-exergy source: the energy needed to heat up the water for the evaporation process is thermal. This allows easier integration with renewable energy, including solar and geothermal.

MSF has some limitations:

1. high specific energy consumptions of up to $SEC = 25\ kWh/m^3$ of produced water (it must be noted, though, that this energy is thermal, and not pure exergy, unlike RO);

2. equipment corrosion due to the high temperatures and presence of seawater, requiring important maintenance;

3. plant complexity and costs, due to multiple stages and to the need to maintain vacuum in the system over time.

Multiple-Effect Distillation (MED)

Multiple-Effect Distillation is the third most common desalination technology in the world, accounting for about 8% of the global desalination capacity [70]. Like MSF, it belongs to the family of evaporation-condensation solutions, exploiting a series of stages -or "effects"- to progressively condense vapor and collect fresh water.
The schematics of a possible configuration of MED plant is reported in 3.5. The input salty water is fed into the first effect, where heat is provided by an external energy source. A portion of the feedwater evaporates and moves towards the next stage, where it finds a lower temperature and condenses. In doing so, it releases latent heat that contributes to the evaporation of more seawater, which moves to the next stage. The remaining brine of each stage is transferred to the next stage. This process continues up to the final stage, where brine is collected and a separate cooling line is used to condensate the last produced vapor. As for MSF, the effects are kept under vacuum for better control of the saturation temperatures.
The re-use of latent heat of vaporization across the effects makes MED a highly energy-efficient process.

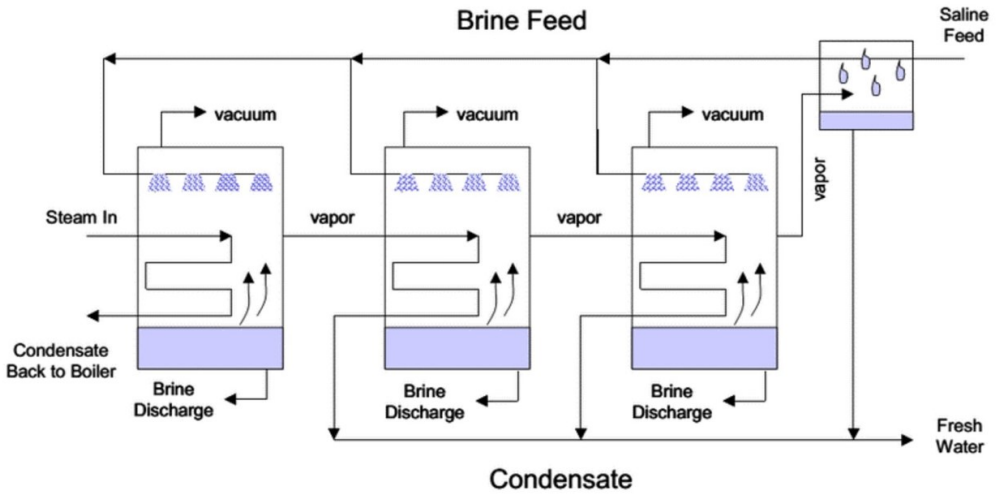

Fig. 3.5 Schematics of a MED plant. Source of the picture: [98].

When compared to MSF, Multiple-Effect Desalination shows some advantages:

1. lower energy consumption due to higher thermal efficiency;
2. lower operational temperature, reducing the risks for corrosion and requiring less maintenance and supervision;

On the other hand, MED has some limitations:

1. high capital costs, due to the multi-stage design and to the large heat transfer areas necessary to work at low temperature such as 70-75°C [91];
2. low under-scalability to smaller sizes, due to inefficiency in case of few stages;
3. impossibility to work at high temperature, due to the scale formation happening because of the precipitation of calcium carbonate and other salts [99]. The precipitated salts layer acts as insulator, reducing the heat transfer.

Membrane Distillation (MD)

Membrane Distillation (MD) is an emerging desalination solution that uses a hydrophobic membrane to separate water vapor from liquid saline water. The technology is not as diffused as the above discussed RO, MSF and MED, but shows a high potential for renewable energy integration given its capability to work at low operating temperatures [86, 100–102].

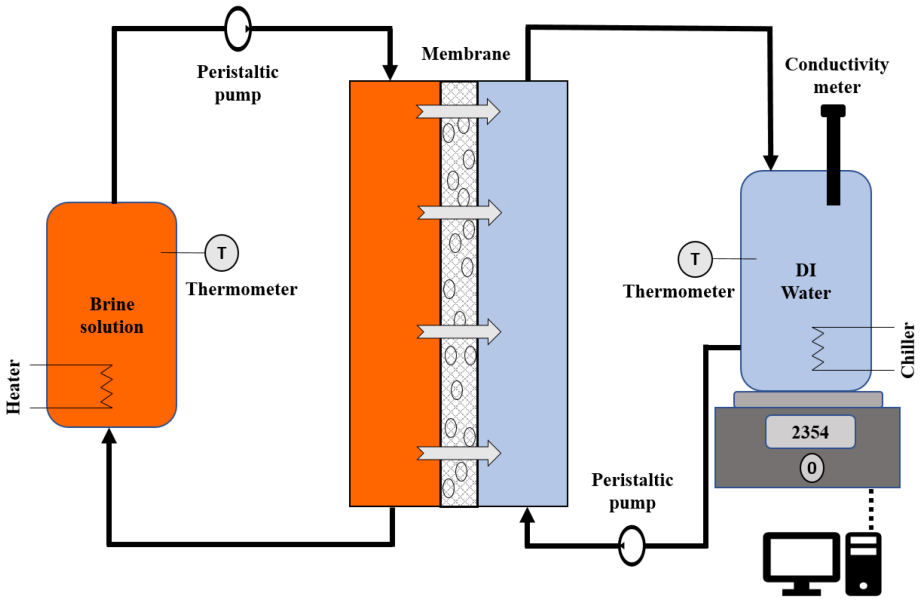

Fig. 3.6 Schematics of a MD plant. Source of the picture: [103].

The key technology behind MD is the membrane, realized in a non-polar hydrophobic porous material able to let water vapor -but not liquid water and other non-volatile

components- pass. This is achieved by preparing the membrane with pores in the diameter range $0.1 - 0.5\ \mu m$, small enough to exploit capillary effect and hinder liquid to reach the opposite surface of the membrane. The process of vapor mass transport is driven by a difference in temperature between the two sides of the membrane, typically 5-20°C. By heating the input seawater, partial vapor pressure increases and water molecules are transferred through the membrane and collected in a fresh-water flow (Fig. 3.6).
Membrane Distillation can be implemented in several configurations, each with advantages and disadvantages, including:

- Direct Contact Membrane Distillation, where hot and cold liquid flows are directly in contact with the two sides of the membrane. Condensation happens in the cold water flow directly at the membrane surface level, with high vapor transfer efficiency. A disadvantage is on the heat losses through the membrane, due to heat conduction mechanism.
- Air Gap Membrane Distillation: an air gap between the membrane and the condensation surface is introduced, reducing heat losses but lowering vapor flux.
- Vacuum Membrane Distillation: a vacuum gap on the cold side increases vapor transfer with respect to Air Gap Membrane Distillation, but increases plant complexity and costs.
- Sweeping Gas Membrane Distillation: a sweeping gas is used to carry vapor away from the membrane, offering further degrees of freedom on the heat and mass transfer control without requiring to manage vacuum but at the cost of efficiency for high flowrates.

Among the MD advantages we list:

1. low driving temperatures compared to MSF and MED (40-80°C), allowing integration with ultralow-grade heat sources;
2. compact and modular design, especially suitable for small-scale water production.

On the other hand, disadvantages include:

1. Membrane scaling and fouling, due to deposition of contaminants on the feedwater side of the membrane;
2. low thermal efficiency when compared with other thermal solutions such as MSF and MED, with STEC reaching 200 kWh/m^3 of produced water [102];
3. low scalability from lab-scale to industrial-scale.

Adsorption Desalination (AD)

Adsorption Desalination (AD) is an emerging thermal desalination technology that exploits the hydrophilic properties of adsorbent materials for the conversion of seawater into fresh water. It combines advantages of previously discussed technologies: it is driven by low-grade heat while not making use of membranes -thus, limiting the maintenance necessary because of fouling. Nevertheless, AD maturity level is still low compared with RO, MSF and MED. Given the high potential, we chose to explore more in depth AD in this research, investigating on the use of calcium alginate as alternative sorbent.
Adsorption Desalination machines work by alternating adsorption and desorption phases (Fig. 3.7a,b), and intermediate transition phases (pre-cooling and pre-heating). During adsorption, the chamber containing feedwater (Evaporator) is put in communication with the environment containing the sorbent (Adsorber module); vapor fills the two chambers and binds to the sorbent micropores. The extraction of vapor driven by the sorbent creates a local depression, which attracts more vapor from the feedwater chamber. If not interrupted, the process would continue until the material is in equilibrium with the saturation conditions at the feedwater temperature, and pressures in the chambers equalize[3]. Being adsorption an exothermic process, heat is dissipated during this phase through an external loop at environmental temperature (20-35°C). During desorption, the module containing the sorbent material is put in communication with the chamber containing the output fresh water (Condenser). The material is heated up using an external source, and the vapor is released back at higher temperature (45-80°C). In such conditions, the vapor condenses at environmental temperature and fresh water is collected. Typically, the whole process occurs under vacuum, to enhance the vapor mobility and have better control on the the saturation conditions in the chambers.
The sequence of pre-heating, desorption, pre-cooling and adsorption is called a *cycle* (Fig. 3.7). Fresh water is produced only during the desorption phase; thus, in order to guarantee a pseudo-constant production rate along the day, usually two or more adsorption modules working alternately are included in an AD plant (while one is in adsorption phase, the other is in desorption phase, and viceversa).
Among the most used KPIs in AD plants (some of them shared with AWH plants), we recall:

- SDWP: Specific Daily Water Production. This is defined as the amount of water produced per day and per unit of sorbent material:

$$SDWP = \frac{V_{H_2O}}{m_{dry} \cdot t_{cycle}} \tag{3.11}$$

[3]In practical applications, though, the adsorption process is often interrupted before the equilibrium is met, both to avoid the material working at too high relative humidity (risking salt deliquescence in case of composites) and to maximize the specific daily water production. The latter aspect is discussed more in detail in Chapter 5.

where V_{H_2O} is the volume of water produced per cycle, m_{dry} is the mass of dry sorbent in the plant, t_{cycle} is the time spent to run a full adsorption-desorption cycle[4]. Typically, the units used are $[V_w] = m^3$, $[m_{dry}] = ton$, $[t_{cycle}] = day$, from which: $[SDWP] = \frac{m^3}{ton \cdot day}$. The definition given in Equation 3.11 is especially useful when the amount of condensed water is measured directly. On the other hand, if that is indirectly estimated based on condensation power, another equivalent definition becomes more practical:

$$SDWP = \int_0^{t_{cycle}} \frac{Q_{cond}}{h_{vap} \cdot m_{dry} \cdot t_{cycle}} dt \tag{3.12}$$

where t is time, H_{vap} is the enthalpy of vaporization at the condensation temperature (as a reference, at 30°C, $H_{vap} = 2430\ kJ/kg$) and Q_{cond} is the condensation energy rejected on the condenser side. If a liquid loop is used to cool down the condenser, then mass flowrate $\dot{m}_{flow}$ and temperature difference $(T_{cd,out} - T_{cd,in})$ between in and out of the condenser are monitored, and $Q_{cond} = \dot{m}_{flow} \cdot c_p \cdot (T_{cd,out} - T_{cd,in})$, with c_p being the specific heat of the used liquid ($c_p = 4186\ \frac{J}{kg \cdot °C}$ for water). The equivalence of Equations 3.11 and 3.12 follows directly from the definition of enthalpy of vaporization: $h_{vap} \cdot V_w = \int_0^{t_{cycle}} Q_{cond} dt$.
In this work, we also propose and use a related KPI:

$$SCWP = \frac{V_w}{m_{dry}} \tag{3.13}$$

which is the amount of water produced during one cycle of operation.

- PR: Performance Ratio. This is defined as the ratio between heat of condensation and heat of desorption:

$$PR = \int_0^{t_{cycle}} \frac{\dot{m}_{H_2O} \cdot h_{vap}}{t_{cycle} \cdot Q_{Des}} dt \tag{3.14}$$

where Q_{Des} is the thermal power provided to the sorption bed during desorption and $\dot{m}_{H_2O}$ is the desalinated water production rate (i.e., the amount of water produced per unit of time).

- SCP: Specific Cooling Power. This is defined as the ratio of the cooling power registered on the evaporating loop during adsorption and the amount of dry material:

$$SCP = \left(\frac{1}{t_{cycle}}\right) \cdot \int_0^{t_{cycle}} \frac{Q_{Evap}}{m_{dry}} dt \tag{3.15}$$

where Q_{Evap} is the evaporation power absorbed by the feedwater during adsorption. If a liquid loop is used to heat up the evaporator, then mass flowrate $\dot{m}_{flow}$ and temperature difference $(T_{ev,in} - T_{ev,out})$ between in and out of the evaporator are monitored, and

[4] In the literature, sometimes the symbol τ is introduced instead, indicating the amount of cycles per day. From which: $t_{cycle} = \frac{1}{\tau}$.

$Q_{Evap} = \dot{m}_{flow} \cdot c_p \cdot (T_{ev,in} - T_{ev,out})$. Sometimes in the literature, SCC (Specific Cooling Capacity) is also found, defined as the product of SCP and the cycle time.

- COP: Coefficient Of Performance. This is defined as the ratio between evaporation energy (that is, cooling effect) and desorption energy:

$$COP = \frac{\int_0^{t_{cycle}} Q_{Evap} dt}{\int_0^{t_{cycle}} Q_{Des} dt} \tag{3.16}$$

We earlier defined $STEC$ as an indicator of the thermal energy $E_{thermal}$ used to produce a liter of fresh water for a generic thermal desalination plant (in this case, $E_{thermal}$ is the desorption energy E_{Des}). Upon definition of proper quantities averages, PR, SCP, COP and STEC can be put in correlation:

$$STEC = \frac{E_{Des}}{V_w} \simeq \frac{h_{vap}}{PR} \simeq \frac{SCP}{SDWP \cdot COP} \tag{3.17}$$

The $\simeq$ in the latter equation is used because the relations would be true if the powers were constant over time[5], but they are not exact in general.

Adsorption Desalination plants have a series of strong points:

1. They are driven by low-exergy sources, such as heat in temperature ranges 40-120°C (depending on the used sorbent [24]).
2. There are no membranes or other components which need frequent cleaning, reducing the need for maintenance and the environmental impact generated by specific chemicals.
3. Evaporation happens at low temperature (25-35°C), thus reducing the risk of scaling and corrosion. Furthermore, since there are few moving parts, the need for maintenance is low.
4. As byproduct, AD plants produce cooling power from the evaporation process, thus making them cogeneration systems. This can be useful in contexts where water scarcity and high cooling demands are requested (e.g., in hot and arid climates).
5. Since no membranes are used, pores fouling is not a risk, meaning that highly salty and contaminated water can be treated as well.

On the other hand, AD plants limitations include:

[5]To be mathematically accurate, this condition is sufficient, but not necessary. What is actually important is that the integral average corresponds to the average quantity used in 3.17. For instance, in case of *PR*, it must be verified that $(1/\bar{Q}_{Des}) = \frac{1}{t_{cycle}} \int_0^{t_{cycle}} \frac{1}{Q_{Des}} dt$, which is surely true if Q_{Des} is constant over time, but not only in such case.

1. Strong dependence on the specific used sorbent;
2. Scalability: currently, most of the existing AD plants are limited to small- or medium-scale prototypes, producing amounts of water at most in the order of hundreds or thousands of liters per day.

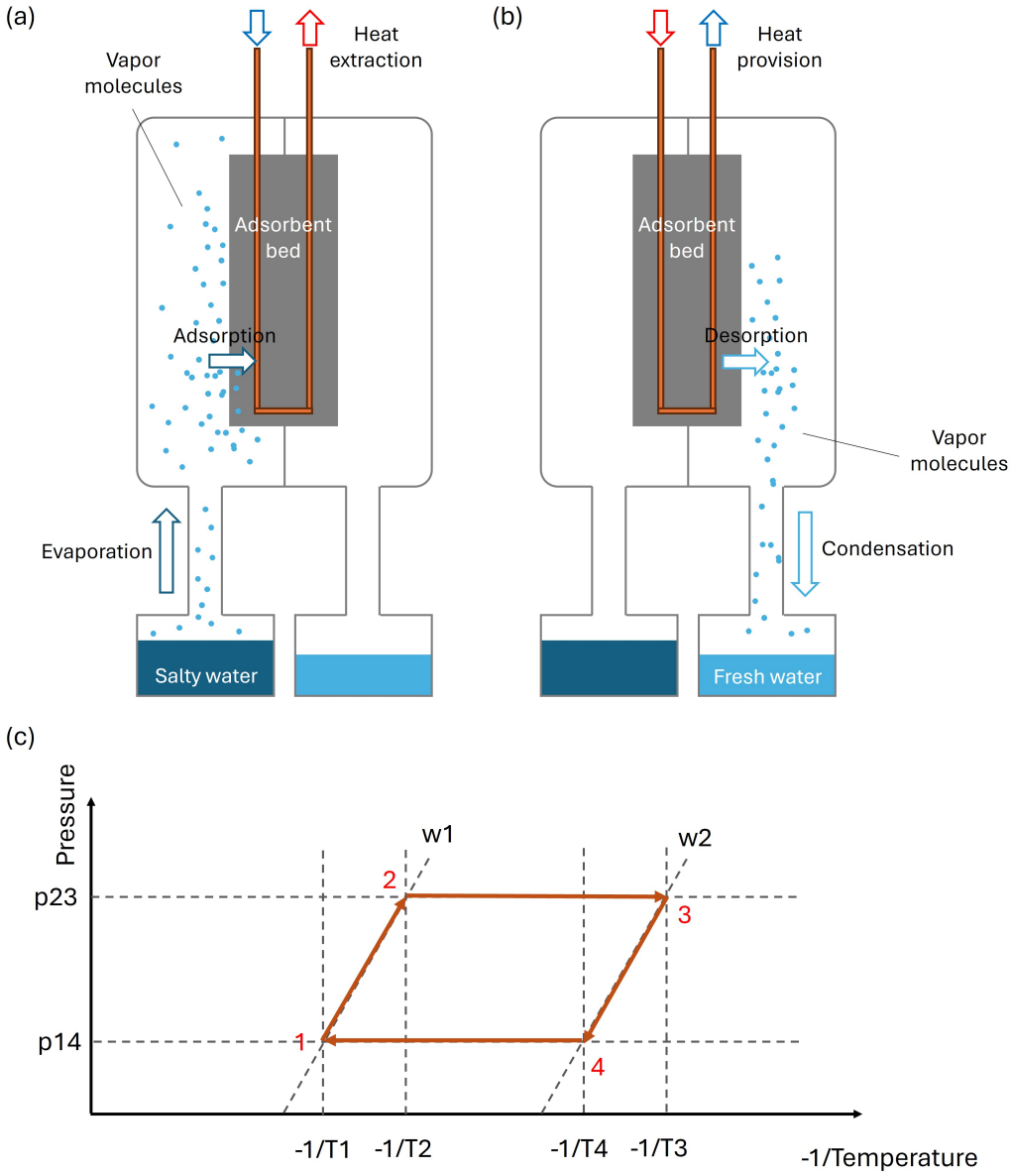

Fig. 3.7 Schematics of an AD plant. (a) Simplified schematics of the adsorption phase in a AD system. (b) Simplified schematics of the desorption phase in a AD system. (c) Diagram of the AD cycle. Isosteric heating 1-2: the adsorbent is heated at constant water uptake; Isobaric Heating/Desorption 2-3: the adsorbent releases water vapor as it is further heated at constant pressure; Isosteric Cooling 3-4: the adsorbent is cooled at constant water uptake; Isobaric Cooling/Adsorption 4-1: the adsorbent adsorbs water vapor as it is cooled at constant pressure.)

As a conclusion, if compared with the other state-of-the-art solutions, AD fits in the low-temperature and low-production area, as schematized in Fig. 3.8.

The performance of AD plants strongly depends on the choice of the sorbent. Using a sorbent with better capacities and kinetics allows to increase the SDWP, thus reducing the plants dimensions and costs. For this reason, the research for new sorbents is crucial.

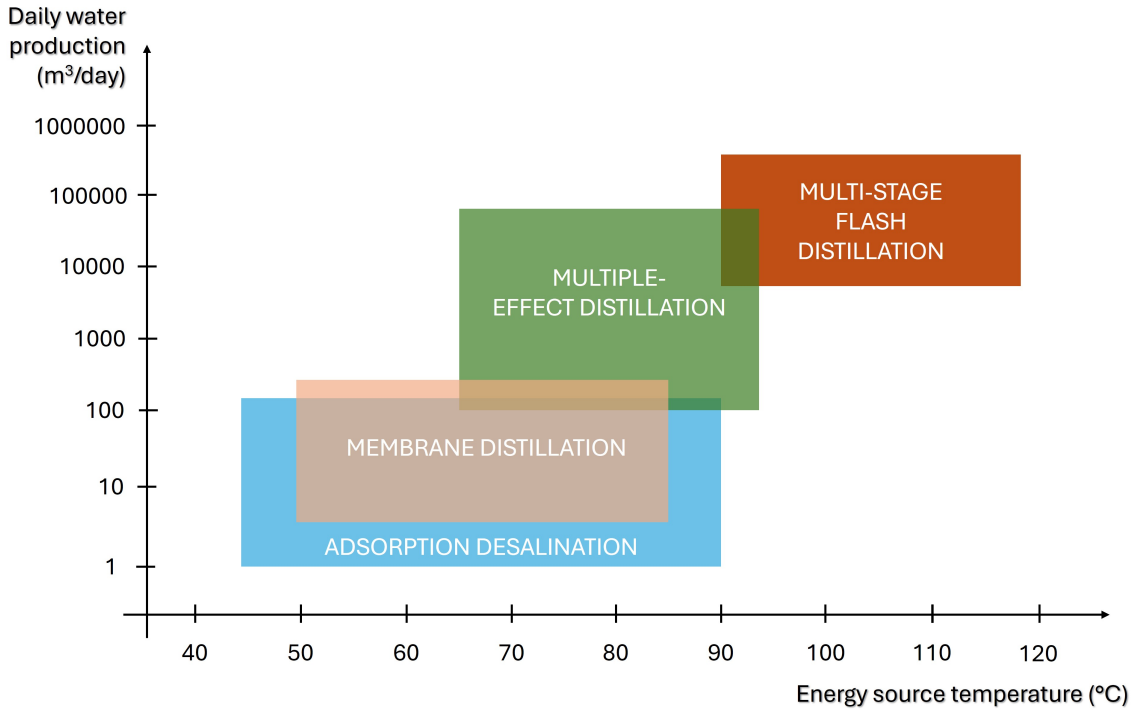

Fig. 3.8 Map of desalination solutions in comparison, based on sources: [24, 104–111]. If compared with other adsorption-based technologies, adsorption desalination plants have relatively low water productivity, but this is also due to the low level of maturity of the technology. On the other hand, similarly to MD, AD allows to exploit ultralow-grade heat (temperature even below 50°C), as it will be demonstrated in chapter 5.

3.4 Requirements for drinkable water

The reduction of salt content is useful in different contexts, including irrigation, industrial processes requiring fresh water (e.g., food processing, cleaning) and human use, like for washing and drinking. When the latter is the scope of the desalination plant, tight requirements must be met in order for water to be potable, thus safe for human consumption. Regulations and guidelines exist around the world:

- the World Health Organization provides guidelines for drinking-water quality and sampling procedures [112];
- in Europe, directive EU 2020/2184 proposes boundaries for a list of parameters that drinkable water should respect [113];

- in Italy, D.Lgs. 18/23 accepts and recognizes directive EU 2020/2184, with no significant variations [114].

As the regulations specify, the reduction of salt content alone is not sufficient to make water drinkable: specific biological risks, acidity, metal content, odor and appearance are equally tight requirements. For this reason, atmospheric water harvesting and water desalination plants are often coupled with pre- and post-processing equipment.
The tables below show in comparison some of the reference values given by the WHO and the EU 2020/2184 (the full list is found at [113, 112]). When a single number is specified, that is the maximum allowed content. When a "-" is specified, that means that the reference regulation does not specify a value.

Parameter	Unit	WHO	EU 2020/2184
Acrylamide	$\mu g/L$	0.5	0.1
Alachlor	$\mu g/L$	20	-
Arsenic	$\mu g/L$	10	10
Benzene	$\mu g/L$	10	1.0
Benzo(a)pyrene	$\mu g/L$	0.7	0.01
Bisphenol A	$\mu g/L$	-	2.5
Boron	$\mu g/L$	2400	1500
Bromate	$\mu g/L$	10	10
Chlorate	$\mu g/L$	700	250
Copper	$\mu g/L$	2000	2000
1,2-Dichloroethane	$\mu g/L$	30	3
Fluoride	$\mu g/L$	1500	1500
Lead	$\mu g/L$	10	5
Nickel	$\mu g/L$	70	20
Nitrate	$\mu g/L$	50000	50000
Pesticides Total	$\mu g/L$	-	0.5
PFAS Total	$\mu g/L$	-	0.5
Uranium	$\mu g/L$	30	30
Vinyl chloride	$\mu g/L$	500	0.5

Table 3.2 Acceptable chemical contaminants amounts in drinking water, according to WHO Guidelines for drinking-water quality [112] and EU 2020/2184 [113]

Parameter	Unit	WHO	EU 2020/2184
Intestinal enterococci	$number/100\ mL$	-	0
Escherichia coli	$number/100\ mL$	0	0
Legionella	CFU/L	-	1000
Coliform bacteria	$number/100\ mL$	0	0
Clostridium perfringens	$number/100\ mL$	0	0

Table 3.3 Acceptable microbiological contaminants amounts in drinking water, according to WHO Guidelines for drinking-water quality [112], and EU 2020/2184 [113].

Parameter	Unit	WHO	EU 2020/2184
Conductivity	$\mu S/cm\ at\ 20°C$	-	2500
Total dissolved solids (TDS)	mg/L	1000*	-
pH	pH	6.5-8.5	4.5-9.5
Color	TCU	15*	**
Odor	-	**	**
Taste	-	**	**
TOC	-	-	**
Turbidity	-	**	**

Table 3.4 Acceptable physical contaminants amounts in drinking water, according to WHO Guidelines for drinking-water quality [112] and EU 2020/2184 [113]. *: This is not a strict constraint, but instead a reference value above which it is said that, generally, water becomes not acceptable by the user. **: Acceptable to consumers and no abnormal change.

In general, at least for the parameters here listed, the requirements for chemicals specified by the EU 2020/2184 are equal or tighter than the WHO specifications. Attention on pesticides and PFAS (Per- and Poly-FluoroAlkyl Substances) is raised by EU only.
Electrical Conductivity (EC) is defined as the inverse of Electrical Resistivity (ρ), the latter being an intensive property of materials representing their ability to resist the passage of electric current. Thus, EC represents the material's capability to conduct electric current, and it is usually measured in Siemens per meter (more commonly, Siemens per centimeter): S/m (S/cm). It is dependent on temperature [115]. The measure of EC is usually carried out using conductivity sensors, which exist in variants exploiting different principles. One option consists in generating a current going through the tested fluid between the sensor's electrodes, and then measuring the resulting potential difference (from which, resistivity can be estimated using Ohm's laws).
Total Dissolved Solids (TDS) is a measure of the total amount of organic and inorganic compounds dissolved in a solution. It is usually measured in parts per million (ppm). The

most accurate method for TDS measurement follows by its definition: a sample of the solution is positioned on a scale, and it is evaporated at 180°C for 3-5 hours until only the non-volatile solid contents remain on the scale plate (ISO 17025). TDS is then estimated as the final mass of solid content divided by the initial mass of solution.
The presence of salts and dissolved contents in water is associated with its increase in conductivity: this is the reason why the two parameters are often confused and regulations only mention one of them. For example, the World Health Organization only suggests values for Total dissolved solids (600 mg/L is a suggested "limit", which can increase up to 1000 mg/L without the user noticing significant changes in palability); on the other hand, EU 2020/2184 only suggests a limit in conductivity (2500 $\mu S/cm$ at 20°C).
Given their correlation, some empirical formulas are proposed in the literature, suggesting that TDS can be estimated starting from the value in conductivity. For instance, a review from Rusydi [116] suggests for fresh water the expression (especially accurate for $EC < 3000\ \mu S/cm$):

$$TDS = 0.65 \cdot EC \tag{3.18}$$

From this, we can estimate that the value of $EC = 2500\ \mu S/cm$ specified by EU would result in a maximum TDS of approximately 1625 mg/L; at the same way, the value $TDS = 1000\ mg/L$ specified by the WHO would result in a maximum EC of approximately 1538 $\mu S/cm$. These are clearly only estimations: the only way to correctly deduce values of EC and TDS in a solution is to perform the direct measurements as specified above.

Chapter 4

Experimental characterization of calcium alginate

4.1 Introduction

Among the non-conventional sorbents introduced in Chapter 2, calcium alginate stands as an interesting alternative for fresh water production applications such as adsorption-based AWH and WD, introduced in Chapter 3. In order to better assess the vapor adsorption potential of calcium alginate, we produced multiple batches of sorbent and experimentally characterized its properties.

In the first part of this chapter, we present the main results. In particular, we discuss the experimental adsorption isotherm of CaAlg samples, along with its classification and the estimation of adsorption enthalpy based on the best-fitting theoretical equilibrium model. Then, we discuss the experimental charging and discharging transients, and diffusivity is estimated based on the best-fitting theoretical dynamics model. Finally, we discuss the experimental aging of the material, when the latter is subjected to multiple cycles.

In the second part of this chapter, we present the methods used to obtain the experimental results. In particular, we describe the calcium alginate synthesis procedure, the experimental equipment and the testing campaigns.

Main objective of the chapter is to characterize calcium alginate, choosing the chemical compositions with the highest performance to be used in AWH and AD units in the next chapter.

4.2 Main results

4.2.1 Equilibrium uptakes

Preliminary comparison

Six calcium alginate compositions were produced and tested (see Methods section for the full description) in order to compare the adsorption capacities and select the material with the best performance for future use. The achieved equilibrium water uptakes of the compositions are reported in table 4.1 (at T=21°C and RH=34%) and in table 4.2 (at T=21°C and RH=47%). The results discussed in this first paragraph are extracted from the published article at [47]. Water uptakes are all referred to a dry condition reached after 5 hours desorption at T=100°C and uncontrolled humidity. As expected, a higher relative humidity (or, a higher vapor pressure) during adsorption increases the water uptake achieved by the samples, reaching 0.88 g/g at T=21°C and RH=47% in case of sample Alg_1Ca_{10} [1]. This value represents a threefold increase with respect to conventional sorbents such as silica-gel samples.
Comparing compositions Alg_1Ca_5 and Alg_1Ca_{10}, we observe that the material sorption capacity increases with the increase of $CaCl_2$ content, while keeping other components constant. The same can be observed by comparing compositions Alg_2Ca_5 and Alg_2Ca_{10}.

Sample	w_{eq} (g/g)	w_{5h} (g/g)	RH_0 (%)	RH_{5h} (%)	RH_{avg} (%)
Alg_1Ca_5	0.515	0.436	26.5	33.4	27.2
Alg_1Ca_{10}	0.610	0.570	22.6	34.4	22.9
Alg_2Ca_5	0.300	0.149	27.2	34.0	29.6
Alg_2Ca_{10}	0.573	0.464	26.4	33.8	24.0
$Alg_1Ca_5G_{0.1}$	0.448	0.407	27.6	33.6	27.8
$Alg_1Ca_5G_{0.025}$	0.518	0.468	27.7	34.6	27.1

Table 4.1 Comparison of water uptake capacities of six CaAlg compositions at RH=34%. These include: equilibrium water uptake at T=21°C and RH=34% (w_{eq}), water uptake after 5 hours adsorbing (w_{5h}) starting from a dry-state at 100°C, relative humidity at the beginning of the adsorption process (RH_0), at the end (RH_{5h}) and in average during the test (RH_{avg}) [47].

[1] In our syntax $Alg_XCa_YG_Z$, X is the mass/mass concentration of sodium alginate, Y is the mass/mass concentration of calcium chloride, Z is the mass/mass concentration of graphite, as measured with respect to the aqueous solutions in which they are dissolved during the production processe. See Methods for details.

Sample	w_{eq} (g/g)	w_{5h} (g/g)	RH_0 $(\%)$	RH_{5h} $(\%)$	RH_{avg} $(\%)$
Alg_1Ca_5	0.683	0.562	28.00	48.10	35.35
Alg_1Ca_{10}	0.880	0.706	30.00	46.20	34.95
Alg_2Ca_5	0.412	0.309	38.10	48.40	40.82
Alg_2Ca_{10}	0.695	0.542	30.50	47.52	36.47
$Alg_1Ca_5G_{0.1}$	0.601	0.527	32.30	46.00	36.87
$Alg_1Ca_5G_{0.025}$	0.647	0.522	35.60	45.87	38.11

Table 4.2 Comparison of water uptake capacities of six CaAlg compositions at RH=47%. These include: equilibrium water uptake at T=21°C and RH=47% (w_{eq}), water uptake after 5 hours adsorbing (w_{5h}) starting from a dry-state at 100°C, relative humidity at the beginning of the adsorption process (RH_0), at the end (RH_{5h}) and in average during the test (RH_{avg}) [47].

On the other hand, comparing compositions Alg_1Ca_5 and Alg_2Ca_5, we observe that increasing the NaAlg content while keeping the $CaCl_2$ concentration constant, lowers the sorption capacity of the hydrogel. The same can be observed by comparing compositions Alg_1Ca_{10} and Alg_2Ca_{10}.

The addition of graphite in the composition has a positive effect on equilibrium when in low amounts: composition $Alg_1Ca_5G_{0.025}$ shows slightly larger uptakes than composition Alg_1Ca_5 at low RH, while instead a further increase such as in $Alg_1Ca_5G_{0.1}$ lowers the sorption capacities. The latter effect might be explained with the fact that graphite flakes occupy pores in the sorbent structure, causing occlusion and limiting the adsorption sites for water particles.

Even in case of small amount of graphite, though, the increase in uptake is very low (about 7%) and might not justify the introduction of graphite as additive in a larger scale production process. For this reason, we find the base composition Alg_1Ca_{10} as the best candidate for further characterization.

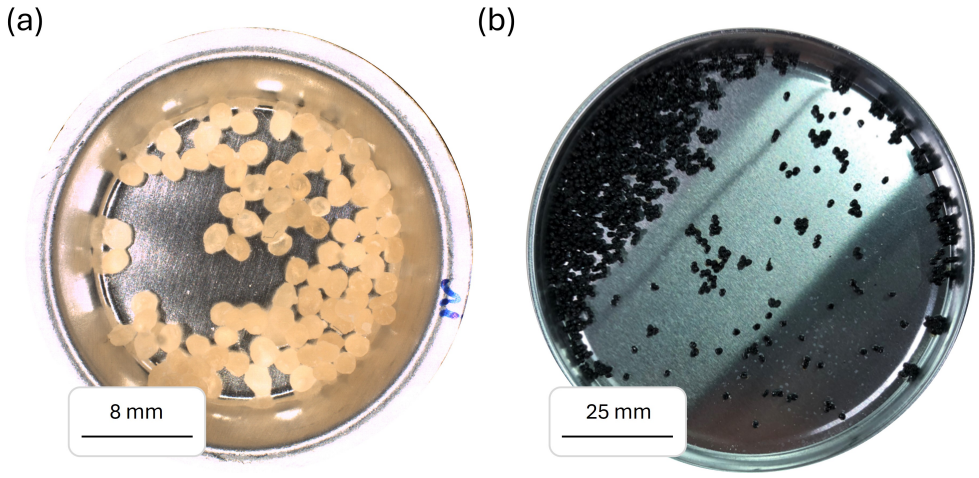

Fig. 4.1 Samples of CaAlg with and without graphite. (a) a sample of CaAlg without graphite (composition Alg_1Ca_{10}). (b) A sample of CaAlg including graphite (composition $Alg_1Ca_5G_{0.1}$).

Isotherm

Composition Alg_1Ca_{10} was found to be the one with the highest performance in terms of equilibrium uptakes at T=21°C and RH=34% or RH=47%. For this reason, a second larger batch was produced for a more exhaustive characterization campaign in a gravimetric vapor sorption analyser (see Methods). The results discussed in this sub-paragraph are extracted from paper [24]. The resulting isotherm at 30°C is shown in figure 4.2a:

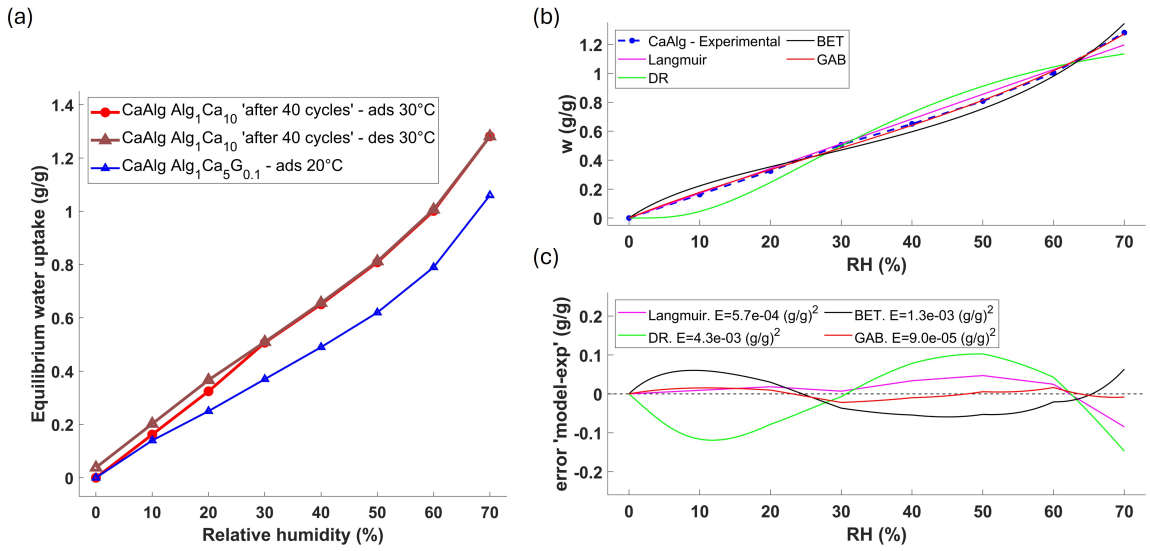

Fig. 4.2 CaAlg isotherms and best-fitting equilibrium models [24]. (a) Alg_1Ca_{10} adsorption and desorption isotherms at 30°C, compared with the adsorption isotherm of $Alg_1Ca_5G_{0.1}$ (b) Alg_1Ca_{10} adsorption isotherm best-fitted by equilibrium models Langmuir, DR, BET, GAB. (c) Errors made by model over experimental data. In the legend, we report the integral E of the square of the error over RH.

The water uptakes are coherent and close to the ones observed in the preliminary comparison: 0.57 g/g vs 0.61 g/g at RH=34%, 0.77 g/g vs 0.88 g/g at RH=47%. The small differences can be explained: the testing equipment and procedure is different (see Methods section), and also a different supplier for the $CaCl_2$ salt was used, the last one having a purity of about 80%. For this reason, the tested sample would be more properly classified as Alg_1Ca_8 and, indeed, shows intermediate capacities between Alg_1Ca_5 and Alg_1Ca_{10}.
In the same graph, we report in comparison the adsorption isotherm at 20°C on a sample of $Alg_1Ca_1G_{0.1}$, made from an external laboratory [47]. This provides an independent proof of the high capacity of CaAlg samples and confirms Alg_1Ca_{10} as the composition with the best performance. The isotherm has a "S" shape (in both compositions) and does not show hysteresis in the high-RH range; thus, it can be classified as type-II (see Chapter 2). In figure 4.2b, the adsorption branch is compared with theoretical models discussed in Chapter 2, such as Langmuir, DR, BET, GAB isotherms. The absolute errors made by the models are reported in 4.2c. We report the best-fitting parameters and average errors of the tested models in table 4.3:

	Langmuir	DR	BET	GAB
Model parameters	$w_{max} = 393\ g/g$ $K = 10^{-8}\ Pa^{-1}$	$w_{max} = 1.23\ g/g$ $\beta = 0.3929$ $H = 2007\ J/mol$	$w_m = 0.425\ g/g$ $c = 8.007$	$w_m = 0.7317\ g/g$ $c = 3.456$ $K = 0.7704$
Integral error E	$5.7 \cdot 10^{-4}\ (g/g)^2$	$4.3 \cdot 10^{-2}\ (g/g)^2$	$1.3 \cdot 10^{-3}\ (g/g)^2$	$9.0 \cdot 10^{-5}\ (g/g)^2$
Physically consistent	No	No	Yes	Yes

Table 4.3 Equilibrium models best-fitting parameters for CaAlg.

	Langmuir	DR	BET	GAB
Model parameters	$w_{max} = 2.4 \cdot 10^8\ g/g$ $K = 3 \cdot 10^{-13}\ Pa^{-1}$	$w_{max} = 0.424\ g/g$ $\beta = 0.0394$ $H = -332\ J/mol$	$w_m = 0.173\ g/g$ $c = 0.614$	$w_m = 0.173\ g/g$ $c = 0.612$ $K = 0.9993$
Integral error E	$1.2 \cdot 10^{-3}\ (g/g)^2$	$4.2 \cdot 10^{-4}\ (g/g)^2$	$2.0 \cdot 10^{-5}\ (g/g)^2$	$2.0 \cdot 10^{-5}\ (g/g)^2$
Physically consistent	No	No	Yes	Yes

Table 4.4 Equilibrium models best-fitting parameters for mesoporous silica-gel.

In the case of Langmuir, the found coefficients are not physically consistent: forcing unconstrained[2] error minimization led to a w_{max} exceeding the admittable range. This is explained with the fact the Langmuir isotherm is not suitable to best-fit type-II isotherms. In the

[2]It is possible to constrain the best-fitting procedure so that w_{max} does not surpass a threshold, but this artificial expedient leads the model to just choose w_{max} equal to the threshold, not providing any physically consistent information.

case of Dubinin-Radushkevich (DR), still the coefficients are not physically consistent, with H being one order of magnitude below the expected energy associated with the adsorption process.

In the case of the BET model, the parameters are physically consistent, being w_m below the maximum capacity and c larger than 2, coeherently with a type-II isotherm [56]. In the case of the GAB model, the parameters are physically consistent as well, being w_m below the maximum capacity, K between 0 and 1, and c larger than 2, coeherently with a type-II isotherm. Compared with the BET model, it leads to lower error over the examinated RH range, thus we chose to proceed our analysis relying on the GAB approximation.

Inverting equation 2.14, we can estimate an adsorption enthalpy of $H_{Ads} = 2600\ kJ/kg$, approximately 7% larger than the latent heat of evaporation of water at the same temperature of 30°C.

We performed the same equilibrium tests over two samples of conventional microporous and mesoporous silica-gels (see Methods). Figure 4.3a shows the Alg_1Ca_{10} isotherm and the silica-gels isotherms in comparison.

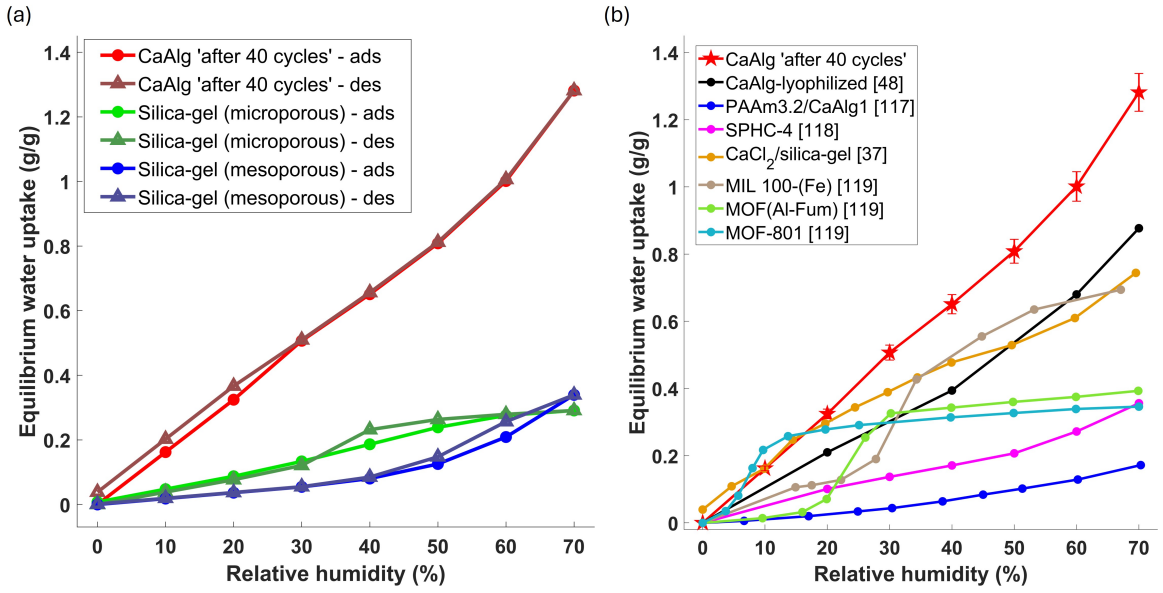

Fig. 4.3 Comparison of CaAlg isotherm at 30°C with silica-gels and samples from the literature. (a) CaAlg adsorption and desorption isotherms at 30°C compared with microporous and mesoporous silica-gels that we tested under the same conditions. (b) CaAlg adsorption isotherm at 30°C compared with samples from the literature [37, 48, 117–119].

The comparison shows that, when tested in identical test conditions, the CaAlg sample reaches water uptakes about four times larger than ordinary silica-gels: at RH=70%, CaAlg reaches 1.28 g/g, with respect to 0.29 g/g for microporous SG and 0.34 g/g for mesoporous SG. Furthermore, the CaAlg isotherm shows a better linearity and a lower hysteresis. The mesoporous silica-gel isotherm can be classified as Type-III or Type-V, depending on the behaviour after RH=70% (not explored in this research). We can best-fit the adsorbing

isotherm using the same models as in table 4.3. The results are reported in table 4.4, and show how the BET and GAB models are still the only models physically consistent with the type of isotherm (more in particular, the obtained $K \approx 1$ for the GAB model makes it coincide with the BET model).
In figure 4.3b, we compare the CaAlg isotherm with results from the literature, including other hydrogels, composites and MOFs. The vertical bars on the CaAlg isotherm represent $\pm$ one standard deviation on the experimental measurement[3]. In the range RH=0-20%, MOF-801 and $CaCl_2$-silica-gel composites show slightly larger equilibrium uptakes; on the other hand, for RH of 30% of higher, the CaAlg capacity largely exceeds the compared sorbents.
We conclude that, concerning equilibrium water uptakes, the designed Alg_1Ca_{10} is our most competitive option to surpass conventional and non-conventional sorbents capacities.

4.2.2 Dynamics

The same six calcium alginate compositions as in 4.2.1 (here referred to as 'S1', 'S2', ..., 'S6', see Methods), were tested for adsorption and desorption transients. The resulting desorption and adsorption transients curves for $T_{Ads} = 21°C$, $RH_{Ads} = 47\%$, $T_{Reg} = 100°C$ are shown in figure 4.4.

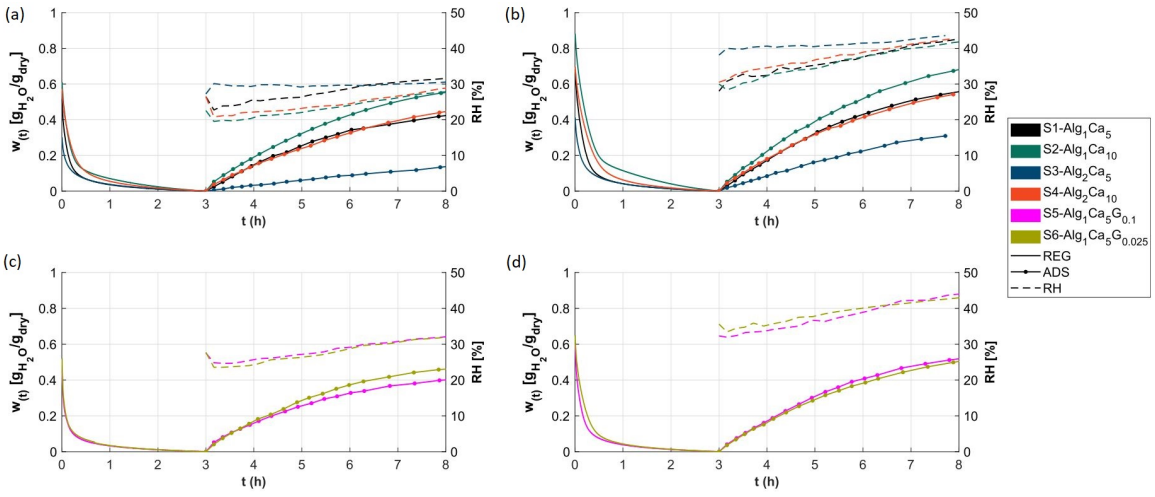

Fig. 4.4 Time-dependent water uptake variation between adsorption and regeneration in CaAlg samples [45]. On the x-axis, the time t in hours; on the left y-axis, the water uptake w(t); on the right y-axis, the relative humidity RH within the conditioning chamber during sorption. (a) Results of samples S1, S2, S3, S4 at RH=34%. (b) Results S1, S2, S3, and S4 at RH=47%. (c) Results of samples S5 and S6 at RH=34%. (d) Results of samples S5 and S6 at RH=47%.

[3]The standard deviation is calculated comparing the resulting isotherm on three different samples of CaAlg; thus, the considered uncertainty is only due to the inhomogeneity of the produced CaAlg beads. The gravimetric analyser has, on the other hand, a balance resolution of 1 μg and a reproducibility of ± 5 μg, which would not be visible if reported on this scale. For this reason, we didn't report uncertainty in the measurements on commercial silica-gel samples, that we assumed to be homogeneous.

The first trait (0-3 hours) of each graph shows the desorption ramp at 100°C and environmental uncontrolled RH; the second trait (3-8 hours) shows the adsorption phase (duration of 5 hours). All the water uptakes have been evaluated assuming as "dry" the condition at the end of the desorption ramp. The initial water uptake in the desorption phase is the one corresponding to equilibrium in the adsorption conditions (see tables 4.1 and 4.2).
In general, samples containing more $CaCl_2$ and less NaAlg perform better, as stated in the equilibrium results section. Nevertheless, higher water uptakes during the adsorption transients might be also explained by the larger equilibrium value rather than a better vapor diffusivity. In order to separate the effect of equilibrium and dynamics contributions, we used the dynamics models described in Chapter 2 to best-fit the experimental data.
In Fig. 4.5a,b we can see how models FD, FDRH, FDSW, LDF, LDFDw, LDFm approximate the desorption and adsorption transients of a sample of Alg_1Ca_5. The absolute errors made by both models over time are shown in Fig. 4.5c,d. In general, LDF-based models provide a better approximation, especially when describing adsorption transients. This might be explained by the fact that FD-based models are derived under specific boundary conditions and assumptions that are not met in the experimental setup, e.g.: vapor pressure in the test environment is not kept exactly constant, preventing the hypotheses of models FD and FDRH to be met; also, sample temperature is not controlled, and important heat effects occurring during adsorption may cause the hypothesis of isothermal process not to be true. Model FDSW performs better, being developed to adapt to change in RH; nevertheless, in case of desorption the approximation is worse and, furthermore, the best-fitted diffusivity in this model does not have an immediate physical interpretation.

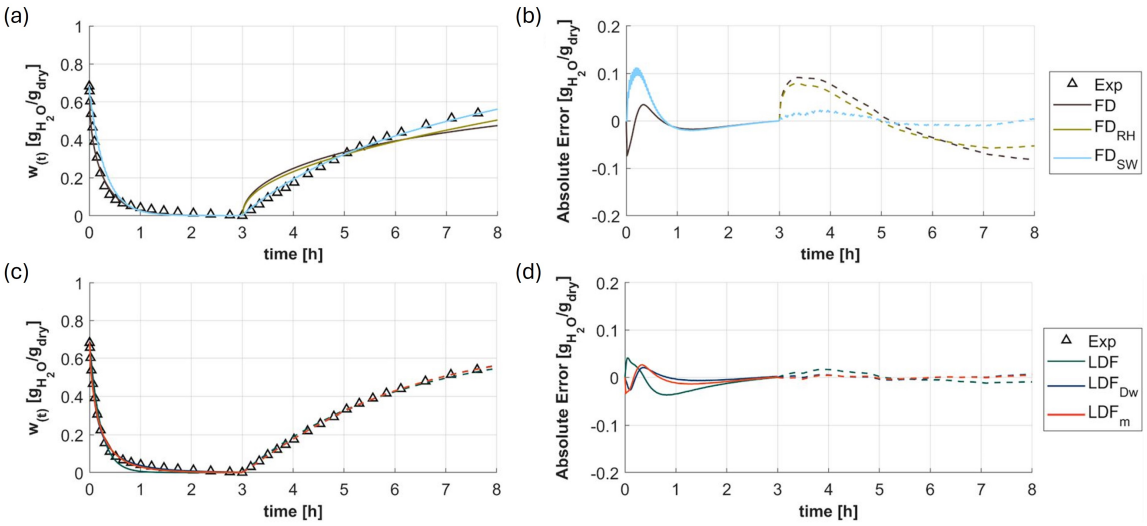

Fig. 4.5 Comparing CaAlg dynamics data with FD-based and LDF-based models [45]. (a) Comparison between the experimental values of the regeneration/sorption test of sample S1 at 47% and the values obtained from models FD, FDRH, and FDSW, using the optimization method of paragraph 2.4. (b) The absolute error with respect to experimental data generated with each model and at each time. (c) and (d) report the same information for the models LDF, LDFDw, and LDFm.

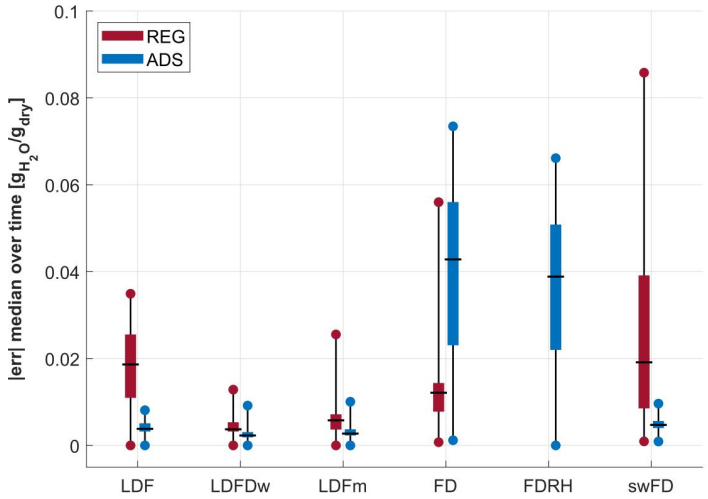

Fig. 4.6 Dynamics models errors in comparison [45]. We plot the average of the error over time generated by each model and categorized by the model typology (a low value means that the model behaved well in best-fitting the adsorption/desorption test). Each error bar contains the error distribution among the six samples (a large error bar means that the model behaved very differently with different samples).

In figure 4.6 we show the errors made by the models in comparison. To build this, we first averaged the error over time per each test; then, we drew the error bar of the samples in comparison. A good model should be able to best-fit the experimental data with low average error over time and low variance between different tests. Model LDFDw resulted being the one with the best performance from this point of view, with an average error about four times smaller than ordinary LDF and more than 10 times smaller with respect to FD in best-fitting adsorption ramps. Interestingly, LDFDw outperformed LDFm both for adsorption and desorption ramps: this supports the idea that the introduction of physically consistent parameters provides not only more information about the process, but also better approximation results.
The best-fitting process produced estimations for diffusivity D, both in adsorption and desorption. The list of values for the LDF-based models is reported in tables 4.5 and 4.6 ($1\ \mu m^2/s \equiv 10^{-12}\ m^2/s$). The best-fitting of FD-based models can be found in [45].

Condition	Ads at T=21°C, RH=34%					Ads at T=21°C, RH=47%				
Model parameter	LDF_D ($\mu m^2/s$)	$LDFDW_a$ ($\mu m^2/s$)	$LDFDW_b$ ($\mu m^2/s$)	$LDFm_D$ ($\mu m^2/s$)	$LDFm_m$	LDF_D ($\mu m^2/s$)	$LDFDW_a$ ($\mu m^2/s$)	$LDFDW_b$ ($\mu m^2/s$)	$LDFm_D$ ($\mu m^2/s$)	$LDFm_m$
Alg_1Ca_5	2.71	2.59	0.662	2.97	1.03	2.54	2.22	1.49	3.24	1.09
Alg_1Ca_{10}	3.40	2.89	2.39	4.22	1.09	2.53	2.49	0.122	2.56	1.00
Alg_2Ca_5	0.767	0.710	1.08	0.904	1.05	1.71	1.35	3.35	2.61	1.156
Alg_2Ca_{10}	2.45	2.31	0.795	2.61	1.02	2.61	2.60	0.0451	2.58	0.996
$Alg_1Ca_5G_{0.1}$	6.78	7.14	-2.13	5.86	0.950	5.72	4.96	3.77	7.13	1.085
$Alg_1Ca_5G_{0.025}$	3.50	3.19	1.69	3.96	1.05	2.54	2.51	0.196	2.58	1.01

Table 4.5 LDF-based models best-fitted parameters during adsorption [45]. $1\ \mu m^2/s \equiv 10^{-12}\ m^2/s$.

Condition	Des at T=100°C, from eq. T=21°C, RH=34%					Des at T=100°C, from eq. T=21°C, RH=47%				
Model parameter	LDF_D $(\mu m^2/s)$	$LDFDW_a$ $(\mu m^2/s)$	$LDFDW_b$ $(\mu m^2/s)$	$LDFm_D$ $(\mu m^2/s)$	$LDFm_m$	LDF_D $(\mu m^2/s)$	$LDFDW_a$ $(\mu m^2/s)$	$LDFDW_b$ $(\mu m^2/s)$	$LDFm_D$ $(\mu m^2/s)$	$LDFm_m$
Alg_1Ca_5	43.8	4.27	166	6.27	0.564	36.8	10.6	77.5	12.9	0.708
Alg_1Ca_{10}	32.1	3.16	102	4.80	0.570	23.2	6.61	38.6	7.36	0.687
Alg_2Ca_5	21.6	1.81	152	2.66	0.538	26.1	2.62	127	3.58	0.555
Alg_2Ca_{10}	29.7	7.45	80.8	8.34	0.664	25.2	12.8	34.8	13.2	0.795
$Alg_1Ca_5G_{0.1}$	103	1.85	502	6.93	0.48	87.8	10.1	278	14.2	0.580
$Alg_1Ca_5G_{0.025}$	62.9	0.377	270	3.40	0.460	35.8	10.5	79.9	11.8	0.693

Table 4.6 LDF-based models best-fitted parameters during desorption [45]. $1\ \mu m^2/s \equiv 10^{-12}\ m^2/s$.

In general, water vapor diffusivities for CaAlg samples are of the order of $10^{-12}\ m^2/s$ in case of adsorption (21°C) and of the order of $10^{-11}\ m^2/s$ in case of desorption (100°C). Sample Alg_1Ca_{10} in particular shows a diffusivity of $3.4 \cdot 10^{-12}\ m^2/s$ according to the LDF model, and an uptake-dependent diffusivity of $(2.9 + 2.4 \cdot w) \cdot 10^{-12}\ m^2/s$ according to the LDFDw model. Diffusivity of samples with graphite is higher with respect to other samples, especially in case of desorption: for this reason, we consider composition $Alg_1Ca_5G_{0.1}$ as an alternative option to include in future research.

Influence of temperature

The low error made by LDFDw model demonstrates that the assumption of constant diffusivity is not reliable when approximating CaAlg adsorption and desorption transients, probably due to the large water uptake range covered. By performing desorption experiments under different conditions, we proved that this is even more evident at higher temperatures. The results in this paragraph are extracted from [45]; more data is provided in Appendix C. The resulting desorption ramps for the six compositions are shown in Fig. 4.7:

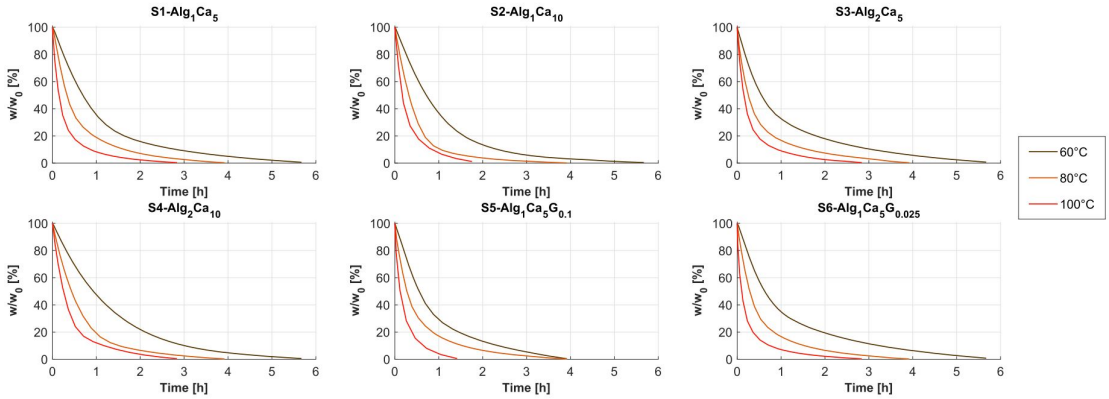

Fig. 4.7 Effect of regeneration temperature on desorption dynamics for each tested CaAlg composition (S1, S2, ..., S6) [45]. In the y-axis, the water uptake normalized to the equilibrium value.

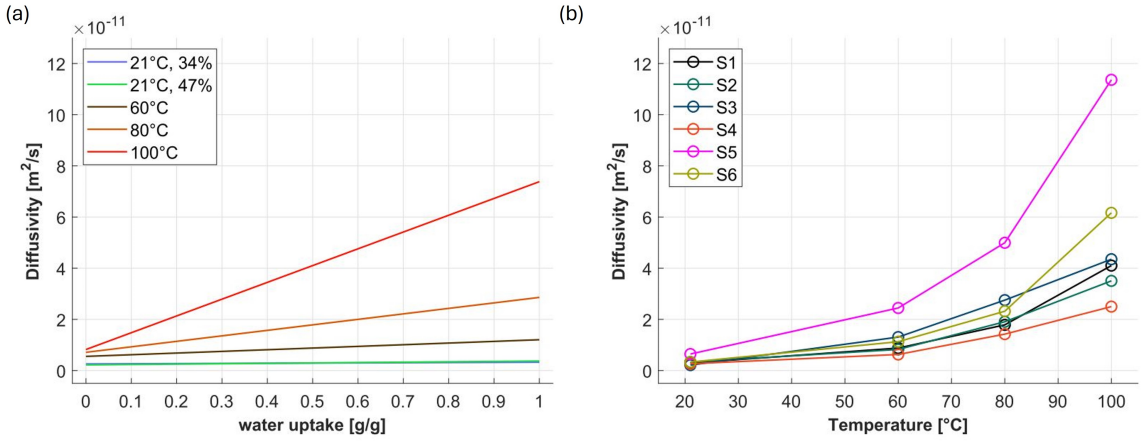

Fig. 4.8 Influence of temperature on diffusivity [45]. (a) Dependence of sample S1 diffusivity on water uptake at different temperatures. (b) Dependence of D on the temperature at a fixed water uptake (0.5 g/g, as a reference) for all samples.

The desorption ramps are shown after having been normalized with respect to the initial equilibrium value, in order to allow an easier comparison of the dynamics (original data is provided in Appendix). As expected, we observed that higher desorption temperatures lead to faster discharging transients. By repeating the best-fitting procedure over these transients using model LDFDw, we derived parameters a and b at different temperatures.
In Fig. 4.8a, we see the functional forms of $D = D(w) = a + b \cdot w$ on sample Alg_1Ca_5 based on the best-fitting procedures at different temperatures. The value of b becomes larger as temperature grows, indicating that the dependence of diffusivity on water uptake is even larger at higher temperatures. In figure 4.8b, we fix uptake at 0.5 g/g and show diffusivity as a function of only temperature, for the six compositions in comparison. As an example, diffusivity for sample Alg_1Ca_{10} at 60°C is about double than at 30°C; at 90°C, diffusivity is about three times with respect to diffusivity at 60°C, revealing a non linear functional form. To include this result in the LDFDw model, we propose a functional dependence on temperature as: $a = a(T) = v_1 + v_2 \cdot (T + 273.15)$ and $b = b(T) = v_3 \cdot e^{-\frac{v_4}{T+273.15}}$, making LDFDw a 4-parameters model. The coefficients v1, v2, v3, v4 can be obtained by best-fitting directly the new LDFDw model over two directions (uptake and temperature) simultaneously. We also propose a non-exact but simplified alternative procedure: first, the base LDFDw model is used to estimate a and b at various temperatures; then, expressions $a(T)$ and $b(T)$ are best-fitted (see Appendix C) over the resulting values to obtain coefficients v_1, v_2, v_3, v_4. We list the resulting values in table 4.7. These parameters should be treated as purely empirical workarounds, and in general they have no specific physical interpretation (at a closer look, v2 might be interpreted as a measure of the influence that temperature has on diffusivity independently from the current water uptake).

	$v1\ (m^2/s)$	$v2\ (1/K)$	$v3\ (m^2/s)$	$v4\ (K)$
Alg_1Ca_5	$-1.95 \cdot 10^{-11}$	$7.48 \cdot 10^{-14}$	$2.02 \cdot 10^{-2}$	$7.30 \cdot 10^{3}$
Alg_1Ca_{10}	$-4.87 \cdot 10^{-11}$	$1.76 \cdot 10^{-13}$	$9.40 \cdot 10^{0}$	$9.78 \cdot 10^{3}$
Alg_2Ca_5	$-1.73 \cdot 10^{-11}$	$6.14 \cdot 10^{-14}$	$2.17 \cdot 10^{-6}$	$3.83 \cdot 10^{3}$
Alg_2Ca_{10}	$-3.35 \cdot 10^{-11}$	$1.23 \cdot 10^{-13}$	$4.28 \cdot 10^{0}$	$9.62 \cdot 10^{3}$
$Alg_1Ca_5G_{0.1}$	$-7.41 \cdot 10^{-11}$	$2.64 \cdot 10^{-13}$	$5.45 \cdot 10^{-4}$	$5.60 \cdot 10^{3}$
$Alg_1Ca_5G_{0.025}$	$-1.04 \cdot 10^{-11}$	$4.52 \cdot 10^{-14}$	$6.98 \cdot 10^{-2}$	$7.56 \cdot 10^{3}$

Table 4.7 Best-fitted parameters to account for temperature dependence in LDFDw model [45].

4.2.3 Cycling aging

Cycling CaAlg in a climatic chamber for over 300 cycles

In [47], sample $Alg_1Ca_5G_{0.1}$ was subjected to over 300 consecutive adsorption-desorption cycles in climatic chamber (see Methods section); periodically, a sample of material was removed and a desorption ramp was performed to compare the material dynamics over time. The result is shown in Fig. 4.9:

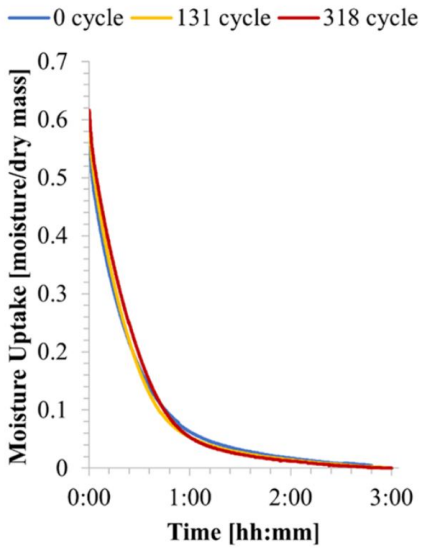

Fig. 4.9 Aging of a CaAlg sample after 0, 131 and 318 cycles in climatic chamber [47]. Reduction of water uptake with a regeneration temperature of 80°C after equilibrating the SA-graphite sample at 21°C and RH=50%. Three different curves correspond to the sample at the beginning of the aging in the climatic chamber (0^{th} cycle), after the 131^{th} and 318^{th} cycles, respectively.

The desorption ramps after 0, 131 and 318 cycles are comparable, demonstrating that thermal cycles on the material do not degrade the water uptake desorption dynamics of the material.

Change in isotherms after 40 cycles in a desalination unit

The effect of material aging was assessed in terms of equilibrium uptakes, as well. Composition Alg_1Ca_{10} was cycled under vacuum in a desalination unit (see Chapter 5), and the resulting isotherm after 0, 20, 30 and 40 was built.
Figure 4.10a shows how the CaAlg isotherm evolved over time. We observed no significant change in the material behaviour as it undergoes successive cycles, except for an initial decrease (during the first 20 cycles). This can be attributed to the fact that the internal structure of material was not completely settled immediately after production: for example, there might have been residual water from the synthesis procedure. Also, being CaAlg a polymeric material, we think that the polymeric chains might need initial cycles to rearrange and assume their final configuration.
Figure 4.10b provides the same information as figure 4.10a, this time with cycles on horizontal axis. This clearly shows the tendency of equilibrium uptake towards an asymptotical value, further proof of material stability. In particular, after the first 20 cycles, the water uptakes for RH=40-70% are 5-10% lower with respect to the uptakes of the material 'as produced'; then, the equilibrium values remain fairly constant after 30 and 40 cycles.

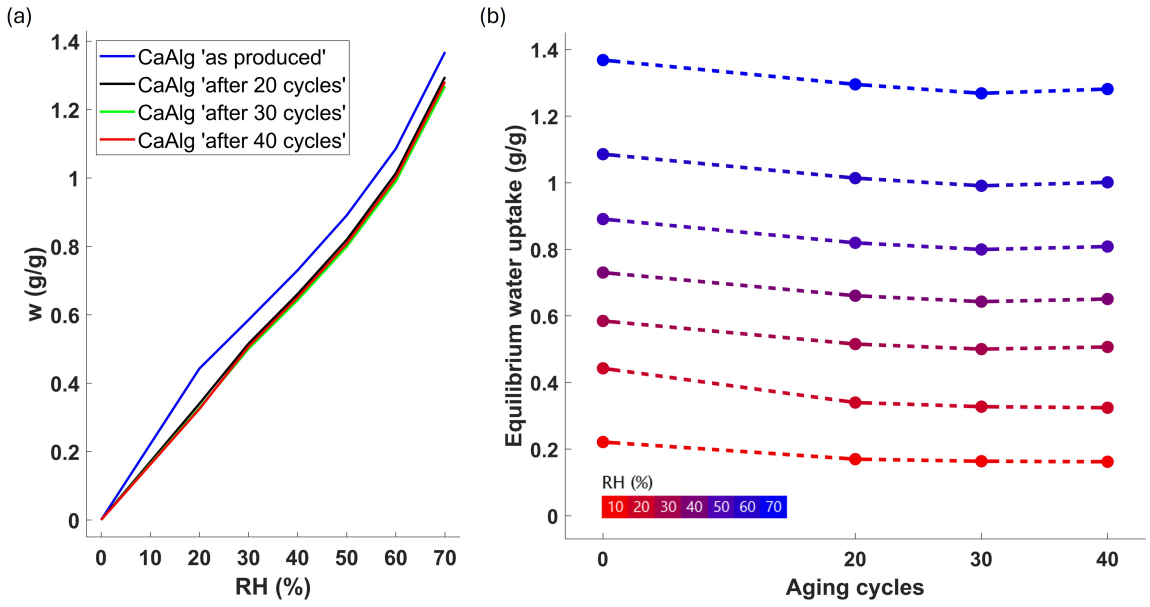

Fig. 4.10 CaAlg adsorption isotherm aging with cycles in a desalination unit. (a) Adsorption isotherm at 30°C of CaAlg samples after 0, 20, 30 and 40 cycles in the desalination unit. (b) Equilibrium water uptakes at RH=40-70% as a function of the testing cycles; below, pictures of the CaAlg after 0, 20, 30, 40 cycles, all taken in equilibrium at RH=40%.

Change in diffusivity

The best-fitting procedure used with the dynamics models LDF and LDFDw was repeated over the charging-discharging data obtained during the construction of the isotherms at 30°C

in the vapor sorption analyser, both for silica-gel samples and for CaAlg Alg_1Ca_{10} samples after 0, 20, 30 and 40 cycles. The full list of best-fitted diffusivities is provided in table 4.8. The resulting diffusivity in case of CaAlg samples are in the same order of magnitude of what estimated with the adsorption-desorption transients discussed above: approximately $3 \cdot 10^{-12}\ m^2/s$ at 30°C. Furthermore, no significant change is observed in best-fitted diffusivities after 0, 20, 30 or 40 cycles, providing a further proof of material stability over time. Silica-gel diffusivity reaches the order of $10^{-11}\ m^2/s$, aligning with values from the literature [68]. The higher diffusivity for silica-gel samples suggests that the CaAlg has a slower adsorption kinetics. This might be compensated by the larger equilibrium uptake only if long cycles are performed: in the case short cycles are required by the application, like for adsorption chillers, the silica-gel may still remain the best choice.

Sample	LDF_D $(\mu m^2/s)$	$LDFDW_a$ $(\mu m^2/s)$	$LDFDW_b$ $(\mu m^2/s)$
CaAlg 'as produced' - s1	2.3165	3.8539	-1.9338
CaAlg 'as produced' - s2	1.9602	3.1908	-1.5355
CaAlg 'as produced' - s3	2.0970	3.4669	-1.7101
CaAlg 'as produced' - s4	2.9736	5.2914	-2.9004
CaAlg 'as produced' - s5	3.2148	5.7963	-3.1579
CaAlg 'as produced' - s6	2.1791	3.8598	-2.0775
CaAlg 'after 20 cycles' - s1	2.9922	5.1280	-2.8659
CaAlg 'after 20 cycles' - s2	2.8662	4.8607	-2.5662
CaAlg 'after 30 cycles' - s1	2.5994	4.3916	-2.3856
CaAlg 'after 30 cycles' - s2	2.4104	3.9398	-2.0154
CaAlg 'after 40 cycles' - s1	2.6270	4.3621	-2.3303
CaAlg 'after 40 cycles' - s2	2.6733	4.4399	-2.2985
Silica-gel 'microporous'	3.7031	4.1324	-3.3240
Silica-gel 'mesoporous'	8.7188	13.778	-24.067

Table 4.8 Best-fitted diffusivities of CaAlg and silica-gel samples. Diffusivities of CaAlg (composition Alg_1Ca_{10}) and silica-gel (micro- and mesoporous), according to models LDF (second column) and LDFDw (third column for parameter a, fourth column for parameter b). ' - s1', ' - s2', ..., ' - s6' are different samples of the same batch. $1\ \mu m^2/s \equiv 10^{-12}\ m^2/s$.

4.3 Methods

4.3.1 Material synthesis

Calcium alginate was obtained via ionotropic gelation, a mechanism where a calcium ion Ca^{2+} replaces a sodium ion Na^+ in the sodium alginate egg-box structure (see Chapter 2 for

details). The same methodology presented in [45] was followed, and it is here presented. Experimentally, ionotropic gelation was achieved by placing in contact a liquid solution of water plus calcium chloride with a liquid solution of water plus sodium alginate. The latter solution was possibly enriched with further additives that are desired in the final hydrogel composition (e.g., graphite).

Fig. 4.11 CaAlg synthesis materials and methods. (a) CaAlg production schematics. (b) NaAlg powder. (c) Graphite powder. (d) Homogeneous NaAlg+water solution. (e) $CaCl_2$ powder. (f) Peristaltic pump moving NaAlg solution. (g) 3D-printed nozzle dripping into the salty solution. (h) 3D drawing of the nozzle. (i) Beads of jellified CaAlg, as collected from the salty solution. (j) CaAlg spheres with excess water, drying in open air. (k) CaAlg beads drying in a oven. (l) Final produced CaAlg.

In order to produce spherical beads of calcium alginate, an experimental setup was built. This drips sodium alginate solution into a solution of calcium chloride (Fig. 4.11a). More in detail, the production procedure consisted of the following steps:

1. A first aqueous solution (sol. *A*) was prepared, consisting of:
   - demineralized water;
   - sodium alginate powder (Fig. 4.11b);
   - possible additives, e.g. graphite (Fig. 4.11c).

   The solution was prepared in a cylindrical container, and homogenized using an electric mixer. Given the low solubility of sodium alginate, some hours were needed in order for the solution to be homogeneous (Fig. 4.11d). Graphite was mixed in the demineralized water and sonicated before adding sodium alginate powder.

2. A second aqueous solution (sol. *B*) was prepared, consisting of:
   - demineralized water;
   - calcium chloride powder (Fig. 4.11e).

   The solution was prepared in a large basin, and homogenized using an electric mixer. Given the exothermic nature of the salt dissolution, we waited some hours in order for the solution to cool down to environmental temperature.

3. A peristaltic pump (Fig. 4.11f) was used to transport solution *A* from its container towards a 3D-printed nozzle (Fig. 4.11g) suspended above the basin containing solution *B*. The nozzle was designed (Fig. 4.11h) to have three holes with 1.8 mm diameter, and the pump flowrate is adjusted by varying the input voltage, such that sol. *A* drops leave the nozzle at a regular rate and fall by gravity into solution *B*. The distance between the nozzle and the sol. *B* surface was chosen of 25-30 cm (a compromise distance found experimentally, such that the spherical shape of alginate spheres is not affected due to the fall). As soon as sol. *A* drops come in contact with sol. *B*, the jellification process starts. An electrical mixer is always running during the process, in order to limit the variations in the local salt concentration. A video of the process is provided at: https://youtube.com/shorts/dSW4IolS4dg (last visited on 26/10/2025).

4. We waited the necessary time for solution *A* to completely jellify [4]; then, for further 12 hours the produced material was left in solution *B*, in order for the jellification process to complete (in particular, to ensure diffusion of Ca^{2+} ions within the beads volume).

[4] As a reference, starting with 10 kg of sol *A* and 90 kg of sol *B* and powering the peristaltic pump at 8V, about 3 hours were needed.

5. The produced spheres were collected using a fine net (Fig. 4.11i), then washed in demineralized water for about 30 seconds in order to remove excess salt on the beads surface.

6. The washed spheres were positioned on large flat surfaces, and let rest for 6 hours in order for most excess water to evaporate (Fig. 4.11j).

7. The produced beads at this point had a grain size of 6-7 millimiters, and contained lot of excess water from the production process. To remove it, the beads were dried in a oven at 75°C[5] for 12 hours (Fig. 4.11k).

8. At the end of the drying process, the beads grain size reduced to approximately 1.5-2.0 mm. At this point, the material was weighted and kept in air-tight containers, to avoid unwanted adsorption as long as the material was not used (Fig. 4.11l).

The demineralized water used to prepare the solutions had a conductivity of $\approx 8\ \mu S/cm$ and was produced using the distillation system Milli-Q® EQ 7000. The NaAlg and CaAlg powders come from suppliers Carlo Erba Reagents and Alquera, respectively. All the setup components (mixer, basin, cylindrical tank, peristaltic pump, nozzle) were fixed in position with the help of an aluminum structure. The chemicals were weighted with scales KERN FKB 65K0.2 (capacity of 65 kg, accuracy of 0.2 g) and KERN PCB 6000-1 (capacity of 6 kg, accuracy of 0.1 g).
The obtained CaAlg beads have a grain size of approximately 1.5 mm, in dry conditions (T=25°C and RH$\approx$ 15%). For the sake of simplicity, the CaAlg beads are approximated as spheres when needed in the calculations in this work, and the grain size is used as sphere diameter. The appearance of the dry material slightly changed when used: working at higher temperatures, its color became browner (Fig. 4.12a), probably due to a charamelization effect of the organic compounds. Also, its diameter slightly decreased from 1.57 mm (average on measurements on 10 beads, with standard deviation of 0.12 mm) to 1.43 mm (average on 10 beads, with standard deviation of 0.10 mm) probably because the produced material still had residual excess water).

[5]This value is chosen so to avoid degradation due to excessive temperature. In [47], we have shown that regenerating CaAlg to up to 80°C does not affect the material's performance.

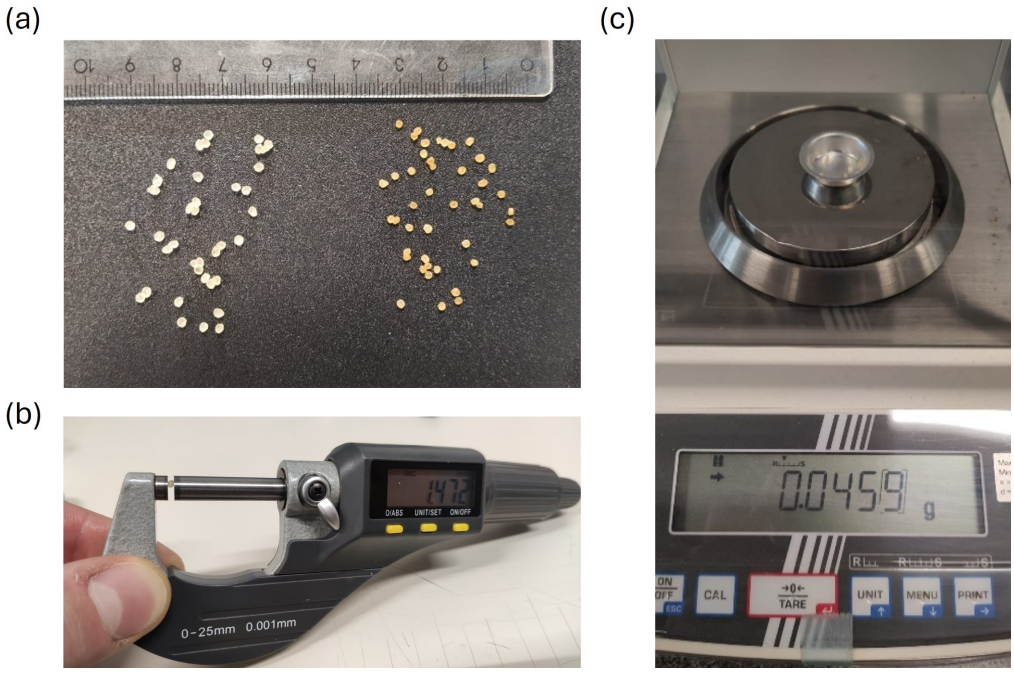

Fig. 4.12 Dry CaAlg beads appearance and properties. (a) CaAlg beads before (left) and after (right) cycling. (b) Micrometer used to measure the beads grain size. (c) Analytic scale used to weight CaAlg beads and estimate density.

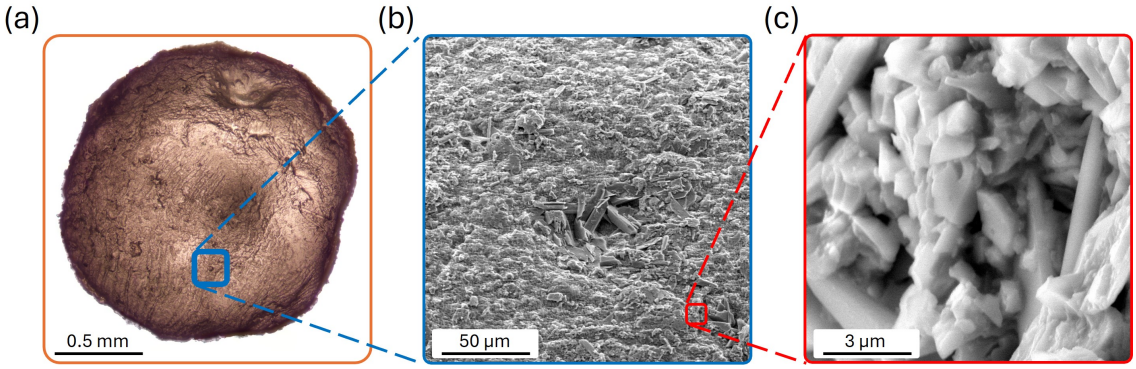

Fig. 4.13 CaAlg bead magnifications under optical and SEM microscopy [24]. (a) Magnification on a single bead of CaAlg under a 5x optical lens, with backlighting and after focus-merging of multiple pictures. (b), A SEM image with magnification 1000x of the surface of a bead of CaAlg. (c), A SEM image with magnification 20000x of the surface of a bead of CaAlg.

The measurements have been taken used a micrometer with accuracy of 0.001 mm. Also, the same beads were weighted on a KERN ABJ320-4NM scale (accuracy of 0.1 mg): by knowing mass and diameter, a density of $\rho_{CaAlg} \approx 2000 \pm 400\ kg/m^3$ was estimated.
The surface of the CaAlg beads appears irregular and rough. This was observed under an optical microscope OPTIKA B-383MET (Fig. 4.13a) and a SEM microscope (Quanta 200 FEG Environmental SEM) (Fig. 4.13b,c).
In total, six different calcium alginate compositions have been produced, with variations in

the NaAlg and graphite concentrations in sol. *A*, and in the $CaCl_2$ concentration in sol. *B*. The samples list with concentration of the components is provided in table 4.9:

	S1	S2	S3	S4	S5	S6
$NaAlg/H_2O$ [%]	1	1	2	2	1	1
$Graphite/H_2O$ [%]	0	0	0	0	0.1	0.025
$CaCl_2/H_2O$ [%]	5	10	5	10	5	5
Label	Alg_1Ca_5	Alg_1Ca_{10}	Alg_2Ca_5	Alg_2Ca_{10}	$Alg_1Ca_5G_{0.1}$	$Alg_1Ca_5G_{0.025}$

Table 4.9 List of produced and tested CaAlg compositions. Each column refers to a different sample. The first and second rows refer to acqueous solution *A*, while the third row refers to acqueous solution *B*, specifying the amounts of chemicals used to produce the samples.

In order to limit the decrease in salt concentration in sol. *B* during the jellification process, the salty solution volume is chosen about 9-10 times larger than the volume of sol. *A*. It was found that with 1 kg of solution *A* at concentration 1% w/w (weight of NaAlg over weight of solution) and 9 kg of solution *B* at concentration 10% w/w (weight of $CaCl_2$ over weight of solution), approximately 20 grams of dry CaAlg are produced. In Chapter 6 we start from this data to propose an improvement in the chemicals consumption efficiency for larger-scale productions.

We report here a side note concerning nomenclature. In order to run the preliminary experimental investigation (section 4.2.1), we first produced a small batch of CaAlg samples. Then, after composition S2 (Alg_1Ca_{10}) was found to be the most promising, further 400-500 grams were produced. Nevertheless, due to a difference in the suppliers used for the chemicals (for $CaCl_2$, specifically), the actual composition of the second batch slightly differed from the first batch. Considering a purity for the used $CaCl_2$ of 77% as specified by the supplier, the actual content of salt in the second solution can be estimated to be approximately 8% w/w, instead of the nominal 10%. This was experimentally confirmed *a posteriori*: 3.202 grams of well-mixed $CaCl_2$ solution were collected before the production process, 3.148 grams more were collected after the production process, and a thermal balance (KERN DBS60-3, with accuracy of 0.001 g) was used to evaporate the two water samples separately at 180°C for 5 hours, as in the standard procedure suggested to measure the total dissolved solids in a water solution. The final amounts of residual salt were, respectively, 0.271 g and 0.241 g, corresponding to 8.46% and 7.66% w/w concentration. Then, it can be safely assumed that all the jellification process happened in a $CaCl_2$ solution having 8.0% ± 0.5% salt concentration. Using the same nomenclature as in [45], the produced CaAlg composition (the same tested in the desalination unit in Chapter 5) should be more properly identified as Alg_1Ca_8. Nevertheless, for the sake of simplicity, we will still refer to it as Alg_1Ca_{10}.

4.3.2 Equilibrium experiments

The assessment of equilibrium water uptakes consisted of two experimental procedures:

1. First, a preliminary experimental campaign where the six produced compositions were tested in adsorption-desorption cycles and the equilibrium values were compared; this experiment is discussed more in detail in the next section, since it was mainly meant to assess materials' dynamics.

2. Second, the construction of a full isotherm curve for a list of samples derived from the composition with the best performance as found in the preliminary campaign, including the material 'as produced', the aged material and two reference silica-gels.

In order to perform Experiment 2, a ProUmid SPSx-1μ High Load gravimetric vapor sorption analyser was used (Fig.4.14a).

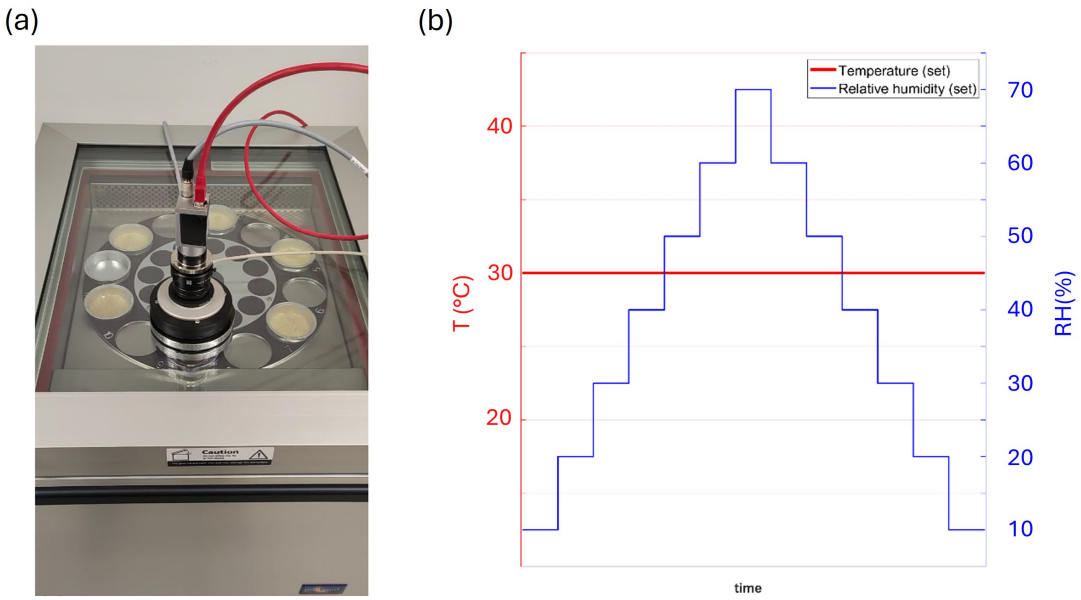

Fig. 4.14 Gravimetric analysis used to produce material's isotherms. (a) Picture of the ProUmid analyser. (b) The set conditions for T (left y-axis) and RH (right y-axis) for the isotherm preparation; the time axis is qualitative, since the duration of each ramp depends on the reaching of the equilibrium conditions: the actual experiment lasted in total approximately 14 days.

As explained in Chapter 2, an isotherm in an equilibrium curve obtained by keeping temperature constant and varying RH step-by-step. For this research, we produced the isotherm of samples of calcium alginate and silica-gels at 30°C and in the RH range 10-70%. The analyser controls the temperature in the machine and gradually brings the relative humidity to 10%; then, it waits until the material reaches equilibrium, and finally increases RH up by further 10% and waits for new equilibrium to be reached. This process goes on until

the material reaches equilibrium at RH=70%; then, a descending step-by-step ramp starts, where RH is brought back in 10%-steps down to 10% (Fig. 4.14b). A mass measurement of the samples is taken once every 40 minutes, and a picture is taken once every equilibrium condition (pictures in Appendix D). The machine considers the samples in equilibrium when all of them have satisfied the following condition: sample mass change during the last 40 minutes was less than 0.05% with respect to its initial net mass. A maximum time of 48 hours for reaching each equilibrium was allowed.
The full list of samples which underwent isotherm constructions is provided in table 4.10:

n.	Sample	Description
1	CaAlg 'as produced' - s1	Sample 1 of virgin CaAlg.
2	CaAlg 'as produced' - s2	Sample 2 of virgin CaAlg.
3	CaAlg 'as produced' - s3	Sample 3 of virgin CaAlg.
4	CaAlg 'as produced' - s4	Sample 4 of virgin CaAlg.
5	CaAlg 'as produced' - s5	Sample 5 of virgin CaAlg.
6	CaAlg 'as produced' - s6	Sample 6 of virgin CaAlg.
7	CaAlg 'after 20 cycles' - s1	Sample 1 of CaAlg after 20 cycles in the AD unit.
8	CaAlg 'after 20 cycles' - s2	Sample 2 of CaAlg after 20 cycles in the AD unit.
9	CaAlg 'after 30 cycles' - s1	Sample 1 of CaAlg after 30 cycles in the AD unit.
10	CaAlg 'after 30 cycles' - s2	Sample 2 of CaAlg after 30 cycles in the AD unit.
11	CaAlg 'after 40 cycles' - s1	Sample 1 of CaAlg after 40 cycles in the AD unit.
12	CaAlg 'after 40 cycles' - s2	Sample 2 of CaAlg after 40 cycles in the AD unit.
13	Silica-gel 'microporous'	Sample of microporous silica-gel (Oker-Chemie, grain size of 0.5-1.5 mm)
14	Silica-gel 'mesoporous'	Sample of mesoporous silica-gel (Oker-Chemie, grain size of 1.5-3.15 mm)

Table 4.10 List of samples for which we have measured an isotherm at 30°C.

The list includes samples of CaAlg 'as produced', as well as CaAlg samples undergone to 20, 30 and 40 cycles of testing under vacuum in a desalination unit (see Chapter 5). Comparing the isotherm of differently aged samples of CaAlg allowed to assess medium-term stability of the material, which is discussed in the Results section. To allow a comparison with a reference sorbent, samples of silica-gels have been tested under the same conditions. In particular, microporous silica-gel beads coming from supplier Oker-Chemie and having grain size of 0.5-1.5 mm, and mesoporous silica-gel beads coming from supplier Oker-Chemie and having grain size of 1.5-3.15 mm.
We observed that the beads dimension changes depending on the equilibrium condition. In case of sample 6 as an example, based on the pictures taken during the isotherm construction (see Appendix D, Fig. D.36), we experimentally measured the relationship between equilibrium RH and bead diameter, at 30°C. At each RH, we measured average and standard

deviation over a sample of 10 CaAlg beads. Per each bead, the diameter was taken as average on three diameters, to account for non perfect sphericity. The resulting trend is shown in Fig. 4.15. When collecting vapor, the grain size increases, of up to 22.6% between RH=10% and RH=70%. This corresponds to a volumetric increase of about 84%. The change in volume might be explained with a modification in the internal structure, due to the unfolding of polymeric chains and changes in the sites shapes and dimensions during the water molecules adsorption.

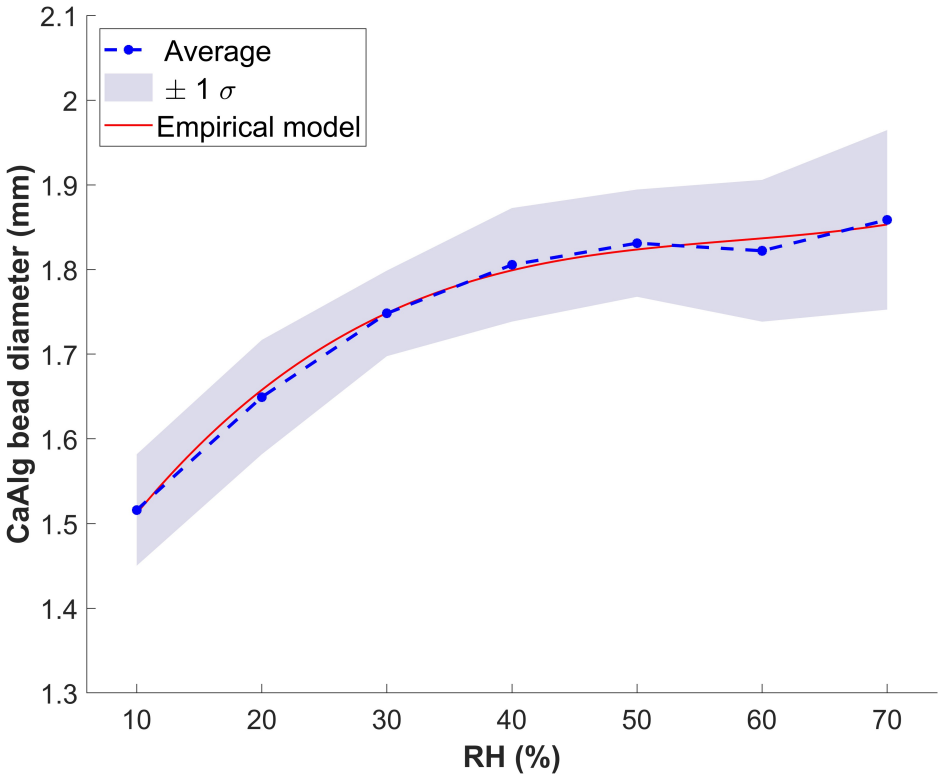

Fig. 4.15 Relationship between equilibrium RH and CaAlg beads diameter. The blue dotted line connects the experimental measurements, each taken as a average over 10 beads. The blue background area encloses ± one standard deviation calculated on the 10 experimental measures. The red curve corresponds to the best-fitting cubic curve: $D(RH) = 2.41 \cdot \left(\frac{RH}{100}\right)^3 - 4.19 \cdot \left(\frac{RH}{100}\right)^2 + 2.55 \left(\frac{RH}{100}\right) + 1.30$.

The diameter never exceeds 2 mm, which is a key upper-bound to consider for the design of the heat exchanger containing the CaAlg beads in a real application (for example, in the application discussed in Chapter 5, the distance of 3 mm between the fins was large enough to host the wet CaAlg beads.). We propose a purely empirical best-fitting cubic formula, to estimate our CaAlg beads diameter D (in mm) as a function of RH (in %):

$$D(RH) = 2.41 \cdot \left(\frac{RH}{100}\right)^3 - 4.19 \cdot \left(\frac{RH}{100}\right)^2 + 2.55 \left(\frac{RH}{100}\right) + 1.30 \tag{4.1}$$

The isotherm curves obtained through the described procedure have been compared with the theoretical equilibrium models introduced in Chapter 2. The models were used

to best-fit the experimental data using the Least-Squares Minimization method [120]: the models parameters were searched in such a way to minimize the sum of the squares of the distances between the experimental points and the model previsions at the same input RH. The MATLAB code written for the scope is reported in the Appendix B. Once the best-fitting parameters are obtained, physical properties such as adsorption enthalpy can be deduced. For example, in case of GAB best-fitting, once c is known, H_{Ads} can be estimated by inverting equation 2.14.

All the samples were preconditioned at 75°C for 12 hours before starting the construction of the isotherms. Nevertheless, the first measurement is taken after the sorbent was in the humid chamber for over 30 minutes, resulting in a condition which cannot be reliably assumed as "dry" (especially considering that most of the uptake happens in the first minutes, given the higher slope of a capacity process). In order to obtain a reliable "dry" condition, the equilibrium condition at $RH = 0\%$ should be achieved. Nevertheless, due to a technical limit with the used sorption analyser, this was not possible; instead, the lowest equilibrium measurement was taken at RH=10%. This poses a limit for the comparison of the sorption isotherm with results from literature, which are usually covering an RH range starting from 0%. To solve this, we decided to linearly extrapolate to the range 0-10% and add an artificial offset to the isotherm in order for it to start with w=0 g/g at RH=0% (Fig. 4.16a).

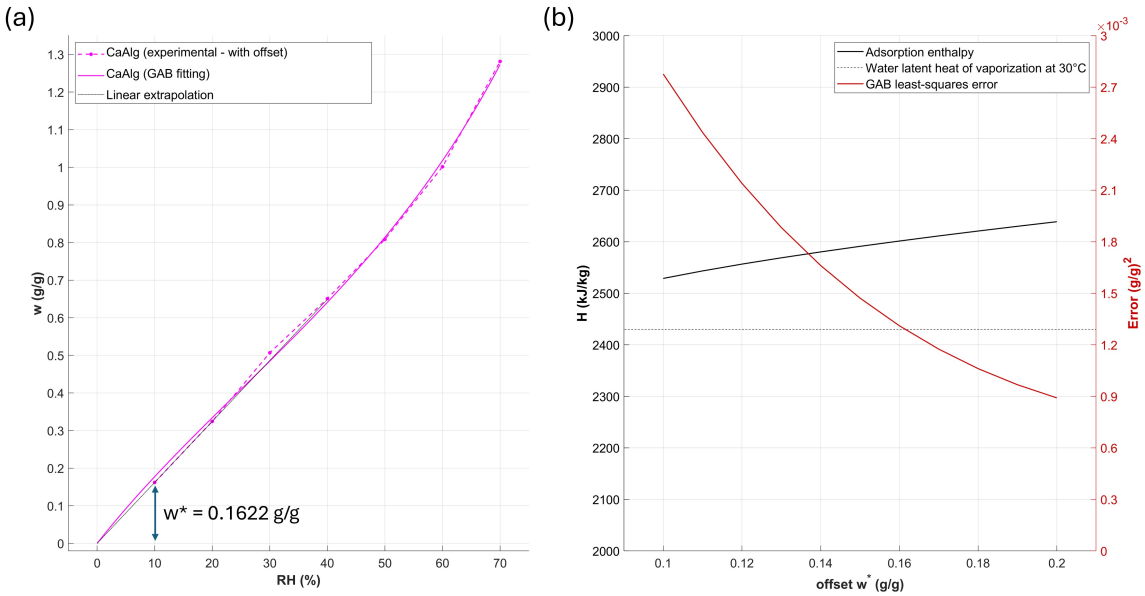

Fig. 4.16 Effect of isotherms offset procedure. (a) CaAlg 'after 40 cycles' isotherm with offset w*, compared with the GAB model. (b) Adsorption enthalpy and GAB best-fitting error as a function of the arbitrary offset.

The linear extrapolation was preferred over other attempted alternatives (including parabolic) because it is a conservative approach (not overestimating the actual uptake). Indeed, due to the convexity in the low RH-range of the "S" shaped isotherm, we can expect

the real isotherm to be even higher than the adjusted one. A confirmation of the behaviour of the isotherm in the low RH range comes from an independent isotherm on a different CaAlg sample found in [47].
The offsetting procedure is clearly arbitrary: in reality, it is not possible to know how lower the equilibrium value at RH=0% would have actually been without performing a proper experiment. Using the GAB model on the original data is not possible, too: by the model definition, at RH=0% the uptake is equal to 0%, which is not compatible with the experimental data (an attempt of best-fitting the GAB or the BET model with the original data was made, and resulted in values for the fitted coefficient out of the range for which the model is significant). An alternative to the proposed procedure would be to keep the original data and add an offset coefficient w* to the GAB model, making it a 4-parameters expression: the result would be identical, though, with the cons that the isotherm would still be not comparable with other data from literature. Since the choice of the offset was arbitrary, for completeness, in Fig. 4.16b it is shown what would happen by choosing a different offset value in the range 0.1-0.2 g/g. Increasing w*, the error of the GAB best-fitting decreases and H_{Ads} increases, but with a sublinear rate. For instance, by using an offset of 0.12 g/g instead of 0.1622 g/g, the value of H_{Ads} changes by 1.8% (2557 kJ/kg instead of 2604 kJ/kg). For what concerns the comparison with the other isotherms from literature: the shape of the isotherm is not changed by applying the offset, so the qualitative considerations are still valid. The equilibrium values are instead modified, but not in such a way to affect the relative position of the isotherm with respect to the samples from literature: even without applying any offset, the equilibrium value at RH=70% is still larger than the other analysed samples (see 4.3), thus the discussion in the results section is still valid. Note that the offsetting procedure does not affect dynamics, but only equilibrium values: for this reason, the best-fitting procedure for estimating diffusivity reported in Appendix refers to the original isotherm data.

An alternative option to the proposed offsetting procedure would be to offset the dry-mass and re-calculate the water uptake at all relative humidities. Indeed, as pointed out by [121], the change of dry-mass affects the isotherm both horizontally and vertically. In figure 4.17, we show how the isotherm would be reshaped with the change of the dry-mass m_{dry}:

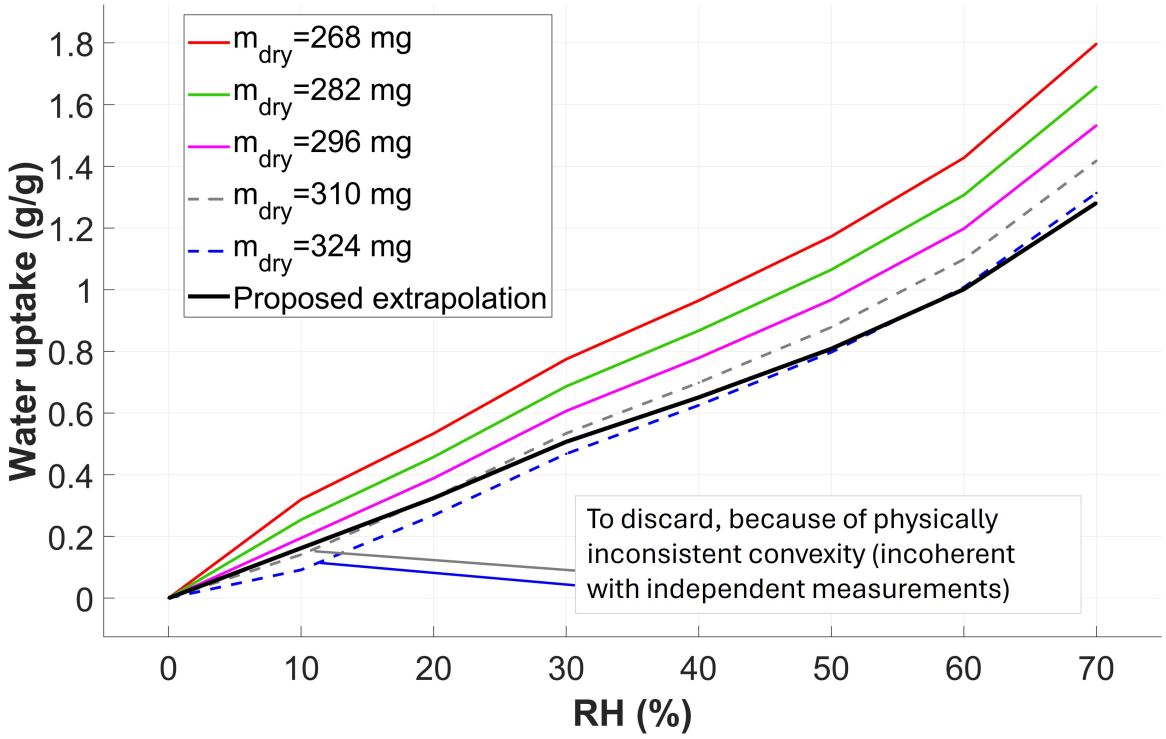

Fig. 4.17 Effect of the dry-mass change on the isotherm. The curves are re-calculated starting from net-mass data, and using the specified values for the unknown dry-mass. The dotted lines are not considered physically consistent with the S-shape expected for this material, which was confirmed by independent measurements [47].

Each curve corresponds to the isotherm re-calculated starting from the original net-mass data and different values for the dry-mass. In comparison, the approximation proposed above as isotherm. As a note, in the original experiment, the lowest registered dry-mass for this specific sample was 324 mg (it was recorded half-way during the settling ramp between the true unknown dry-condition and the equilibrium condition at RH=10%, where the mass was 353.7 mg); for this reason, we only considered for the unknown m_{dry} values lower or equal than 324 mg.

The dry-mass values larger than 296 mg, though, lead to isotherms whose shape is incoherent with the observed S-shape that we expect from this material (confirmed by independent experiments, see blue curve in Fig. 4.2); so, we will consider as the first acceptable isotherm the magenta curve, evaluated with $m_{dry} = 296\ mg$. Under this assumption, the proposed extrapolated isotherm (black) is surely an underestimation of the actual isotherm, at all relative humidities (with relative errors comprised between 16% and 17%). In case the actual dry-mass is lower than 296 mg, the underestimation becomes even more important. In all cases, the proposed solution is conservative.

4.3.3 Assessment of dynamics and aging

In order to assess the dynamics and stability of calcium alginate samples, we conducted the following experimental procedure on the six CaAlg compositions:

1. The samples were preconditioned for more than 24 hours at environmental temperature T_{Ads} and controlled relative humidity RH_{Ads}.

2. The samples underwent desorption at constant temperature T_{Reg} and ambient vapor pressure in a thermal balance (KERN DBS60-3, accuracy of 0.3 mg), where a mass measurement was taken once every five seconds, for a total of 3 hours.

3. The samples underwent an 5-hours long adsorption ramp at the same temperature T_{Ads} and relative humidity RH_{Ads} of the preconditioning phase. During this phase, the samples were periodically weighed with an analytical scale (KERN ABJ 320-4NM, accuracy of 0.3 mg), for a total of 6 times in the first hour, 8 times in the next two hours, 4 times in the last two hours.

For the experiments, the preconditioning and adsorption ramps were conducted at environmental temperature of about $T_{Ads} \approx 21°C$. We tested two relative humidities in comparison: RH=30% and RH=50% [6].
The desorption phase was performed at three different temperatures: $T_{Reg} = 60°C$, $T_{Reg} = 80°C$, $T_{Reg} = 100°C$. The thermal balance controlled temperature during the process using a radiating lamp.

The experimental data was compared with the theoretical dynamics models introduced in Chapter 2. As for the best-fitting procedure used for the isotherms analysis, the Least-Squares Minimization method was used to determine the best approximation for the models parameters. This allowed to estimate the diffusivities D of the adsorption and desorption processes, which are an indication of the kinetics of the process.

The same best-fitting procedure was repeated over the charging-discharging data obtained during the construction of the isotherms in the vapor sorption analyser (discussed in the previous section):

[6] Due to non perfect control, the actual RH were closer to 34% and 47%, as specified in the tests results.

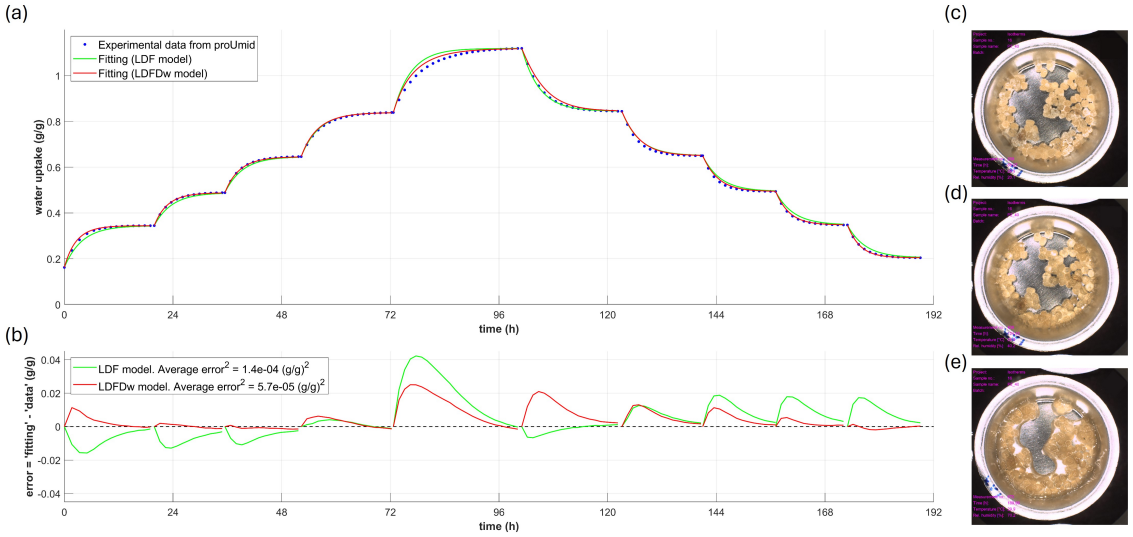

Fig. 4.18 Isotherms construction: best-fitting of transient curves. (a) Water uptake of sample CaAlg 'after 40 cycles' during Experiment A, with T=30°C and RH ranging between 20% and 70%, compared with LDF and LDFDw best-fittings. (b) Absolute error made by the two models. (c) Sample appearance at RH=20%. (d) Sample appearance at RH=40%. (e) Sample appearance at RH=70%, showing salt deliquescence.

In Fig. 4.18a,b, we see models LDF and LDFDw best-fitting the adsorption and desorption ramps of an aged sample (CaAlg 'after 40 cycles'), allowing another way of estimating the material's diffusivity. Both best-fitting procedures results are discussed in the Results section. Fig. 4.18c,d,e show a sample of CaAlg in equilibrium under three different conditions during the construction of the isotherm: RH=10%, RH=40% and RH=70%. The latter case is particularly interesting since it shows that the CaAlg sample is subject to salt liquefaction. At high relative humidities, there is the risk to that the calcium ions are irreversibly lost from the material, changing the material's composition and thus invalidating the isotherm. This is the reason why the isotherms were stopped at RH=70%, which was experimentally observed to be still a fairly stable condition, as almost all of the water uptake was recovered during the descending branch of the isotherm.

As an important note, in this simplified best-fitting procedure we did not considered the change in volume for the CaAlg beads (Fig. 4.15), nor the heat exchanges occurring during the adsorption and desorption processes. As a consequence, the resulting diffusivities may be distorted and partially lose their physical consistency. Future models (e.g., lattice models including the flexibility of the framework and the heat effects) may be used to retro-fit the collected data and improve the consistency of the diffusion coefficients.

In order to assess the material long-term stability over cycling, we performed an aging procedure in a climatic chamber ($T_{Ads} = 21°C$, $RH_{Ads} = 50\%$, $T_{Des} = 75°C$). A sample of

$Alg_1Ca_5G_{0.025}$ was subjected to over 300 consecutive cycles in a climatic chamber (ATT DM340), each consisting of an adsorption at 21°C and RH=50% followed by a desorption at 75°C and uncontrolled RH.
After 0, 131 and 318 cycles the sample was preconditioned at 21°C and RH=50%, then subjected to a desorption at 80°C, to assess whether the cycling procedure had any effect on the desorption transient. The resulting curves are shown in Fig. 4.9.

4.4 Conclusions

We reported in this chapter the results achieved with the characterization of CaAlg. Here below the main points:

- First, we produced 6 different CaAlg compositions, varying the concentration of $CaCl_2$, NaAlg and graphite in the aqueous solutions used for the sorbent production. We then compared the water uptake equilibrium of the six samples, and found that an increase in $CaCl_2$ and a decrease in NaAlg contents improve the sorption capacities. In particular, we found out that **composition $\mathbf{Alg_1Ca_{10}}$ has the highest water uptake potential**. We selected this composition for future testing of CaAlg for adsorption desalination (see next Chapter), where adsorption capacity is a key factor in order to increase the amount of water stored at each cycle.

- We produced a larger batch of composition Alg_1Ca_{10} and tested into a gravimetric vapor sorption analyser. The isotherm at 30°C and in the RH range 10-70% was built and classified as a **type-II isotherm well-fitted by GAB model**. We estimated an adsorption enthalpy $\mathbf{H_{Ads}}$ **of 2600 kJ/kg at 30°C**, about 7% larger than the heat of liquefaction of water at the same temperature (2430 kJ/kg, or 44 kJ/mol).

- We performed adsorption-desorption experiments to compare the dynamics of different compositions. We tested theoretical models LDF, LDFDw, LDFm, FD, FDRH, FDSW over experimental data, and found out that **model LDFDw best-fits adsorption and desorption transients**. When best-fitted with model LDFDw, composition $Alg_1Ca_5G_{0.1}$ shows the highest diffusivity, reaching approximately $7 \cdot 10^{-12}\ m^2/s$ at 21°C. We selected this composition for future testing of CaAlg for atmospheric water harvesting (see next Chapter), where, especially at low ambient RH, kinetics is a key factor to achieve a competitive plant.

- We run adsorption-desorption transients at various temperatures (60°C, 80°C, 100°C), and observed that **the dependence of CaAlg diffusivity on water uptake cannot be neglected at high temperatures**, justifying the use of model LDFDw in cases of high

uptake ranges and high temperatures involved. We proposed a functional form for LDFDw parameters as a function of temperature.

- We assessed the medium-term stability of CaAlg samples when subjected to multiple cycles under vacuum, in a desalination unit. After being only initially affected by cycling, the adsorption isotherm at 30°C reaches an asymptotical behaviour with a fairly **stable equilibrium water uptake over 40 cycles under realistic conditions**.
- We assessed the long-term stability of CaAlg samples when subjected to hundreds of adsorption-desorption cycles in climatic chamber. **We observed no significant change in the desorption dynamics after 318 consecutive cycles**, proving the sorbent as a stable material on the medium-long term.

Chapter 5

Experimental testing of calcium alginate in lab-scale machines

5.1 Introduction

In Chapter 4, we have proved that calcium alginate has greater adsorption capacity with respect to conventional sorbents. We tested various compositions, and chose the two with the best performances, having the potential to increase the water production rate in Atmospheric Water Harvesting and Adsorption Desalination units [45]. In this Chapter, we are going to assess this experimentally.
In the first part, we present the main results. First, we produce and test a CaAlg coating in a machine for AWH. We comment the thermodynamic variables in an exemplificative cycle, the cycle stability over time, the water production achieved and the water quality obtained. Finally, we compare the results with plants from the literature. Second, we produce a batch of CaAlg spherical beads and test it in a machine for AD. As for the previous application, we comment the thermodynamic variables in an exemplificative cycle, the cycle stability over time, the water production achieved and the water quality obtained. Finally, we compare the results with the ones achieved using a mesoporous silica-gel and with plants from the literature. Third, we extrapolate the achieved material performances to ultralow-grade heat contexts applications, providing examples where CaAlg can be a better choice with respect to conventional sorbents.
In the second part of the chapter, we present the used methodology. First, we describe the AWH unit and the sorbent coating production procedure, as well as the experimental campaign with CaAlg in the AWH unit and the water analysis made on the condensed samples. Second, we describe the desalination unit, as well as the experimental campaign with CaAlg in the machine and the water analysis made on the condensed samples.

5.2 Main results

5.2.1 CaAlg for atmospheric water harvesting

We designed and manufactured a AWH unit (Fig. 5.1) [47, 122] able to perform adsorption and regeneration cycles on a coating of adsorbent material. The working principle has been discussed in Chapter 2: first, the sorbent is put in communication with the atmosphere and adsorbs water vapor; then, the sorbent is heated up and the released vapor condenses on a surface at a lower temperature. More details on the AWH unit are provided in the Methods section.

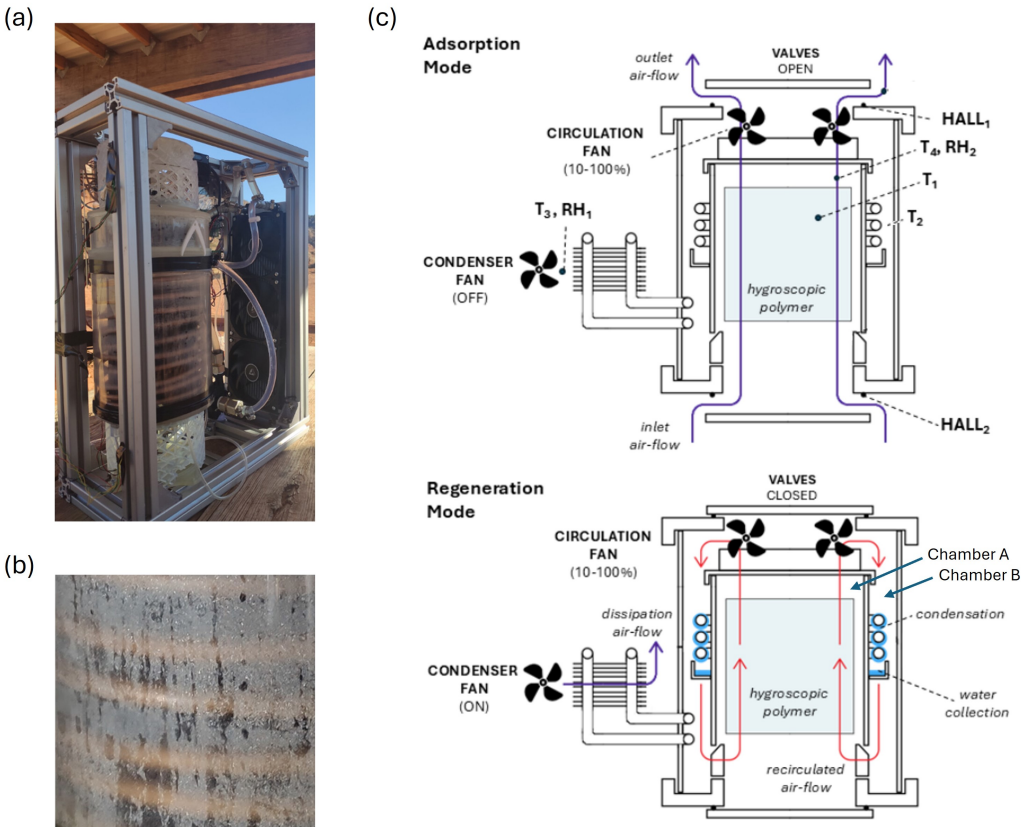

Fig. 5.1 AWH unit [47]. (a) A picture of the AWH unit, enclosed in a frame to be tranported and tested in arid environment (Texas desert). Overall volume: 40 × 21 × 50 cm. (b) Water droplets condensing on the internal surface of the machine during the desorption phase. (c) A schematics of the machine during the adsorption and desorption phases [122]. The machine contains 4 temperature sensors: T1 (monitoring the exchanger temperature, next to the heater), T2 (next to the condenser coils), T3 (ambient temperature), T4 (outlet temperature, after the exchanger). The machine contains two relative humidity sensors: RH1 (ambient humidity) and RH2 (outlet humidity).

Given the results achieved with the preliminary testing of calcium alginate (see Chapter 3), we used the unit to test AWH with one of the optimized composition. In particular, we produced a coated heat exchanger using $Alg_1Ca_5G_{0.1}$ (see Methods for details on the coating procedure) [47], which showed good adsorption capacity and faster dynamics with respect to

other compositions. The AWH unit including the CaAlg-coated heat exchanger was tested both in laboratory and in outdoor environment. We were able to obtain a water production even in arid climates such as the Texas desert (Fig. 5.1a,b) [47], demonstrating that calcium alginate is indeed suitable to achieve atmospheric water harvesting.
We monitored the thermodynamical variables (Fig. 5.1c) during the normal cycling of the machine (details in the Methods section). We show in Fig. 5.2 the detail of one cycle.

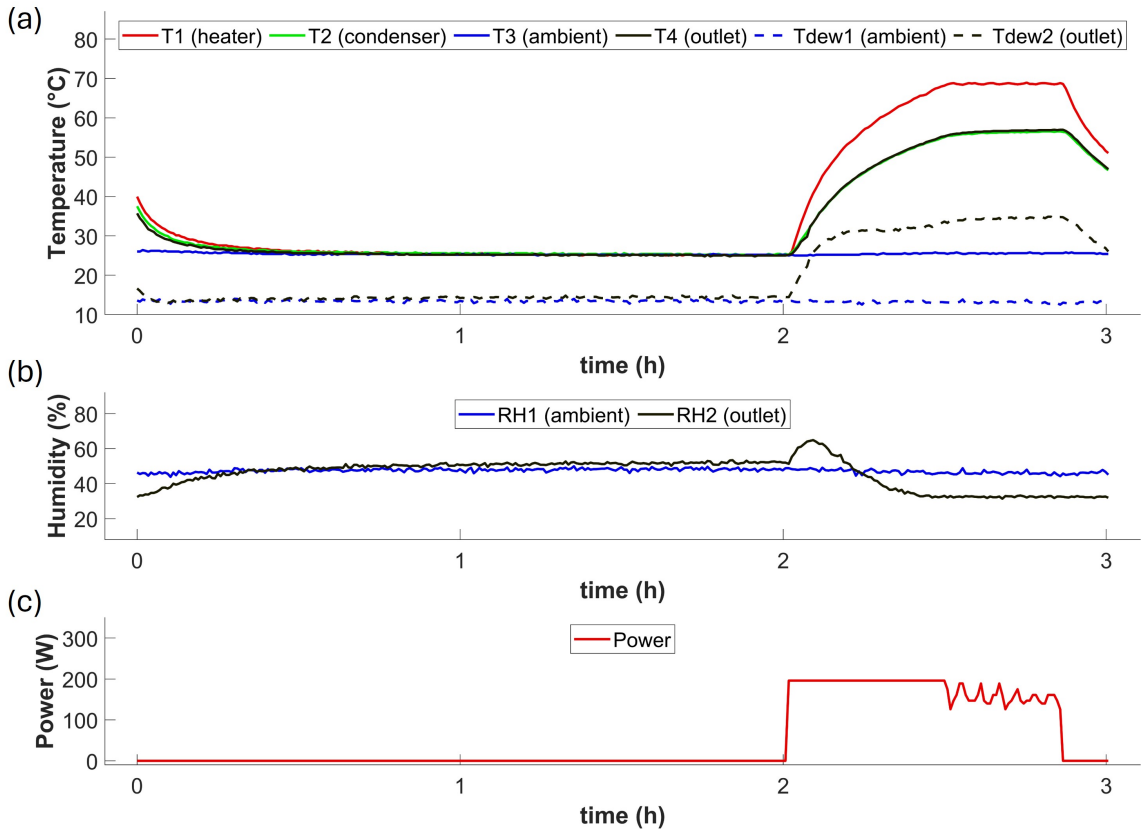

Fig. 5.2 A representative cycle with the AWH unit. (a) Temperatures in the AWH unit during a cycle: T1 (desorption temperature), T2 (vapor temperature above the condenser coil), T3 (ambient temperature), T4 (temperature after the coated exchanger), Tdew1 (dew-point temperature in the ambient), Tdew2 (dew-point temperature after the coated exchanger). (b) Relative humidities in the AWH unit: RH1 (ambient humidity), RH2 (humidity after the coated exchanger). (c) Input power during desorption.

Fig. 5.2 shows temperatures, relative humidities and absorbed power in the machine. We can identify and comment the two working phases of the cycle:

1. Adsorption (time 0-2 h): during this phase, the chamber containing the material is connected with the environment and vapor is adsorbed. Dew-point temperature and RH in the machine increase during the adsorption process, with asymptotic behaviour (corresponding to the material approaching full capacity). No power is provided to the material during this phase (with a proper setup, it would be possible to extract heat during the adsorption process, instead).

2. Desorption (time 2-3 h): during this phase, the chamber is isolated from the environment and heat is provided to the material. A feedback control loop is used to control the desorption temperature T1 (70°C in this particular test); the first 20-30 minutes are used to overcome the thermal inertia and heat up the exchanger. The vapor is released at a dew-point temperature which is 5-10°C higher than the ambient temperature, allowing condensation on the condenser coils where water at environmental temperature is flowing (approximately 11 mL of fresh water condensed during this specific cycle). During this phase, power is provided to the material using an electric heater to simulate a generic thermal source, for an average of about 50 W along the whole cycle and 150 W in the desorption phase only. This allows to estimate a Specific Thermal Energy Consumption (eq. 3.17) of approximately 13.6 kWh/L.

Figure 5.3 shows the continuation of the same experiment for a total of more than 2.5 days (62 hours) of consecutive cycling.

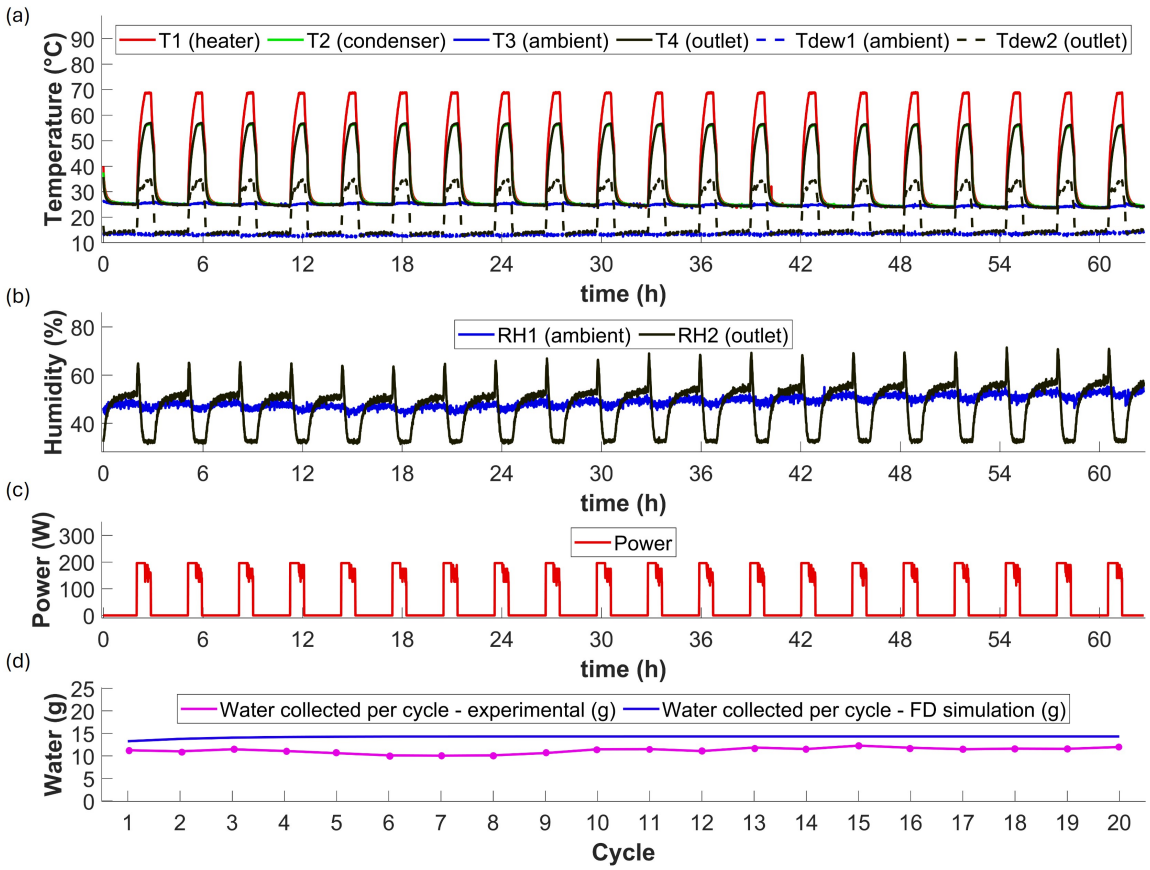

Fig. 5.3 A test of 20 consecutive cycles with the AWH unit (test 3 in table 5.2). (a) Temperatures in the AWH unit during a 62-hours test comprising 20 consecutive cycles. (b) Relative humidities in the AWH unit. (c) Input power during desorption. (d) Water production during the test: experimental (magenta line) vs simulated (blue line).

The considerations on adsorption and desorption cycles are the same as above. Here, we observe the repeatability of the process as a proof of the system stability over time. In Fig.

5.3d (magenta line), we show the water production achieved during the testing period, in terms of grams collected per cycle.
We can observe that the AWH unit achieved a fairly constant water production rate ($11.2 \pm 0.62\ g/cycle$), which is a further proof of the material's stability. On average, in one day, the total water production resulted being of 89 grams. Considering that the alginate coating had a dry-mass of $m_{dry} = 97.5\ g$, we can estimate a Specific Daily Water Production (see eq. 3.11) of approximately $0.91\ m^3/day/ton$ for these particular test conditions.
We can approximate the alginate coating as a plane sheet of sorbent; we can then compare the achieved results with the estimation made by one of the FD-based models for plane diffusion introduced in Chapter 2. Given the high dependency of D with water uptake observed in Chapter 4, we chose to use the numerical model 2.34, assuming: $D(w) = (4.9610^{-12} + 3.77 \cdot 10^{-12} \cdot w)\ m^2/s$ (see Methods section). The resulting estimation for water productivity is shown in Fig. 5.3d (blue line).
We observe that the actual production is, on average, only about 79% of the model estimation, and this discrepancy would further increase if we used a higher diffusivity for desorption phases. We can attribute this difference to two main reasons:

1. the hypotheses of the model are not perfectly met (for instance, the coating is not infinite, but instead the boundary effect due to the shape of the exchanger are not negligible);

2. the assumption that all the water uptake difference is converted into collected water is wrong. Indeed, during the experimental testing of the unit, we noticed that a large amount of water drops stayed on the surface of the condenser loop coil at the end of the desorption process, and were adsorbed back during the next adsorption. This introduces an inefficiency in the process: a portion of Δw covered by the material during the cycling process is not an actually useful effect, but instead internal recycling of the same water molecules.

Water quality

We measured the quality of the condensed water and of a sample of distilled water, for reference (details in the Methods section). The results are reported in the table below, compared with WHO and EU normatives (see Chapter 2).

Parameter	Unit	WHO	EU 2020/2184	Distilled water	This research (AWH)
Conductivity	$\mu S/cm$	-	2500	26	103
pH	pH	6.5-8.5	4.5-9.5	6.6	6.0
Alachlor	$\mu g/L$	20	-	<	<
Arsenic	$\mu g/L$	10	10	<	<
Benzene	$\mu g/L$	10	1.0	<	<
Benzo(a)pyrene	$\mu g/L$	0.7	0.01	<	<
Boron	$\mu g/L$	2400	1500	<	<
Bromate	$\mu g/L$	10	10	<	<
Chlorate	$\mu g/L$	700	250	<	<
Copper	$\mu g/L$	2000	2000	2	14536
1,2-Dichloroethane	$\mu g/L$	30	3	<	<
Fluoride	$\mu g/L$	1500	1500	<	<
Lead	$\mu g/L$	10	5	1	1
Nickel	$\mu g/L$	70	20	6	1
Nitrate	$\mu g/L$	50000	50000	2	<
Uranium	$\mu g/L$	30	30	<	<
Vinyl chloride	$\mu g/L$	500	0.5	<	<

Table 5.1 Parameters in the condensed water during the AWH campaign with CaAlg, compared with the limits from EU 2020/2184 [113] and WHO Guidelines for drinking-water quality regulations [112]. The symbol "<" means that the measured value is below the analysis sensitivity.

We observe a conductivity of 103 $\mu S/cm$, that is below both the limit suggested for drinkable water by EU regulation and the WHO (see Chapter 3), proving the absence of significant salts contaminations. A similar result is observed for pH: we measured a value of 6.0, within the range suggested by EU and slightly below the lower limit suggested by WHO. On the other hand, we observe a content of metallic copper (Cu) significantly above the limits: 14536 $\mu g/L$, about 7 times larger respect to the EU and WHO upper bound of 2000 $\mu g/L$. This can be explained by a design choice, since the coil where water drops condense is made of copper: the water drops collect metal from the surface of the coil[1] and transport it to the bottom of the machine, where water is collected. Replacing the copper coil with a stainless steel coil should reduce the presence of metallic contaminants, with the drawback of a worse heat exchange during condensation.
For what concerns odor and taste: immediately after the extraction of the condensed water from the machine, we could smell a scent of charamelized sugar, most probably coming from the organic components of the sorbent after being heated up to 65-70°C. Nevertheless, the smell disappeared in few seconds, indicating that such organic compounds were volatile, and mostly present in the exchanger chamber instead that dissolved in the collected water. The condensed water was tasteless.

[1]Effect probably amplified by the high temperatures reached in the chamber during the desorption phase.

Machine performance

Test		1	2	3	4	5	6	7	8
T_{amb} (°C)		28	25	26	25	24	24	24	25
RH_{amb} (°C)		45	45	50	50	50	55	60	60
t_{Ads} (°C)		90	120	120	120	120	120	120	120
T_{Des} (°C)		65	70	70	70	65	65	65	70
t_{Des} (min)		60	60	60	60	60	60	60	60
n_{cycles}		13	19	20	17	22	23	23	21
SCWP (mL/cycle/kg)	Average	78	149	114	112	119	123	128	100
	Std. dev.	10	16	6	13	9	11	10	10
SDWP (m^3/day/ton)	Average	0.75	1.19	0.91	0.90	0.95	0.98	1.03	0.80
	Std. dev.	0.09	0.13	0.05	0.11	0.07	0.09	0.08	0.08
STEC (kWh/L)	Average	23.1	10.9	13.5	13.9	16.5	16.0	15.3	15.7
	Uncertainty	1.01	0.36	0.45	0.54	0.39	0.36	0.35	0.49

Table 5.2 Results of the experimental campaign with the CaAlg coating in the AWH device. The testing conditions are reported in the first six rows, followed by KPIs such as specific water production per cycle (SCWP), per day (SDWP) and the energy cost per Liter (STEC). Volumes (mL, m^3, L) refer to the amount of condensed water; masses (kg, ton) refer to the amount of dry sorbent; energies (kWh) refer to the positive thermal energy entering the system during desorption.

We report in table 5.2 the complete list of tests we performed with the AWH prototype, including the results on SCWP, SDWP, STEC. Test 3 (reported in Fig. 5.3) shows the best reproducibility. In case of test 2, we achieved the lowest STEC (10.9 kWh/L) and the maximum SDWP of 1.19 m^3/day/ton.

In Fig. 5.4 we provide a map comparing the achieved SDWP with other AWH plants from the literature [123–127]. This research achieves among the best water productivities, even when compared with larger plants (bottom-right corner in the diagram), being only surpassed by plants working at higher desorption temperature (85°C), like [125]. As a comment, the discrepancy between the SDWP achieved by the different plants may also be due to a difference in the type of plants and in the processes: for example, [125] used a home-made device to test very small amounts of material (~10^{-2} kg); on the other hand, [123] used a larger solar-driven device employing larger amounts of materials (~10^{1} kg).

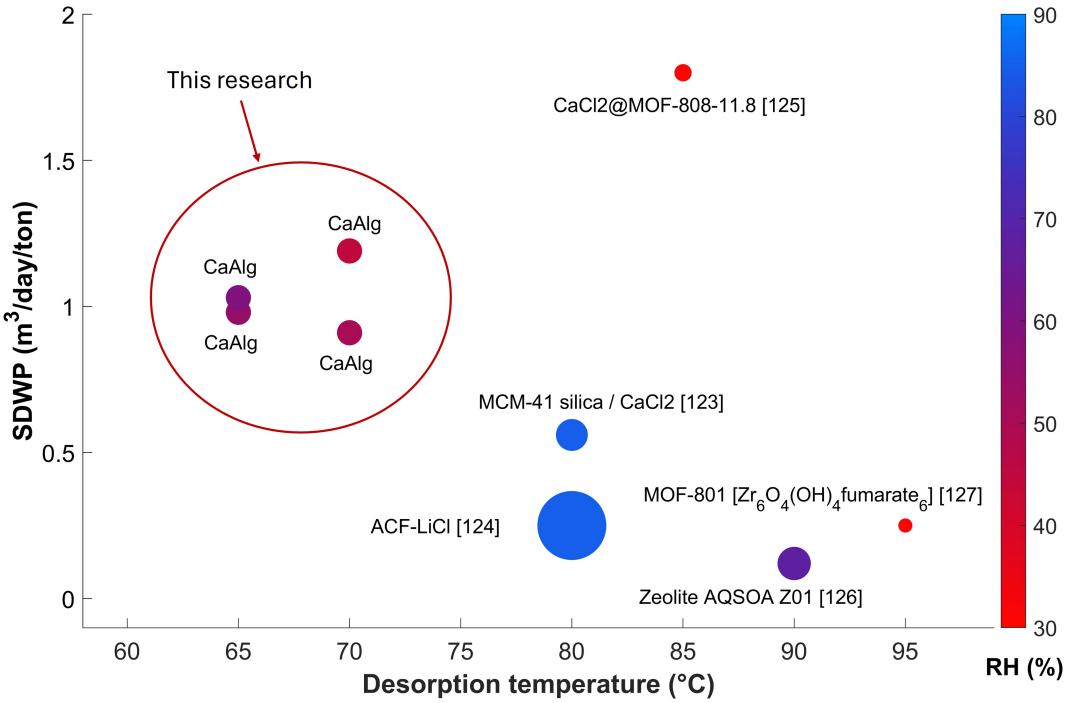

Fig. 5.4 Map of AWH unit performance in comparison with plants from the literature. SDWP is shown as a function of desorption temperature. The dot's color shows the working relative humidity (RH) during adsorption. The cube of the dot's area is proportional to the mass of sorbent in the plant. The adsorption temperature of the listed plants is not always comparable, being comprised between 15°C and 30°C.

5.2.2 CaAlg for water desalination

To assess the potential of CaAlg for water desalination, we produced a batch of sorbent beads and tested it into an Adsorption Desalination prototype, shown in Fig. 5.5. Furthermore, to allow a fair comparison, we repeated some of the tests using a reference silica-gel under the same conditions. Given the results achieved with the preliminary testing of calcium alginate (see Chapter 4), we decided to use the composition Alg_1Ca_{10}, which showed the best adsorption capacity and still a good dynamics. The working principle of the unit is the same as explained in Chapter 3: first, the sorbent is put in communication with a first chamber (EV tank) containing the feedwater (i.e., the salty water to evaporate); then, the sorbent (in the Adsorber) is heated up and the released vapor condenses on the surface of the condenser chamber (CD pipe). The process occurs under vacuum, to enhance the mass transfer rate. More details on the desalination unit are provided in the Methods section. The results discussed in this section are extracted from journal article [24].

We monitored the thermodynamical variables during normal cycling operation. We show in Fig. 5.6 the detail of a single cycle of a test done with CaAlg as sorbent (similar considerations apply to the case of silica-gel). In particular, Fig. 5.6 shows temperatures, vapor pressure and thermal power exchanged with the adsorbent.

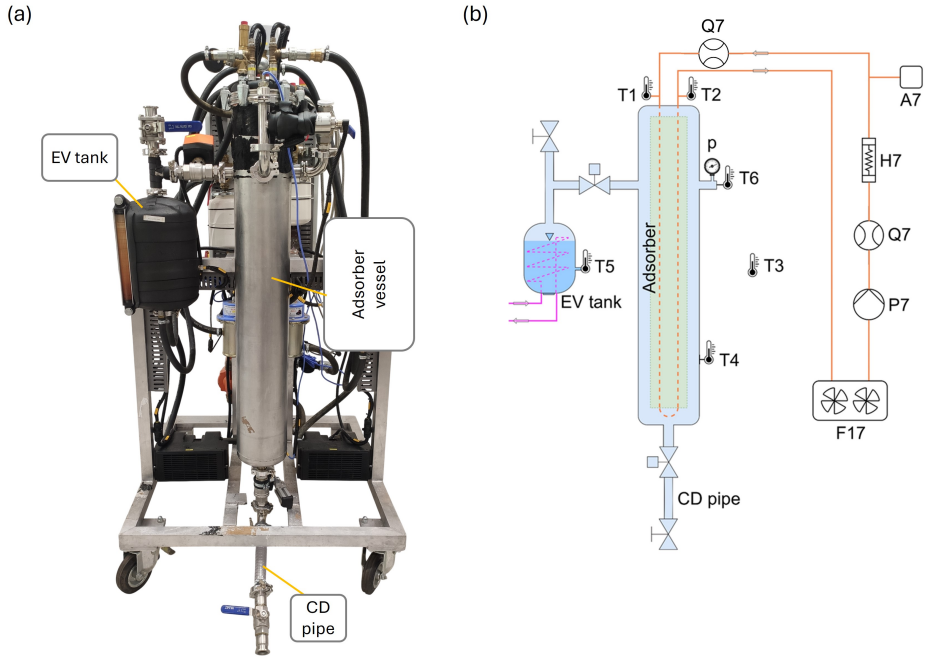

Fig. 5.5 Adsorption desalination unit. (a) A picture of the machine, where the main chambers are indicated. (b) A simplified schematics of the main vacuum chambers in the machine. This includes six temperature sensors (T1, T2, T3, T4, T5, T6), one pressure sensor (p), one flowmeter (Q7).

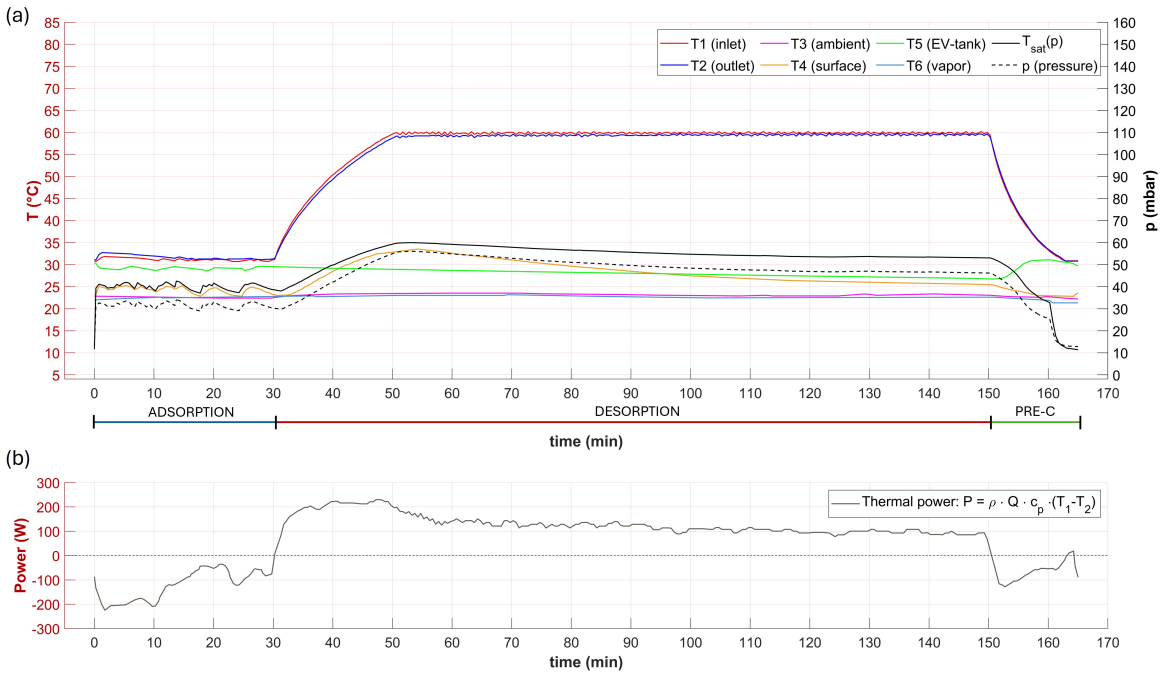

Fig. 5.6 A representative cycle with the AD unit. (a) Temperatures T1 (inlet of the adsorber), T2 (outlet of the adsorber), T3 (ambient), T4 (vessel surface), T5 (evaporating water), T6 (vapor), Tsat (saturation temperature at the vapor pressure in the adsorber) on the left axis, vapor pressure p on the right axis, shown as a function of the test time. (b) Thermal power P exchanged at the adsorber heat exchanger over time.

We can identify and comment three working phases.

First, "Adsorption" (time 0-30 minutes): during this phase, the chamber containing the sorbent (Adsorber) is connected with the chamber containing feedwater (EV tank). Water vapor migrates towards the sorbent and the water level in the EV tank decreases. Temperature T2 (outlet of the heat exchanger containing the sorbent) is greater than temperature T1 (inlet of the exchanger), meaning that the thermal power exchanged with the material is negative, as a demonstration of adsorption (which is an exothermic process).

Second, "Desorption" (time 30-150 minutes): during this phase, the adsorber is connected with a chamber (CD pipe) at the bottom of the adsorber. A feedback control loop is used to control the desorption temperature T1 (60°C in this particular test). We simulate the heat source using an electric heater, and the first 20 minutes are used to overcome the thermal inertia of the machine and heat up the exchanger. The released vapor condensed on the internal surface of the adsorber cylindrical vessel. The condensed drops fall under the action of gravity and are collected in the CD pipe (in this specific cycle, about 150 mL were collected). Temperature T1 is greater than temperature T2, thus the thermal power exchanged with the sorbent is positive; this is explained both because of thermal inertia in the system and because of the occurring of desorption (which is an endothermic process). Pressure increases in the initial part of the desorption phase (pre-heating), then stabilizes and slowly decreases during condensation. We can estimate a positive average power of 103.5 W for 120 minutes, from which we can evaluate a STEC of 1.38 kWh/L.

Third, "Pre-Cooling" (time 150-165 minutes): during this phase, the Adsorber is isolated from the other chambers and temperatures T1 and T2 drop down to the adsorption temperature, in preparation for the subsequent cycle.

Ambient temperature during the cycle is approximately 23°C, with some 1-2°C oscillations due to the position of the sensor and to the difficulty to control the temperature of the room.
Figure 5.7 shows another experiment using shorter desorption time (45 min) and going on for multiple consecutive cycles, for a total of 9 hours (6 full cycles in total). Note that both the experiment above and this test used fresh water as input feedwater; nevertheless, as clarified later, when using salty water we saw no significant influence on the thermodynamic cycle. The considerations on adsorption and desorption thermodynamics still apply, and are the same as above (fig 5.7a,b). Here, we observe the repeatibility of the process, as a proof of the material stability over time. Interestingly, water production is stable as well, after the initial 2-3 cycles of settling. On average, the water production per cycle is of 130 mL; considering

a cycle duration of 1.5 hours and a dry-mass of sorbent of 386 g, we can estimate a SDWP (see eq. 3.11) of approximately 6 $m^3/day/ton$ for these particular test conditions.

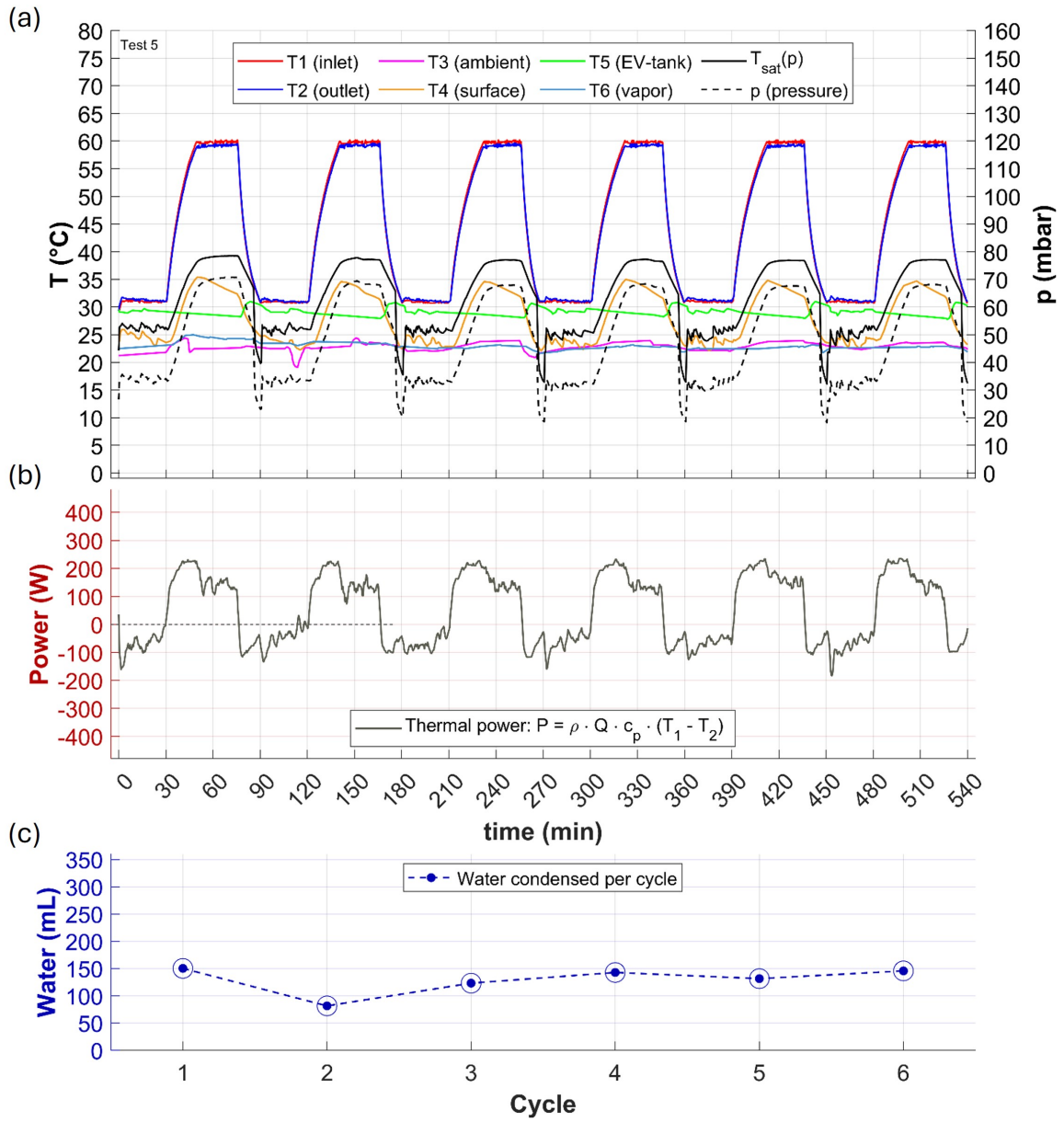

Fig. 5.7 One-day test showing 6 consecutive cycles with the AD unit. (a) Temperatures and pressure in the AD unit. The test consists of 6 consecutive cycles, each of them composed by adsorption phase ADS, desorption phase DES, pre-cooling phase PC. Temperatures T1 (inlet of the adsorber), T2 (outlet of the adsorber), T3 (ambient), T4 (vessel surface), T5 (evaporating water), T6 (vapor temperature, not included in the analysis), T_{sat} (saturation temperature at the vapor pressure in the adsorber) are shown on the left axis as a function of test time; vapor pressure p is shown on the right axis. (b) Thermal power (positive when absorbed by the adsorber) is shown as a function of test time. It is evaluated as the product of external circuit's water density ρ, flowrate Q, specific heat c_p and the temperature difference $(T1 - T2)$. (c) Water collected in the CD pipe at the end of each of the six cycles. This specific test used fresh water as for input feedwater.

Water quality

We run further cycles using salty water as evaporating liquid, and measured the quality of the produced water (see Methods section for the description of the samples and measurement procedures). The resulting values are reported in table 5.3, where sample 3 is feedwater with seawater salinity, while sample 5 is the produced water.

Sample	Solid content (mg/L)	Conductivity at 20°C ($\mu S/cm$)	PH	TOC (ppm)	Inorganic Carbon (ppm)	Copper (ppb)
1	8*	8	5.4	1.13	0.549	5.77
2	23*	22	5.6	n.a.	n.a.	n.a.
3	**34500**	**50700**	**5.6**	**<3.43** **	**n.a.**	**1.54**
4	93*	85	5.7	n.a.	n.a.	n.a.
5	**274** ± **35** *,***	**245** ± **32** ***	**7.9** ± **0.1** ***	**6.80** ± **5.7** ***	**1.77** ± **0.51** ***	**7.03** ± **2.2** ****
6	157	144	7.0	n.a.	n.a.	n.a.

n.a.: not available. * Value estimated by the measuring instrument starting from conductivity. ** Inorganic Carbon for this sample not available; the reported value "3.43 ppm" is the Total Carbon, an overestimation of the TOC. *** Average ± standard deviation on 3 samples. **** Average ± standard deviation on 2 samples.

Table 5.3 Analyses results of the water produced with CaAlg in the AD unit. Each sample corresponds to a different tested condition (see Methods). In case of sample 5 (produced water), measurement were replicated and averaged over three distinct samples.

For what concerns pH, the measured value of 7.9 is contained in the admittable range proposed by both the WHO and EU regulations. Nevertheless, further investigation is suggested to understand whether the apparent increase in pH between the starting salty water (5.6) and the condensed clean water may indicate that compounds dissolved in the process. For what concerns the organic content, a carbon analysis was performed. This allowed to estimate the TOC (Total Organic Content) as well as the Inorganic Carbon present in the water samples. An increase in the Total Carbon was seen between the starting salty water (sample 3, with 3.43 ppm) to the final condensed clean water (sample 5, with 8.57 ppm, of which about 6.8 ppm are net TOC). On the other hand, an increase in the Total Carbon was observed between the distilled water (sample 1, with Total Carbon of 1.68 ppm) and the salty water (sample 3, before being processed by the sorbent, with 3.43 ppm), too. This shows that the contamination in the testing environment was high, and comparable to the measured amounts: looking at the orders of magnitude of the measured quantities, it is probable that a fraction of the TOC in sample 5 derives from unwanted contamination in the machine, unrelated to the use of calcium alginate. To have a clear picture and understand whether the CaAlg releases organic compounds in the condensed water, further testing in a more controlled testing environment is necessary.

For what concerns copper, the metal is never present in sensible amounts. This shows that there is no contamination from the heat exchanger copper parts (opposite to the case of AWH testing).
For what concerns conductivity, an actual desalination effect was indeed achieved: when starting from salty water with sea-level salt concentration, we obtained an output conductivity of 245 $\mu S/cm$, resulting in a rejection ratio of over 99.2%. The obtained conductivity is below both the limits suggested by EU and the WHO regulations (see Chapter 3).
For what concerns odor and taste: even in this case, immediately after the extraction of the condensed water from the machine, we could smell a scent of charamelized sugar. Nevertheless, the smell disappeared in few seconds, and the water was tasteless.

Machine performance

We report in table 5.4 the complete list of results from tests we performed with the AD prototype, including the tests with silica-gel (see Methods) that we performed after the campaign with CaAlg in order to have a reference performance for comparison.
In figure 5.8a, we plot the specific water production achieved with CaAlg and with silica-gel as a function of desorption temperature (vertical bars represent $\pm$ one standard deviation). The materials have been compared under the same conditions: t_{Ads}=30 min, T_{Ads}=30°C, t_{Des}=120 min. As we can observe from the graph, CaAlg can reach specific productions larger than silica-gel (up to 90%) and other plants from the literature [128, 129].

Test		1	2	3	4	5	6	7	8	9
Sorbent		CA	CA	CA	CA	CA	CA	SG	SG	SG
T_{Des} (°C)		60	45	75	60	60	60	60	45	75
t_{Des} (min)		120	120	120	60	45	30	120	120	120
SCWP (mL/cycle/kg)	Last cycle	451	254	523	370	377	197	199	243	341
	Average	449	268	603	408	334	260	252	209	316
	Std. dev.	110	37	210	81	66	64	110	70	66
SDWP ($m^3/day/ton$)	Last cycle	3.93	2.22	4.51	5.07	6.04	3.78	1.74	2.12	2.94
	Average	3.92	2.34	5.20	5.59	5.35	4.99	2.20	1.82	2.72
	Std. dev.	0.99	0.33	1.8	1.1	1.1	1.2	0.99	0.61	0.57
STEC (kWh/L)	Average	1.38	1.55	1.41	1.05	0.97	1.01	1.50	1.37	1.48
	Uncertainty	0.66	0.74	0.68	0.50	0.47	0.48	0.72	0.66	0.71

Table 5.4 Results of the experimental campaign in the AD unit on CaAlg (CA) and mesoporous silica-gel (SG). The testing conditions are reported in the first three rows, followed by KPIs such as specific water production per cycle (SCWP), per day (SDWP) and the energy cost per Liter (STEC). The evaporation temperature is 30°C for all tests; the condensing temperature is 23°C for all tests. Volumes (mL, m^3, L) refer to the amount of condensed water; masses (kg, ton) refer to the amount of dry sorbent; energies (kWh) refer to the positive thermal energy entering the system during desorption.

In figure 5.8b, we plot the SDWP achieved with CaAlg as a function of desorption time. All the tests shared the other parameters: t_{Ads}=30 min, T_{Ads}=30°C, T_{Des}=60°C. The black curve is experimentally derived considering the average production per cycle (vertical bars represent $\pm$ 1 standard deviation), while the purple curve refers to the production of the last cycle of the test. The latter can be considered a more reliable estimation of the regime production, since the first cycles might still be affected by the initial state of charge of the material (see also the simulated water uptake for the AWH unit, in Fig. 5.18). We found that an optimal SDWP of 6.04 $m^3/day/ton$ can be achieved at an intermediate desorption time of 45 minutes.

We used the analytical model "LDFDw" -a variation of the Linear Driving Force model "LDF"- (see eq. 2.52) to best-fit the charging and discharging transient of the CaAlg in Chapter 4, and found that the diffusivity at 30°C can be estimated as a function of water uptake w as: $D = (4.4399 \cdot 10^{-12} - 2.2985 \cdot 10^{-12} \cdot w)\ m^2/s$. Starting from this result, we simulated adsorption-desorption transient processes and derived the red curve in Fig. 5.8b (see Methods section for details). The result is close to the experimental outcome, except that the latter has slower dynamics. This can be explained by the fact that approximately 20 minutes are needed at the beginning of each desorption phase to bring the adsorber at the target temperature, due to the large thermal inertia, meaning that the effective desorption time is shorter than the nominal one.

A further indicator we can evaluate is the thermal COP (see eq. 3.16), as the ratio between cooling capacity and heating capacity. For example, considering test 5 (fig 5.7), we can estimate the cooling capacity as the integral of thermal power over adsorption[2], and heating capacity as the integral of thermal power over desorption, then divide them and taking their absolute value, to have: $COP = 0.27 \pm 0.03$, where we reported average $\pm$ one standard deviation over the 6 cycles. Actually, this KPI is mostly used to evaluate performances of adsorption chillers (where the cooling power is the useful effect), rather than desalination plants; this is the reason why we didn't include it in the results table above. Nevertheless, it is worth mentioning it at least once to support the idea that a small-scale machine has intrinsic low efficiency[3]. Also, test 5 is the result of cycle optimization: test 3, in comparison, sees the COP dropping down to $COP = 0.17 \pm 0.06$. Using a different sorbent such as silica-gel

[2]This is done under the approximation that the heat of evaporation from the EV tank is the same as the heat of adsorption in the exchanger (based on the proximity of latent heat of evaporation and adsorption enthalpy). This is clearly not exact, but we do not have information on the exchanged power in the EV tank.

[3]In the author's experience, larger machines work more than proportionally better than smaller machines. A possible explanation is here provided. Geometrically, volumes and amounts of sorbent scale with the cube of the machine size, while surfaces scale with the square of the machine size; since the thicknesses of the walls of vacuum chambers and exchangers are typically not modified while scaling, the thermal mass of inactive metals is proportional to the square of the machine size rather than the cube. Thus, small applications may suffer from longer settling times that, if a proper heat recovery strategy is not applied, will cause lower efficiencies.

does not help: test 9, identical to test 3 but with different sorbent, sees an even lower COP of $COP = 0.12 \pm 0.04$. In Chapter 6 we show a larger plant with greater efficiency.

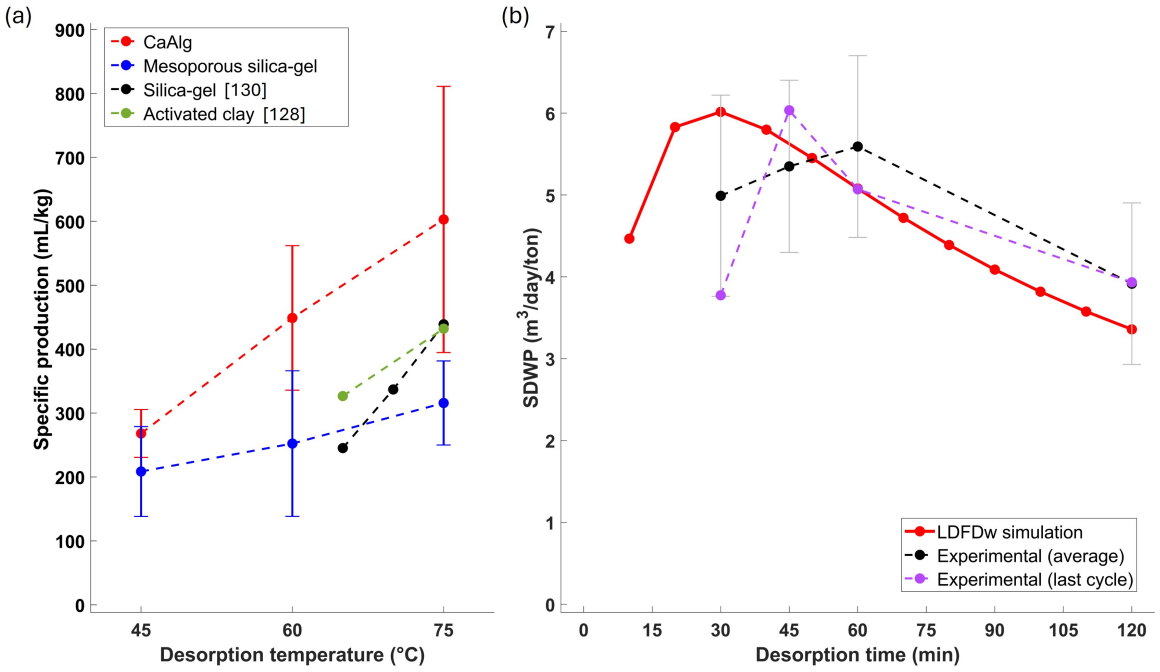

Fig. 5.8 Water production with CaAlg and silica-gel in the AD unit, as a function of temperature and time. (a) Average specific water production per cycle (SCWP) over 3 cycles as a function of test desorption temperature. Experimental results for CaAlg and mesoporous silica-gel are shown, as achieved in the desalination unit with adsorption time of 30 minutes, ads temperature of 30°C, des time of 120 min. Vertical bars indicate ± one standard deviation. Results achieved with different plants from literature are shown in comparison [128, 130]. (b) Specific daily water production (SDWP) as a function of test desorption time t_{Des}. Experimental results for CaAlg are shown, as achieved in the desalination unit with t_{Ads} of 30 minutes, T_{Ads} of 30°C, T_{Des} of 60°C. The graph contains the experimental SDWP evaluated considering the average production of the day (black, with vertical bars indicating ± one standard deviation), the experimental SDWP evaluated considering the production from the last cycle of the day (purple), the theoretical SDWP simulated with the model LDFDw.

In Fig. 5.9 we provide a map comparing the achieved SDWP with other AD plants from the literature [4] [131–138]. As we can observe, most of the existing plants use high-temperature sources to run desorption (75-95°C), with some of them reaching SDWP above 10 $m^3/day/ton$. On the other hand, in case of temperature below 65°C, we achieved one of the best water production to our knowledge, comparable with the plant using aluminium fumarate [131][5], despite the small size of our plant and subsequent intrinsic inefficiencies.

[4]When the STEC was not directly available from the literature, we estimated it starting from other reported indicators, using eq. 3.17.

[5]This plant, though, uses a slightly lower condenser temperature, of 20°C. This goes in the direction of increasing the water productivity.

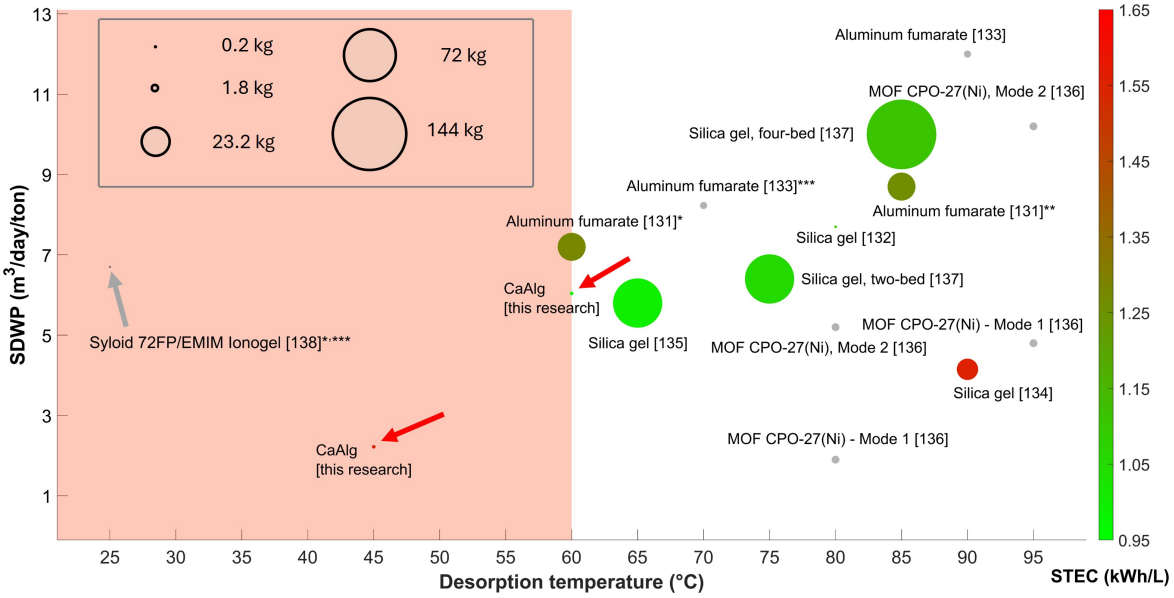

Fig. 5.9 Map showing the performance of the desalination unit in comparison with adsorption-desalination plants from the literature. SDWP is shown as a function of desorption temperature. The dot's color shows the needed Specific Thermal Energy Consumption (STEC) - when not provided, it was estimated using the available data and eq. 3.17. The dot's area is proportional to the amount of sorbent in the plant. The ultralow-grade heat region for temperatures below 60°C is colored in orange. All reported plants use a condenser temperature comprised between 25°C and 30°C, except for * (20°C) and for our plant (23°C). All reported plants use an evaporator temperature comprised between 27°C and 30°C, except for ** (24°C) and *** (20°C).

Also, we achieved one of the smallest specific thermal energy consumptions (0.97 kWh/L). A special mention must be made for the case of [138]: the authors achieved an extraordinary SDWP of 6.7 m^3/day/ton with a ionogel (silica-gel matrix impregnated with a ionic liquid called 1-ethyl-3-methylimidazolium, or EMIM) using a hot source of only 25°C and a temperature difference of only 5°C between desorption and adsorption phases. Such innovative material has unique high potential in exploting extremely ultralow-grade heat sources, even though it might sound less economically attractive if compared with silica-gel or CaAlg (see also section 6.2.2).

5.2.3 Extrapolating to large-scale ultralow-grade waste heat driven applications

The results achieved with CaAlg in AWH and AD prototypes indicate that such sorbent has the potential to work where other materials can hardly compete: the ultralow-grade heat range. This is defined in [139] as the temperature range below 80°C, which is typically not used for production of work. This is clearly due to the low exergetic potential of such sources: we can easily estimate that the efficiency of an ideal Carnot cycle working between

an ambient temperature of 20°C and a hot-source temperature 60°C would be as low as 12%:

$$\eta_{Carnot} = 1 - \frac{T_{cold}}{T_{hot}} = 1 - \frac{20 + 273.15}{60 + 273.15} = 0.12 \tag{5.1}$$

On the other hand, a temperature source of 60°C is sufficient to get a useful effect from thermally-driven adsorption-based machines such as the ones studied in this chapter. In particular, when using CaAlg, we observed a sensible water production already at 65-70°C in the case of AWH (even at relatively low RH, around 45%), and we demonstrated water desalination even at 45-60°C in the case of AD.

As a further note of credit, this was achieved despite in both cases we tested the sorbent in sub-optimal conditions. First, the used AWH unit had large water collection inefficiencies due to the accumulation of water drops on the condenser coil. Second, the desalination unit had very large thermal inertia and vapor diffusion limitations due to the geometry of the channels that hindered the mobility of water molecules. In the next Chapter 6 we demonstrate that, with proper design and in larger-scale machines, such inefficiencies are reduced, with potential increases in water productivity and decreases in thermal energy expense.

The achieved results open options for the integration of adsorption-based technologies with ultralow-grade waste heat sources. Figure 5.10 is extracted from [139]:

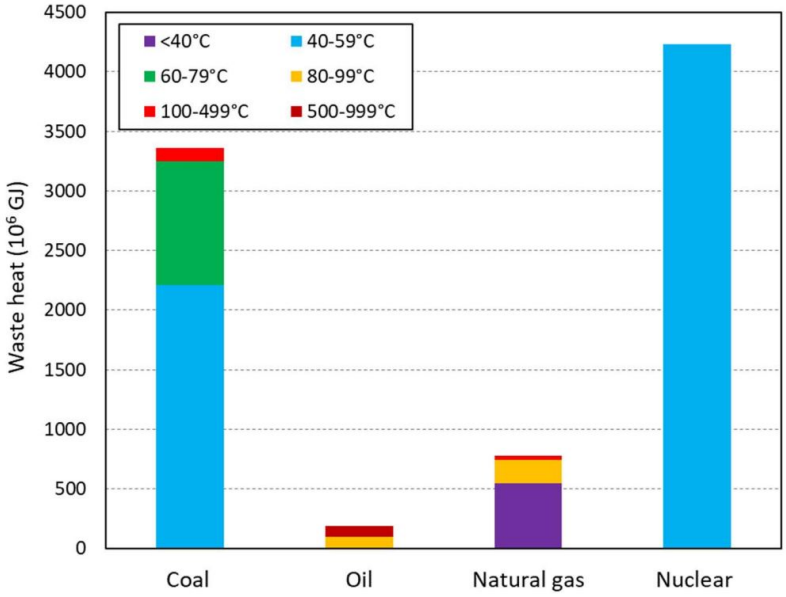

Fig. 5.10 Waste heat generation from the EU power sector in 2018. Source: [139].

As we deduce from the picture, in one year (2018) and in the EU only, about $6500 \cdot 10^6$ *GJ* are rejected in the temperature range 40-59°C, mostly by coal and nuclear plants condenser loops. Further $1000 \cdot 10^6$ *GJ* are rejected in the temperature range 60-79°C from wall losses in coal plants. This accounts for a total of $7500 \cdot 10^6$ *GJ* in the ultralow-grade heat temperature range 40-79°C, which is the studied interval for the experiments with AWH and AD in this

research.

Power plants are not the only source of ultralow-grade waste heat. Another important application gaining interest lately is data-centre cooling, where the heat produced from CPUs and GPUs computing must be dissipated in order to keep the racks at the optimal temperature and guarantee the designed performance (typically, 60-70°C). It is estimated that, in total, data centres in the world consume about 3% of the whole electrical energy and dissipate it as heat [140]. Nevertheless, it is quite difficult to harvest such heat and use it for other purposes. The main limitation in this case is the extremely high energy density, reaching up to 70 W/cm^2 in late generation processors. This makes heat extraction difficult, requiring to use liquid cooling with temperature differences of 20°C or above between the chip and the fluid, with the latter having a temperature between 40°C and 50°C. CaAlg might offer a solution, since its desorption can be driven at such low temperatures.

In general, with a proper configuration using CaAlg, we can exploit part of this waste heat. We propose in the next paragraphs some quantitative examples of integration, where we extrapolate the results achieved in Chapters 4 and 5 to large-scale architectures.

Combined power production - AWH plant

We can use the rejected heat from wall losses in coal-fired power plants to run an AWH device. This combined device would provide fresh water in desert areas, far from coasts and in areas where most of electricity production is provided by this type of power plants (e.g., central Asia or south Africa).
Assuming a 300 MW coal-fired power plant, a plant efficiency of 37.5%, and a fraction of wall losses equal to 19.4% [139], we can estimate a heat source of: $Q_{hot} = \frac{300\ MW}{37.5\%} \cdot 19.4\% = 155\ MW$. Clearly, due to practical implementation, not all this heat can be effectively accessed. For the purpose of this simulation, we suppose to build a liquid-liquid heat exchange architecture harvesting only 1‰ of this amount, leaving us with a 155 kW liquid stream (e.g., water, or water and glycol mixture) at 65-70°C.
The liquid stream can be directed through a battery of CaAlg-coated heat exchangers (we will assume that we have a high flowrate, such that the temperature gradient of the liquid stream going through the exchanger is negligible). The exchanger must be properly chosen, and we propose here a simplified design procedure:

1. Identify the amount of available thermal energy E_{hot} in one operational cycle desorption phase; in this case, assuming $t_{Ads} = 120\ min$ and $t_{Des} = 60\ min$, $E_{hot} = Q \cdot 1\ h = 155\ kW \cdot (1\ h) = 155\ kWh = 558000\ kJ$.

2. Identify the adsorption (environmental) temperature and relative humidity, and the desorption (hot-source) temperature; in this case, respectively, $T_{Ads} = 25°C$, $RH_{Ads} = 45\%$ and $T_{Des} = 75°C$.

3. Based on the results of CaAlg dynamics characterization, identify the water uptake range within which the sorbent state of charge oscillates between adsorption and desorption in one cycle, at the working temperatures and relative humidities identified in point 2; in this case, based on the models developed in Chapter 2 and best-fitted over the results in Chapter 4, this is estimated to be: $\Delta w \approx 0.3\ g/g$.

4. Supposing that all the available thermal energy is used to run the material desorption, and assuming a desorption enthalpy of $H_{Des} \approx 2600\ kJ/kg$ (based on the results for CaAlg equilibrium characterization in chapter 4, and under the approximation that $H_{Ads} \approx H_{Des}$), estimate the amount m_{dry} of dry-sorbent to be used:

$$E_{hot} = H_{Des} \cdot \Delta w \cdot m_{Dry} \quad \rightarrow \quad m_{dry} = \frac{E_{hot}}{H_{Des} \cdot \Delta w} = 715\ kg = 0.715\ ton \tag{5.2}$$

5. Assuming to replicate a coated configuration like the one in the AWH prototype (97.5 g of dry sorbent per exchanger), and adding a 10% safety to account for inefficiencies in heat exchange, design a battery employing the required number of exchangers (8000 in this case). Given that each exchanger fits within a cylinder with diameter 120 mm and height 150 mm, we can estimate a total volume of $2.4\ m\ \times 2.4\ m\ \times 3.0\ m$.

6. Evaluate the absolute daily water production DWP, multiplying the range of uptake covered in one cycle by the number of cycles per day ($n_c = 8$, in this case, since one full cycle lasts 3 hours) and the amount of dry material:

$$DWP = \Delta w \cdot n_c \cdot m_{dry} = 1.7\ m^3/day = 1700\ L/day \tag{5.3}$$

Note that, given the chosen ratio 1:2 between desorption and adsorption times in this specific simulation, the hot-source is actually used only one-third of the time. In order to have at least part of the sorbent always desorbing, we can replicate the module for a total of 3 times, and add a valves sistem to connect it to the power plant as schematized in Fig. 5.11. This triplicates the amount of material (about 2.1 tons) and the produced water (about 5100 liters per day).

Of course, for an application of such scale, the heat exchanger design must be re-though from scratch: replicating the aluminum exchanger in the prototypal device would introduce unnecessary weight and complexity. Thus, the actual volume and weight of the machine would reasonably be drastically lower than what estimated.

Given the higher diffusivity that silica-gel has with respect to CaAlg, an idea would be to coat the exchangers with silica-gel instead. Nevertheless, shorter cycles not necessarily

imply higher daily productions: the useful effect of performing more cycles in a day might be compensated by a lower Δw per cycle, thus generating an overall lower SDWP. Further investigation is needed on this point.

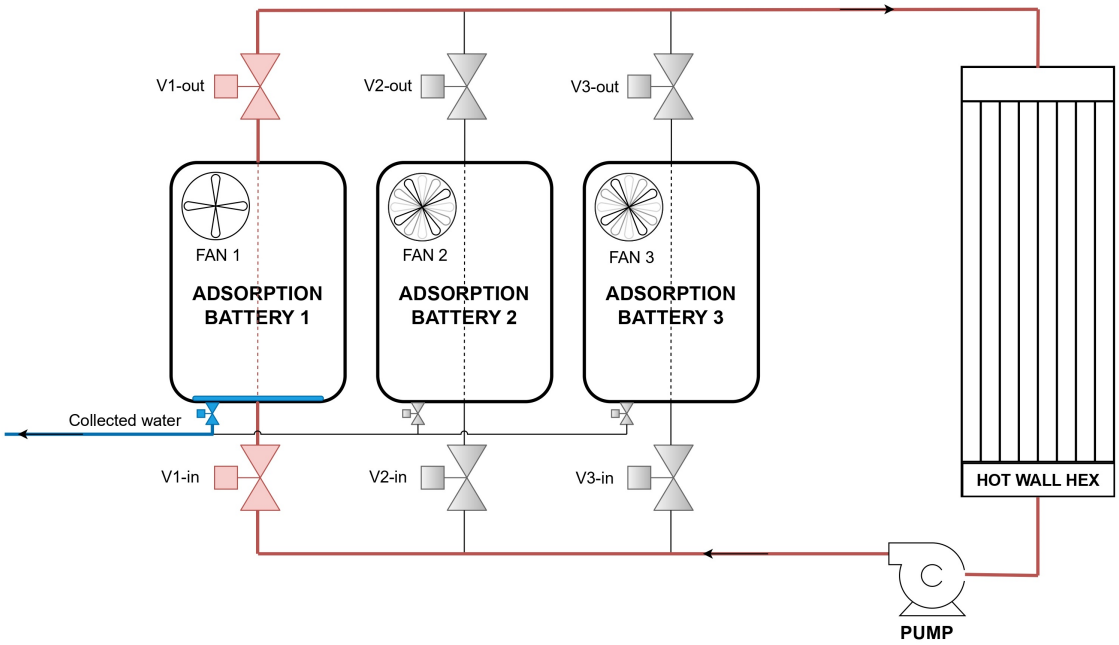

Fig. 5.11 Combined power production - AWH plant integrated architecture. A simplified P&ID of three batteries of coated heat exchangers, connected to an external exchanger dissipating heat from the wall. In this configuration, module 1 is desorbing (forced convection FAN 1 OFF, and hydraulic valves V1-in and V1-out open), while module 2 and 3 are adsorbing (forced convection fans ON, and hydraulic valves closed). During normal operation, the three module rotationally alternate their role (1 des, 2 and 3 ads; 2 des, 1 and 3 ads; 3 des, 1 and 2 ads). The generic exchanger HOT WALL HEX (whose specific design is not here specified) is exchanging heat with the power plant wall.

Combined data centre cooling - AD plant

We can use the heat rejected by CPUs and GPUs racks to run an Adsorption Desalination plant. This combined device would provide computational power and simultaneously fresh water in areas close to coasts, like in the middle-east or in the U.S.A. west coast. The produced fresh water can be used for drinking purposes (arid regions in the middle-east use desalination plants as main provider of such resource) or for industrial reasons (for example, chemical industry).

Suppose to have a $Q = 50\ kW$ data centre rack, including CPUs and/or GPUs, where heat is dissipated via liquid cooling or two-phase cooling, with the fluid temperature leaving the racks at 45°C. Since the heat source is already a fluid stream, we can approximate that all the heat can be effectively harvested (in reality, the exchangers do not have unitary efficiency). We can produce CaAlg beads and fill a number of heat exchangers to exploit such heat to treat water. We propose here a simplified design procedure:

1. Identify the amount of available thermal energy E_{hot} in one operational cycle desorption phase; in this case, assuming $t_{Ads} = 30\ min$ and $t_{Des} = 120\ min$, $E_{hot} = Q \cdot 2\ h = 50\ kW \cdot (2\ h) = 100\ kWh = 360000\ kJ$.

2. Identify the adsorption and the desorption temperatures; in this case, respectively, $T_{Ads} = 30°C$ and $T_{Des} = 45°C$.

3. Based on the results of CaAlg dynamics characterization, identify the water uptake range within which the sorbent state of charge oscillates between adsorption and desorption in one cycle, at the working temperatures identified in point 2; in this case, based on the results from Chapter 4 (we used model LDFDw and evaluated diffusivities using the results from Section 4.2.2), this is estimated to be: $\Delta w \approx 0.1\ g/g$.

4. Supposing that all the available thermal energy is used to run the material desorption, and assuming a desorption enthalpy of $H_{Des} \approx 2600\ kJ/kg$ (based on the results for CaAlg equilibrium characterization in chapter 4, and under the approximation that $H_{Ads} \approx H_{Des}$), estimate the amount m_{dry} of dry-sorbent to be used:

$$E_{hot} = H_{Des} \cdot \Delta w \cdot m_{Dry} \quad \rightarrow \quad m_{dry} = \frac{E_{hot}}{H_{Des} \cdot \Delta w} = 1385\ kg = 1.385\ ton \tag{5.4}$$

5. Assuming to replicate a finned configuration like the one in the AD prototype (up to 1 kg of dry sorbent can fit per exchanger), design a battery employing the required number of exchangers (approximately 1400 in this case). Given that each exchanger fits within a cylinder with diameter 120 mm and height 1000 mm, we can estimate a total volume of $3.12\ m\ \times 3.24\ m\ \times 2.0\ m$.

6. Evaluate the absolute daily water production DWP, multiplying the range of uptake covered in one cycle by the number of cycles per day ($n_c = 9.6$, in this case, since one full cycle lasts 2.5 hours) and the amount of dry material:

$$DWP = \Delta w \cdot n_c \cdot m_{dry} = 1.3\ m^3/day = 1300\ L/day \tag{5.5}$$

We see that, contrary to the simulation run for the *power - AWH combined plant* in the previous paragraph, here most of the effect is water desalination, making data centre cooling a side effect. Indeed, in this simulation, the amount of sorbent needed to achieve the cooling effect is quite large with respect to the hot power available, and this is explained by multiple considerations:

- First, CaAlg has a relatively low desorption enthalphy (2600 kJ/kg), making it not the best choice for cooling applications, where materials such as zeolites and other non-conventional materials with larger enthalpies[6] may still result as the best choice;
- Second, the simulation was run under sub-optimal assumptions. The efficacy can be increased by optimizing the machine design (this would decrease the cycle times, and thus increase n_c), and by using a hot-source at 50-60°C (this would increase Δw). Indeed, in principle, we can cool down data centres racks even at this temperature, if we accept to use the CPU at higher temperature (70°C, still in the admittable range for CPUs to work at good efficiency) and with a heat exchange solution at higher transmittance, such as two-phase cooling, as being currently under investigation in the EU project DYMAN [142].

Even in this example, it is possible to duplicate the module containing the sorbent to always have part of the material desorbing. Of course, the heat exchanger solution for such large-scale system can be re-though in order to save space and weight. Both these improvements are done in Chapter 6, where we designed and assembled an industrial-scale adsorption-based machine.

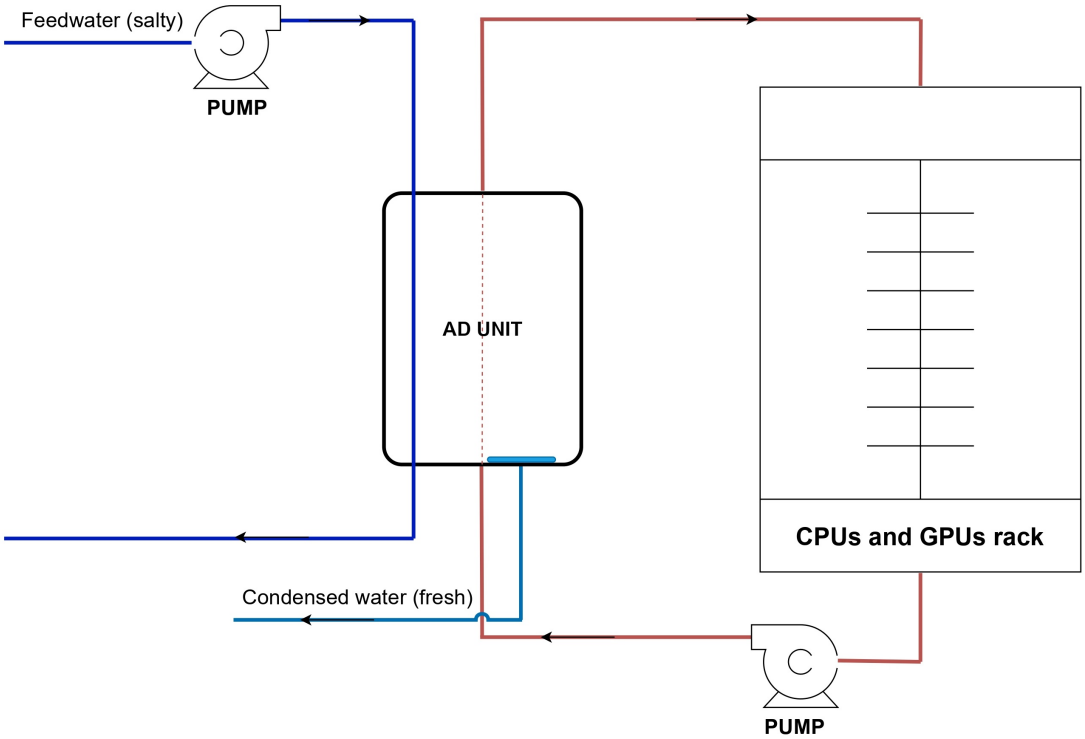

Fig. 5.12 Combined data centre cooling - AD plant integrated architecture. A simplified diagram of an Adsorption Desalination unit connected with an external supercomputing rack.

[6] As an example, in [141] it was measured for MOF-801, zeolite 13X and zeolite MgY, respectively, an enthalpy of about 3000 kJ/kg, 3900 kJ/kg, 4000 kJ/kg.

5.3 Methods

5.3.1 AWH unit description

In collaboration with the company Aquaseek SRL SB, we produced a small prototype for Atmospheric Water Harvesting. The machine consists of a series of concentric chambers (Fig. 5.1c):

A. An internal cylindrical chamber containing the sorbent material;

B. An external chamber (the annular region between two plexiglass cylinders) containing a copper coil connected with the condenser circuit.

During adsorption, two valves (one at top of the unit, one at bottom) open, and put in communication the chambers with the external environment. An electric fan is used to force convection through the coated exchanger, increasing vapor adsorption kinetics.
During desorption, the valves close and isolate the chambers with respect to the external environment. An electric heater provides heat to the material in chamber A, and the released vapor at high dew-point temperature is free to circulate between chambers A and B. Once in chamber B, the vapor condenses on the surface of the copper coil and is collected at the bottom of the machine.
Chamber A hosts about 97.5 grams of calcium alginate $Alg_1Ca_5G_{0.1}$, which coats the surface of a finned heat exchanger. To produce the coating, the process described in Chapter 4 was adapted:

1. Preparation of solution *A* is identical as in the previously discussed procedure.

2. Preparation of solution *B* is identical as in the previously discussed procedure.

3. Solution *A* is placed inside a mould designed to contain the object which must be coated with CaAlg, in this case an aluminum radial exchanger as shown in Fig. 5.13. The mould external surface is provided with small holes, which are kept closed using a plastic cover in this phase, avoiding sol. *A* to leak from the mould.

4. The mould is positioned in the basin containing solution *B* (Fig. 5.14), and the plastic cover closing the holes in the mould is removed, allowing solution *B* to penetrate and react with solution *A*. 12 hours are waited so that the calcium ions have the chance to properly diffuse and complete the jellification process over the whole volume of hydrogel. The mould passage areas not identical in all directions: to reduce the risk for inhomogeneity in the $CaCl_2$ solution, an electric mixer is constantly operating.

5. The mould is removed from the basin, opened and let dry (first in still air, then in a oven at 70°C for 12 hours), causing the coating to shrink and adhere to the exchanger fins surface.

The result is a layer with thickness of approximately 0.5 mm of CaAlg covering the surface of the exchanger, for a total of 97.5 grams of dry-mass. The average thickness was measured after drying using a TB 1000-0.1FN ultrasound thickness gauge [47]. The mass of aluminium of the exchanger is 1433 g. The remaining mass (accessories, cables, thermistor, plastic parts...) is about 1 kg.
The prototype is provided with a list of sensors and actuators as listed in table 5.5.
During desorption, sensor T1 is used as feedback variable for the sorbent temperature control. A modified proportional control algorithm was developed (Fig. 5.16a), and the user is allowed to select the desired desorption set temperature T0. The user can also choose the adsorption and desorption times.
Note that, despite the control on temperature T1, it is not guaranteed that all the sorbent is homogeneously heated. Using a thermal camera TESTO 882, we have noticed that the tip of the fins reaches a lower temperature than the core. For example, in Fig. 5.15 we have a set temperature T_0=80°C, but the temperature distribution ranges from about 73.5°C on the fins to about 85°C in a small area around the electrical resistor, due to initial overshooting in the control algorithm. This inhomogeneity causes the average sorbent desorption temperature to be lower than the nominal target temperature.

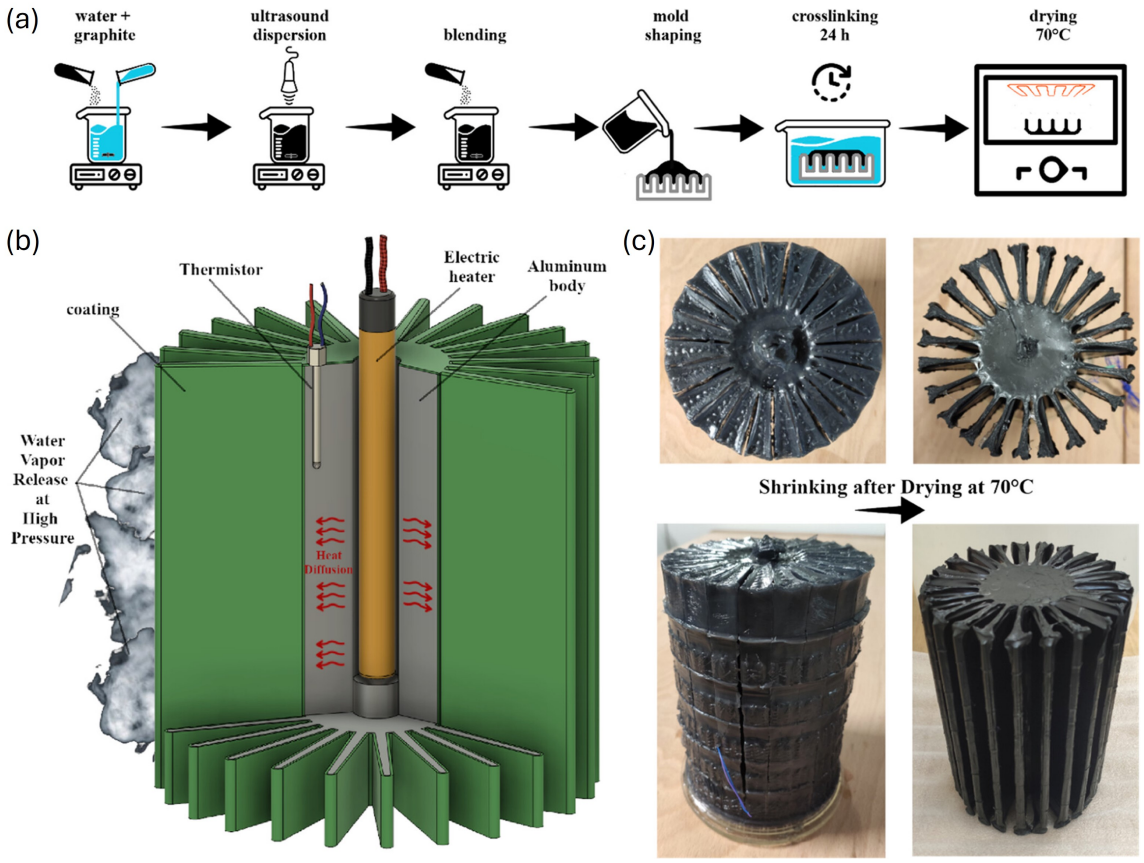

Fig. 5.13 CaAlg coating materials and methods [47]. (a) Schematics of the methodology used to generate the NaAlg-graphite coating on the aluminum radial heat sink. (b) Schematics of the aluminum exchanger containing the electric heater to provide thermal energy for moisture regeneration from the NaAlg-graphite coating covering the aluminum body of the radial heat sink. (c) Pictures showing the shrinking of the coating right after cross-linking and once dried in the ventilated oven at 70°C.

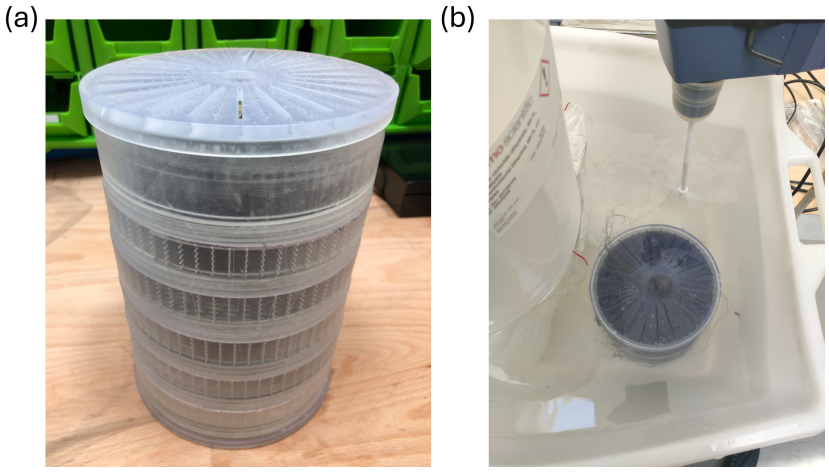

Fig. 5.14 CaAlg coating realization. (a) 3D-printed mould containing the heat exchanger. (b) Large basin containing water + $CaCl_2$ solution, where the mould containing the aluminium heat exchanger and the NaAlg+graphite solution is submerged. A rotating mixer keeps the solution homogeneous during jellification.

Component	Type	Scope	Description
T1	Sensor	Monitoring the coated HEX temperature.	NTC thermistor 10kOhm. Accuracy: $\pm$ 0.5°C.
T2	Sensor	Monitoring the temperature above the condenser coil.	NTC thermistor 10kOhm. Accuracy: $\pm$ 0.5°C.
T3	Sensor	Monitoring ambient temperature.	NTC thermistor 10kOhm. Accuracy: $\pm$ 0.5°C.
T4	Sensor	Monitoring the temperature at the outlet of the machine.	NTC thermistor 10kOhm. Accuracy: $\pm$ 0.5°C.
RH1	Sensor	Monitoring ambient relative humidity.	Honeywell HIH-4000-001. Accuracy: $\pm$0.2%.
RH2	Sensor	Monitoring the relative humidity at the outlet of the machine.	Honeywell HIH-4000-001. Accuracy: $\pm$0.2%.
HALL1	Sensor	Monitoring the opening/closing of the top valve.	Hall-effect.
HALL2	Sensor	Monitoring the opening/closing of the bottom valve.	Hall-effect.
SCALE	Sensor	Monitoring the water production.	Load cell (1 kg).
F1	Actuator	Forcing convection in the internal chamber.	EBM Papst 3312 N/2N3P, 12V, 5.5W.
P1	Actuator	Circulation pump running water in the condenser coil.	Brushless AW500S, 12V, max flowrate 800L/h.
F2	Actuator	Fans dissipating the condensation heat into the environment.	RND components 460-00077, 12V, 195m3/h.
H1	Actuator	Providing the power to heat up the aluminum heat exchanger coated with the sorbent.	Electric heater, peak consumption of 700 W.
P2	Actuator	Peristaltic pump extracting the condensed water from the machine.	Grothen G328.
MOTOR1	Actuator	Motor used to open/close the top valve.	DC motor JGY-370 12V 150 rpm.
MOTOR2	Actuator	Motor used to open/close the bottom valve.	DC motor JGY-370 12V 150 rpm.

Table 5.5 Desalination unit components.

Fig. 5.15 Temperature distribution on the coated exchanger as seen through a thermal camera.

The AWH software was entirely developed in Arduino® [143] and allows to monitor and control the prototype remotely, through an IoT architecture [122]. The control electronics was developed ad-hoc, including a dedicated PCB (Fig. 5.16b) and the necessary power equipment.

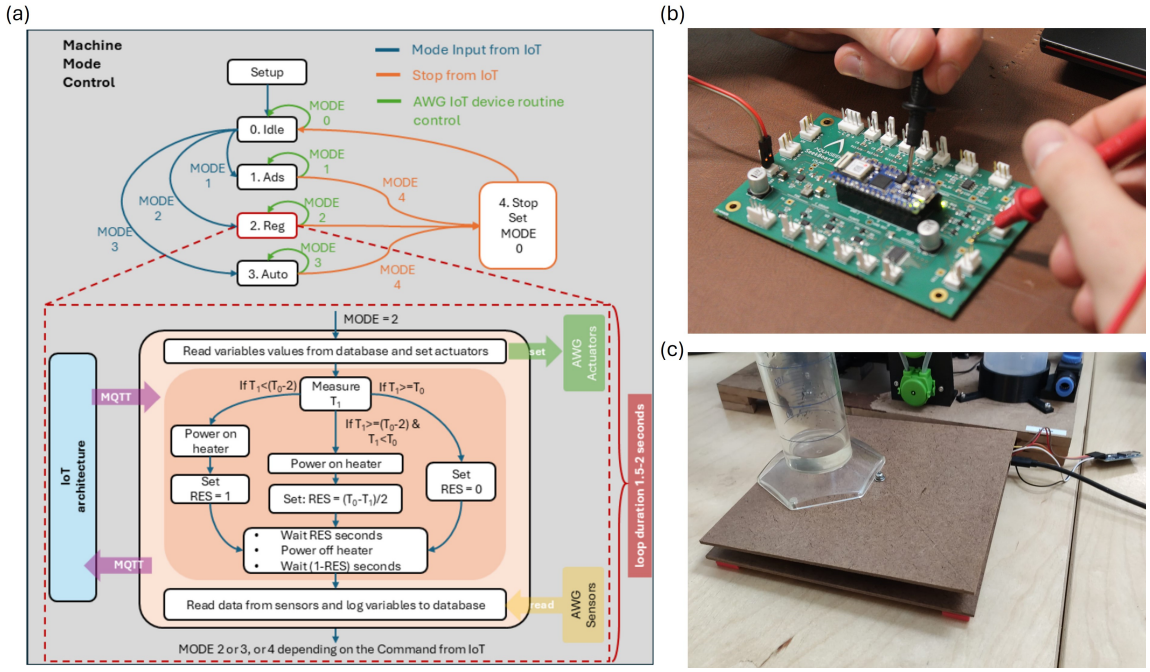

Fig. 5.16 AWH unit control logic. (a) Schematics of the control logic of the AWH unit, as developed [122]. (b) Arduino-based PCB to control the unit. (c) Simple scale produced using a 1-kg load cell.

The water production was monitored gravimetrically, by means of a scale connected with the control board (Fig. 5.16c). The scale was built using a load-cell with capacity 1 kg. After a calibration campaign, we estimated an accuracy of $\pm$ 0.5 g.

Experiments

The following experiments were conducted with the AWH prototype in lab environment:

Test	1	2	3	4	5	6	7	8
T_{Amb} (°C)	28	25	26	25	24	24	24	25
RH_{Amb} (°C)	45	45	50	50	50	55	60	60
t_{Ads} (°C)	90	120	120	120	120	120	120	120
T_{Des} (°C)	65	70	70	70	65	65	65	70
t_{Des} (min)	60	60	60	60	60	60	60	60
n_{cycles}	13	19	20	17	22	23	23	21

Table 5.6 Experimental campaign with the CaAlg coating in the AWH device.

The machine was also tested in open arid environments, such as in a wine-production facility on Pantelleria island in Italy (Fig. 5.17a) and in the Texas desert in the USA (a picture is shown in Fig. 5.17b). These tests had the scope to demonstrate that a water production is achievable in such conditions as well; nevertheless, data collected in both cases were qualitatively identical to the tests in laboratory. For this reason, we decided to comment here only the latter tests, conducted with better monitoring on the environment and water production.

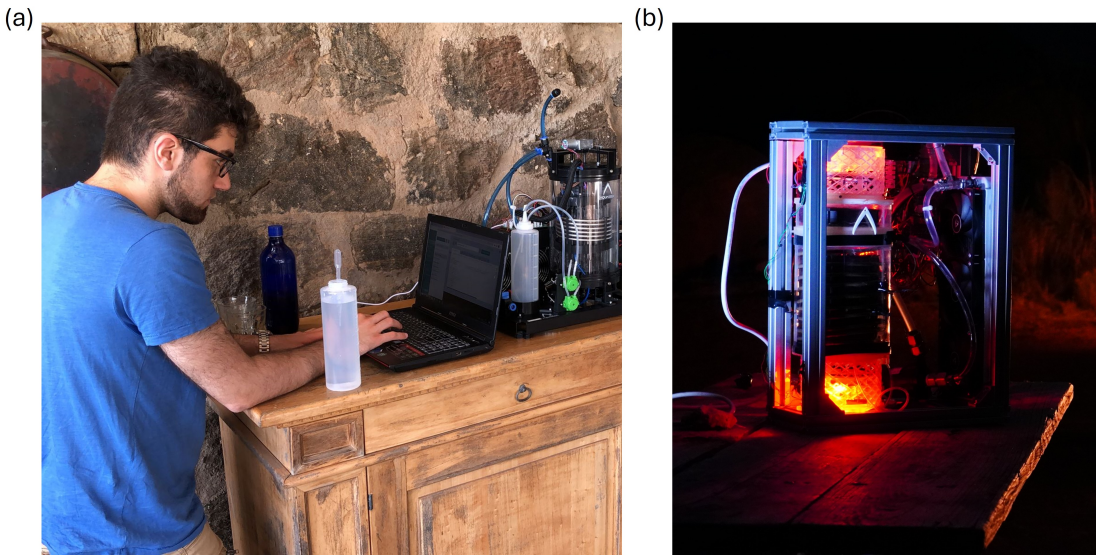

Fig. 5.17 On-site testing of the AWH unit. (a) A picture of the author updating the C++ firmware of the AWH prototype in Pantelleria - Italy. (b) The AWH unit in Texas - USA (picture by V. Gentile).

Data analysis

The control board is based on an Arduino Nano 33 IoT, using a 10-bits Analog-Digital-Converter to translate voltage differences measured at the sensors level to digital values a (0-1023) and then into physical variables. In particular, in case of the 10k thermistors, the temperature is evaluated as follows:

$$T(a) = \frac{1}{(1/T_0) - (1/B) \cdot \log\left[(R^*/R_0) \cdot (1024/a - 1)\right]} - 273.15 \tag{5.6}$$

where $R^* = 1240\ \Omega$, $R_0 = 10000\ \Omega$, $B = 3988\ K$ (except for sensor T_1, where $B = 4300\ K$), $T_0 = 298.15\ K$. Also, $a = 1024 \cdot V_{read}/V_0$, where V_{read} is the measured voltage, and $V_0 = 5\ V$. The relative humidity is evaluated as follows:

$$RH(a) = \frac{V_0 \cdot (a/1024) - offset}{slope} \tag{5.7}$$

where $V_0 = 5\ V$, $offset = 0.826\ V$, $slope = 0.0323\ V/\%$.
Since temperature and relative humidities are measured in the environment (sensors T3 and RH1) and at the outlet of the exchanger (sensors T4 and RH2), it is possible to evaluate the dew-point temperature of vapor in such conditions. We used the formula:

$$T_{dew}(T,RH) = \frac{1}{\frac{1}{C+T} - \frac{\log(RH)}{B}} - C \tag{5.8}$$

with $B = 3984.92$°C and $C = 233.426$°C. The formula is derived by inverting the definition of vapor quality and the expression for saturation vapor pressure in 2.6.
Since the control algorithm is based on PWM (Pulse-Width Modulation), we can evaluate the electrical power used during desorption multiplying the maximum power of the heater by the duty-cycle in which the heater was on in order to keep controlling the temperature:

$$Power = P_{max} \cdot DC_{\%} \tag{5.9}$$

where $P_{max} = 700\ W$ and DC oscillates between 0 (heater off) and 1 (heater always on). For example, if the control algorithm chooses to turn on the heater for 25% of the time, then $DC = 0.25$ and $Power = 175\ W$.

Since we know the layer thickness and the material properties (Chapter 4), we can estimate the concentration along the coating during cycling using the plane-sheet FD numerical model presented in Chapter 2.

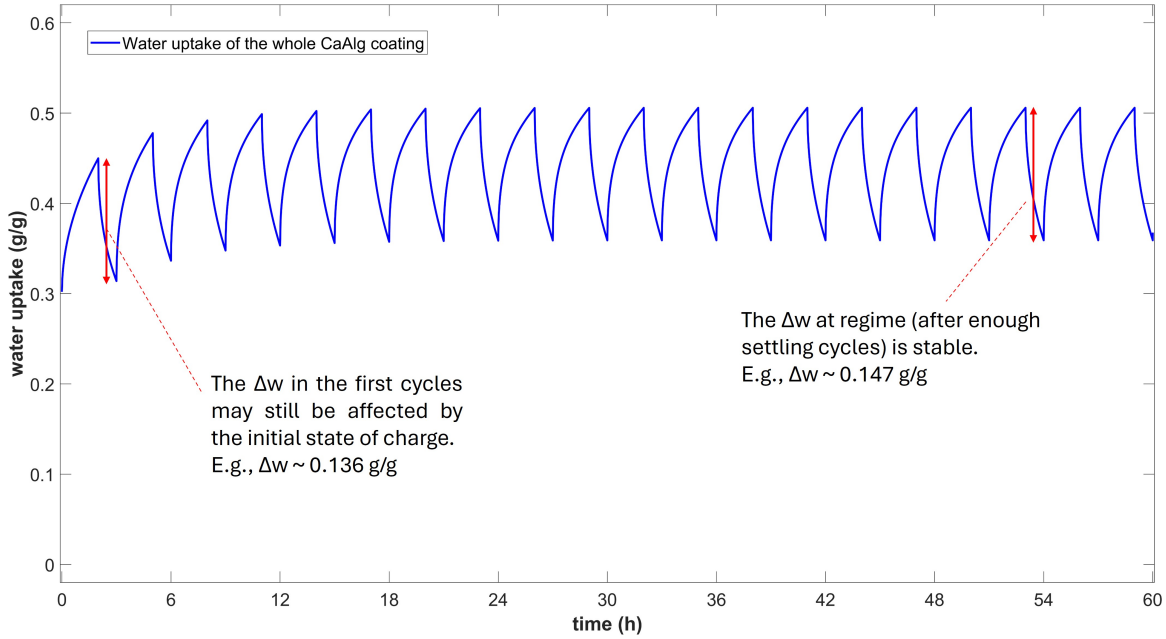

Fig. 5.18 FD-based numerical simulation of the water uptake in the CaAlg coating.

The simulation is analogous to the one shown in Fig. 2.11, with different physical parameters: coating thickness is 0.5 mm, while diffusivity is written as a function of concentration based on the results in 4.2.2 (for simplicity, we assumed as diffusivity the ones of adsorption at RH=40%). The equilibrium concentration are assumed 0.6 g/g for adsorption (we refer to the isotherm for RH=50%), and a value of 0.1 g/g was assumed for desorption. The difference is that, this time, we repeated the adsorption and desorption phase for more consecutive cycles. This video shows an analogous simulation we did with different parameters, showing how concentration and uptake changes over time and space: https://www.youtube.com/watch?v=4PG2l8mOEiY (last visited on 26/10/2025).
In figure 5.18, concentration is integrated over the volume of material and the resulting water uptake of the coating is shown. It is interesting to see that, according to the model, some cycles are needed in order for the adsorbent to oscillate between the same two values. This is due to the fact that adsorption and desorption times are fixed, and some cycles are necessary to avoid the initial state of charge of the material (here assumed $w_0 = 0.3\ g/g$) to affect $w(t)$. Under the assumption that all the Δw is converted in collected water, we can multiply Δw by the dry-mass of sorbent to obtain the grams of water produced per cycle. This is plotted in Fig. 5.3d, in comparison with experimental data.

Water analysis

To assess the quality of the produced water and identify possible contaminants, we performed a complete chemical analysis of potability at SMAT (Società Metropolitana Acque Torino S.p.A.). We tested for the same analysis one sample of produced water and one sample of distilled water, for reference. The list of analysed parameters and the correspondent analysis method and accuracy are reported in table 5.7.

Parameter	Unit	Uncertainty	Sensitivity	Method
Conductivity	$\mu S/cm$	15-30%	10	ISTISAN 2007/31 Pag 55 Met ISS BDA 022
pH	pH	$\pm$ 0.13	4.0	ISTISAN 2007/31 Pag 68 Met ISS BDA 023
Alachlor	$\mu g/L$	n.a.	0.01	UNI EN ISO 27108:2013
Arsenic	$\mu g/L$	n.a.	1	LLAPO076/B Rev. B 2021
Benzene	$\mu g/L$	n.a.	0.2	ISTISAN 2007/31 Pag 187 Met ISS CAD004
Benzo(a)pyrene	$\mu g/L$	n.a.	0.003	APAT CNR IRSA 5080 Man 29 2003
Boron	$\mu g/L$	n.a.	20	LLAPO076/B Rev. B 2021
Bromate	$\mu g/L$	n.a.	2	ISTISAN 2007/31 Pag 126 Met ISS.CBB.006-B
Chlorate	$\mu g/L$	n.a.	40	LLAPO132/C Rev. C 2020
Copper	$\mu g/L$	n.a.	1	LLAPO076/B Rev. B 2021
1,2-Dichloroethane	$\mu g/L$	n.a.	0.5	ISTISAN 2007/31 Pag 164 Met ISS CAA036
Fluoride	$\mu g/L$	n.a.	0.03	ISTISAN 2007/31 Pag 115 Met SS CBB 037
Lead	$\mu g/L$	n.a.	1	LLAPO076/B Rev. B 2021
Nickel	$\mu g/L$	n.a.	1	LLAPO076/B Rev. B 2021
Nitrate	$\mu g/L$	$\pm$ 0.2	1	ISTISAN 2007/31 Pag 115 Met ISS CBB 037
Uranium	$\mu g/L$	n.a.	1.0	LLAPO076/B Rev. B 2021
Vinyl chloride	$\mu g/L$	n.a.	0.1	LLAPO002/B Rev.B 2021

Table 5.7 SMAT analyses of the water produced with CaAlg in the AWH unit. We report the measured parameters in the condensed water, along with uncertainty (n.a.=not available), sensitivity and measurement method.

5.3.2 AD unit description

In adsorption-based technologies, the separation of water from contaminated liquid solutions is obtained operating a working cycle based on three consecutive phases: adsorption, desorption, pre-cooling. First, a vacuum chamber (EV tank) containing the evaporating feedwater is put in communication with a second vacuum chamber (Adsorber) containing the sorbent under test. During this phase (adsorption), water vapor evaporates and is physically bonded on material micropores. Then, the communication between EV tank and adsorber is interrupted, and the desorption process starts. During this phase, increasing sorbent temperature, physical bonds between water and sorbent break, and water vapor is released back. The latter condenses and it is collected from a third vacuum chamber (CD tank). Finally, all

the chambers are isolated, and the machine is cooled down in preparation for the next cycle (pre-cooling phase). The adsorption and desorption phases are represented in figure 5.19.

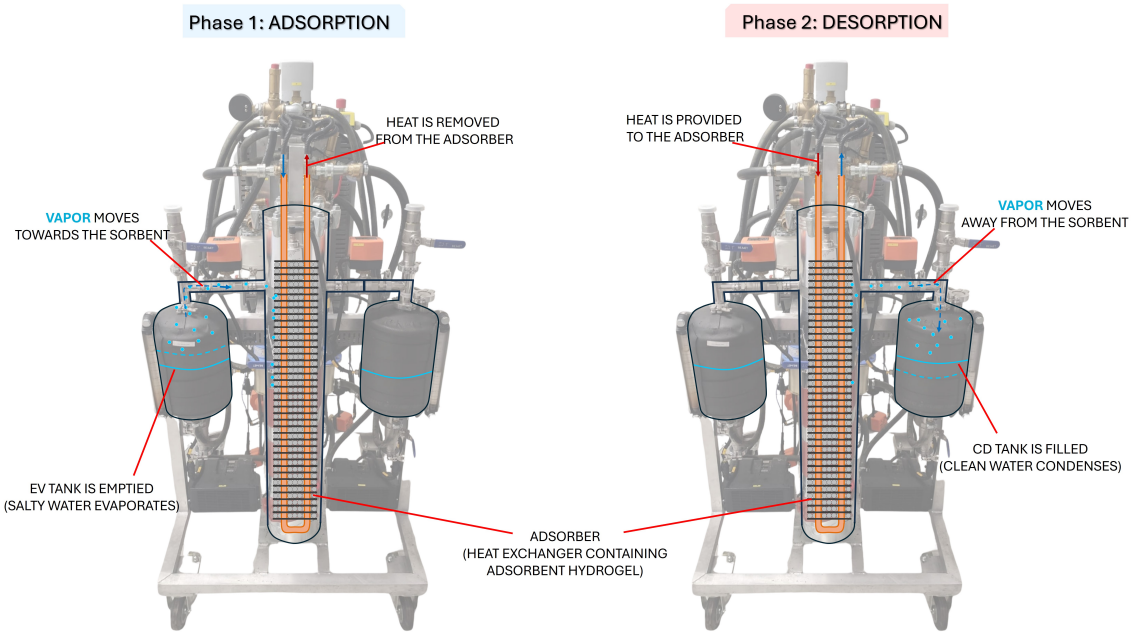

Fig. 5.19 Desalination unit principle, original design (not used). Phase 1: Adsorption. Evaporator (EV tank) and adsorber are connected, the vapor moves away from the salty water tank and fills the sorbent. Phase 2: Desorption. Condenser and adsorber are connected, the vapor moves away from the sorbent and fills the clean water tank (CD tank).

Even though the working principle shown above is correct, the engineered solution shows some limitations: we observed that the channel connecting the adsorber with the CD tank had a small section, not allowing water vapor to easily migrate between the two tanks, causing instead unwanted condensation on the internal walls of the adsorber. For this reason, we modified the initial prototype design by removing the CD tank and instead placing a pipe (CD pipe) at the bottom of the adsorber, to exploit gravity and collecting condensed water from there instead (see Fig. 5.20a,b). This is the final design used to run all the AD-related tests in this research. More details on this design change are provided in Appendix E.
The choice of a proper heat exchanger is crucial, in order for the sorbent material to efficiently exchange both thermal energy and vapor mass with the environment. For this research, we positioned the material in a finned coil heat exchanger and placed the latter in the adsorber chamber of the desalination unit (see Fig. 5.20c,d). Based on the result shown in figure 4.15, the distance of 3 mm between the exchanger fins is enough to host the CaAlg beads, even after the change in volume occurring during adsorption.

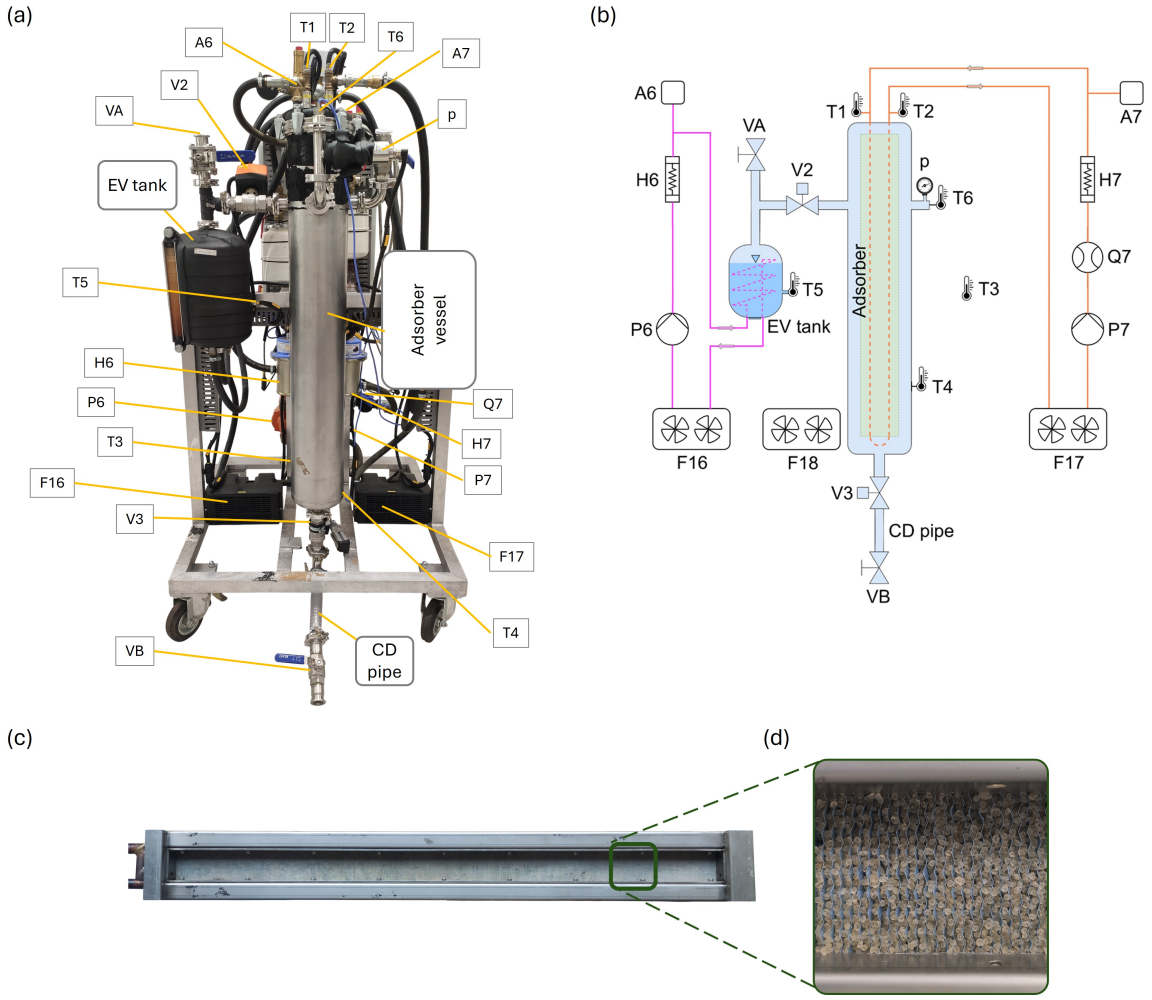

Fig. 5.20 Desalination unit description, final design. (a) Desalination unit. The Evaporator (EV) tank contains the feedwater; the adsorber vessel contains the heat exchanger filled with the sorbent material; the Condenser (CD) pipe collects the desalinated water. (b) Schematics of the desalination unit, showing the vacuum circuit (blue areas), the external pressurized circuit exchanging heat with the adsorber (orange), the external pressurized circuit exchanging heat with the EV tank (magenta). The unit is provided with temperature sensors (T1, T2, T3, T4, T5, T6), a pressure sensor (p), a flowmeter (Q7), four valves (V2, V3, VA, VB), two pumps (P6, P7), three dry-coolers (F16, F17, F18), two electric heaters (H6, H7), safety accessories (A6, A7). (c) Heat exchanger containing the sorbent material under test. (d) Detail of the heat exchanger, where the 3-mm large spaces among the fins are filled with CaAlg beads.

In Fig. 5.20b we show the schematics of the setup, including the vacuum circuit (blue areas), the external hydraulic circuits exchanging heat with the machine (orange and magenta loops), temperature sensors, pressure sensor, flowmeter and actuators. The prototype used to test CaAlg and silica-gel for desalination is a single-bed desalination unit from the German company Sorption Technologies GmbH (Fig. 5.20a, b). The main vacuum circuit of the machine (blue areas in Fig. 5.20b) consists of:

- the evaporator (EV tank), a stainless steel and vacuum-proof container of approximately 5 Liters, containing the water to be treated;

- the adsorber vessel (adsorber), a stainless steel and vacuum-proof cylinder (approximately 20 cm diameter and 100 cm length) which contains the heat exchanger filled (Fig. 5.20a) with the adsorbent material under test;
- the condenser (CD pipe), a vacuum-proof reinforced plastic pipe (approx. 400 mL) positioned at the bottom of the machine.

A temperature sensor T5 is placed in the vacuum circuit, submerged in the feedwater in the EV tank. In the adsorber, a pressure sensor is placed: this is measuring the absolute total pressure p around the sorbent, which, when no air or other gases are trapped in the machine, corresponds to the vapor pressure and can be used for further considerations (the machine was checked for leakages and no significant ones were found). The vacuum pressure during a test ranges between 10 mbar and 80 mbar, depending on the test conditions and on the cycle phase. A second circuit in the machine (orange loop on the right in Fig. 5.20b), consisting of an external pressurized hydraulic closed loop moving water at 1.5 bar, is used to transfer thermal energy to the sorbent during the desorption phase and extract energy from the sorbent during the adsorption phase. The copper pipes exchange heat with the material through the exchanger fins. Two temperature sensors T1 and T2 are placed in this circuit respectively at the inlet and outlet of the exchanger. A flowmeter Q7 is placed in the circuit: the flowrate was found to be constant during the tests and equal to 3.4 L/min (with uncertainty of ± 0.2 L/min). A pump P7 provides the necessary flowrate. An electric heater H7 and a small dry-cooler F17 are used to control the temperature of the water in the loop, in the range 25°C-80°C according to the needs. The electric heater H7 plays an important role, since it simulates the thermal load that, in a real application, is provided by a low-exergy thermal source (e.g., solar panels, low-temperature process waste heat, and so on). The implemented control logic activates the heater whenever the T1 temperature is more than 1°C below the set adsorber temperature. The dry-cooler F17 is used for heat dissipation into the environment; it runs whenever the T1 temperature is more than 1°C above the set adsorber temperature. Since there is no buffer tank, but only heater and dry-cooler to act on the water temperature, 15-20 minutes are necessary for the machine to work against the thermal inertia of the system (the adsorber vessel and exchanger together weight 23 kg in total, most of which is stainless steel AISI-316) and bring the adsorber temperature up to the desired value at the beginning of each working phase. A third circuit (the magenta hydraulic loop in Fig. 5.20b) is used to control the temperature of the feedwater in the EV tank. This loop circulates pressurized water at 1.5 bar and contains similar previous circuit: a pump P6, an electric heater H6, a dry-cooler F16 and the necessary safety accessories A6. Unlike the previous circuit, it is not provided with any temperature sensors and any flowmeter; nevertheless, the flow can be reasonably estimated to be the same as in the other circuit (3.4 L/min), given the similar geometry and since the pumps and all the other components are identical. The temperature T5 is used as feedback value for the temperature

control: H6 will heat up the circuit water until T5 is more than 1°C below the set value for the adsorption temperature and F16 will start when T5 is more than 1°C above the same value.

Component	Type	Scope	Description
T1	Sensor	Monitoring the water temperature at the inlet of the adsorber (external orange loop)	Class-A PT1000. Accuracy: ± 0.3°C.
T2	Sensor	Monitoring water temperature at the outlet of the adsorber (external orange loop)	Class-A PT1000. Accuracy: ± 0.3°C.
T3	Sensor	Monitoring ambient temperature.	Class-A PT1000. Accuracy: ± 0.3°C
T4	Sensor	Monitoring temperature of the external surface of the adsorber vessel.	Class-A PT1000. Accuracy: ± 0.3°C.
T5	Sensor	Monitoring water temperature in the EV tank (under vacuum).	Class-A PT1000. Accuracy: ± 0.3°C.
T6	Sensor	Monitoring vapor temperature in the adsorber (under vacuum); measurements not reliable due to influence of external temperature.	Class-A PT1000. Accuracy: ± 0.3°C.
p	Sensor	Monitoring vapor pressure in the adsorber (under vacuum).	JC627CA-3A1F3W3 absolute pressure sensor, 0-200 mbar. Accuracy: ±0.5 mbar.
Q7	Sensor	Monitoring water flow (external orange loop).	Hall-effect type flowmeter, with range 2-100 L/min, model YF-G1. Accuracy: ±5%.
V2	Actuator	Opening/closing the vapor passage between the EV water tank and the adsorber.	Electric valve 220VAC, internal diameter 20 mm. Opening/closing time: 20 s.
V3	Actuator	Opening/closing the vapor passage between the adsorber and the CD water pipe.	Electric valve 220VAC, internal diameter 20 mm. Opening/closing time: 20 s.
VA	Actuator	Allowing water replacement in the EV tank.	Manual ball valve, internal diameter 25 mm.
VB	Actuator	Allowing water collection from the CD pipe.	Manual ball valve, internal diameter 25 mm.
P6	Actuator	Circulating water in the EV (external magenta loop)	IBO OHI15-60/130 pump, peak consumption of 93 W.
H6	Actuator	Providing the power to heat up the EV water during evaporation (external magenta loop).	SKU800T electric heater, peak consumption of 1800 W.
F16	Actuator	Dissipating the heat to cool down the EV water (external magenta loop).	Dry-cooler, size 30x9x35 cm, air velocity of 4.0 m/s.
P7	Actuator	Circulating water in the adsorber (external orange loop).	IBO OHI15-60/130 pump, peak consumption of 93 W.
H7	Actuator	Providing the power to heat up the sorbent during desorption (external orange loop).	SKU800T electric heater, peak consumption of 1800 W.
F17	Actuator	Dissipating the heat to cool down the sorbent during adsorption (external orange loop).	Dry-cooler, size 30x9x35 cm, air velocity of 4.0 m/s.
F18	Actuator	Dissipating the heat of condensation, cooling down the adsorber vessel surface.	Table fan, electric consumption of 33 W. Air velocity at the vessel surface: 1.42 m/s.
A6	Actuator	Safety hydraulic components (external magenta loop).	Expansion vessel, safety valve calibrated at 3.0 bar, manometer, air vent valve, manual tap for filling and emptying of the circuit.
A7	Actuator	Safety hydraulic components (external orange loop).	Expansion vessel, safety valve calibrated at 3.0 bar, manometer, air vent valve, manual tap for filling and emptying of the circuit.

Table 5.8 Desalination unit components.

Finally, since the condensation process on the adsorber vessel's walls is exothermic and such heat must be dissipated, a further dry-cooler F18 has been positioned next to the vessel: by blowing air at 1.42 m/s ± 0.24 m/s (average and standard deviation on 6 measurements at the vessel surface, taken with an anemometer Testo 410i 729), it helps in cooling the vessel walls. In order to monitor such temperature, a sensor T4 has been installed in contact with the vessel external surface, on the opposite side with respect to F18. A temperature sensor T3 is positioned at the centre of the machine frame, distant from pipes, heaters and fans, and used to measure the room air temperature. A further temperature sensor T6 is positioned in the adsorber, under vacuum, next to the pressure sensor, but its measurements were affected by external temperature due to its placement, so it was not included in the main analysis. Table 5.8 contains the complete list of sensors and actuators in the machine.

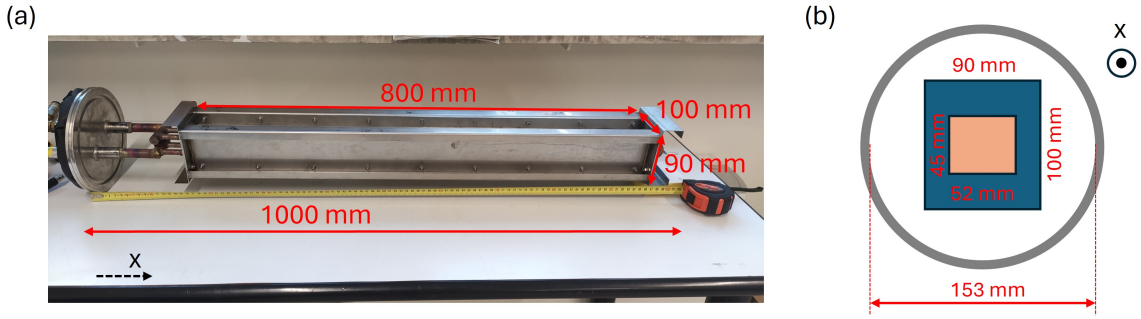

Fig. 5.21 Geometry of the adsorber heat exchanger. (a) A picture of the empty heat exchanger, with the main geometric features. (b) A simplified schematics of the cross-sectional view at half height, showing the vessel chamber (the grey circular ring) containing the rectangular heat exchanger after installation. The latter includes a stainless steel structure (blue) and a series of fins (orange).

The geometry of the adsorber is better explained in Fig. 5.21a,b. The heat exchanger is a structure with length 1000 mm, width of 90 mm and depth of 100 mm (these include the stainless steel supporting structure). The finned portion alone, containing the sorbent, is a parallelepiped with length 800 mm, width of 45 mm and depth of 52 mm, approximately. The fins are in aluminum, and their spacing is 3 mm, placed along the length of the parallelepiped. The pipes distributing the fluid are made of copper. A fine mesh is used to cover two of the four exchanger sides and keep the material inside (see also Fig. 5.22). Assuming that 10% of the volume is occupied by the fins, the space left for the sorbent is approximately 1.68 liters. Assuming a sphere packing factor of 30%[7] and a material density of 2000 kg/m^3, we can expect that at most 1 kg of sorbent can fit in the exchanger.
On the other hand, the adsorber vessel is a stainless steel cylindrical enclosure ("adsorber vessel" in Fig. 5.20a), with internal diameter 153 mm and length of 1000 mm. The cross-sectional view in Fig. 5.21b shows that a large gap is comprised between the exchanger and the vessel, for a void fraction of about 87%, if calculated with respect to the internal exchanger

[7]Since the fins distance is larger but still comparable with the beads diameter, most of the volume is not used, and we are distant from the theoretical 60-80% we expect from spheres packing in a large container.

(i.e., the volume hosting the sorbent). A better design may use two coaxial cylinders or two parallelepipeds, in order to reduce the void volume and promote vapor compression and condensation, as well as to decrease the thermal mass and the material cost and weight.

Experiments

Each experimental test consists of the repetition of 3-6 consecutive cycles at fixed conditions. Each cycle consists of three sequential phases:

1. Adsorption phase: valve V2 is opened and valve V3 is closed, so that the feedwater in the EV tank evaporates, fills the EV tank and adsorber chamber, and it is adsorbed by the sorbent material; the exchanger is cooled down by the external circuit and the EV tank water is heated up by the other external circuit.
2. Desorption phase: valve V2 is closed and valve V3 is opened; the material is heated up by the external circuit, using the heater H7, and water condenses on the adsorber internal walls and falls by gravity into the CD pipe.
3. Pre-cooling phase: valves V2 and V3 are closed; the material is cooled down again in preparation for the adsorption phase of the successive cycle; during this time interval the CD pipe is emptied from the condensed water and vacuum is made again in this portion of circuit.

The parameters that can be controlled during a test are: T_{EV} (EV tank temperature during adsorption, with control feedback sensor T5), T_{Ads} (adsorber temperature during adsorption, with control feedback sensor T1), T_{Des} (adsorber temperature during desorption, with control feedback sensor T1), t_{Ads} (adsorption time, i.e. the duration of the adsorption phase), t_{Des} (desorption time, i.e. the duration of the desorption phase), t_{PC} (pre-cooling time, i.e. the duration of the pre-cooling phase).
Before starting the actual experimental campaign, the material has been subjected to 50 cycles under vacuum within the machine, adsorbing and desorbing vapor in conditions analogous to the ones of the subsequent experimental campaign. This allowed the material to stabilize and lose any residual water from production, as well as to characterize the material aging over the cycles: after 20, 30 and 40 cycles, the machine was opened and a small sample of material was removed and stored for successive testing, to check how the material performance changed (see Chapter 4).
After the preliminary cycles, a full experimental campaign (tests 1->9 in Table 5.9) has been performed, using the aged material. In the campaign, T_{Ads} and T_{EV} were kept constant, both equal to 30°C; the adsorption time t_{Ads} was kept constant and equal to 30 minutes; t_{PC} was chosen always equal to 15 minutes (17 minutes for the tests at 75°C). On the other hand, the

desorption temperature T_{Des} and time t_{Des}, as well as the sorbent material, were changed in a one-factor-at-a-time approach to explore three different directions:

- change in desorption temperature T_{Des};
- change in desorption time t_{Des};
- change in sorbent.

This one-factor-at-a-time approach does not guarantee to fully characterize the machine, but provides an idea of the basic influence of such parameters. The following experiments were conducted with the AD prototype:

Test	1	2	3	4	5	6	7	8	9
Sorbent	CA	CA	CA	CA	CA	CA	SG	SG	SG
T_{Ads} (°C)	30	30	30	30	30	30	30	30	30
t_{Ads} (min)	30	30	30	30	30	30	30	30	30
T_{Des} (°C)	60	45	75	60	60	60	60	45	75
t_{Des} (min)	120	120	120	60	45	30	120	120	120

Table 5.9 Experimental campaign on CaAlg (CA) and mesoporous silica-gel (SG). The testing conditions are reported in the first three rows, followed by KPIs such as specific water production per cycle (SCWP), per day (SDWP) and the energy cost per Liter (STEC). Volumes (mL, m^3, L) refer to the amount of condensed water; masses (kg, ton) refer to the amount of dry sorbent; energies (kWh) refer to the positive thermal energy entering the system during desorption.

A preliminary start-up procedure is carried out every time the material is replaced (before test 1 and before test 7) requiring the following steps:

1. release the vacuum from the machine;
2. remove the exchanger from the adsorber vessel;
3. unscrew a protection mesh preventing the material from leaving the space between the fins (Fig. 5.22);
4. remove the previous material;
5. fill with the new material;
6. screw the protection mesh in place again;
7. insert the exchanger in place;
8. heat up the adsorber to 75°C using the external orange circuit;

9. restore vacuum in the chamber (a 250W double-stage vacuum pump has been used for the purpose).

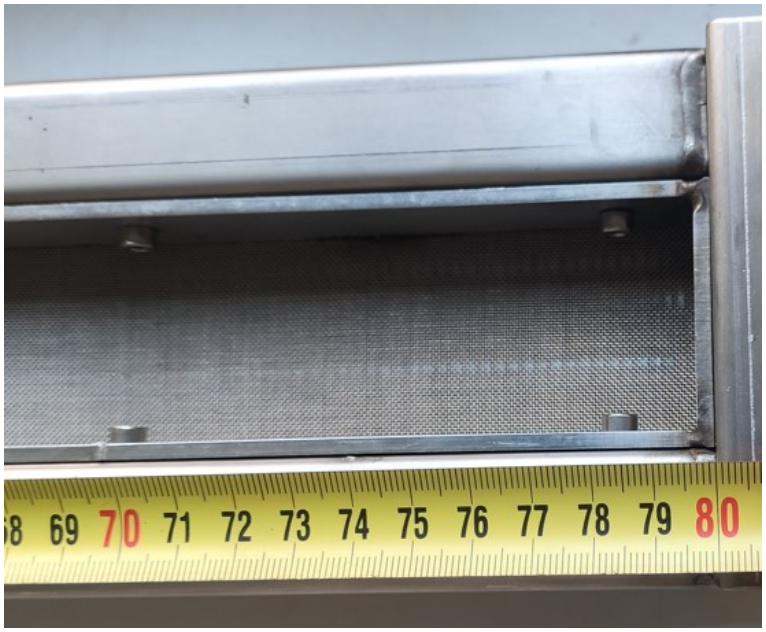

Fig. 5.22 Detail of the fine mesh used to cover the exchanger sides, keeping the material inside. A ruler (in cm) is placed for reference.

At the end of the procedure, after the adsorber cools down to environmental temperature, the pressure sensor measures 0.5 mbar of residual gas (air + vapor) in the chamber. The first 2-3 cycles run after the machine is opened are not considered in the experimental campaign, since the results would be affected by a vacuum level which is not reachable again during the normal operation of the machine.

Then, per each test, the normal experimental procedure is here described:

a. the water level in the EV tank is restored (approximately 4.5 L at the beginning of all tests);

b. the vacuum pump is powered 10 minutes to remove any residual air in the EV tank before starting the test;

c. the testing parameters are adjusted according to Table 1;

d. the external circuits are powered and the temperatures of both EV tank and adsorber are brought to 30°C, in preparation for the adsorption phase of the first cycle;

e. the first cycle starts and phases 1 to 3 run in sequence;

f. during phase 3, the condensed water is collected from the CD pipe and weighted on a KERN PCB 6000-1 scale (accuracy of 0.1 g);

g. the vacuum pump is connected to the CD pipe (valve VB) and it is powered for 1 minute to remove the air entering the CD pipe during the water collection and 1 further minute with V3 open to remove any residual vapor in the chamber [8];

h. points e to g repeat for the successive cycles of the day.

All the tests started in the morning around 9:00 a.m. CET and have taken place during the month of March 2025, trying to minimize the influence of seasonal variations in the room temperature.

Data analysis

Starting from vapor pressure, we evaluated saturation temperature T_{sat} using Antoine equation (eq. 2.6).
Starting from the test results, we evaluated two performance indicators. The first one is Specific Daily Water Production (SDWP), a KPI indicating the amount of condensed water achievable in 24 hours of continuous operation and defined as in equation 3.11; the second one is Specific Thermal Energy Consumption (STEC), a KPI indicating the amount of positive thermal energy used to condensate one Liter of water and defined as in equation 3.17.
The thermal power exchanged with the heat exchanger containing the sorbent was evaluated as follows:

$$P = \rho \cdot Q \cdot c_p \cdot (T_1 - T_2) \tag{5.10}$$

being the variable $\rho = 1000\ kg/m^3$ the density of the water in the external circuit, $c_p = 4186\ J/(kg \cdot K)$ its specific heat and $Q = 3.4\ L/min$ the volumetric flowrate in the external circuit. In the plot in the results section, the original data has been smoothed with a moving average. Unfortunately, the uncertainties in the temperature measurements translate in high uncertainties in the energy calculations. Even by assuming ρ and c_p to be exact, and taking into account only the uncertainty on Q ($\pm 0.2\ L/min$) and temperatures T_1 and T_2 (± 0.27°C

[8] The step of opening valve V3 for one further minute with the vacuum pump on was introduced when we noticed that the desalination unit offers a limitation in the vapor mobility due to the high pressure drops introduced by the portion of circuit between the EV tank and the adsorber (including valve V2). The small diameter of the connection makes the vapor movement difficult and, if the pressure close to the inlet of the adsorber chamber is high, there might be no vapor passage or even backflow from the adsorber chamber to the EV tank. In principle this step would not be necessary, since the adsorbent material itself is already able to reduce the pressure in the chamber below the saturation pressure in the EV tank, but it was included as a standard step to have repeatability among cycles. The same was included for all tests and all cycles, both for CaAlg and mesoporous silica-gel, to allow a fair comparison. The work introduced in the machine by powering the vacuum pump during the cycle (approximately 4 Wh) is negligible with respect to the thermal energy exchanged with the material (100÷300 Wh) and comparable with the electronic consumptions of the microcontroller during the cycle (approximately 5 Wh).

for class-A PT1000s at 60°C), here is how the uncertainties propagate to P:

$$\left(\frac{\Delta P}{P}\right) = \sqrt{\left(\frac{0.2\ L/min}{Q}\right)^2 + \left[\frac{\sqrt{(0.27\ °C)^2 + (0.27\ °C)^2}}{T_1 - T_2}\right]^2} \tag{5.11}$$

For instance, in the case of a representative cycle from the first test of the campaign (test 1), 20 minutes after the desorption phase starts, it was measured: T1=59.5°C, T2=58.7°C,Q=3.4 L/min, from which: $P = 189\ W\ \pm\ 91\ W$. A relative uncertainty of 48% (which drops down to 38% during adsorption, due the lower uncertainty of $\pm 0.21°C$ at 30°C for class-A PT1000s) makes the evaluated power unreliable for quantitative considerations.
The same high uncertainty propagates to the calculation of the Specific Thermal Energy Consumption: $STEC = \frac{E_{hot}}{V_w} = \frac{\bar{P} \cdot t_{cycle}}{V_w}$, where $\bar{P}$ is the "hot" power during the test averaged over time, V_w is the volume of condensed water and t_{cycle} is the total cycle time (adsorption plus desorption and pre-cooling phases times). Assuming negligible uncertainty on V_w (the scale used to measure the collected water has an accuracy of 0.1 g, while the volume V_w is in the order of $10^2\ mL$), and since t_{cycle} is set and exact by definition, the relative uncertainty of STEC coincides with the one of $\bar{P}$. If, for simplicity, we assume $\frac{\Delta \bar{P}}{\bar{P}} \approx 48\%$ as above, then we have $\frac{\Delta STEC}{STEC} \approx 48\%$. For this reason, quantitative considerations based on STEC have limited validity.

In order to evaluate the theoretically optimal cycle times, we used model LDFDw and simulated a full day of cycling of CaAlg (Fig. 5.23a). As for the diffusivity at 30°C (which was used to simulate adsorption), the experimental curves obtained with the ProUmid analyser were best-fitted (Chapter 4) and the resulting expression $D = a + b \cdot w$ is used, with $a = 4.4399 \cdot 10^{-12}\ m^2/s$ and $b = -2.2985 \cdot 10^{-12}\ m^2/s$. For the diffusivity at 60°C (which was used to simulate desorption), since no experimental data was available, it was assumed $D_{60°C} = 2 \cdot D_{30°C}$, following the results obtained in Chapter 4.
As for the equilibrium values to run the models: for adsorption at 30°C it was used $w_{Ads,eq} = 1.12\ g/g$ (that is the value suggested by the isotherms before the offsetting procedure, see Chapter 4); for desorption, since no isotherm at 60°C was available, it was assumed $w_{Des,eq} = 0.00\ g/g$ (the implications of this assumption are discussed below). For the simulation, the adsorption time and temperature are fixed at 30 min and 30°C respectively, while the desorption temperature is fixed at 60°C, to replicate the conditions in the desalination unit. The desorption time is chosen among 10 min, 30 min and 120 min, and the evolution of the uptake in the material along multiple successive cycles over the day is simulated.
The red curve in Fig. 5.23a refers to the shortest simulated desorption time, 10 min: after some initial cycles (the amount of which depends on the initial state of charge of the material, here assumed to be 0.0 g/g), the uptake oscillations stabilize in the range 0.6404-0.7026 g/g. Such values are compatible with the chosen adsorption and desorption times, in such a way

that at the end of a full adsorption-desorption cycle the uptake is again the same as it was at the beginning of the cycle. In this case, the cycle time (excluding pre-cooling) equals to 40 minutes (30 min adsorption + 10 min desorption), and the theoretical SDWP can be evaluated as: $SDWP = \frac{0.7026\ mL/g - 0.6404\ mL/g}{40\ min\ /\ 60\ min} \cdot 24\ h = 2.24\ mL/day/g\ = 2.24\ m^3/day/tons.$
The yellow curve in Fig. 5.23a refers to an intermediate desorption time, 30 min: here the cycle time is longer (1 h), but even greater is the difference in the two uptakes between which the material charge oscillates, from which a SDWP of 3.06 $m^3/day/tons$ (larger than in the previous case) follows.

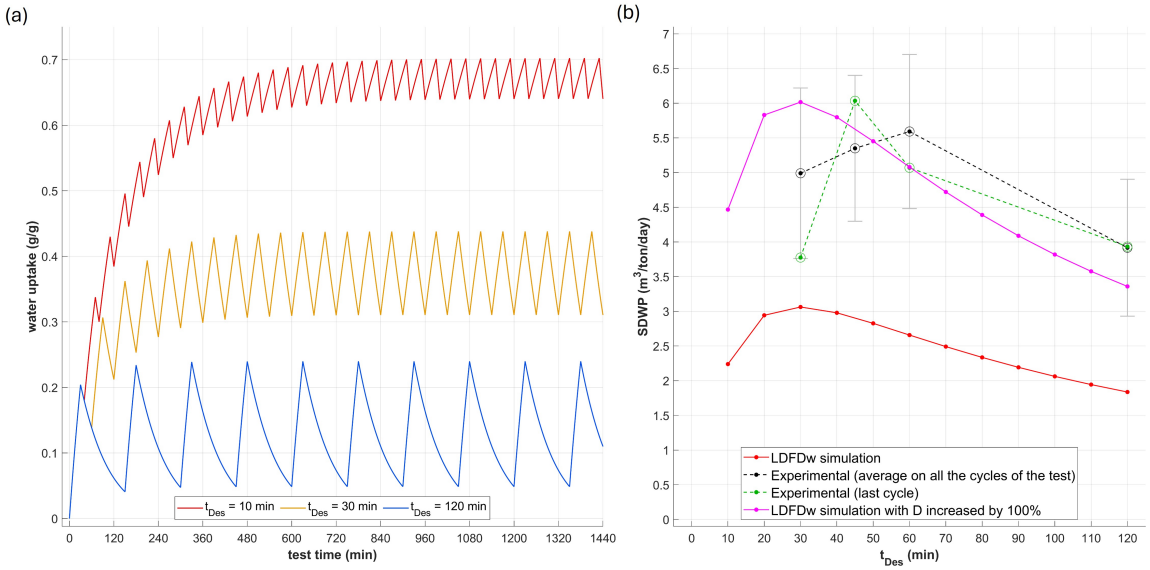

Fig. 5.23 Desorption time optimization. (a) Numerical simulation of 24 hours of repetitive cycling with CaAlg beads, at different desorption times but fixed adsorption time, adsorption temperature and desorption temperature; the model LDFDw was used. (b) Simulated vs experimental SDWP as a function of desorption time t_{Des}.

The blue curve in Fig. 5.23a refers to the case where the desorption time is 2 h long: in this case, the SDWP decreases down to 1.84 $m^3/day/tons$, because the benefit of greater water production is not compensated by the increase of length of the cycle.
The procedure can be repeated for a denser range of desorption times, and an optimal SDWP as a function of desorption time can be found. This is shown here for desorption times ranging from 10 to 120 minutes in 10-min steps in the red curve on Fig. 5.23b: it is evident that a desorption time of 30 minutes is a good compromise and allows to maximize the SDWP, at least theoretically. Note that, repeating the same simulation using the standard LDF model instead of the modified LDFDw, the maximum would be slightly shifted down (SDWP= 2.36 $m^3/day/ton$) and to the left ($t_{Des} = 21\ min$), but the results and considerations are qualitatively the same. Interestingly, the latter result with LDF model can also be deduced without numerical simulation: under proper assumptions, the problem of optimizing cycle times can be solved analytically, as we propose in Appendix F.
All the simulations have been carried out with a fixed adsorption time of 30 min (the same as

in the experimental campaign); in case the adsorption time increases, the maximum is shifted to the right (higher adsorption times require higher desorption times in order to restore the same water content in the material).
Exploiting the available experimental data, it is possible to plot in comparison the actual SDWP of the CaAlg when used in the desalination unit. This is shown in Fig. 5.23b in dotted lines, both considering the average on all the cycles of the test (black line, with bars for $\pm$ one standard deviation) and considering only the last cycle (green line); the latter choice might result in a more reliable approximation, since the initial cycles might be affected by the starting daily uptake. The two curves are slightly different, but in both cases there is a maximum for a desorption time around 45-60 minutes. Two considerations follow:

- the experimental optimal SDWP is approximately 100% larger than the theoretical one. This can be in part explained by the fact that the assumed value $w_{Des,eq}$ for desorption might be overestimated (details are provided below), and in part by the fact that the diffusivities used in the model are obtained in conditions different from the experiments: they are derived from the tests with the ProUmid analyser, working under positive pressure. In the real desalination unit, though, the adsorption and desorption processes happen under vacuum: this might contribute to increase the effective diffusivity, since the water molecules in the chamber are not hindered by gas molecules in reaching or leaving the sorbent. By repeating the simulation assuming 100% larger diffusivities, the maximum SDWP increases up to the value of 6.02 $m^3/day/ton$ (magenta line in Fig. 5.23b), similar to the experimental one. The latter curve is reported in the results section.

- the desorption time at which the experimental optimal SDWP is found is larger, being the whole curve shifted to the right. This can be explained by the fact that in a real machine the material is not immediately brought to the ideal set conditions: the high thermal inertia of the system, as well as the difference existing in the heat exchanger between the feedback temperature T1 of the water in the pipes and the actual temperature of the material, suggest that the material desorbed at an effective temperature which was lower, in average, than the nominal one. Also, most probably the material temperature is not uniform in the exchanger, being greater around the centre of the fins where the copper pipes pass, and lower close to the exchanger sides.

An equilibrium value during desorption of $w_{Des,eq} = 0.00\ g/g$ is clearly not the actual value, but no information is available for the material sorption properties at 60°C. Nevertheless, it was simulated that a different value does not affect the shape of the result nor the qualitative discussion that followed. Indeed:

- by repeating the same simulation using a larger $w_{Des,eq}$, the maximum is still found at the same optimal desorption time, only lower (e.g., with $w_{Des,eq} = +\ 0.20\ g/g$, the maximum is at $t_{Des} = 30\ min$ and SDWP$= 2.30\ m^3/day/ton$);
- on the other hand, using a lower $w_{Des,eq}$, the maximum is still found at the same desorption time, only higher (e.g., with $w_{Des,eq} = -\ 0.20\ g/g$, the maximum is at $t_{Des} = 30\ min$ and SDWP$= 3.91\ m^3/day/ton$).

Water analysis

The main campaign above was conducted using demineralized water. After that, in order to test the ability of the hydrogel to work with a salty solution, some further cycles using salty water were performed after the main experimental campaign, with adsorption temperature of 30°C, adsorption time of 30 min, desorption temperature of 60°C and desorption time of 75 min[9]. To this end, a salty solution of water and NaCl at a concentration of 3.5% w/w (simulating sea water [144]) was prepared. The solution was positioned in the EV tank. The water level was not monitored cycle by cycle as for the main campaign, but part of the condensed water was collected and analysed, together with other water samples: one sample of distilled water, one of distilled water after stationing in the EV tank, one of salty "sea" water, one of condensed water starting from distilled water, one of condensed water starting from salty "sea" water, one of commercial water. The list of samples is reported in table 5.10:

Sample	Description
1	Distilled water
2	Distilled water after standing in the EV tank
3	"seawater"
4	Condensed water starting from sample n.2
5	Condensed water starting from sample n.3
6	Reference commercial water LEVISSIMA naturale

Table 5.10 List of analysed water samples.

For each collected sample the following experimental measurements were performed:

- Conductivity ($\mu S/cm$). Sensor RS PRO 1410 was used, with accuracy of 1 $\mu S/cm$.
- Residual solid content (mg/L). Sensor RS PRO 1410 was used, with resolution of 1 mg/L (the tool uses an estimated default conversion formula to convert conductivity into salt concentration). In the case of samples 3 and 5, a thermal-balance KERN

[9]The behaviour of the machine was analogous to the other experiments using demineralized water; see test "10" in Appendix D.

DBS60-3 (accuracy 0.001 g) was used to evaporate the solutions at 180°C for 5 hours and confirm the estimation (Fig. 5.24).

- PH. The sensor DrMeter-PH838 (accuracy of 0.05 PH) was used.
- Presence of organic compounds. A TOC (Total Organic Carbon) analysis was performed, from which Total Carbon and Inorganic Carbon were measured and the TOC was evaluated. Analyses were performed by the DIATI department at Polito, with total organic carbon (TOC) analyser LCSH FA (Shimadzu, Italy; catalytic oxidation on Pt at 680°C).
- Presence of copper (Cu). Analyses were performed by the DIATI department at Polito, with ICPMS (inductively coupled plasma-mass spectrometry) by ThermoScientific (model iCAP RQ), using kinetic energy discrimination (KED).

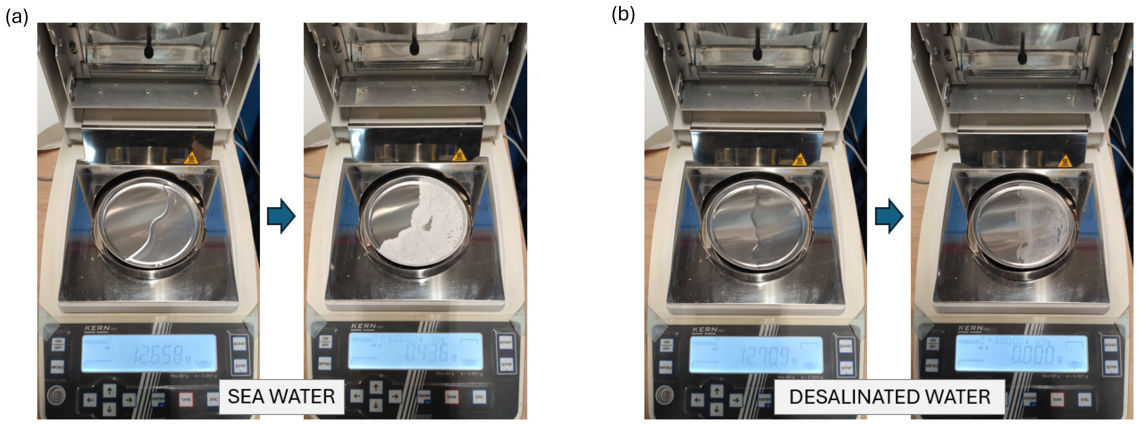

Fig. 5.24 Residual solid content evaluation. (a) After evaporating 12.658 g of salty water from sample 3 at 180°C for 5 hours, the residual solid content is 0.436 g, thus confirming an initial 'sea water' salinity of 3.4-3.5% w/w. (b) After evaporating 12.709 g of desalinated water from sample 5 at 180°C for 5 hours, the residual solid content is below the scale resolution.

5.4 Conclusions

We reported in this chapter the results achieved testing CaAlg in prototypal AWH and AD units. Here below the main points:

- First, we produced a coating of CaAlg on the surface of a finned heat exchanger and placed it in a AWH prototype. This was tested in lab environment as well as in arid climates, **achieving a water production of up to 1.19 $\mathbf{m^3/day/ton}$**. This demonstrated the feasibility of CaAlg for water production in an open-cycle application and medium-low RH levels. When compared with other existing plants, our system is among the best despite the relatively low driving temperature.

- Medium-term stability was assessed, demonstrating a **stable cycle and water production over 2.5 days of consecutive testing** with the AWH unit. The produced water had a conductivity of 103 $\mu S/cm$, below the limits suggested by both EU regulation and WHO.

- We produced a batch of CaAlg beads and tested it under vacuum, in real working conditions, in a AD prototype. We achieved a water transfer from an evaporator containing salty water to a condenser, reaching **SDWP of up to 6.04 $m^3/day/ton$ under optimized cycling times** (30 min adsorption at 30°C, 45 min desorption at 60°C). When compared with other existing plants, this value is among the largest in the temperature range below 65°C. The estimated Specific Thermal Energy Consumption (STEC) of 0.97 kWh/L is among the lowest throughout the analysed plants, indicating a high thermal efficiency despite the small-scale of the unit (386 g of sorbent).

- Medium-term stability was assessed, demonstrating a **stable cycle and water production over 6 consecutive cycles under vacuum**. The water condensed by the machine using salty feedwater has been analysed, and **a desalination effect was indeed achieved, with a salt rejection rate of over 99.2%**.

- We achieved a sub-optimal water production **even with a desorption temperature as low as 45°C** (SDWP of 2.2 m^3/day/ton): this makes the integration of adsorption-based solutions using CaAlg with ultralow-grade waste heat sources an interesting option. We proposed possible scaling-up for integration with the power sector and data-centre cooling.

Chapter 6

Design and testing of a medium-scale adsorption machine

6.1 Introduction

In Chapter 4 we have characterized CaAlg compositions in comparison, and selected the ones with the best performances in terms of equilibrium capacity and adsorption dynamics. Then, in Chapter 5 we have tested the chosen compositions in real adsorption prototypes for the production of fresh water, both starting from humid air and starting from salty feedwater, assessing the material potential when subjected to realistic cycling conditions. CaAlg outperformed most of the competitors, despite the small-scale of the prototypes preventing from the full exploitation of its potential.

In this chapter, we present a medium-scale machine (75 kg of sorbent) from Sorption Technologies, using a silica-gel composite, to prove how machine performance and efficiency increase with the scale of the plant. The author was involved in the design and testing of the unit, based on the improvements suggested by the performed campaigns with the small-scale units.

In the first part of this chapter we present the main results obtained with the medium-scale machine, commenting the thermodynamic variables in an exemplificative cycle, the cycle stability over time, the chilling capacity, the water production achieved. Then, we extrapolate the results to the use of CaAlg as sorbent and discuss the necessary adjustments to use the machine for water desalination. We also mention the economic scalability of using CaAlg instead of a $CaCl_2$/silica-gel composite.

In the second part of this chapter, we discuss the used methodology. First, the AC unit is described, including the 3D-design and the data-acquisition system. Second, the testing rig used to run the experiments on the AC unit is described, including its design and assembling, and the description of the experimental campaign with the $CaCl_2$/silica-gel composite.

6.2 Main results

6.2.1 Adsorption-based unit using a CaCl2/silica-gel composite

We present here the results achieved with a two-modules adsorption machine produced by Sorption Technology, as part of EU project HyperGryd, in the context of EU H2020 program (Grant Agreement No. 101036656) [145]. The machine is designed as an Energy Storage solution to be integrated within a larger infrastructure, comprising: thermal energy storage solutions, electric energy storage and transport, solar collectors, hydropower and windpower plants, a district heating network and biomass boilers (Fig. 6.1a). The HyperGryd project scope is to share a common database and platform that collects data from all the plants (including the adsorption-based unit), use them for simulation and optimize the overall system operation according to the consumer requirements. More details about the project are found at https://hypergryd.eu/ (last visited on 26/10/2025). Further discussion on the performance of the produced machine has been published in [37].
The machine was designed, assembled and tested in company spaces at Mönchengladbach, Germany (Fig. 6.1b). The schematics of the machine is provided in Fig. 6.1c. Details on the machine design and testing are provided in the Methods section.
Note that, even though the machine is used as a thermal energy storage solution, the working principle is the same as for adsorption chilling (AC) and water desalination (except for some engineering details discussed is 6.2.2), which are all parallel useful effect achieved during the normal operation of the machine.

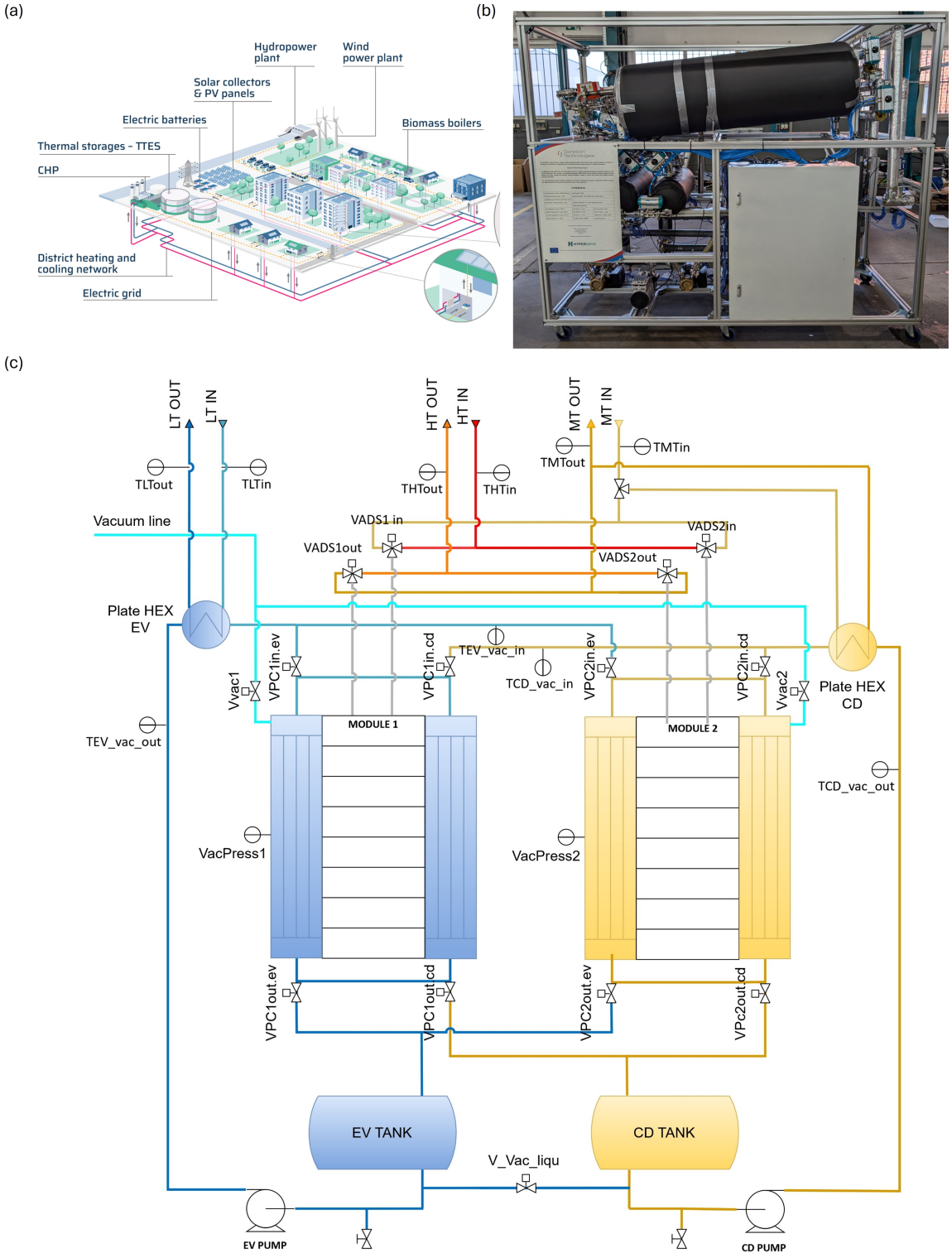

Fig. 6.1 HyperGryd concept: prototype picture and P&ID. (a) Concept of an integrated architecture for EU project HyperGryd (source: [145]). (b) Adsorption machine developed for the HyperGryd project. (c) P&ID of the machine.

We monitored the thermodynamical variables during the normal cycling of the AC unit (details in the Methods section). We show in Fig. 6.2 the detail of a 2-cycles test (test no. 9 in table 6.1):

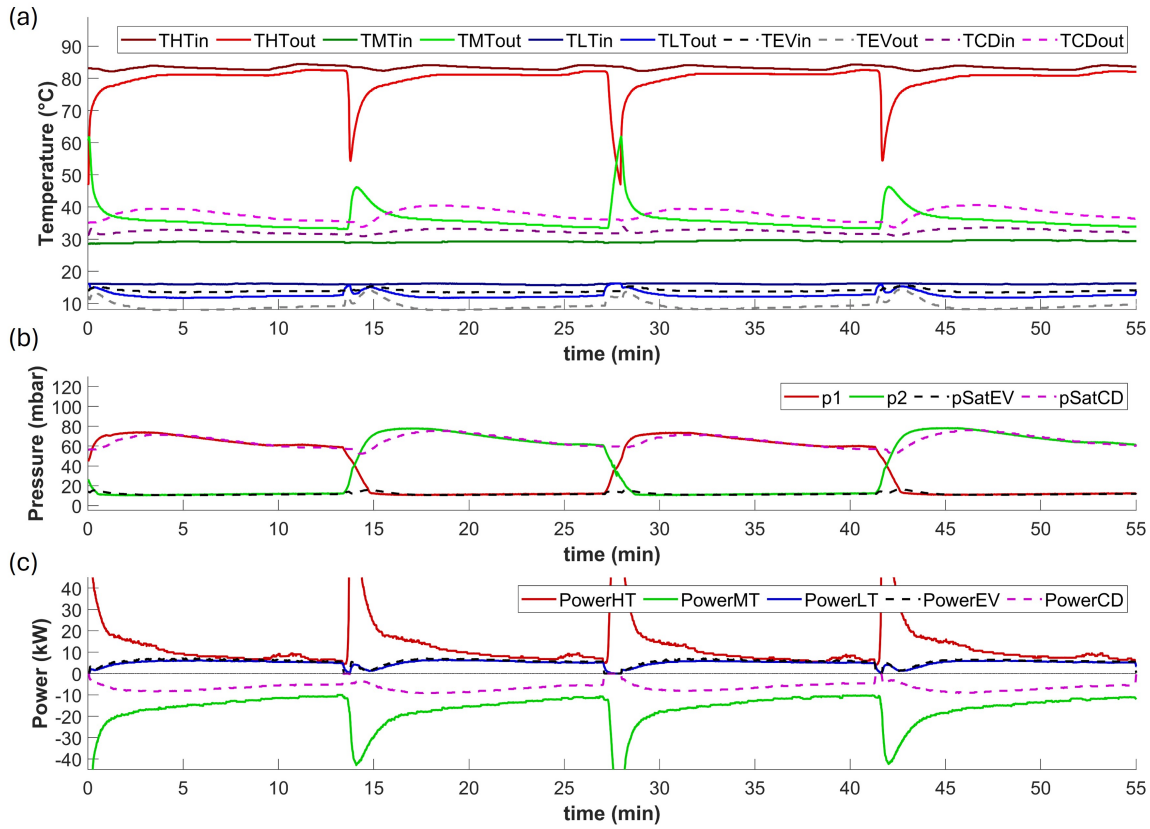

Fig. 6.2 Thermodynamic variables in the AC unit. (a) Temperatures in the AC unit during a representative test, including two complete adsorption-desorption cycles. The solid lines (THTin, THTout, TMTin, TMTout, TLTin, TLTout) show the inlet and outlet temperatures of the desorbing module, the dissipating loop and the chilling loop, respectively. The dotted lines (TEVin, TEVout, TCDin, TCDout) show the inlet and outlet temperatures of the refrigerant loops on the evaporator and condenser sides, respectively. (b) Vapor pressures p1 and p2 in modules 1 and 2, respectively, compared to saturation pressures evaluated at TEVin and TCDin. (c) Thermal power exchanged with the machine through the heating loop (HT), dissipating loop (MT) and chilling loop (LT), compared with the powers exchanged on the vacuum-side internal loops (evaporator and condenser sides).

Fig. 6.2 shows temperatures, pressures and thermal powers in the machine. We can identify two cycles and comment the working phases of the first cycle as an example:

1. Module 1 desorbing, module 2 adsorbing (time 0-13.5 min): during this phase, half of the sorbent (about 37.5 kg in module 1) is being heated up to 80°C (THT in), and the remaining half (about 37.5 kg in module 2) is cooled down to 30°C (TMTin). Due to a combination of thermal inertia, external water mixes and heat of adsorption/desorption, it takes some minutes for the modules to reach the target temperatures. The pressure in the first module (p1) increases with temperature, then starts decreasing over time

with condensation happening[1]; most interestingly, p1 matches the saturation pressure evaluated at the TCDin temperature, as expected during desorption. Analogously, the pressure p2 in the second module matches the saturation pressure on the evaporator side, as expected during adsorption. The HT loop power is positive (THTin>THTout, since we are providing heat to the sorbent), and decreasing over time, while the vapor desorbs from the material; viceversa, the MT loop power is negative (TMTin<TMTout, since we are extracting heat from the machine) and with absolute value decreasing over time, while the material saturates with vapor. The power peaks at the very start of the phase are due to partial mixing of HT and MT loops due to the valves transitioning. The chilling effect is observed in the LT loop power, which perfectly matches the evaporator loop power evaluated on the vacuum side.

2. Module 1 adsorbing, module 2 desorbing (time 13.5-27 min): during this phase, module 1 and 2 switch their role. The same considerations from the previous point apply, this time with p2 matching the saturation pressure in the condenser side and p1 matching the saturation pressure in the evaporator side.

The flow-rates (not plotted here) are constant during the test. In particular, indicating volumetric flow-rate with F, we have: $F_{EV} = 18\ L/min$, $F_{CD} = 18\ L/min$, $F_{HT} = 56\ L/min$, $F_{MT} = 37\ L/min$, $F_{LT} = 20\ L/min$.
In general, the process appears repeatable, except for a slight asymmetry between module 1 and module 2 (the exchanged powers are lower when module 2 is desorbing), maybe due to a slightly different amount of sorbent or a non perfectly symmetric construction. The slight oscillations in the THTin circuits are due to non-perfect control of the HT loop temperature in the testing rig (see Methods section).
After the initial minutes where the HT and MT flows mix and the thermal inertia of the machine is overcome, the machine enters a pseudo-steady state condition. In reality, the internal conditions are still changing, since adsorption and desorption are happening in the two modules, but from an energetic point of view these powers are comparable. Thus, if we consider a reference volume comprising the whole unit and excluding the external circuits (see the P&ID in Fig. 6.1c), we should have: $Q_{HT} + Q_{LT} + Q_{MT} = 0$. Indeed, if we consider time t=5 min, we have: $Q_{HT} = 9.34\ kW$, $Q_{LT} = 5.99\ kW$, $Q_{MT} = -15.2\ kW$, and $Q_{HT} + Q_{LT} + Q_{MT} = 0.13\ kW$, which is a fairly good validation of the first principle of thermodynamics. Of course, the energy balance is not perfect, due to effects including dissipation with the environment and introduction of electrical power $P_{Aux} \approx 0.47\ kW$. The thermal COP is $COP = \frac{Q_{LT}}{Q_{HT}} = 0.37 = 37\%$, and the EER is $EER = \frac{Q_{LT}}{P_{Aux}} = 9.7$.
We didn't monitor the water production directly, but we can estimate (see Methods) it to be about 17.3 Liters of water during the whole test. From that, we estimate a SDWP of $SDWP = \frac{17.3\ kg}{75\ kg \cdot (55\ min/1440\ min/day)} \simeq 6\ m^3/day/ton$.

[1]Note that this is the same effect we have observed with the tests in the desalination unit, see Appendix D.

The thermodynamic behaviour of all other tests is shown in Appendix D, while the main KPIs are discussed in the next section.

Machine performance

We report in this section the complete list of tests we performed with the AC prototype, including the results on EER, COP, first principle verification (FPV), SDWP, SCP (see Methods section).

Test	1	2	3	4	5	6	7	8	9	10	11
TMTin (°C)	30	30	35	35	35	30	30	30	30	30	30
THTin (°C)	70	70	80	80	80	80	80	80	80	80	80
TLTin (°C)	20	25	12	16	20	12	12	16	16	20	20
phase time (min)	15	15	13.5	13.5	13.5	13.5	13.5	13.5	13.5	13.5	13.5
T_{EV} (°C)	18.6	20.6	17.5	15.2	10.2	13.3	16.4	8.96	8.62	11.9	11.6
T_{CD} (°C)	35.7	37.1	38.0	38.5	38.8	39.6	40.4	34.6	33.1	35.4	35.1
n. of cycles	1	1	3	2	3	3	2	3	2	3	4
EER	3.97	9.00	3.47	5.87	8.15	6.06	7.14	8.87	9.70	11.3	11.3
COP	0.24	0.43	0.18	0.29	0.34	0.26	0.29	0.35	0.37	0.42	0.40
FPV (%)	118	112	113	107	109	111	109	112	111	109	109
SDWP (m^3/day/ton)	4.11	5.15	4.57	4.88	5.55	5.56	5.75	5.70	6.04	6.24	6.60
SCP (W/kg)	29.7	66.7	43.9	66.2	24.3	42.5	56.5	43.4	50.8	60.9	66.6

Table 6.1 Results of the experimental campaign with the $CaCl_2$/silica-gel in the AC device. The testing conditions are reported in the first seven rows, followed by KPIs such as EER, COP, FPV, SDWP, SCP.

In figure 6.3a, we compare EER and COP for tests 6, 8 and 10, which were performed under the same conditions and for the same number of cycles. We can observe that both efficiencies increase with the LT temperature, as expected in a cooling device (the lower the temperature to keep, the more difficult it is for the device to operate). Also, we observe that the COP reaches values as high as 0.42. In general, the COP of most of the performed tests is higher than what we observed with the small desalination device working at similar temperatures, which reached a value of 0.27 under optimized conditions. This result supports the hypothesis that a larger device has, in general, lower inefficiencies.
The FPV parameter is close to 100%, deviating at most by 18%, confirming the reliability of temperature and flow measurements, and thus the energy balances.
In Fig. 6.3b (solid line), we show that the estimated SDWP increases with the desorption temperature, under fixed conditions (tests 1 and 10), as expected. We achieved values higher than 6 $m^3/day/ton$ at a temperature of 80°C, which is in the average, if compared with the map of desalination devices (Fig. 5.9); nevertheless, as clarified in the Methods section, this value is only approximated, and probably overestimated by 20-30%.

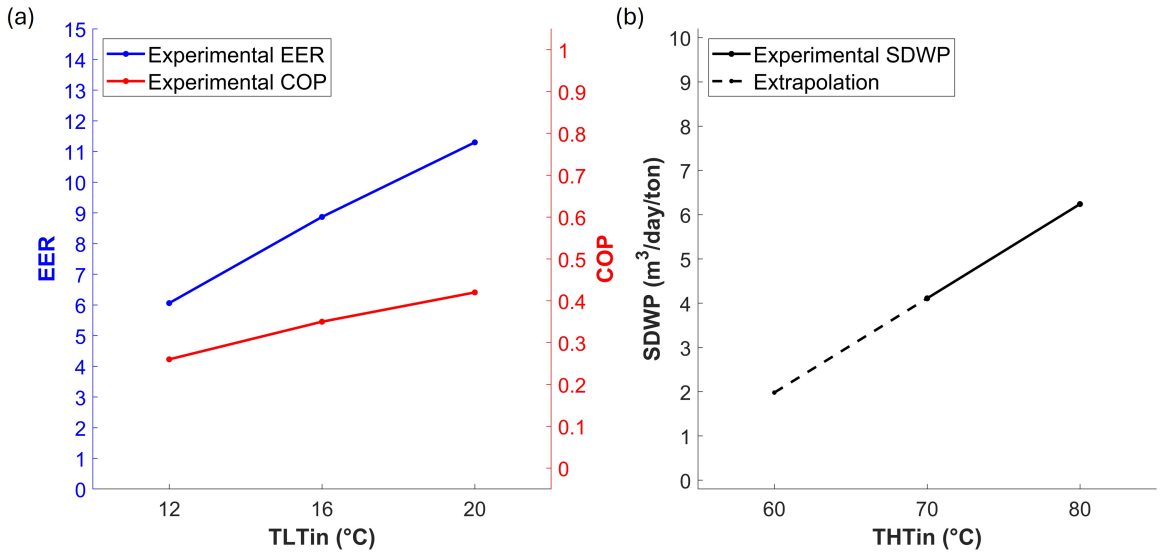

Fig. 6.3 KPIs in the AC campaign. (a) EER and COP as a function of TLTin. (b) SDWP as a function of THTin.

6.2.2 Extrapolation to desalination using CaAlg as sorbent and economic considerations

A SDWP of 6 $m^3/day/ton$ is similar to the best results achieved with CaAlg in the small desalination unit in Chapter 5. Nevertheless, for this analysis we used a much more efficient device (we achieved a COP up to 56% larger) and we worked at higher temperatures (80°C instead of 60°C). This suggests that, replacing the $CaCl_2$/silica-gel composite with CaAlg would further increase the water production. Unfortunately, we cannot attempt this in the time of this research because we would need to produce an amount of sorbent that is far beyond the capability of the built production setup. For this reason, in this section we are going to simulate what would be the expected increase in performance from such a change, and what would be needed to achieve such production.

The machine presented in this chapter is not immediately suitable to work with salty feedwater, since the internal surface of the modules would be wetted by both salty water (during adsorption) and fresh water (during desorption), increasing contamination and decreasing the desalination effect. One way to convert the machine to work as a desalination device is to split each module in half adding a stainless steel separator: one portion only sees salty water, while one portion only sees fresh water. This would lower the exchange area (since only one phase changer is working at a time), but this can be compensated by replacing the refrigerant pumps with larger devices. In this section we will assume that the device has been adapted accordingly, since the costs would be the same no matter the sorbent used.

Scaling up the production process

We can linearly extrapolate the results to estimate what would be the SDWP at a temperature of 60°C (Fig. 6.3b, dotted line) [2], getting a value of 1.98 $m^3/day/ton$. Compared with CaAlg working at the same temperature ($SDWP = 6.04\ m^3/day/ton$ between 60°C and 30°C), this is about three times lower, meaning that we would require about one third of the sorbent -or 25 kg- to achieve the same water production.

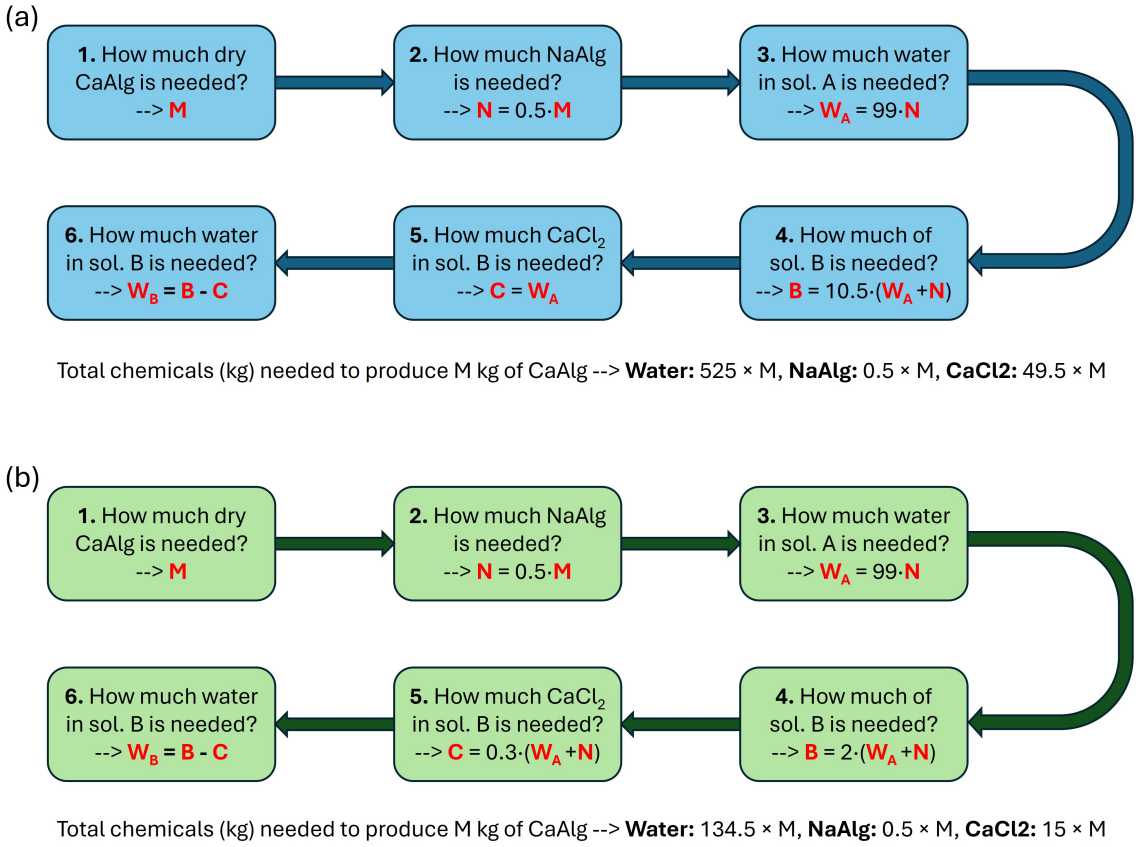

Fig. 6.4 Design algorithms for scaling up CaAlg production. (a) First design approach to produce M kg of CaAlg, where enough salty solution is produced so that concentration does not change significantly during the production. (b) Second design approach to produce M kg of CaAlg, where concentration is kept constant by continuously adding salt during the production process.

Based on the production process described in Chapter 4, we know that, in order to produce 5 kg of dry CaAlg, we need about 2.5 kg of NaAlg powder. Since we want a NaAlg concentration of 1% in the NaAlg-water solution, we need 247.5 Liters of water, for a total of 250 kg of solution A. Since we want solution B not to change significantly its salt concentration over time, we want a solution B with a volume about ten times larger, ideally made of 250 kg of $CaCl_2$ and 2375 L of water. This way, assuming that the decrease in calcium ions does not

[2] This is clearly an approximation, but comparing the results in Chapter 5 (Fig. 5.8) we have seen that the change of productivity with temperature is not far from being linear, at least in small temperature intervals.

affect sensibly the salt concentration, the latter decreases from 10.5% (at the beginning of the process) to 9.5% (after total dilution of solution A into solution B). The design procedure just described is schematized in Fig. 6.4a.
Nevertheless, this approach is not convenient, since it requires large basins and big amounts of water and salt. Instead, we can use a much lower volume of solution B and artificially keep salt concentration constant, by adding small amounts of $CaCl_2$ regularly, during the process. For example, assume the second solution to be double the volume of sol. A, i.e. to use 50 kg of $CaCl_2$ and 450 L of water. After the first 12.5 kg of solution A are mixed with solution B, we would have a concentration of $50/(500+12.5) = 9.8\%$, and we can immediately compensate by adding further 1.25 kg of $CaCl_2$; this brings salt concentration to 51.25/512.5=10% again. We can repeat the process all over again, until all the 250 kg of solution A has mixed into solution B, that, at the end of the process, is about 750 kg in total, 75 kg of which are represented by $CaCl_2$. The design procedure just described is schematized in Fig. 6.4b.

Using the second approach, we can size the required containers to be about 250 L (to contain solution A) and 750 L (to contain solution B). Also, we can estimate the amount of chemicals needed to produce 5 g of dry CaAlg beads to be 2.5 kg of NaAlg and 75 kg of $CaCl_2$. Since we need a total of 25 kg, we can repeat the production process five times, for a total of 12.5 kg of NaAlg powder and 375 kg of $CaCl_2$. Also, we need approximately 3.4 m^3 of demineralized water.

Economic feasibility

The global cost of sodium alginate oscillated in the last years and, in 2024, the minimum registered price was 7.13 $/kg, or 6.58 €/kg [146]. In 2024, the cost of calcium chloride consolidated around 1.325 RMB/kg, or 0.16 €/kg [147]. For safety, we will assume current prices to be 20-25% larger, with NaAlg costing 7.90 €/kg and $CaCl_2$ costing 0.20 €/kg. The demineralized water has a negligible cost in comparison -about 1 euro per cubic meter-, so it will not be considered for this simplified analysis. Finally, in total, the raw materials needed to produce 25 kg of calcium alginate add up to:

$$Cost_{CaAlg,\ 25\ kg} = (7.90\ €/kg) \cdot 12.5\ kg_{NaAlg} + (0.20\ €/kg) \cdot 375\ kg_{CaCl_2} = €\ 173.75$$

or: $Cost_{CaAlg} = 6.95\ €/kg$. The costs distribution for raw materials is quite balanced, as shown in Fig. 6.5a. We can compare this result to the $CaCl_2$/silica-gel composite used above. According to [37], the price for 100 kg of finished product is € 500, meaning that the total amount of 75 kg (necessary to achieve an effect comparable with 25 kg of CaAlg) costs € 375, which is more than double with respect to CaAlg (Fig. 6.5b).

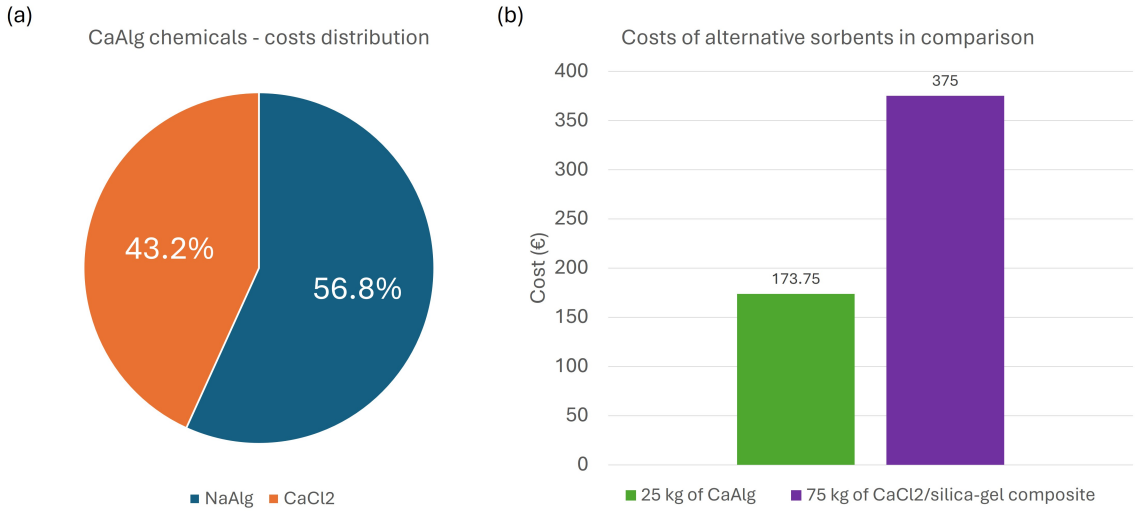

Fig. 6.5 Economic considerations of replacing sorbents with CaAlg. (a) Costs distribution of raw chemicals needed to produce CaAlg. (b) Comparison of costs if using CaAlg or an equivalent amount of $CaCl_2$/silica-gel in the machine described in this chapter.

As a conclusion, using CaAlg instead of $CaCl_2$/silica-gel in this specific application implies an overall resources saving of about 54%. Of course, this analysis was carried over under many assumptions, including:

- arbitrary SDWP extrapolation below 70°C in the case of the $CaCl_2$/silica-gel composite;
- cost of NaAlg only 20% higher than the global minimum[3];
- comparable manufacturing costs for CaAlg and $CaCl_2$/silica-gel composite (fixed costs for building up the production plants, maintenance, salaries, and so on).

On the other hand, there is a further point in favor of CaAlg which was not considered in the above analysis: using less material means needing smaller heat exchangers, with a significant save in resources. Tens of kg of stainless steel and copper can be avoided, and the overall volume, weight and cost of the machine would be lower.

In [148], a more comprehensive method is proposed to estimate whether a new sorbent is commercially attractive, if compared with silica-gel, when used in a chiller. First, Performance Ratio "*PR*" (not to be confused with the PR defined in 3.14), and Cost Ratio "*CR*" must be calculated, as a function of the material cost and the maximum Specific Cooling Capacity (SCP) achieved with the studied material and with silica-gel in comparison:

- $PR = SCP_{MAX,\,CaAlg} \,/\, SCP_{MAX,silica-gel}$; $\qquad CR = Cost_{CaAlg} \,/\, Cost_{silica-gel}$.

[3]The actual costs can be higher, especially for small productions. At October 2025, we find costs on the global market in the order of 15 €/kg (up to 30 €/kg in the EU market), meaning that the 25 kg of needed CaAlg would cost about € 263, almost as much as the $CaCl_2$/silica-gel composite.

where [148] suggests $SCP_{MAX,silica-gel} = 300\ W/kg$ and $Cost_{silica-gel} = 8\ €/kg$. Referring to the tests carried out with CaAlg in the desalination unit, we can estimate a maximum cooling capacity of 99 W, obtained, specifically, during Test "3" [4]. Since we used 0.386 kg of material, the resulting $SCP_{MAX,\ CaAlg}$ is estimated to be $SCP_{MAX,\ CaAlg} = 256.5\ W/kg$. From this, we can calculate: $PR = 0.855$; $CR = 0.869$. The method in [148] combines the two evaluated indicators to calculate the total cost as the sum of *COH* (Cost Of Hydraulics) and *COAM* (Cost of Adsorption Material). The proposed expression is the following:

$$COH + COAM = (PR^{-1}) \cdot 349\ €/kW\ +\ (CR) \cdot 27\ €/kW \tag{6.1}$$

Applying this with silica-gel ($PR = CR = 1$), ends with a total of $COH + COAM = 376\ €/kW$. On the other hand, in the case of CaAlg, we obtain $COH + COAM = 432\ €/kW$. The difference is only 13%, making the two solutions comparable and making CaAlg commercially interesting. In Fig. 6.6, we propose the original diagram from [148] showing other sorbents in comparison and enriched with the result for CaAlg, which is second only to silica-gel. Considering the limitations in the used desalination plant, the author believes that the actual potential of CaAlg can be higher and surpass silica-gel under a proper machine design.

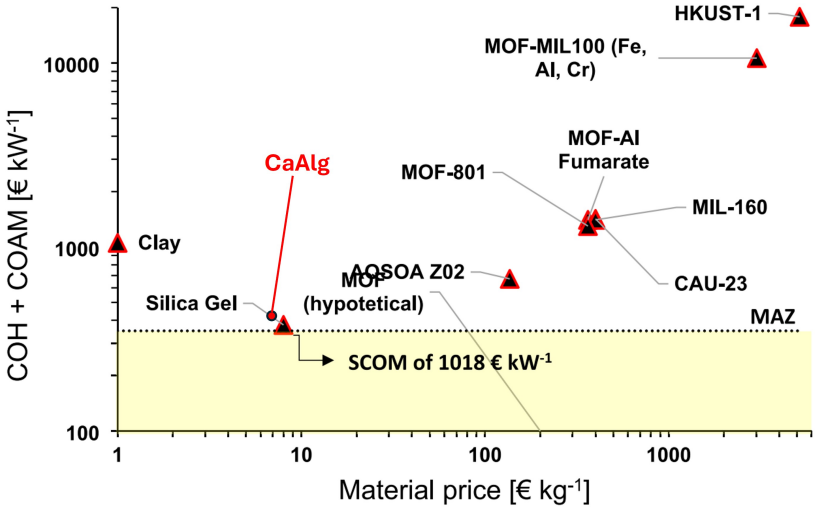

Fig. 6.6 Commercial attractiveness of CaAlg if compared with other sorbents. The base picture is taken from [148]. The CaAlg point is added based on the best results and estimations from this work.

Even if approximate, these analyses give a rough idea about the economic feasibility of using calcium alginate, and make its large-scale production an actually interesting option. In comparison, materials with higher performance may suffer from lower economic feasibility. This is the case of MOFs or the ionogel presented in Fig. 5.9: we can apply the above analysis in the latter case, assuming a cost of 590 €/kg for the EMIM [149] (which is used for 57%

[4] As discussed above, since we do not have the required sensors to directly evaluate the actual cooling capacity as occurring in the EV tank, we estimated this value starting from the power exchanged at the adsorber level, and assuming that the heat of evaporation and heat of adsorption are equal.

of the sorbent composition [138]) and a max SCP of 500 W/kg (estimated from the available data in [138]), to get: $COH + COAM = 1344\ €/kW$, which is comparable with MOF-801.

6.3 Methods

6.3.1 Adsorption-based unit description

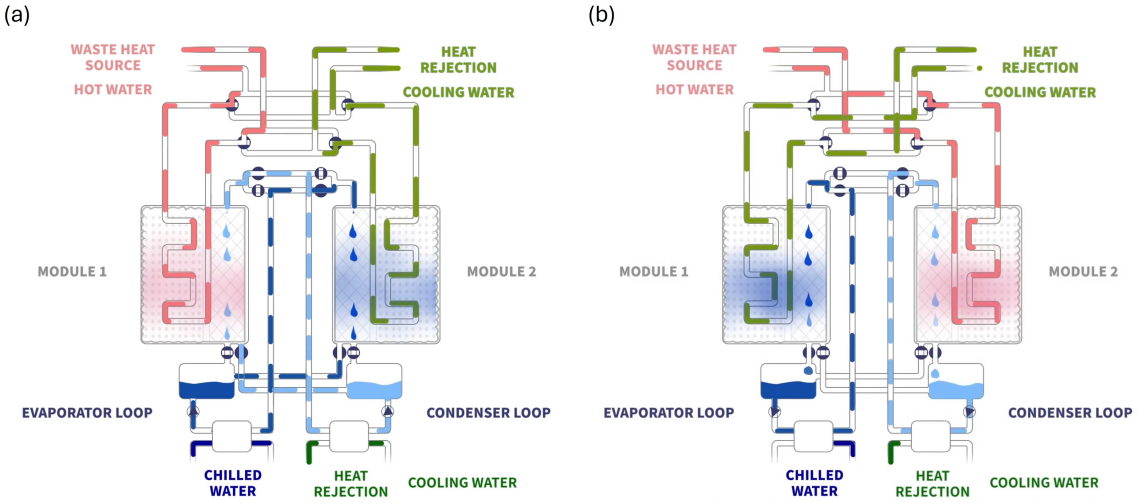

Fig. 6.7 AC unit working principle. (a) Phase A: module 1 desorbs, module 2 adsorbs, and a cooling effect is extracted from the EV loop ("chilled water"). (b) Phase C: module 1 adsorbs, module 2 desorbs. The screenshots are extracted from the video at the link https://www.youtube.com/watch?v=rqE_W2WOBEE (last visited on 26/10/2025).

The company Sorption Technologies [150] produces adsorption chillers based on an improved patented concept where both feedwater and condensed water are continuously recirculated in the modules containing the adsorbent (Fig. 6.7). In total, the machine undergoes 5 phases:

A: module 1 desorbs, module 2 adsorbs (Fig. 6.7a). A pump is used to circulate water from the condenser tank (CD tank) into module 1, where it goes through an exchanger named "Phase Changer" which splits the water flow into several small drops and increases the exchange area for evaporation and condensation. Another pump is used to circulate water from the evaporator tank containing feedwater (EV tank) into module 2, where it goes through a Phase Changer. The evaporator and condensation happens directly on the water drops, and the EV tank and CD tank levels change over time depending on how much vapor is exchanged with the sorbent. In parallel, four external pressurized circuits are exchanging heat with the machine (typically, water is used):

- HT loop (red): an external heat source at high temperature (e.g., 80°C) is used to provide energy for the material in module 1 to desorb;

  - MTads loop (light green): an external loop circulating water at environmental temperature (e.g., 30°C) is used to extract heat from module 2 adsorbing;
  - MTcd loop (dark green): an external loop circulating water at environmental temperature (e.g., 30°C) is used to extract heat from the water condensing in the CD tank;
  - LT loop (blue): an external loop circulating *chilled* water at low temperature (e.g., 12°C) is used to provide energy for the EV tank water to evaporate.

  Typically, the MTads and MTcd loops are managed using a single external MT loop, which splits after entering the machine frame.

B: (not shown in the video) the external valves are actuated in preparation for Phase C;

C: module 1 adsorbs, module 2 desorbs (Fig. 6.7b). The behaviour is the same as in phase A, but this time the CD tank loop and the external HT loop are connected to module 2, while the EV tank loop and external MTads loop are connected to module 1.

D: (not shown in the video) the external valves are actuated in preparation for Phase A;

E: (not shown in the video) the EV tank and CD tank are connected for short time, to repristinate the water levels (this is not possible if the machine is used for desalination, where instead the EV tank must be filled with new salty water and the CD tank must be emptied from fresh water).

Given that only phases A and C are functional for the chilling effect, in the Results section we call them, respectively, phase 1 and phase 2, thus neglecting the influence of the other phases (except for the effect of initial water mixing, which is discussed). All the phases happen with the material being under vacuum, at a pressure typically lower than 100 mbar. The author was involved in designing the prototype for the HyperGryd project based on the project requirements, including: number of modules (2), total mass of sorbent (75 kg), flowrate in the EV and CD loops (20 L/min), testing temperatures (up to 90°C).

3D design

Based on the experience with the small desalination unit (see Appendix E), we decided to place the EV and CD tanks under the module containing the sorbent, in order to exploit gravity and collect possible water condensing on the internal surfaces of the adsorber vessel. Nevertheless, due to project requirements, simply placing the module vertically above the tanks was not possible, since the total height of the machine could not exceed 2.1 meters and the heat exchangers alone are 1.25 m long (excluded the container, Fig. 6.8a) and about 1.2 meters are needed to vertically fit the tanks and the circulation pumps. For this reason, we

decided to tilt the module by 83° with respect to the vertical to the floor: enough to limit the total height of the machine (Fig. 6.8b) but still not too much so to allow the drops to reach the bottom by gravity (based on drainage gradient theoretical considerations, and experiments).

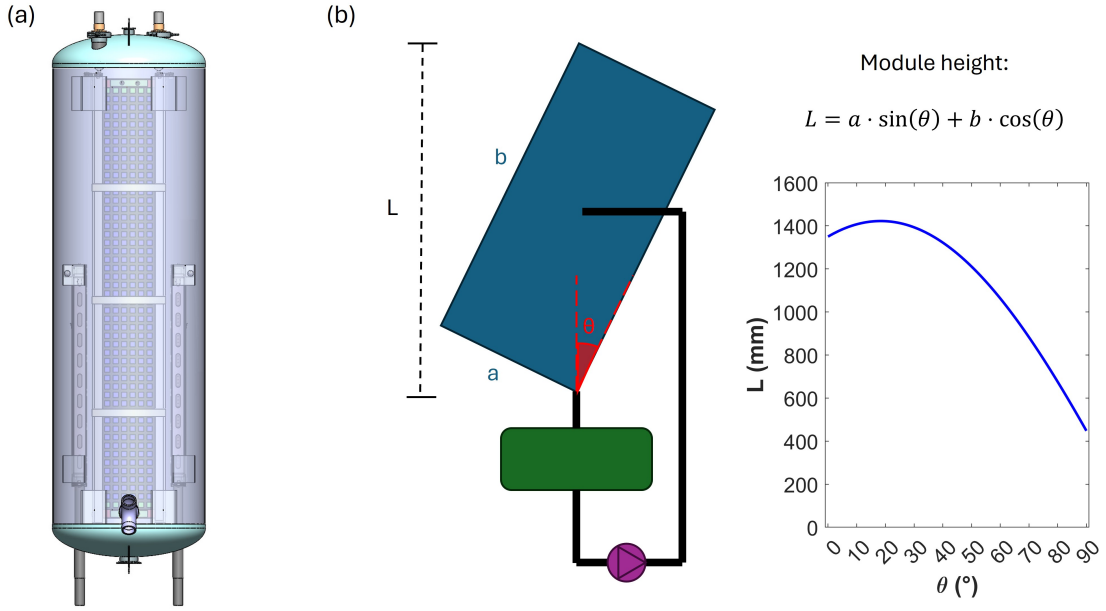

Fig. 6.8 AC module tilting strategy. (a) CAD of the module containing the adsorber, seen from below. (b) Schematics of the module (blue) tilted by an angle θ, and the resulting height as a function of the angle ($a = 448\ mm$, $b = 1350\ mm$). We observe that it is necessary to surpass about 37° in order to achieve a useful reduction in total height.

The vacuum circuits were designed and assembled using ISO-KF components and flexible pipes. Most of the connections have internal diameter 25 mm, except for the connections at the bottom of the modules, connecting to the vessels, which have diameter 40 mm. We used butterfly valves, bistable, with pneumatic actuation.
The Phase Changers (PC) are porous structures made of stainless steel and resin, which help in the water distribution. Each module contains two PCs: one on the left, one on the right of the heat exchanger (they can be seen in Fig. 6.8a). When the water flow from the pumps reach the PCs, it is dispersed into smaller drops, and the surface area which is useful for evaporation and condensation increases. This improves the dynamics of the sorption process. The external circuits (HT, MT and LT loops) were realized using copper pipes DN25 and compression fittings. We included the proper accessories, including air venting valves and filling/drainage valves. In order to allow the copper pipe enter the module containing the heat exchanger without losing vacuum, we designed a custom brass component (Fig. 6.9): the initial design is based on a ISO-KF25 stainless steel flange, but the internal diameter was adapted to 28.15 mm and the part length increased, so to be compatible for copper-brass brazing of 28 mm copper pipes. The final assembly has a volume of 2450 mm x 990 mm x 2000 mm, see Fig. 6.10.

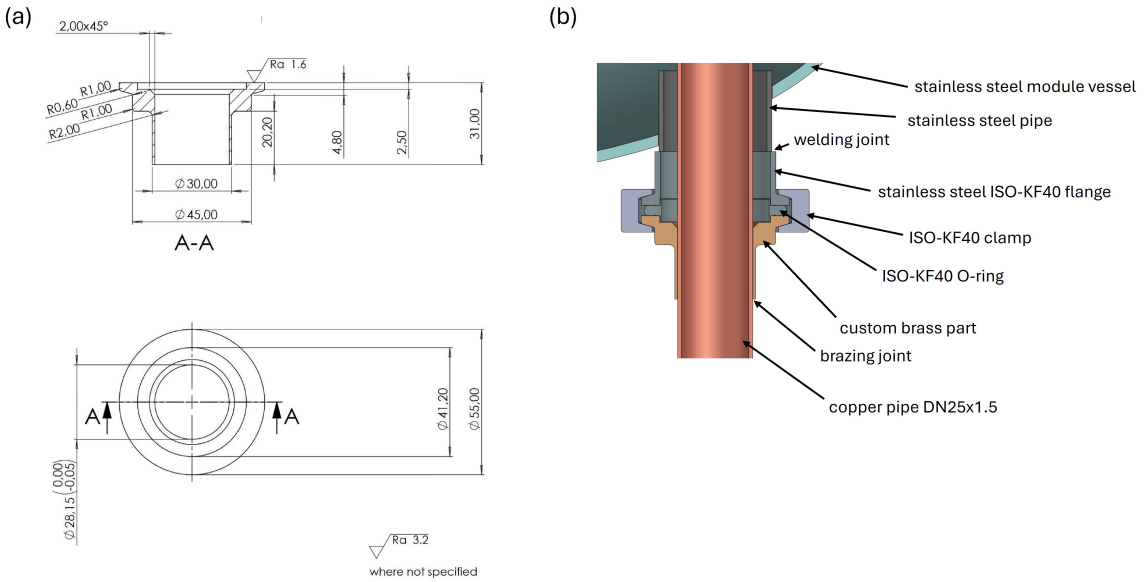

Fig. 6.9 Custom brass feedthrough. (a) 2D drawing of the custom brass component. (b) Cross-sectional view of the custom component assembly.

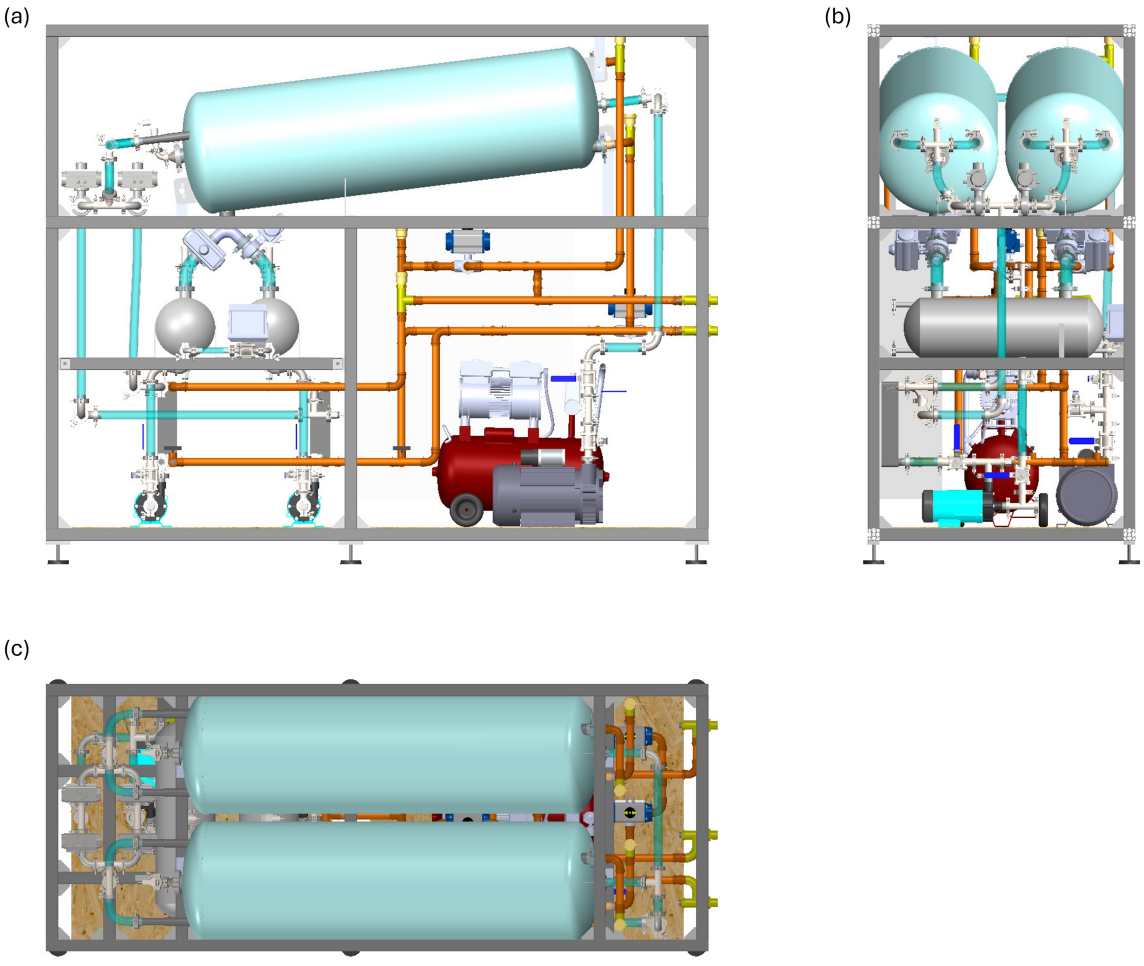

Fig. 6.10 CAD of the designed adsorption machine. (a) Front view. (b) Side view. (c) Top view.

Monitoring, control and data acquisition

The full list of sensors and actuators in the AC unit is provided in table 6.2.

Component	Type	Scope	Description
THTin	Sensor	Monitoring the water temperature at the inlet of the desorbing module (HT loop).	Class-A PT1000. Accuracy: ± 0.3°C.
THTout	Sensor	Monitoring the water temperature at the outlet of the desorbing module (HT loop).	Class-A PT1000. Accuracy: ± 0.3°C.
TMTin	Sensor	Monitoring the water temperature at the inlet of the dissipation circuits (MT loop), including the adsorbing module and the CD loop plate HEX.	Class-A PT1000. Accuracy: ± 0.3°C.
TMTout	Sensor	Monitoring the water temperature at the outlet of the dissipation circuits (MT loop), including the adsorbing module and the CD loop plate HEX.	Class-A PT1000. Accuracy: ± 0.3°C.
TLTin	Sensor	Monitoring the water temperature at the inlet of EV loop plate HEX (LT loop).	Class-A PT1000. Accuracy: ± 0.3°C.
TLTout	Sensor	Monitoring the water temperature at the outlet of EV loop plate HEX (LT loop).	Class-A PT1000. Accuracy: ± 0.3°C.
TEV-vac-in	Sensor	Monitoring the water temperature at the inlet of the machine on the EV loop (vacuum loop EV).	Class-A PT1000. Accuracy: ± 0.3°C.
TEV-vac-out	Sensor	Monitoring the water temperature at the outlet of the machine on the EV loop (vacuum loop EV).	Class-A PT1000. Accuracy: ± 0.3°C.
TCD-vac-in	Sensor	Monitoring the water temperature at the inlet of the machine on the CD loop (vacuum loop CD).	Class-A PT1000. Accuracy: ± 0.3°C.
TCD-vac-out	Sensor	Monitoring the water temperature at the outlet of the machine on the CD loop (vacuum loop CD).	Class-A PT1000. Accuracy: ± 0.3°C.
VacPress1	Sensor	Monitoring vapor pressure in the module 1.	Thyracont VCC200MA4 absolute pressure sensor, 0-200 mbar. Accuracy: ±0.5 mbar.
VacPress2	Sensor	Monitoring vapor pressure in the module 2.	Thyracont VCC200MA4 absolute pressure sensor, 0-200 mbar. Accuracy: ±0.5 mbar.
FlowHT	Sensor	Monitoring water flow in the external HT loop.	Magnetic-inductive flow meter MVM-250-PA.
FlowMT	Sensor	Monitoring water flow in the external MT loop.	Magnetic-inductive flow meter MVM-250-PA.
FlowLT	Sensor	Monitoring water flow in the external LT loop.	Magnetic-inductive flow meter MVM-250-PA.
FlowEV	Sensor	Monitoring water flow in the internal EV loop.	Vortex flow meter G1MAS009.
FlowCD	Sensor	Monitoring water flow in the internal CD loop.	Vortex flow meter G1MAS009.
PowerAux	Sensor	Powermeter to monitor electrical consumption of the pumps.	-
PumpEV	Actuator	Pumping water through the internal EV loop.	Three-phase side-channel pump.
PumpCD	Actuator	Pumping water through the internal CD loop.	Three-phase side-channel pump.
VADS1in	Actuator	3-way valve (see P&ID).	Butterfly valve. Pneumatic, bistable, 3-7 bar.
VADS1out	Actuator	3-way valve (see P&ID).	Butterfly valve. Pneumatic, bistable, 3-7 bar.
VADS2in	Actuator	3-way valve (see P&ID).	Butterfly valve. Pneumatic, bistable, 3-7 bar.
VADS2out	Actuator	3-way valve (see P&ID).	Butterfly valve. Pneumatic, bistable, 3-7 bar.
VPC1in.cd	Actuator	2-way valve (see P&ID).	Butterfly valve. Pneumatic, bistable, 3-7 bar.
VPC1in.ev	Actuator	2-way valve (see P&ID).	Butterfly valve. Pneumatic, bistable, 3-7 bar.
VPC2in.cd	Actuator	2-way valve (see P&ID).	Butterfly valve. Pneumatic, bistable, 3-7 bar.
VPC2in.ev	Actuator	2-way valve (see P&ID).	Butterfly valve. Pneumatic, bistable, 3-7 bar.
VPC1out.ev	Actuator	2-way valve (see P&ID).	Butterfly valve. Pneumatic, bistable, 3-7 bar.
VCP1out.cd	Actuator	2-way valve (see P&ID).	Butterfly valve. Pneumatic, bistable, 3-7 bar.
VPC2out.ev	Actuator	2-way valve (see P&ID).	Butterfly valve. Pneumatic, bistable, 3-7 bar.
VPC2out.cd	Actuator	2-way valve (see P&ID).	Butterfly valve. Pneumatic, bistable, 3-7 bar.
V-Vac-liqu	Actuator	2-way valve (see P&ID).	Butterfly valve. Pneumatic, bistable, 3-7 bar.
V3W	Actuator	3-way valve (see P&ID).	Electric, proportional, 0-10V.

Table 6.2 AC unit components.

The monitoring and control of the machine is managed via a Siemens® PLC (Climatix POL648.10) connected to a series of expansion modules, with which it communicates via MODBUS protocol, wired architecture (MODBUS RTU) [151] (Fig. 6.11a). The PLC is connected to a computer via Ethernet cable, to exchange data via MODBUS TCP/IP. In this case, Siemens SCOPE ® [152] was used as DAQ interface (Fig. 6.11b).

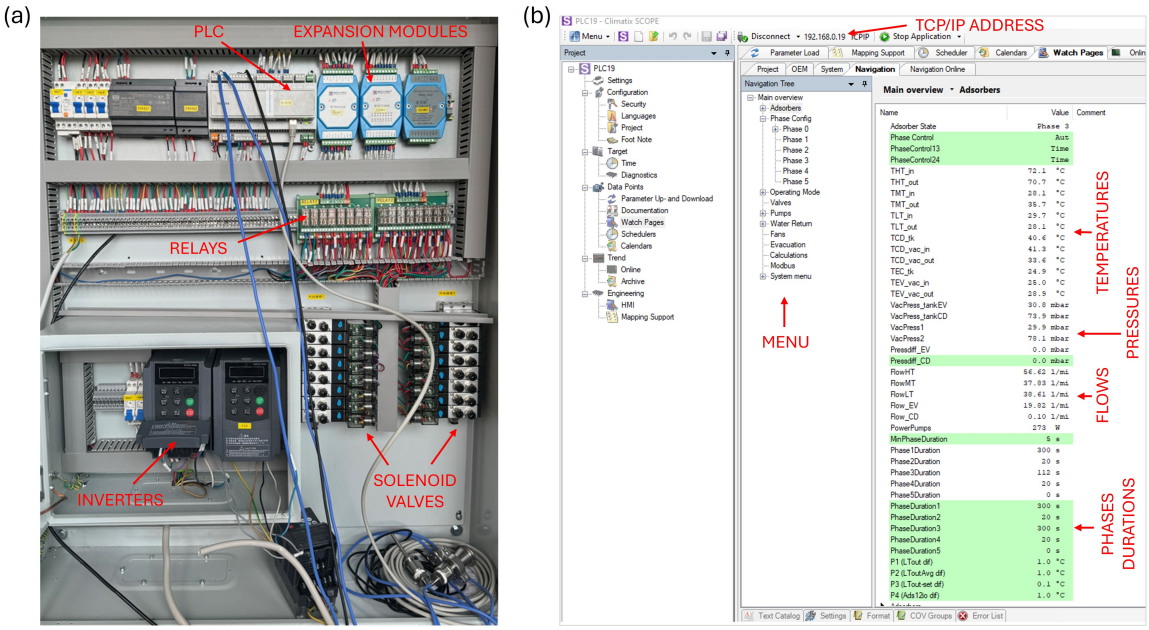

Fig. 6.11 DAQ hardware and software. (a) Control cabinet, including Siemens PLC, expansion modules, relays to control the solenoid valves, inverters to control the pumps velocity, solenoid valves to control the pneumatic actuators. (b) Siemens SCOPE software interface.

We collected one sample per second from all sensors at the same time, and post-analysed data with MATLAB.

The PLC was programmed to open or close the valves and start/stop the pumps according to the configuration required by the working phases (see table 6.3). Normally, the machine cycles through phases 1->5 and then back to 1 again. In the test plotted in this document, phase 5 was skipped, and used to repristinate the water levels only after the tests.

Actuator	Phase 1	Phase 2	Phase 3	Phase 4	Phase 5
VADS1in	1	0	0	1	1
VADS1out	1	1	0	0	0
VADS2in	1	0	0	1	1
VADS2out	1	1	0	0	0
VPC1in.cd	1	0	0	0	0
VPC1in.ev	0	0	1	0	0
VPC2in.cd	0	0	1	0	0
VPC2in.ev	1	0	0	0	0
VPC1out.ev	0	0	1	1	0
VCP1out.cd	1	1	0	0	0
VPC2out.ev	1	1	0	0	0
VPC2out.cd	0	0	1	1	0
V-Vac-liqu	0	0	0	0	1
V3W	70%	70%	70%	70%	70%
PumpCD	1	1	1	1	0
PumpEV	1	1	1	1	0
PumpHT	1	1	1	1	1
PumpMT	1	1	1	1	1
PumpLT	1	1	1	1	1

Table 6.3 Actuators configuration during each phase in the AC unit. In case of 2W valves, 0 = closed, 1 = open. In case of 3W valves, 0 means that the central connection is connected to the pipe on the left in the P&ID, 1 means that the central connection is connected to the pipe on the right in the P&ID. In case of pumps, 0 = off, 1 = on. The proportional valve V3W was positioned at 70% of its full span, after initial calibration, in order to equally share the MT flow between the CD exchanger and the adsorbing module.

6.3.2 Testing apparatus and procedure

In order to test the machine, we designed and built a Testing rig in the company spaces. The system includes three buffer tanks containing water at hot temperature (HT tank, up to 95°C), environmental temperature (MT tank, 25-35°C), and low temperature (LT tank, 5-25°C) and the necessary pumps and piping to provide the three water temperature levels to the machine under test. The system P&ID is shown in Fig. 6.12:

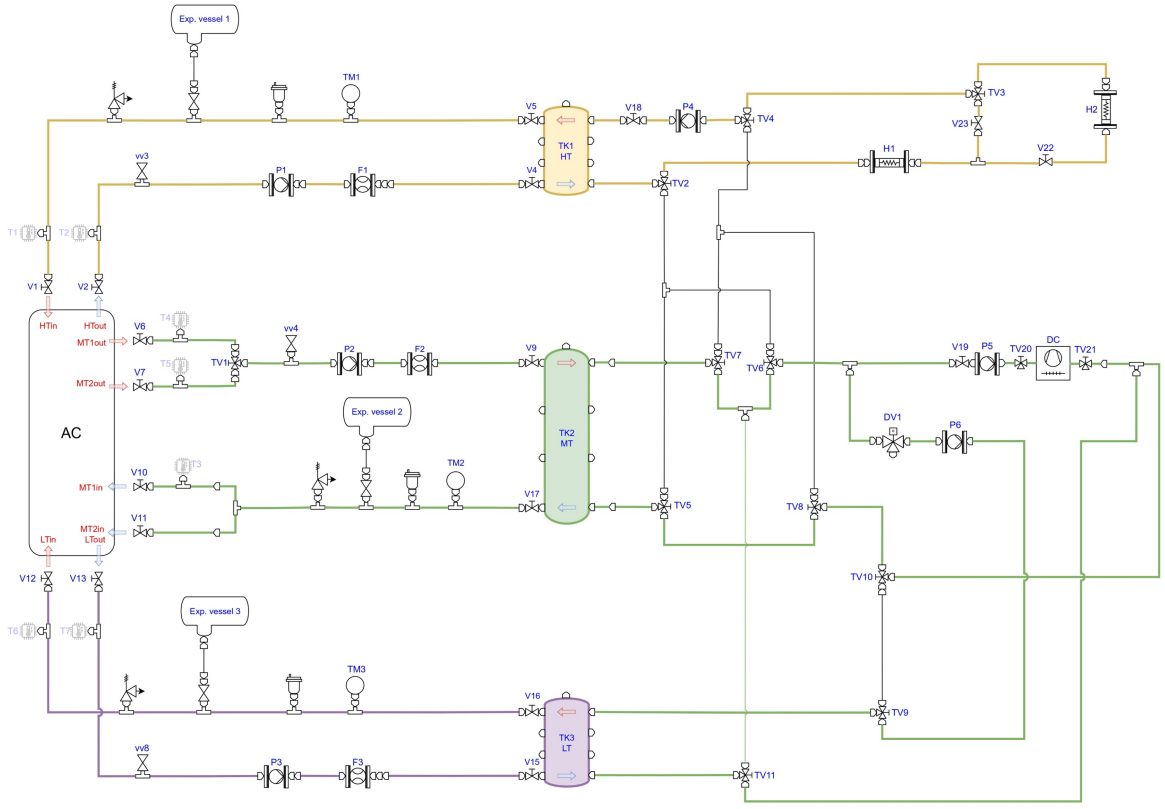

Fig. 6.12 AC Testing Rig P&ID. The circuit includes three tanks (TK1-HT, TK2-MT, TK3-LT), six pumps (P1, P2, P3, P4, P5, P6), two electric heaters (H1, H2), one dry-cooler (DC), safety components, thermomanometers (TM1, TM2, TM3), three flowmeters (F1, F2, F3), and a series of two-way valves (Vx) and three-way valves (TVx). The colored paths show how water circulates during the normal operation of the system.

Two electric heaters (50 kW and 12 kW) are used to provide the necessary heat to keep the HT tank at the desired desorption temperature, while a dry-cooler is used to dissipate heat from the MT loop, blowing air at room temperature. More in general, depending on the chosen valves configuration, the system can be used for:

- Pre-heating the HT tank;
- Pre-heating the MT tank;
- Pre-heating the LT tank;
- Cooling-down the HT tank;
- Cooling-down the MT tank;
- Cooling-down the LT tank;
- Normal operation (circuits highlighted in Fig. 6.12), where the HT tank and LT tank are heated and kept in temperature, while the MT tank is cooled-down to dissipate heat.

The system was first designed via CAD (Fig. 6.13a), then assembled (Fig. 6.13b) over a surface of 9 m x 4 m.

(a)

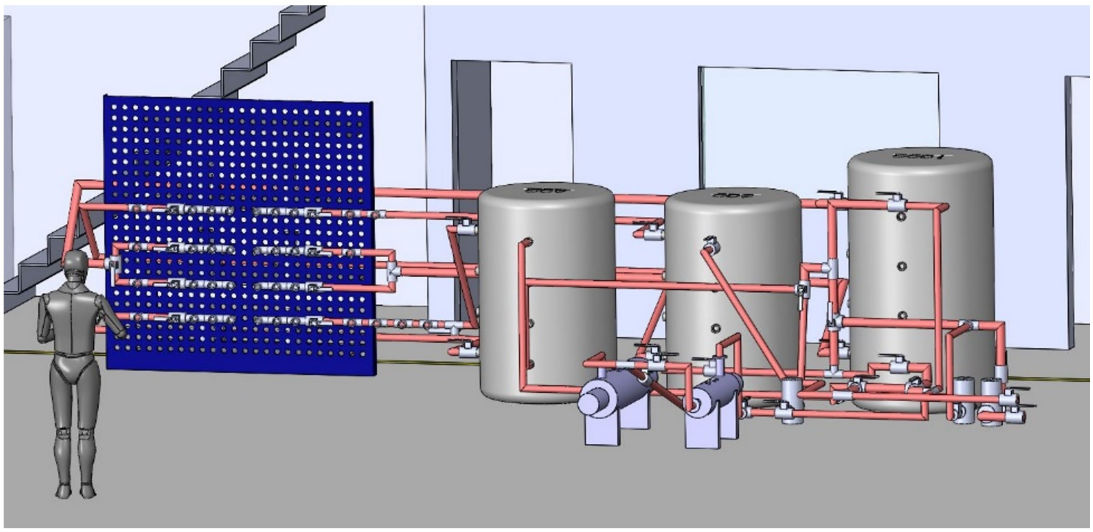

(b)

Fig. 6.13 AC Testing Rig appearance. (a) Preliminary 3D-design of the testing rig. (b) A picture of the finished setup, assembled based on the 3D-design.

Experiments

Prior to running experiments, air was extracted from the machine by connecting a vacuum pump to the modules and tanks, one by one, with the CD pump and EV pump running to ensure all the gas is released. The final pressure is 23 mbar, about the saturation pressure of vapor at room temperature (20°C), meaning that most of the residual atmosphere in the machine is indeed composed of water vapor.
To run each experiment, the following procedure was carried out:

1. We connected the machine to the computer, open the software and started collecting data.
2. We started the air compressor to provide power to the pneumatic valves.
3. We turned on the external rig pumps, heaters and dry-cooler and waited until the tanks are in temperature to start the test.
4. We adjusted cycle times and started the test.
5. Once the test was over: we stopped the machine, turned off external rig pumps, heaters and dry cooler, stopped the compressor, and detached the machine from the computer.

The temperatures provided by the testing rig (HT, MT and LT loops) were adjusted depending on the experiment. The adsorption and desorption times are identical and equal to a value "phase time" (common to phase A and C), adjusted depending on the experiment. The list of all tested conditions is provided in table 6.4.

Test	1	2	3	4	5	6	7	8	9	10	11
TMTin (°C)	30	30	35	35	35	30	30	30	30	30	30
THTin (°C)	70	70	80	80	80	80	80	80	80	80	80
TLTin (°C)	20	25	12	16	20	12	12	16	16	20	20
phase time (min)	15	15	13.5	13.5	13.5	13.5	13.5	13.5	13.5	13.5	13.5
n. of cycles	1	1	3	2	3	3	2	3	2	3	4

Table 6.4 Experimental campaign in the AC device. All tests were made using the composite $CaCl_2$/silica-gel.

The flow-rates F during all tests are constant and equal to: $F_{EV} = 18\ L/min$, $F_{CD} = 18\ L/min$, $F_{HT} = 56\ L/min$, $F_{MT} = 37\ L/min$, $F_{LT} = 20\ L/min$.

6.4 Conclusions

In this chapter, we tested a $CaCl_2$/silica-gel composite in a medium-scale adsorption machine, and discussed how the results and costs would change if replacing the composite with CaAlg. Here the main outcomes:

- First, we designed and assembled an adsorption machine and filled it with 75 kg of sorbent, a $CaCl_2$/silica-gel composite. We tested the machine under different conditions,

proving that the machine efficiency is higher (COP up to 56% larger) than in the small-scale device tested for desalination in Chapter 5. This suggests that, when used in a larger plant, CaAlg could reach better performance than what observed.

- We estimated a specific daily water production above 6 $m^3/day/ton$, using $CaCl_2$/silica-gel and a desorption temperature of 80°C. This is comparable with the production achieved with CaAlg in the small-scale unit and at 60°C, providing a further confirmation of the potential of the bioderived hydrogel at low temperatures.

- Extrapolating our results, we estimated that about 25 kg of CaAlg would be sufficient to achieve an SDWP equivalent to the use of 75 kg of $CaCl_2$/silica-gel, with 60°C desorption temperature. This results in a material cost reduction of about 54%.

Chapter 7

Conclusions and future perspectives

The objective of this research was to investigate Calcium Alginate (CaAlg) hydrogel for adsorption-based fresh water production. Based on a preliminary literature review, we identified and experimented two distinct approaches: water generation through Atmospheric Water Harvesting (AWH) and water treatment through Adsorption Desalination (AD).

First, we produced small batches of six different calcium alginate samples, where we varied the quantity of sodium alginate, calcium chloride and graphite in the chemical composition. We experimentally characterized the samples and found out that compositions Alg_1Ca_{10} and $Alg_1Ca_5G_{0.1}$ have, respectively, the highest water uptake potential and the fastest dynamics during the adsorption and desorption processes. The type-II material's isotherm at 30°C shows equilibrium uptakes of up to 1.28 g/g at a relative humidity of 70%, a fourfold increase with respect to commercial microporous and mesoporous silica-gels tested under the same conditions, and larger than the analysed sorbents from the literature. We provided a novel Linear Driving Force based model named LDFDw, which is particularly useful to simulate adsorption and desorption transients when large water uptake ranges are involved. Using LDFDw, we estimated a water vapor diffusivity of $D = 3 \cdot 10^{-12}$ m^2/s, about three times lower than silica-gel. When aged over repetitive cycling, CaAlg shows a stable uptake over 40 cycles of testing under vacuum, and over 300 cycles of testing in a climatic chamber.

We think that our results on material characterization corroborate the known potential of calcium alginate, already partially observed in the literature. Our main contributions consist in having optimized the CaAlg composition to maximize equilibrium water uptakes and dynamics, and having shown the sorbent's medium-term stability when tested under vacuum. On the other hand, we believe that further research is necessary in the direction of long-term stability assessment, especially when the material is used at high relative humidities, where we observed salt deliquescence. We suggest to measure the material's isotherms at larger temperatures and vapor pressures, to provide a complete material characterization within

the range of the possible working conditions occurring in an adsorption-based application. Furthermore, in order to have a clearer understanding of the macro-behaviour of calcium alginate, we suggest that SEM pictures at higher magnification are taken, and X-ray spectroscopy is used, to better assess the material's microstructure. This would help in clarifying the reasons behind the limited deliquescence observed, as well as the nature and properties of the salt crystals confined in the material structure. The described analyses should be conducted on sorbent samples under different conditions (e.g., equilibrium at different vapor pressures and temperatures) and undergone to different production processes (to understand the effect of parameters such as: room temperature, humidity, reaction time, beads size -different diameters may lead to different kinetics-, drying time and drying temperature).

Second, we tested CaAlg in a lab-scale adsorption-machine for AWH. We produced a coating of 97.5 grams of dry $Alg_1Ca_5G_{0.1}$ hydrogel on the surface of a finned heat exchanger and placed it in an atmospheric water generator. We run experiments in controlled laboratory environment as well as in arid climates, demonstrating the feasibility of CaAlg for this application even at medium-low relative humidities and desorption temperatures. In particular, we have observed a stable production over 2.5 days of consecutive testing, and achieved a peak specific daily water production of 1.19 m^3/day/ton (at an adsorption temperature of 25°C, relative humidity of 45% and desorption temperature of 70°C). The produced water was analysed, showing a conductivity of 103 $\mu S/cm$ and a chemical composition within the requirements of the *EU 2020/2184* and *WHO Guidelines for drinking-water quality* regulations, except that for Cu contamination due to the use of copper pipes in the condenser coils.
Compared with results from the literature, our system is among the ones with the highest performance, achieving competitive water productivity at relatively low temperature and humidity. This suggests that CaAlg-based atmospheric water generators can produce fresh water even in arid climates and be potentially integrated with renewable heat sources such as solar plants. On the other hand, further effort is necessary in the engineering process of a AWH machine integrating CaAlg. We suggest avoiding components in copper or aluminium -which may contaminate the produced water-, and use instead stainless steel alloys such as AISI 316; also, we suggest investigating further heat exchanger designs, in order to increase the sorbent's packing density while still allowing proper heat and vapor transfer. Generative artificial intelligence might be useful to explore alternative exchangers designs, and computational fluid dynamics can be used for their validation.

Third, we tested CaAlg in a lab-scale adsorption-machine for AD. We produced 386 grams of dry Alg_1Ca_{10} hydrogel pseudo-spherical beads, and placed them in the finned coil heat exchanger of an adsorption desalination unit. We run experiments under vacuum, demonstrating the potential of CaAlg for this application even at absolute pressures of 10-100

mbar and temperatures lower than 80°C. We achieved water production, and observed a desalination effect, with a salt rejection rate of over 99.2% starting from seawater salinity. The final conductivity (245 $\mu S/cm$), TOC and Cu contents stand within the limits suggested by *EU 2020/2184* and *WHO Guidelines for drinking-water quality* regulations. When compared to mesoporous silica-gel tested in the same conditions, CaAlg achieved water productions up to 90% larger (this result refers to a test run with 30 min adsorption at 30°C, and 120 min desorption at 75°C). Using CaAlg, we demonstrated a stable water production over 6 consecutive cycles, and achieved a peak specific daily water production of 6.04 m^3/day/ton at a desorption temperature of 60°C and optimized cycle times (30 min adsorption at 30°C, 45 min desorption). We estimated a specific thermal energy consumption as low as 0.97 kWh/L, despite the sub-optimal machine design. Furthermore, we achieved water production (2.2 m^3/day/ton) even with a desorption temperature as low as 45°C.
The latter result is remarkable, since it makes integration of ultralow-grade heat sources an interesting option. Low exergy sources such as heat dissipated by power plants or data centres are of no use for most industrial purposes; instead, we propose CaAlg-based adsorption desalination as an option for recycling such waste energy, providing at the same time a chilling effect and fresh water production, especially in coastal regions where seawater is largely available. Also, as for our knowledge, this was the first time CaAlg has been tested under vacuum for adsorption-based water desalination. On the other hand, we think that further research is necessary in order to consider CaAlg as a robust industrial alternative to conventional sorbents. Due to limitations in our experimental setup, we were only able to test long cycles (1-2 hours), where the effects of adsorption dynamics became negligible. We do not exclude that, at shorter cycles, silica-gel can still be a competitive alternative for adsorption desalination, since the decrease in water uptake capacity might be compensated by its higher water vapor diffusivity. We suggest that a new testing rig is built in order to characterize the productivity of CaAlg-based adsorption machines at shorter cycle durations (5-30 minutes).

Last, we extrapoled the results achieved with CaAlg to the use in a larger-scale adsorption machine. We estimated that replacing a $CaCl_2$/silica-gel composite with CaAlg could reduce the material's weight and cost by 67% and 54%, respectively. This is a preliminary and purely theoretical analysis: the production of large amounts of CaAlg might still result challenging and hide further costs. Also, depending on the market availability, the CaAlg production cost may increase until being comparable to the analysed composite. In this case, though, we still believe CaAlg can be a more sustainable choice, since it is bio-based and should have a lower environmental impact with respect to silica-gel composites. To confirm this hypothesis, we suggest that future research shall assess the life cycle of calcium alginate, with special focus on its biodegradability.

References

[1] Guilherme Baggio, Manzoor Qadir, and Vladimir Smakhtin. Freshwater availability status across countries for human and ecosystem needs. *Science of The Total Environment*, 792:148230, 2021. ISSN 0048-9697. doi: https://doi.org/10.1016/j.scitotenv.2021.148230.

[2] UNICEF, 2024. URL https://www.unicef.org/stories/water-and-climate-change-10-things-you-should-know. Last visited on 26/10/2025.

[3] URL https://www.unicef.org/wash/water-scarcity. Last visited on 26/10/2025.

[4] NPR. URL https://www.npr.org/sections/goatsandsoda/2016/07/07/484793736/millions-of-women-take-a-long-walk-with-a-40-pound-water-can. Last visited on 26/10/2025.

[5] Frank Biermann, Norichika Kanie, and Rakhyun E Kim. Global governance by goal-setting: the novel approach of the un sustainable development goals. *Current Opinion in Environmental Sustainability*, 26-27:26–31, 2017. ISSN 1877-3435. doi: https://doi.org/10.1016/j.cosust.2017.01.010. Open issue, part II.

[6] URL https://sdgs.un.org/goals/goal6. Last visited on 26/10/2025.

[7] Jay P. Graham, Mitsuaki Hirai, and Seung-Sup Kim. An analysis of water collection labor among women and children in 24 sub-saharan african countries. *PLOS ONE*, 11 (6):1–14, 06 2016. doi: 10.1371/journal.pone.0155981.

[8] Jason Woods et al. Humidity's impact on greenhouse gas emissions from air conditioning. *Joule*, 6:726–741, 2022. doi: https://doi.org/10.1016/j.joule.2022.02.013.

[9] L. Chen, S.H. Chen, L. Liu, and B. Zhang. Experimental investigation of precooling desiccant-wheel air-conditioning system in a high-temperature and high-humidity environment. *International Journal of Refrigeration*, 95:83–92, 2018. ISSN 0140-7007. doi: https://doi.org/10.1016/j.ijrefrig.2018.08.015.

[10] Primož Poredoš, He Shan, and Ruzhu Wang. Dehumidification with solid hygroscopic sorbents for low-carbon air conditioning. *Joule*, 6(7):1390–1393, 2022. ISSN 2542-4351. doi: https://doi.org/10.1016/j.joule.2022.06.020.

[11] Nicola Armaroli and Vincenzo Balzani. *Energia per l'astronave Terra*. Zanichelli, 2011.

[12] URL https://sdgs.un.org/goals/goal9. Last visited on 26/10/2025.

[13] URL https://sdgs.un.org/goals/goal13. Last visited on 26/10/2025.

[14] Stephen Hawking. *Le mie risposte alle grandi domande*. Rizzoli, 2019.

[15] URL https://eur-lex.europa.eu/eli/reg/2020/852/oj. Last visited on 26/10/2025.

[16] D. M. Ruthven. *Principles of Adsorpion and Adsorption processes*. Wiley, 1984.

[17] David Danaci, Mai Bui, Niall Mac Dowell, and Camille Petit. Exploring the limits of adsorption-based co2 capture using mofs with pvsa – from molecular design to process economics. *Mol. Syst. Des. Eng.*, 5:212–231, 2020. doi: 10.1039/C9ME00102F.

[18] N.O. Lemcoff. Nitrogen separation from air by pressure swing adsorption. In A. Dąbrowski, editor, *Adsorption and its Applications in Industry and Environmental Protection*, volume 120 of *Studies in Surface Science and Catalysis*, pages 347–370. Elsevier, 1999. doi: https://doi.org/10.1016/S0167-2991(99)80557-6.

[19] Seyed Hamed Barghi, Theodore T. Tsotsis, and Muhammad Sahimi. Chemisorption, physisorption and hysteresis during hydrogen storage in carbon nanotubes. *International Journal of Hydrogen Energy*, 39(3):1390–1397, 2014. ISSN 0360-3199. doi: https://doi.org/10.1016/j.ijhydene.2013.10.163.

[20] Márcio Santos Rocha. Chapter 2 - intermolecular interactions and dna solutions. In *DNA Interactions with Drugs and Other Small Ligands*, pages 7–22. Academic Press, 2023. ISBN 978-0-323-99139-1. doi: https://doi.org/10.1016/B978-0-32-399139-1.00009-7.

[21] Luca Riboldi and Olav Bolland. Overview on pressure swing adsorption (psa) as co2 capture technology: State-of-the-art, limits and potentials. *Energy Procedia*, 114:2390–2400, 2017. ISSN 1876-6102. doi: https://doi.org/10.1016/j.egypro.2017.03.1385. 13th International Conference on Greenhouse Gas Control Technologies, GHGT-13, 14-18 November 2016, Lausanne, Switzerland.

[22] E. Smolková-Keulemansová and L. Feltl. Chapter 9 - physical methods of gas analysis. In *Analysis of Substances in the Gaseous Phase*, volume 28 of *Comprehensive Analytical Chemistry*, pages 123–221. Elsevier, 1991. doi: https://doi.org/10.1016/S0166-526X(05)80099-6.

[23] L.T. Zhuravlev. The surface chemistry of amorphous silica. zhuravlev model. *Colloids and Surfaces A: Physicochemical and Engineering Aspects*, 173(1):1–38, 2000. ISSN 0927-7757. doi: https://doi.org/10.1016/S0927-7757(00)00556-2.

[24] Matteo Calò, Vincenzo Gentile, Matteo Fasano, and Eliodoro Chiavazzo. Calcium alginate hydrogel for high yield adsorption based desalination driven by ultralow-grade heat. *CellPress*, 2025. doi: 10.2139/ssrn.5412795.

[25] Xin Li, Zhong Li, Qibin Xia, and Hongxia Xi. Effects of pore sizes of porous silica gels on desorption activation energy of water vapour. *Applied Thermal Engineering*, 27(5):869–876, 2007. ISSN 1359-4311. doi: https://doi.org/10.1016/j.applthermaleng.2006.09.010.

[26] Yuri I. Aristov, Mikhail M. Tokarev, Angelo Freni, Ivan S. Glaznev, and Giovanni Restuccia. Kinetics of water adsorption on silica fuji davison rd. *Microporous and Mesoporous Materials*, 96(1):65–71, 2006. ISSN 1387-1811. doi: https://doi.org/10.1016/j.micromeso.2006.06.008.

[27] Curtis Strong, Ye Carrier, and F. Handan Tezel. Experimental optimization of operating conditions for an open bulk-scale silica gel/water vapour adsorption energy storage system. *Applied Energy*, 312:118533, 04 2022. doi: 10.1016/j.apenergy.2022.118533.

[28] Karmen Margeta and Anamarija Farkaš. Introductory chapter: Zeolites - from discovery to new applications on the global market. In Karmen Margeta and Anamarija Farkaš, editors, *Zeolites*, chapter 1. IntechOpen, Rijeka, 2020. doi: 10.5772/intechopen.92907.

[29] Istvan Palinko, Zoltán Kónya, A. Kukovecz, and I. Kiricsi. *Zeolites*, pages 819–857. Springer, 01 2013. ISBN 9783642205941. doi: 10.1007/978-3-642-20595-8_22.

[30] Hojatollah Moradi, Hedayat Azizpour, Hamed Hadizadeh Saroghi, Amin Esmaeili, and Nariman Rezamandi. Prediction of water adsorption isotherm on 13x zeolite in different temperatures and investigating the effect of non-framework cations using dynamic simulation. *Applied Surface Science Advances*, 18:100522, 2023. ISSN 2666-5239. doi: https://doi.org/10.1016/j.apsadv.2023.100522.

[31] Elena David and Adrian Armeanu. Cr/13x zeolite and zn/13x zeolite nanocatalysts used in pyrolysis of pretreated residual biomass to produce bio-oil with improved quality. *Nanomaterials*, 12:1960, 06 2022. doi: 10.3390/nano12121960.

[32] Prabhu Azhagapillai et al. Water vapor adsorption capacity loss of molecular sieves 4a, 5a, and 13x resulting from methanol and heptane exposure. *ACS Omega*, 7:6463–6471, 2022. doi: doi:10.1021/acsomega.1c03370.

[33] Radovan Kukobat, Ranko Škrbić, Pascale Massiani, Karima Baghdad, Franck Launay, Maria Sarno, Claudia Cirillo, Adolfo Senatore, Esad Salčin, and Suzana Gotovac Atlagić. Thermal and structural stability of microporous natural clinoptilolite zeolite. *Microporous and Mesoporous Materials*, 341:112101, 2022. ISSN 1387-1811. doi: https://doi.org/10.1016/j.micromeso.2022.112101.

[34] Simone Salustro, Luca Lavagna, Vito Fernicola, Denis Smorgon, Alessio Mondello, Eliodoro Chiavazzo, and Matteo Pavese. Thermal characterization and cost analysis of cement-based composite materials for thermochemical energy storage. *Journal of Energy Storage*, 93:112308, 2024. ISSN 2352-152X. doi: https://doi.org/10.1016/j.est.2024.112308.

[35] L. Lavagna, D. Burlon, and R et al Nisticò. Cementitious composite materials for thermal energy storage applications: a preliminary characterization and theoretical analysis. *Scientific Reports*, 10:12833, 2020. doi: 10.1038/s41598-020-69502-0.

[36] Antonio Fotia, Vincenza Brancato, Emanuela Mastronardo, Luigi Calabrese, and Andrea Frazzica. Enhancement of cacl2/silica gel composites sorbent stability for low-grade thermal energy storage. *Journal of Energy Storage*, 132:117679, 2025. ISSN 2352-152X. doi: https://doi.org/10.1016/j.est.2025.117679.

[37] Valeria Palomba, Andrea Frazzica, Vincenza Brancato, Antonino Bonanno, Yannan Zhang, Matteo Calò, Gabriele Penello, Gabriel Yarce, and Walter Mittelbach. Experimental proof of a thermal system for cooling and storage applications employing cacl2/silica gel composite adsorbent. *Energy Conversion and Management*, 341:120072, 2025. ISSN 0196-8904. doi: https://doi.org/10.1016/j.enconman.2025.120072.

[38] Larisa Gordeeva, A. Gubar, L. Plyasova, V. Malakhov, and Yuri Aristov. Composite water sorbents of the salt in silica gel pores type: The effect of the interaction between the salt and the silica gel surface on the chemical and phase compositions and sorption properties. *Kinetics and Catalysis*, 46:736–742, 09 2005. doi: 10.1007/s10975-005-0130-8.

[39] Giovanni Trezza, Luca Bergamasco, Matteo Fasano, and Eliodoro Chiavazzo. Minimal crystallographic descriptors of sorption properties in hypothetical mofs and role in sequential learning optimization. *npj Computational Materials*, 8:123, 2022. doi: 10.1038/s41524-022-00806-7.

[40] Nobel prize for chemistry 2025. URL https://www.nobelprize.org/prizes/chemistry/2025/press-release/. Last visited on 26/10/2025.

[41] Lifeng Ding and A. Yazaydin. Hydrogen and methane storage in ultrahigh surface area metal–organic frameworks. *Microporous and Mesoporous Materials*, 182:185–190, 12 2013. doi: 10.1016/j.micromeso.2013.08.048.

[42] Omar Farha, Ibrahim Eryazici, Nak Cheon Jeong, Brad Hauser, Christopher Wilmer, Amy Sarjeant, Randall Snurr, Sonbinh Nguyen, A Yazaydın, and Joseph Hupp. Metal-organic framework materials with ultrahigh surface areas: Is the sky the limit? *Journal of the American Chemical Society*, 134:15016–21, 08 2012. doi: 10.1021/ja3055639.

[43] Mohammad Aghajani Hashjin et al. Enhanced atmospheric water harvesting efficiency through green-synthesized mof-801: a comparative study with solvothermal synthesis. *Scientific Reports*, 13:16983, 2023. doi: 10.1038/s41598-023-44367-1.

[44] Hadiseh Masoumi. Chapter 5 - composite and hybrid polymeric adsorbents. In Ahad Ghaemi, Reza Norouzbeigi, and Hadiseh Masoumi, editors, *Polymeric Adsorbents*, pages 177–204. Elsevier, 2024. ISBN 978-0-323-99746-1. doi: https://doi.org/10.1016/B978-0-323-99746-1.00011-2.

[45] Vincenzo Gentile, Matteo Calò, Michael Bozlar, Marco Simonetti, and Forrest Meggers. Water vapor mass transfer in alginate–graphite bio-based hydrogel for atmospheric water harvesting. *International Journal of Heat and Mass Transfer*, 219: 124794, 2024. ISSN 0017-9310. doi: https://doi.org/10.1016/j.ijheatmasstransfer.2023.124794.

[46] James Templeman, Michael Rogers, John Cant, Brian Mcbride, and Vern Osborne. Effects of a wax organogel and alginate gel complex on holy basil (ocimum sanctum) in vitro ruminal dry matter disappearance and gas production. *Journal of the science of food and agriculture*, 98, 02 2018. doi: 10.1002/jsfa.8973.

[47] Vincenzo Gentile, Michael Bozlar, Matteo Calò, Marco Simonetti, and Forrest Meggers. Alginate biopolymeric coated heat exchanger for atmospheric water harvesting. *ACS ES&T Water*, 4(4):1874–1882, 2024. doi: 10.1021/acsestwater.3c00847.

[48] Arn Mignon, Didier Snoeck, Kenny D'Halluin, Lieve Balcaen, Frank Vanhaecke, Peter Dubruel, Sandra Van Vlierberghe, and Nele De Belie. Alginate biopolymers: Counteracting the impact of superabsorbent polymers on mortar strength. *Construction and Building Materials*, 110:169–174, 2016. ISSN 0950-0618. doi: https://doi.org/10.1016/j.conbuildmat.2016.02.033.

[49] Georgios Archimidis Tsalidis, Daniel Dias, Antonio Martins, Vasileia Vasilaki, João Miguel Ribeiro, and Evina Katsou. Assessing the iso hierarchy validity in circular wastewater treatment life cycle assessments: A portuguese case study. *Resources, Conservation and Recycling*, 215:108146, 2025. ISSN 0921-3449. doi: https://doi.org/10.1016/j.resconrec.2025.108146.

[50] Susbin Raj Wagle, Bozica Kovacevic, Corina Mihaela Ionescu, Daniel Walker, Melissa Jones, Louise Carey, Ryusuke Takechi, Momir Mikov, Armin Mooranian, and Hani

Al-Salami. Pharmacological and biological study of microencapsulated probucol-secondary bile acid in a diseased mouse model. *Pharmaceutics*, 13(8), 2021. ISSN 1999-4923. doi: 10.3390/pharmaceutics13081223.

[51] Anna Ekman Nilsson, Kristina Bergman, Laura Pilar Gomez Barrio, Eduarda M. Cabral, and Brijesh Kumar Tiwari. Life cycle assessment of a seaweed-based biorefinery concept for production of food, materials, and energy. *Algal Research*, 65:102725, 2022. ISSN 2211-9264. doi: https://doi.org/10.1016/j.algal.2022.102725.

[52] Ankur Kumar, Ashish Kothari, Prashant Kumar, Arpana Singh, Kanchan Tripathi, Jitender Gairolla, Manju Pai, and Balram Ji Omar. Introduction to alginate: Biocompatible, biodegradable, antimicrobial nature and various applications. In Ihana Aguiar Severo, André Bellin Mariano, and José Viriato Coelho Vargas, editors, *Alginate*, chapter 2. IntechOpen, Rijeka, 2023. doi: 10.5772/intechopen.110650.

[53] Letizia Aghemo, Luca Lavagna, Eliodoro Chiavazzo, and Matteo Pavese. Comparison of key performance indicators of sorbent materials for thermal energy storage with an economic focus. *Energy Storage Materials*, 55:130–153, 2023. ISSN 2405-8297. doi: https://doi.org/10.1016/j.ensm.2022.11.042.

[54] R.C. RODGERS and G.E. HILL. Equations for vapour pressure versus temperature: Derivation and use of the antoine equation on a hand-held programmable calculator. *British Journal of Anaesthesia*, 50(5):415–424, 1978. ISSN 0007-0912. doi: https://doi.org/10.1093/bja/50.5.415.

[55] Lihua Hu, Zhongping Yang, Yaoguang Wang, Yan Li, Dawei Fan, Di Wu, Qin Wei, and Bin Du. Facile preparation of water-soluble hyperbranched polyamine functionalized multiwalled carbon nanotubes for high-efficiency organic dye removal from aqueous solution. *Scientific Reports*, 7, 06 2017. doi: 10.1038/s41598-017-03490-6.

[56] Stephan Breitenbach, Marcel Skoglund, Jelena Lillepärg, Thomas Emmler, and Frank Mantwill. On the influence of sorbents on the static stiffness of air springs. *Forschung im Ingenieurwesen*, 88, 07 2024. doi: 10.1007/s10010-024-00752-4.

[57] A. L. Myers. Thermodynamics of adsorptionin porous materials. *AIChE Journal*, 2004. doi: 10.1002/aic.690480115.

[58] Tawfik A. Saleh. Chapter 4 - aisotherm models of adsorption processes on adsorbents and nanoadsorbents. In Tawfik A. Saleh, editor, *Surface Science of Adsorbents and Nanoadsorbents*, volume 34 of *Interface Science and Technology*, pages 99–126. Elsevier, 2022. doi: https://doi.org/10.1016/B978-0-12-849876-7.00009-9.

[59] Yuzhi Zhou, Ye Li, Dongxue Liu, Dongbin Liu, Lidong Xu, and Chang Liu. Adsorption optimization of uranium(vi) onto polydopamine and sodium titanate co-functionalized mwcnts using response surface methodology and a modeling approach. *Colloids and Surfaces A: Physicochemical and Engineering Aspects*, 627:127145, 2021. ISSN 0927-7757. doi: https://doi.org/10.1016/j.colsurfa.2021.127145.

[60] ISO. URL https://cdn.standards.iteh.ai/samples/71014/9410fd032fa44c459a550d78c14aa4fc/ISO-9277-2022.pdf. Last visited on 26/10/2025.

[61] Ernesto O. Timmermann. Multilayer sorption parameters: Bet or gab values? *Colloids and Surfaces A: Physicochemical and Engineering Aspects*, 220(1):235–260, 2003. ISSN 0927-7757. doi: https://doi.org/10.1016/S0927-7757(03)00059-1.

[62] Jiří Blahovec and Stavros Yanniotis. Gab generalized equation for sorption phenomena. *Food and Bioprocess Technology*, 1:82–90, 01 2008. doi: 10.1007/s11947-007-0012-3.

[63] Crank J. *The Mathematics of Diffusion*. J. Am. Chem. Soc, 1975. doi: 10.1021/ja01562a072.

[64] Peter Wilson and H. Alan Mantooth. Chapter 3 - design analysis. In *Model-Based Engineering for Complex Electronic Systems*, pages 27–78. Newnes, Oxford, 2013. ISBN 978-0-12-385085-0. doi: https://doi.org/10.1016/B978-0-12-385085-0.00003-8.

[65] The MathWorks Inc. Matlab version: 9.10.0 (r2021a). URL https://www.mathworks.com. Last visited on 26/10/2025.

[66] Stefano Brandani and Enzo Mangano. The zero length column technique to measure adsorption equilibrium and kinetics: lessons learnt from 30 years of experience. *Adsorption*, 27:1–33, 04 2021. doi: 10.1007/s10450-020-00273-w.

[67] Zhong Li and Ralph T. Yang. Concentration profile for linear driving force model for diffusion in a particle. *AlChE Journal*, 45, 1999.

[68] Ibrahim I. El-Sharkawy. On the linear driving force approximation for adsorption cooling applications. *International Journal of Refrigeration*, 34(3):667–673, 2011. ISSN 0140-7007. doi: https://doi.org/10.1016/j.ijrefrig.2010.12.006.

[69] Bourhan Tashtoush and Anas Alshoubaki. Atmospheric water harvesting: A review of techniques, performance, renewable energy solutions, and feasibility. *Energy*, 280: 128186, 2023. ISSN 0360-5442. doi: https://doi.org/10.1016/j.energy.2023.128186.

[70] Yousef A. Tayeh. A comprehensive review of reverse osmosis desalination: Technology, water sources, membrane processes, fouling, and cleaning. *Desalination and Water Treatment*, 320:100882, 2024. ISSN 1944-3986. doi: https://doi.org/10.1016/j.dwt.2024.100882.

[71] Luisa Martínez-Acosta, Alvaro Alberto López-Lambraño, and Alvaro López-Ramos. Design criteria for planning the agricultural rainwater harvesting systems: A review. *Applied Sciences*, 9(24), 2019. ISSN 2076-3417. doi: 10.3390/app9245298.

[72] Alexandra Cassivi, Anne Carabin, Caetano Dorea, Manuel J. Rodriguez, and Stéphanie Guilherme. Domestic access to water in a decentralized truck-to-cistern system: a case study in the northern village of kangiqsualujjuaq, nunavik (canada). *Journal of Water and Health*, 22(5):797–810, 04 2024. ISSN 1477-8920. doi: 10.2166/wh.2024.246.

[73] Megbar Wondie. Modeling cloud seeding technology for rain enhancement over the arid and semiarid areas of ethiopia. *Heliyon*, 9(4):e14974, 2023. ISSN 2405-8440. doi: https://doi.org/10.1016/j.heliyon.2023.e14974.

[74] Manzoor Qadir, Gabriela C. Jiménez, Rebecca L. Farnum, and Peter Trautwein. Research history and functional systems of fog water harvesting. *Frontiers in Water*, Volume 3 - 2021, 2021. ISSN 2624-9375. doi: 10.3389/frwa.2021.675269.

[75] Maestre-Valero, Victoriano Álvarez, V. Baille, Bernardo Martin-Gorriz, and Belen Gallego-Elvira. Comparative analysis of two polyethylene foil materials for dew harvesting in a semi-arid climate. *Journal of Hydrology*, 410:84–91, 11 2011. doi: 10.1016/j.jhydrol.2011.09.012.

[76] Vincenzo Gentile, Michael Bozlar, Forrest Meggers, and Marco Simonetti. Liter-scale atmospheric water harvesting for dry climates driven by low temperature solar heat. *Energy*, 254:124295, 2022. ISSN 0360-5442. doi: https://doi.org/10.1016/j.energy.2022.124295.

[77] Ahmed Qandil, Ali Othman, and N. Beithou. Experimental analysis of atmospheric water harvester using ammonia vapour absorption system. *Journal of Ecological Engineering*, 24:221–229, 02 2023. doi: 10.12911/22998993/156612.

[78] Binoe Abuan and Menandro Berana. Ejector profile modelling for heat-driven ejector refrigeration system without involving shock. 11 2015. doi: 10.1115/IMECE2015-52521.

[79] Mikah Inkawhich, Jeb Shingler, Remington S. Ketchum, Wei Pan, Robert A. Norwood, and Kerri L. Hickenbottom. Temporal performance indicators for an integrated pilot-scale membrane distillation-concentrated solar power/photovoltaic system. *Applied Energy*, 349:121675, 2023. ISSN 0306-2619. doi: https://doi.org/10.1016/j.apenergy.2023.121675.

[80] Bourhan Tashtoush and Anas Alshoubaki. Atmospheric water harvesting: A review of techniques, performance, renewable energy solutions, and feasibility. *Energy*, 280:128186, 2023. ISSN 0360-5442. doi: https://doi.org/10.1016/j.energy.2023.128186.

[81] Andrew Marsh. URL https://andrewmarsh.com/software/psychro-chart-web/. Last visited on 26/10/2025.

[82] Alessandra Criscuoli, Alfredo Capuano, Michele Andreucci, and Enrico Drioli. Low-temperature direct contact membrane distillation for the treatment of aqueous solutions containing urea. *Membranes*, 10:176, 08 2020. doi: 10.3390/membranes10080176.

[83] J.-C. Schrotter, S. Rapenne, J. Leparc, P.-J. Remize, and S. Casas. *2.03 - Current and Emerging Developments in Desalination with Reverse Osmosis Membrane Systems*. Elsevier, Oxford, 2010. ISBN 978-0-08-093250-7. doi: https://doi.org/10.1016/B978-0-08-093250-7.00047-5.

[84] Lauren F. Greenlee, Desmond F. Lawler, Benny D. Freeman, Benoit Marrot, and Philippe Moulin. Reverse osmosis desalination: Water sources, technology, and today's challenges. *Water Research*, 43(9):2317–2348, 2009. ISSN 0043-1354. doi: https://doi.org/10.1016/j.watres.2009.03.010.

[85] Regione Sicilia. URL https://pti.regione.sicilia.it/portal/page/portal/PIR_PORTALE/PIR_LaStrutturaRegionale/PIR_AssEnergia/PIR_Dipartimentodellacquaedeirifiuti/PIR_Bandi/PIR_20131118IMPIANTODISSALAZIONEPANTELLERIA/Relazione%20Dissalatore%20Pantelleria.pdf. Last visited on 26/10/2025.

[86] Matteo Morciano, Matteo Fasano, Luca Bergamasco, Alessandro Albiero, Mario Lo Curzio, Pietro Asinari, and Eliodoro Chiavazzo. Sustainable freshwater production using passive membrane distillation and waste heat recovery from portable generator sets. *Applied Energy*, 258:114086, 2020. ISSN 0306-2619. doi: https://doi.org/10.1016/j.apenergy.2019.114086.

[87] Jolanta Bohdziewicz, Michał Bodzek, and Ewa Wąsik. The application of reverse osmosis and nanofiltration to the removal of nitrates from groundwater. *Desalination*, 121(2):139–147, 1999. ISSN 0011-9164. doi: https://doi.org/10.1016/S0011-9164(99)00015-6.

[88] David Warsinger, Karan Mistry, Kishor Nayar, Hyung Won Chung, and John V. Entropy generation of desalination powered by variable temperature waste heat. *Entropy*, 17:7530–7566, 10 2015. doi: 10.3390/e17117530.

[89] P. Ranjitha Raj, J.S. Jayakumar, and R. Ajith Kumar. On the selection of humidification dehumidification desalination system cycle for high productivity, low energy consumption and low capital cost. *Desalination*, 586:117876, 2024. ISSN 0011-9164. doi: https://doi.org/10.1016/j.desal.2024.117876.

[90] Rachit Singh Patel, Prathyusha Mekala, Deepjyoti Mech, and Marc Busch. Desalination of seawater using gas hydrate technology – current status and future direction. 12 2013.

[91] Mitul Prajapati, Manan Shah, and Bhavna Soni. A review of geothermal integrated desalination: A sustainable solution to overcome potential freshwater shortages. *Journal of Cleaner Production*, 326:129412, 2021. ISSN 0959-6526. doi: https://doi.org/10.1016/j.jclepro.2021.129412.

[92] Chun Deng and Xiao Feng. 13 - water network integration with multiple partitioning interception units. In Jiří Jaromír Klemeš, editor, *Handbook of Process Integration (PI) (Second Edition)*, Woodhead Publishing Series in Energy, pages 437–465. Woodhead Publishing, second edition edition, 2023. ISBN 978-0-12-823850-9. doi: https://doi.org/10.1016/B978-0-12-823850-9.00030-X.

[93] Sultan Alnajdi, Ali Naderi Beni, Albraa A. Alsaati, Mitul Luhar, Amy E. Childress, and David M. Warsinger. Practical minimum energy use of seawater reverse osmosis. *Joule*, 8(11):3088–3105, 2024. ISSN 2542-4351. doi: https://doi.org/10.1016/j.joule.2024.08.005.

[94] U. Spohn. *MEMBRANE TECHNIQUES | Dialysis and Reverse Osmosis*. Elsevier, Oxford, second edition edition, 2005. ISBN 978-0-12-369397-6. doi: https://doi.org/10.1016/B0-12-369397-7/00367-8.

[95] A. Alhadidi, A.J.B Kemperman, B. Blankert, J.C. Schippers, M. Wessling, and W.G.J. van der Meer. Silt density index and modified fouling index relation, and effect of pressure, temperature and membrane resistance. *Desalination*, 273(1):48–56, 2011. ISSN 0011-9164. doi: https://doi.org/10.1016/j.desal.2010.11.031. Special issue to mark the 45th Anniversary of launching Desalination journal and to honour Professor David Hasson for his enormous support and contribution to Desalination.

[96] Isnaeni Nurjanah, Ting-Ting Chang, Sheng-Jie You, Chih-Yung Huang, and Wu-Yang Sean. Reverse osmosis integrated with renewable energy as sustainable technology: A review. *Desalination*, 581:117590, 2024. ISSN 0011-9164. doi: https://doi.org/10.1016/j.desal.2024.117590.

[97] Wartsila. URL https://www.wartsila.com/waw/freshwater/multi-stage-flash-evaporators. Last visited on 26/10/2025.

[98] Waterman Australia. URL https://watermanaustralia.com/vacuum-multi-effect-distillation-desalination/. Last visited on 26/10/2025.

[99] Aiman Eid Al-Rawajfeh, Heike Glade, and Joachim Ulrich. Scaling in multiple-effect distillers: the role of co2 release. *Desalination*, 182(1):209–219, 2005. ISSN 0011-9164. doi: https://doi.org/10.1016/j.desal.2005.04.013. Desalination and the Environment.

[100] Matteo Morciano, Matteo Fasano, Uktam Salomov, Luigi Ventola, Eliodoro Chiavazzo, and Pietro Asinari. Efficient steam generation by inexpensive narrow gap evaporation device for solar applications. *Scientific Reports*, 7:11970, 2017. doi: 10.1038/s41598-017-12152-6.

[101] Matteo Morciano, Matteo Fasano, Svetlana V. Boriskina, Eliodoro Chiavazzo, and Pietro Asinari. Solar passive distiller with high productivity and marangoni effect-driven salt rejection. *Energy Environ. Sci.*, 13:3646–3655, 2020. doi: 10.1039/D0EE01440K.

[102] Eliodoro Chiavazzo, Matteo Morciano, Francesca Viglino, Matteo Fasano, and Pietro Asinari. Passive solar high-yield seawater desalination by modular and low-cost distillation. *Nature Sustainability*, 1:763–772, 2018. doi: 10.1038/s41893-018-0186-x.

[103] Mohanad Kamaz, Arijit Sengupta, Ashley Gutierrez, Yu-Hsuan Chiao, and Ranil Wickramasinghe. Surface modification of pvdf membranes for treating produced waters by direct contact membrane distillation. *International Journal of Environmental Research and Public Health*, 16(5), 2019. ISSN 1660-4601. doi: 10.3390/ijerph16050685.

[104] Noreddine Ghaffour, Thomas M. Missimer, and Gary L. Amy. Technical review and evaluation of the economics of water desalination: Current and future challenges for better water supply sustainability. *Desalination*, 309:197–207, 2013. ISSN 0011-9164. doi: https://doi.org/10.1016/j.desal.2012.10.015.

[105] Pankaj P. Gohil, Hemangi Desai, Amit Kumar, and Rupesh Kumar. Current status and advancement in thermal and membrane-based hybrid seawater desalination technologies. *Water*, 15(12), 2023. ISSN 2073-4441. doi: 10.3390/w15122274.

[106] Pablo López-Porfiri, Sebastián Ramos-Paredes, Patricio Núñez, and Patricia Gorgojo. Towards the technological maturity of membrane distillation: the md module performance curve. *npj Clean Water*, 6, 2023. ISSN 2059-7037. doi: 10.1038/s41545-023-00234-0.

[107] Sakineh Tavakkoli, Omkar R. Lokare, Radisav D. Vidic, and Vikas Khanna. A techno-economic assessment of membrane distillation for treatment of marcellus shale produced water. *Desalination*, 416:24–34, 2017. ISSN 0011-9164. doi: https://doi.org/10.1016/j.desal.2017.04.014.

[108] Sajedeh Rooholamini, Mohsen Salimi, Amirhossein Amirfakhraei, Majid Amidpour, Mona Zamani Pedram, and Taleb Zarei. Advances in sustainable adsorption desalination configuration, materials, and challenges: A state-of-the-art review. *Cleaner Engineering and Technology*, 26:100946, 2025. ISSN 2666-7908. doi: https://doi.org/10.1016/j.clet.2025.100946.

[109] Yonghyun Shin, Jihyuk Choi, Youngkyu Park, Yongjun Choi, and Sangho Lee. Influence of operation conditions on the performance of pilot-scale vacuum membrane distillation (vmd). *Desalination and Water Treatment*, 97:1–7, 2017. ISSN 1944-3986. doi: https://doi.org/10.5004/dwt.2017.20664.

[110] Ali Naeimi Tabasian, Alberto Saija, Matteo Morciano, Matteo Fasano, Alberto Tiraferri, and Eliodoro Chiavazzo. Performance analysis of a scalable solar-assisted pilot scale adsorption desalination and cooling system. *Energy Conversion and Management*, 343:120190, 2025. ISSN 0196-8904. doi: https://doi.org/10.1016/j.enconman.2025.120190.

[111] URL https://www.waterworld.com/home/article/16202745/low-energy-adsorption-desalination-and-cooling-plant-opened-in-saudi-arabia. Last visited on 26/10/2025.

[112] WHO. URL https://iris.who.int/bitstream/handle/10665/352532/9789240045064-eng.pdf. Last visited on 26/10/2025.

[113] URL https://eur-lex.europa.eu/legal-content/EN/TXT/PDF/?uri=CELEX:32020L2184. Last visited on 26/10/2025.

[114] Gazzetta Ufficiale. URL https://www.gazzettaufficiale.it/eli/id/2023/03/06/23G00025/sg. Last visited on 26/10/2025.

[115] Serge Zhuiykov. Solid-state sensors monitoring parameters of water quality for the next generation of wireless sensor networks. *Sensors and Actuators B: Chemical*, 161 (1):1–20, 2012. ISSN 0925-4005. doi: https://doi.org/10.1016/j.snb.2011.10.078.

[116] Anna Rusydi. Correlation between conductivity and total dissolved solid in various type of water: A review. *IOP Conference Series: Earth and Environmental Science*, 118:012019, 02 2018. doi: 10.1088/1755-1315/118/1/012019.

[117] Alexander P. Safronov, Nadezhda M. Kurilova, Lidiya V. Adamova, Tatyana F. Shklyar, Felix A. Blyakhman, and Andrey Yu. Zubarev. Hydrogels based on polyacrylamide and calcium alginate: Thermodynamic compatibility of interpenetrating networks, mechanical, and electrical properties. *Biomimetics*, 8, 2023. ISSN 2313-7673. doi: 10.3390/biomimetics8030279.

[118] Hemant Mittal, Ali Al Alili, and Saeed M. Alhassan. Adsorption isotherm and kinetics of water vapors on novel superporous hydrogel composites. *Microporous and Mesoporous Materials*, 299:110106, 2020. ISSN 1387-1811. doi: https://doi.org/10.1016/j.micromeso.2020.110106.

[119] Ramy H. Mohammed, Tahmid Hasan Rupam, Roberto Nunez, Jeremy Spitzenberger, Shahab K. Mohammadian, Jaewon Lee, Bidyut Baran Saha, and Hongbin Ma. Comparative analysis of four metal-organic frameworks for adsorption desalination. *Colloids and Surfaces A: Physicochemical and Engineering Aspects*, 673:131750, 2023. ISSN 0927-7757. doi: https://doi.org/10.1016/j.colsurfa.2023.131750.

[120] Kjell A. Doksum Peter J. Bickel. *Mathematical Statistics - Basic Ideas and Selected Topics, Volumes I-II Package*. 2015.

[121] Stefano Brandani, Enzo Mangano, and Giulio Santori. Water adsorption on aqsoa-fam-z02 beads. *Journal of Chemical and Engineering Data*, 67:1723–1731, 07 2022. doi: 10.1021/acs.jced.1c00942.

[122] Francesco Gaggini, Rafael Natalio Fontana Crespo, Matteo Calò, Vincenzo Maria Gentile, Alberto Macii, and Edoardo Patti. An internet of things ecosystem for atmospheric water generators. *IEEE Access*, 13:77565–77581, 2025. doi: 10.1109/ACCESS.2025.3562742.

[123] J.G. Ji, R.Z. Wang, and L.X. Li. New composite adsorbent for solar-driven fresh water production from the atmosphere. *Desalination*, 212(1):176–182, 2007. ISSN 0011-9164. doi: https://doi.org/10.1016/j.desal.2006.10.008.

[124] J.Y. Wang, J.Y. Liu, R.Z. Wang, and L.W. Wang. Experimental investigation on two solar-driven sorption based devices to extract fresh water from atmosphere. *Applied Thermal Engineering*, 127:1608–1616, 2017. ISSN 1359-4311. doi: https://doi.org/10.1016/j.applthermaleng.2017.09.063.

[125] Hong An, Yang Chen, Yong Wang, Xiaohua Liu, Yongheng Ren, Ziliang Kang, Jinping Li, and Libo Li. High-performance solar-driven water harvesting from air with a cheap and scalable hygroscopic salt modified metal–organic framework. *Chemical Engineering Journal*, 461:141955, 2023. ISSN 1385-8947. doi: https://doi.org/10.1016/j.cej.2023.141955.

[126] Alina LaPotin, Yang Zhong, Lenan Zhang, Lin Zhao, Arny Leroy, Hyunho Kim, Sameer R. Rao, and Evelyn N. Wang. Dual-stage atmospheric water harvesting device for scalable solar-driven water production. *Joule*, 5(1):166–182, 2021. ISSN 2542-4351. doi: https://doi.org/10.1016/j.joule.2020.09.008.

[127] Hyunho Kim, Sameer R. Rao, and Eugene A. et al. Kapustin. Adsorption-based atmospheric water harvesting device for arid climates. *Nature Communications*, 9: 1191, 2018. ISSN 2041-1723. doi: 10.1038/s41467-018-03162-7.

[128] Ehab S. Ali, Ahmed A. Askalany, K. Harby, Mohamed Refaat Diab, Bahgat R.M. Hussein, and Ahmed S. Alsaman. Experimental adsorption water desalination system utilizing activated clay for low grade heat source applications. *Journal of Energy Storage*, 43:103219, 2021. ISSN 2352-152X. doi: https://doi.org/10.1016/j.est.2021.103219.

[129] Xiaolin Wang and Kim Choon Ng. Experimental investigation of an adsorption desalination plant using low-temperature waste heat. *Applied Thermal Engineering*, 25(17): 2780–2789, 2005. ISSN 1359-4311. doi: https://doi.org/10.1016/j.applthermaleng.2005.02.011.

[130] Xiaolin Wang, Hui Tong Chua, and Kim Choon Ng. Experimental investigation of silica gel–water adsorption chillers with and without a passive heat recovery scheme. *International Journal of Refrigeration*, 28(5):756–765, 2005. ISSN 0140-7007. doi: https://doi.org/10.1016/j.ijrefrig.2004.11.011.

[131] Mahmoud Elsheniti, Raya AL-Dadah, Saad Mahmoud, and İsmail Solmaz. Numerical and experimental investigation of multiple heat exchanger modules in cooling and desalination adsorption system using metal organic framework. *Energy Conversion and Management*, 251:114934, 01 2022. doi: 10.1016/j.enconman.2021.114934.

[132] Christopher Olkis, Stefano Brandani, and Giulio Santori. Design and experimental study of a small scale adsorption desalinator. *Applied Energy*, 253:113584, 2019. ISSN 0306-2619. doi: https://doi.org/10.1016/j.apenergy.2019.113584.

[133] Eman Elsayed, Raya AL-Dadah, Saad Mahmoud, Paul Anderson, and Ahmed Elsayed. Experimental testing of aluminium fumarate mof for adsorption desalination. *Desalination*, 475:114170, 2020. ISSN 0011-9164. doi: https://doi.org/10.1016/j.desal.2019.114170.

[134] Ahmed S. Alsaman, Ahmed A. Askalany, K. Harby, and Mahmoud S. Ahmed. Performance evaluation of a solar-driven adsorption desalination-cooling system. *Energy*, 128:196–207, 2017. ISSN 0360-5442. doi: https://doi.org/10.1016/j.energy.2017.04.010.

[135] Kim Choon Ng, Kyaw Thu, Anutosh Chakraborty, Bidyut Baran Saha, and Won Gee Chun. Solar-assisted dual-effect adsorption cycle for the production of cooling effect and potable water. *International Journal of Low-Carbon Technologies*, 4(2):61–67, 05 2009. ISSN 1748-1317. doi: 10.1093/ijlct/ctp008.

[136] Mohamed Ghazy, Ahmed A. Askalany, E.M.M. Ibrahim, A.S.A. Mohamed, Ehab S. Ali, and Raya AL-Dadah. Solar powered adsorption desalination system employing cpo-27(ni). *Journal of Energy Storage*, 53:105174, 2022. ISSN 2352-152X. doi: https://doi.org/10.1016/j.est.2022.105174.

[137] Kyaw Thu, Kim Ng, Bidyut Saha, Anutosh Chakraborty, and Shigeru Koyama. Operational strategy of adsorption desalination systems. *International Journal of Heat and Mass Transfer*, 52:1811–1816, 03 2009. doi: 10.1016/j.ijheatmasstransfer.2008.10.012.

[138] Christopher Olkis, Hongsheng Dong, Stefano Brandani, and Giulio Santori. Ionogels at the water-energy nexus for desalination powered by ultralow-grade heat. *Journal of Chemical and Engineering Data*, 67:1723–1731, 07 2022. doi: 10.1021/acs.jced.1c00942.

[139] Mauro Luberti, Robert Gowans, Patrick Finn, and Giulio Santori. An estimate of the ultralow waste heat available in the european union. *Energy*, 238:121967, 2022. ISSN 0360-5442. doi: https://doi.org/10.1016/j.energy.2021.121967.

[140] Yueting Hao, Haojie Zhou, Tong Tian, Wei Zhang, Xin Zhou, Qingfei Shen, Tong Wu, and Ji Li. Data centers waste heat recovery technologies: Review and evaluation. *Applied Energy*, 384:125489, 2025. ISSN 0306-2619. doi: https://doi.org/10.1016/j.apenergy.2025.125489.

[141] H. Kim, H. Cho, and S. et al. Narayanan. Characterization of adsorption enthalpy of novel water-stable zeolites and metal-organic frameworks. *Scientific Reports*, 6:19097, 2016. doi: https://doi.org/10.1038/srep19097.

[142] DYMAN. URL https://dyman-project.eu/. Last visited on 26/10/2025.

[143] Arduino. URL https://www.arduino.cc/. Last visited on 26/10/2025.

[144] Nasreen and Editor Ijmtst. Ocean salinity. *International Journal for Modern Trends in Science and Technology*, 8:296–302, 01 2022. doi: 10.46501/IJMTST0801052.

[145] HYPERGRYD. URL https://hypergryd.eu/. Last visited on 26/10/2025.

[146] Tridge. URL https://dir.tridge.com/prices/sodium-alginate. Last visited on 26/10/2025.

[147] IMARC Group. URL https://www.marketresearch.com/IMARC-v3797/. Last visited on 26/10/2025.

[148] Shihab AL-Hasni and Giulio Santori. The cost of manufacturing adsorption chillers. *Thermal Science and Engineering Progress*, 39:101685, 2023. ISSN 2451-9049. doi: https://doi.org/10.1016/j.tsep.2023.101685.

[149] URL https://www.proionic.com/product/1-ethyl-3-methylimidazolium-bisfluorosulfonylimide/. Last visited on 26/10/2025.

[150] Sorption Technologies GmbH. URL https://sorption-technologies.com/. Last visited on 26/10/2025.

[151] Modbus. URL https://www.modbustools.com/modbus.html. Last visited on 26/10/2025.

[152] Siemens. Siemens scope v11.64. URL https://www.siemens.com/it/it/prodotti/buildingtechnologies/hvac/oem/climatix.html.

[153] Geogebra. URL https://www.geogebra.org/. Last visited on 26/10/2025.

Appendix A

Models derivation

Step-by-step derivation of FD-based numerical model for large uptake ranges

We can start from equation 2.31, where this time $D = D(C)$, and expand the derivatives:

$$\frac{\partial C(x,t)}{\partial t} = \frac{\partial}{\partial x}\left[D(C)\cdot\frac{\partial C(x,t)}{\partial x}\right] \tag{A.1}$$

$$= \frac{\partial D(C)}{\partial x}\cdot\frac{\partial C(x,t)}{\partial x} + D(C)\cdot\frac{\partial^2 C(x,t)}{\partial x^2} \tag{A.2}$$

$$= \frac{\partial D(C)}{\partial C}\cdot\frac{\partial C(x,t)}{\partial x}\cdot\frac{\partial C(x,t)}{\partial x} + D(C)\cdot\frac{\partial^2 C(x,t)}{\partial x^2} \tag{A.3}$$

$$= \frac{\partial D(C)}{\partial C}\cdot\left[\frac{\partial C(x,t)}{\partial x}\right]^2 + D(C)\cdot\frac{\partial^2 C(x,t)}{\partial x^2} \tag{A.4}$$

We can approximate the spatial derivatives with a finite difference method, for example with equispaced centered difference quotients[1]:

$$\left.\frac{\partial C(x,t)}{\partial x}\right|_{x=x_j} \cong \frac{C_{j+1}-C_{j-1}}{2h} \to \left[\left.\frac{\partial C(x,t)}{\partial x}\right|_{x=x_j}\right]^2 \cong \frac{C_{j+1}^2 - 2\cdot C_{j-1}\cdot C_{j+1} + C_{j-1}^2}{4h^2} \tag{A.5}$$

$$\left.\frac{\partial^2 C(x,t)}{\partial x^2}\right|_{x=x_j} \cong \frac{C_{j+1}-2C_j+C_{j-1}}{h^2} \tag{A.6}$$

[1]This is not the optimal choice in general, and may result in unwanted oscillations in proximity of the domain borders and inefficiencies in computation. Indeed, since we are modeling diffusion (which happens at each moment along a preferred direction, according to the instantaneous concentration gradient), implementing direction-sensitive methods would be a more effective technique. Nevertheless, the computational resources required for the analyses carried out in this research are not significantly large, and the proposed sub-optimal implementation is already sufficient for our purposes.

where C_j is the approximation of C at the spatial coordinate x_j, and h is the spatial interval between two adjacent points on the spatial grid, and whose nodes go from $j=0$ to $j=N+1$ (so there are N internal nodes, $j=0$ is the leftmost node near the wall, and $j+1$ the rightmost one near the environment). The function $D(C)$ is known, so no further approximation is needed for evaluating its derivative, which can be analytically or numerically calculated and preliminarily evaluated at the generic C_j.
For what concerns time derivatives, we can approximate them numerically by using "forward Euler method" (an explicit method, stable only for sufficient small value of time increments) or "backward Euler method" (no stability issues, but larger computational cost) [64]. For example, with forward Euler method:

$$\left.\frac{\partial C(x,t)}{\partial t}\right|_t \cong \frac{C^{t+1}-C^t}{\Delta t} \tag{A.7}$$

Where C^t is the concentration at time instant t and Δt is the discrete time increment (constant for simplicity). From this, the generic discretized Fick equation is written as follows:

$$\begin{aligned}\frac{{C_j}^{t+1}-{C_j}^t}{\Delta t} = \left.\frac{\partial D(C)}{\partial C}\right|_{{C_j}^t} \cdot \frac{\left(C^t_{j+1}\right)^2 - 2\cdot C^t_{j-1}\cdot C^t_{j+1} + \left(C^t_{j-1}\right)^2}{4h^2} + \\ + D\left({C_j}^t\right)\cdot\frac{C^t_{j+1}-2{C_j}^t+C^t_{j-1}}{h^2}\end{aligned} \tag{A.8}$$

for each node j in the spatial grid $\left(x_0, x_1, x_2, \ldots x_j, \ldots x_N, x_{N+1}\right)$ and for each time t in the time grid. At this point, eq. A.8 must be adjusted to fit the boundary conditions. In particular, at the node $j=0$ it must be imposed a null derivative of C respect to t, and at $j=N+1$ it must be imposed a known value of $C=C_{eq}(t)$ over time. First of all, the equation for node $j=0$:

$$\begin{aligned}\frac{{C_0}^{t+1}-{C_0}^t}{\Delta t} = \left.\frac{\partial D(C)}{\partial C}\right|_{{C_0}^t} \cdot \frac{\left({C_1}^t\right)^2 - 2\cdot {C_{-1}}^t\cdot {C_1}^t + \left({C_{-1}}^t\right)^2}{4h^2} + \\ + D\left({C_0}^t\right)\cdot\frac{{C_1}^t-2{C_0}^t+{C_{-1}}^t}{h^2}\end{aligned} \tag{A.9}$$

Where a "virtual" node at $j=-1$ was added before $j=0$ for being able to write the equation. In order to preserve the 2nd order approximation, C_{-1} is chosen in such a way that the Neumann condition at $j=0$ approximated with centered difference quotient is satisfied. In particular:

$$\frac{{C_1}^t-{C_{-1}}^t}{2h} \cong J^t_{x=0} = 0 \qquad \rightarrow \qquad {C_{-1}}^t = {C_1}^t \tag{A.10}$$

Substituting into eq. A.8, the left boundary equation becomes:

$$\frac{{C_0}^{t+1}-{C_0}^t}{\Delta t} = D\left({C_0}^t\right)\cdot 2\cdot\frac{{C_1}^t-{C_0}^t}{h^2} \tag{A.11}$$

For what concerns the other boundary condition, one possibility is to reduce by 1 the number of unknown variables, substituting $\left[C_{eq}(t)\right]^t$ in place of of C^t_{N+1}. Another possibility we prefer, is to keep unvaried the number of unknowns, substituting the last equation with a trivial imposition of the value. For the equation at the node $j = N+1$:

$$C^{t+1}_{N+1} = C_{eq}(t+1) \tag{A.12}$$

Finding the numerical solution to the spatial distribution of concentration at time t+1 corresponds to update each spatial component to a new value which is function of some values of the spatial distribution vector at the previous time t. In formulae, keeping on the left side of the equations only variables evaluated at time $t+1$, we can write the system of algebraic equation in eq. 2.35.

Step-by-step LDFDw model derivation

The following mathematical derivation has been first published in [45]. We start from the LDF formulation:

$$\begin{cases} \frac{dw(t)}{dt} = \frac{F_0 \cdot D(w)}{R_p^2} \cdot \left[w_{eq} - w(t)\right] \\ D(w) = a + b \cdot w \\ w(t_0) = w_0 \end{cases} \tag{A.13}$$

where t is time, w is water uptake, F_0 is a shape factor equal to 15 for spherical geometries, R_p is the particle radius, D is the diffusivity, w_0 is the water uptake at the starting time t_0, w_{eq} it is the equilibrium water uptake. In this case, it is supposed that D varies linearly with w, and it is not dependent on time as an independent variable or on temperature or other physical quantities: this allows to close the problem and evaluate analytically and conveniently the solution of the Cauchy problem.
Here the step-by-step procedure:

$$\begin{aligned} \frac{dw}{dt} =& \frac{F_0 \cdot D}{R_p^2} \cdot \left(w_{eq} - w\right) = \\ =& \frac{F_0}{R_p^2} \cdot (a + b \cdot w) \cdot \left(w_{eq} - w\right) \end{aligned}$$

By separation of variables:

$$\frac{dw}{(a+b\cdot w)\cdot\left(w_{eq}-w\right)}=\frac{F_0}{R_p^2}\cdot dt$$

$$\int_{w_0}^{w}\frac{1}{(a+b\cdot\widetilde{w})\cdot\left(w_{eq}-\widetilde{w}\right)}d\widetilde{w}=\int_{t_0}^{t}\frac{F_0}{R_p^2}d\widetilde{t}$$

$$\int_{w_0}^{w}\frac{1}{(a+b\cdot\widetilde{w})\cdot\left(w_{eq}-\widetilde{w}\right)}d\widetilde{w}=\frac{F_0}{R_p^2}\cdot(t-t_0) \tag{A.14}$$

(A.15)

Re-writing the integrand in the definite integral on the left with partial fraction decomposition:

$$\frac{1}{(a+b\cdot x)\cdot\left(w_{eq}-x\right)}=\frac{A}{a+b\cdot x}+\frac{B}{w_{eq}-x}=\frac{Aw_{eq}-Ax+Ba+Bbx}{(a+b\cdot x)\cdot\left(w_{eq}-x\right)}$$

From which:

$$\begin{cases}Aw_{eq}+Ba=1\\-A+Bb=0\end{cases}\quad\rightarrow\quad\begin{cases}A=\frac{b}{a+bw_{eq}}\\B=\frac{1}{a+bw_{eq}}\end{cases} \tag{A.16}$$

The definite integral is now sum of two elementary integrals:

$$\int_{w_0}^{w}\frac{1}{(a+b\cdot\widetilde{w})\cdot\left(w_{eq}-\widetilde{w}\right)}d\widetilde{w}=$$

$$=\int_{w_0}^{w}\left(\frac{b}{a+bw_{eq}}\cdot\frac{1}{a+b\cdot\widetilde{w}}+\frac{1}{a+bw_{eq}}\cdot\frac{1}{w_{eq}-\widetilde{w}}\right)d\widetilde{w}=$$

$$=\frac{b}{a+bw_{eq}}\cdot\int_{w_0}^{w}\frac{1}{a+b\cdot\widetilde{w}}d\widetilde{w}+\frac{1}{a+bw_{eq}}\cdot\int_{w_0}^{w}\frac{1}{w_{eq}-\widetilde{w}}d\widetilde{w}=$$

$$=\frac{b}{a+bw_{eq}}\cdot\left[\frac{\log|a+b\cdot\widetilde{w}|}{b}\right]_{w_0}^{w}+\frac{1}{a+bw_{eq}}\cdot\left[-\log\left|w_{eq}-\widetilde{w}\right|\right]_{w_0}^{w}=$$

$$=\frac{1}{a+bw_{eq}}\cdot\left[\log\left|\frac{a+b\cdot\widetilde{w}}{w_{eq}-\widetilde{w}}\right|\right]_{w_0}^{w}=$$

$$=\frac{1}{a+bw_{eq}}\cdot\left[\log\left|\frac{a+b\cdot w}{w_{eq}-w}\right|-\log\left|\frac{a+b\cdot w_0}{w_{eq}-w_0}\right|\right]$$

Going back to the A.14:

$$\int_{w_0}^{w} \frac{1}{(a+b\cdot\widetilde{w})\cdot\left(w_{eq}-\widetilde{w}\right)} d\widetilde{w} = \frac{F_0}{R_p^2}\cdot(t-t_0)$$

$$\frac{1}{a+bw_{eq}}\cdot\left[\log\left|\frac{a+b\cdot w}{w_{eq}-w}\right| - \log\left|\frac{a+b\cdot w_0}{w_{eq}-w_0}\right|\right] = \frac{F_0}{R_p^2}\cdot(t-t_0)$$

$$\frac{1}{a+bw_{eq}}\cdot\left[\log\left|\frac{a+b\cdot w}{w_{eq}-w}\right| - \log\left|\frac{a+b\cdot w_0}{w_{eq}-w_0}\right|\right] = \frac{F_0}{R_p^2}\cdot(t-t_0)$$

$$\log\left|\frac{a+b\cdot w}{w_{eq}-w}\right| = \log\left|\frac{a+b\cdot w_0}{w_{eq}-w_0}\right| + \frac{F_0\cdot\left(a+b\cdot w_{eq}\right)}{R_p^2}\cdot(t-t_0)$$

Since $a+b\cdot w$ is the expression for the diffusion coefficient D, according to its physical meaning, such contribution is always strictly positive.
Instead, the expression $w_{eq}-w = w_{eq}-w(t)$ might be instantaneously positive or negative, according to the equilibrium value the material is pointing at.
In the case of desorption (regeneration), $w_{eq} < w(t) < w_0,\ \forall t > 0$; in case of adsorption, $w_{eq} > w(t) > w_0, \forall t > 0$.
In the case of adsorption, the calculations proceed then as follows:

$$\log\left(\frac{a+b\cdot w}{w_{eq}-w}\right) = \log\left(\frac{a+b\cdot w_0}{w_{eq}-w_0}\right) + \frac{F_0\cdot\left(a+b\cdot w_{eq}\right)}{R_p^2}\cdot(t-t_0)$$

$$\frac{a+b\cdot w}{w_{eq}-w} = K_1\cdot e^{K_2\cdot(t-t_0)} \tag{A.17}$$

(A.18)

where:

$$K_1 = \frac{a+b\cdot w_0}{w_{eq}-w_0} \qquad K_2 = \frac{F_0\cdot\left(a+b\cdot w_{eq}\right)}{R_p^2} \tag{A.19}$$

Instead, in case of desorption, the calculations proceed as follows:

$$\log\left(\frac{a+b\cdot w}{-w_{eq}+w}\right) = \log\left(\frac{a+b\cdot w_0}{-w_{eq}+w_0}\right) + \frac{F_0\cdot\left(a+b\cdot w_{eq}\right)}{R_p^2}\cdot(t-t_0)$$

$$\frac{a+b\cdot w}{-w_{eq}+w} = -K_1\cdot e^{K_2\cdot(t-t_0)}$$

$$\frac{a+b\cdot w}{w_{eq}-w} = K_1\cdot e^{K_2\cdot(t-t_0)}$$

where, again:

$$K_1 = \frac{a + b \cdot w_0}{w_{eq} - w_0} \qquad K_2 = \frac{F_0 \cdot \left(a + b \cdot w_{eq}\right)}{R_p^2} \tag{A.20}$$

just as before. So, the same expression A.17 is still valid for both processes, without needing to redefine the coefficients. We can now evaluate w(t):

$$\begin{aligned} a + b \cdot w &= \left(w_{eq} - w\right) \cdot K_1 \cdot e^{K_2 \cdot (t - t_0)} \\ \left[b + K_1 \cdot e^{K_2 \cdot (t - t_0)}\right] \cdot w &= w_{eq} \cdot K_1 \cdot e^{K_2 \cdot (t - t_0)} - a \\ w(t) &= \frac{w_{eq} \cdot K_1 \cdot e^{K_2 \cdot (t - t_0)} - a}{K_1 \cdot e^{K_2 \cdot (t - t_0)} + b} \end{aligned} \tag{A.21}$$

It is possible to further manipulate the expression as follows:

$$\begin{aligned} w(t) &= \frac{w_{eq} \cdot K_1 \cdot e^{K_2 \cdot (t - t_0)} - a}{K_1 \cdot e^{K_2 \cdot (t - t_0)} + b} \\ w(t) - w_0 &= \frac{w_{eq} \cdot K_1 \cdot e^{K_2 \cdot (t - t_0)} - a}{K_1 \cdot e^{K_2 \cdot (t - t_0)} + b} - w_0 \\ w(t) - w_0 &= \frac{\left(w_{eq} - w_0\right) \cdot K_1 \cdot e^{K_2 \cdot (t - t_0)} - (a + b \cdot w_0)}{K_1 \cdot e^{K_2 \cdot (t - t_0)} + b} \\ \frac{w(t) - w_0}{w_{eq} - w_0} &= \frac{\left(w_{eq} - w_0\right) \cdot K_1 \cdot e^{K_2 \cdot (t - t_0)} - (a + b \cdot w_0)}{\left(w_{eq} - w_0\right) \cdot K_1 \cdot e^{K_2 \cdot (t - t_0)} + \left(w_{eq} - w_0\right) \cdot b} \end{aligned}$$

Finally, substituting back the expressions or K_1 and K_2 and dividing both terms of the fraction by $(a + b \cdot w_0)$:

$$\frac{w(t) - w_0}{w_{eq} - w_0} = \frac{e^{\frac{F_0 \left(a + b \ w_{eq}\right)}{R_p^2} \cdot t} - 1}{e^{\frac{F_0 \left(a + b \ w_{eq}\right)}{R_p^2} \cdot t} + b \cdot \left(\frac{w_{eq} - w_0}{a + b \ w_0}\right)} \tag{A.22}$$

which is the analytical solution in eq. 2.52.

Appendix B

MATLAB codes

Backward-Euler numerical integration of FD

The MATLAB code below allows to perform numerical integration of the FD model from eq. 2.36.

```
%% INPUT parameters
% Diffusivity as a function of concentration (and, its derivative)
fD = @(C) 8e-11 + 1e-16*C;                                          % (m^2/s)
dfD = @(C) 1e-16;                                          % (m^2/s)/(kg/m^3)

% Initial concentration, homogeneous in the coating
C_iniz = 0.0;

% External concentration over time (equilibrium for the sorbent)
fCeq = @(t) 0.6 + 0.0*t;

% Geometry
L = 1e-3;                                          % Coating thickness (m)

% Simulation parameters
tf = 18000;                                % Simulation time (in seconds)
Nt = 2990;                     % Number of internal nodes on the time axis
Nx = 148;                     % Number of internal nodes on the space axis
FF_options = optimoptions('fsolve','Display','off',...        % Tolerances
    'FunctionTolerance',1e-6,'OptimalityTolerance',1e-6,...
    'StepTolerance',1e-6,'MaxIterations',400);

%% CALCULATIONS
t0 = 0;
x0 = 0;
xf = L;
dt = (tf-t0)/(Nt+1);
h = (xf-x0)/(Nx+1);
xx = linspace(x0, xf, Nx+2)';
tt = linspace(t0, tf, Nt+2)';
C0 = C_iniz*ones(Nx+2,1);                                  % Initial matrix C
C0(Nx+2) = fCeq(tt(1));
C = zeros(Nx+2,Nt+2);        % Matrix C: it has Nx+2 rows and Nt+2 columns
C(:,1)=C0;
```

```
C_new = zeros(Nx+2,1);
for m=2:(Nt+2)                          % Solving algorithm, column by column
 C_old = C(:,m-1);
 F_Cnew = @(CC_new) FF(CC_new, C_old, m, tt, dt, h, fD, dfD, fCeq);
 C_new = fsolve(F_Cnew, C_old, FF_options);
 C(:,m)=C_new;
end

%% VISUALIZATION
col=[0.8,0,0; 0.6,0.2,0.2; 0.4,0.4,0.2; 0.2,0.6,0.4; 0,1,0.4; 0,0.8,0.8];
fig1 = figure;
fig1.Units = 'normalized';
fig1.Position = [0.01,0.07,0.98,0.82];
hold on
Cmin=min(min(C));
Cmax=max(max(C));
pl = [];
pl(end+1)=plot(xx,C(:,1),'Color',col(1,:),...
'DisplayName','t = 0 min','linewidth',1.5);
pl(end+1)=plot(xx,C(:,floor((Nt+2)*5*60/tf)),'Color',col(2,:),...
    'DisplayName','t = 5 min','linewidth',1.5);
pl(end+1)=plot(xx,C(:,floor((Nt+2)*30*60/tf)),'Color',col(3,:),...
    'DisplayName','t = 30 min','linewidth',1.5);
pl(end+1)=plot(xx,C(:,floor((Nt+2)*60*60/tf)),'Color',col(4,:),...
    'DisplayName','t = 60 min','linewidth',1.5);
pl(end+1)=plot(xx,C(:,floor((Nt+2)*180*60/tf)),'Color',col(5,:),...
    'DisplayName','t = 180 min','linewidth',1.5);
pl(end+1)=plot(xx,C(:,(Nt+2)),'Color',col(6,:),...
    'DisplayName','t = 300 min','linewidth',1.5);
fill([0,L,L,0],[Cmin-1,Cmin-1,Cmax+1,Cmax+1],[0.5,0.5,0.5],...
    'FaceAlpha',0.14);
fill([-L,0,0,-L],[Cmin-1,Cmin-1,Cmax+1,Cmax+1],[0.2,0.2,0.2],...
    'FaceAlpha',0.74);
plot([0,0],[Cmin-1,Cmax+1],'k--','linewidth',2);
plot([L,L],[Cmin-1,Cmax+1],'k--','linewidth',2);
xlabel('x (m)');
ylabel('C(t,x) (kg/m^3)');
xlim([-L/4,L*2]);
ylim([Cmin-0.05,Cmax+0.05]);
ax = gca;
ax.FontSize = 18;
text(0.03,0.97,'WALL','Units','normalized')
text(0.29,0.97,'COATING','Units','normalized')
text(0.72,0.97,'ENVIRONMENT','Units','normalized')
title(strcat('Local concentration C(t,x)'),'FontSize',11);
legend(pl,'Location','east','FontSize',17);

%% Auxiliary function for numerical resolution of the non-linear system
function [out] = FF(C_new, C_old, mm, tt, dt, h, fD, dfD, fCeq)
out = zeros(size(C_new));
Len = length(C_new);
out(1) = C_old(1)+dt*(2*fD(C_new(1))*(C_new(2)-C_new(1))/(h^2))-C_new(1);
for j=2:(Len-1)
 out(j) = C_old(j)+dt*((dfD(C_new(j)))*(((C_new(j+1))^2-...
     2*(C_new(j-1))*(C_new(j+1))+(C_new(j-1))^2)/(4*(h^2)))+...
    (fD(C_new(j)))*(((C_new(j+1))-2*(C_new(j))+...
    (C_new(j-1)))/(h^2))) - C_new(j);
end
out(Len) = fCeq(tt(mm))-C_new(Len);
end
```

Best-fitting through Least-Squares Minimization

The MATLAB code below allows to perform Least-Squares Minimization (LSM) of a generic error between a model and experimental data, with the objective of best-fitting model's parameters. The same approach was used multiple times during this work, to best-fit kinetics models parameters (e.g., diffusivity), equilibrium models parameters, and so on (the occurrences are listed in the main text). Depending on the specific case, the model expression, tolerances and dataset were adjusted. In the example below, we best-fit isotherm data on CaAlg using GAB model[1].

```
%% Experimental data
RHexp = 0:0.1:0.7;                                                    % x
wexp = [0, 0.1622, 0.3244, 0.50687, 0.65092, 0.80848, 1.0014, 1.2814]; % y

%% Fitting
% General idea: we will define an array "a" containing the parameters to
% be best-fitted. For example, for GAB, "a" is such that: a(1) = wm;
% a(2) = c; a(3) = K. Then, the model is written as a function of only
% "a" and RH. We can finally build an "error" function as the difference
% between model and data, and minimize that function.
% Define the model you are going to use to fit your data (e.g., GAB):
model = @(a, RH) a(1)*a(2)*a(3)*RH./((1-a(3)*RH).*(1+a(3)*RH*(a(2)-1)));
% The first-iteration values are chosen and saved into "a0":
a_0 = [0.5, 2, 0.8];                                        % wm_0, c_0, K_0
% Define the error function between model and data, according to LSM:
err = @(a) sum((model(a, RHexp) - wexp).^2);
% Find the optimal "a_opt" that minimizes err:
options = optimset('TolX', 1e-9, ...            % optimization tolerances
    'TolFun', 1e-9, 'MaxFunEvals', 1000, 'MaxIter', 1000);
a_opt = fminsearch(err, a_0, options); % use fmincon if under constraints
disp("optimal wm: ");
disp(a_opt(1));
disp("optimal c: ");
disp(a_opt(2));
disp("optimal K: ");
disp(a_opt(3));

%% Evaluate the model over a RH range and plot it in comparison to data
RH = linspace(0,0.7,300);
w_bestFitted = model(a_opt, RH);
figure, hold on
plot(100*RHexp, wexp, 'b.-','linewidth',2,'MarkerSize',21);
plot(100*RH, w_bestFitted, 'r-','linewidth',1.2);
ax = gca;
ax.FontSize = 18;
xlabel("RH (%)", "FontWeight", "Bold");
ylabel("w (g/g)", "FontWeight", "Bold");
xlim([-3,73]);
ylim([-0.05,1.35]);
xticks(0:10:70);
yticks(0:0.2:1.6);
legend("Experimental", "Best-fitting model", 'FontSize',17);
```

[1]Note: in most cases, we applied the LSM method to best-fit non-linear expressions. Care must be used in these cases, as the convergence to the optimal value is not automatically guaranteed as in the case of linear expressions, and often we had to arbitrarily attempt different first-iteration values.

Appendix C

Models best-fitting results

FD-based and LDF-based models best-fitting

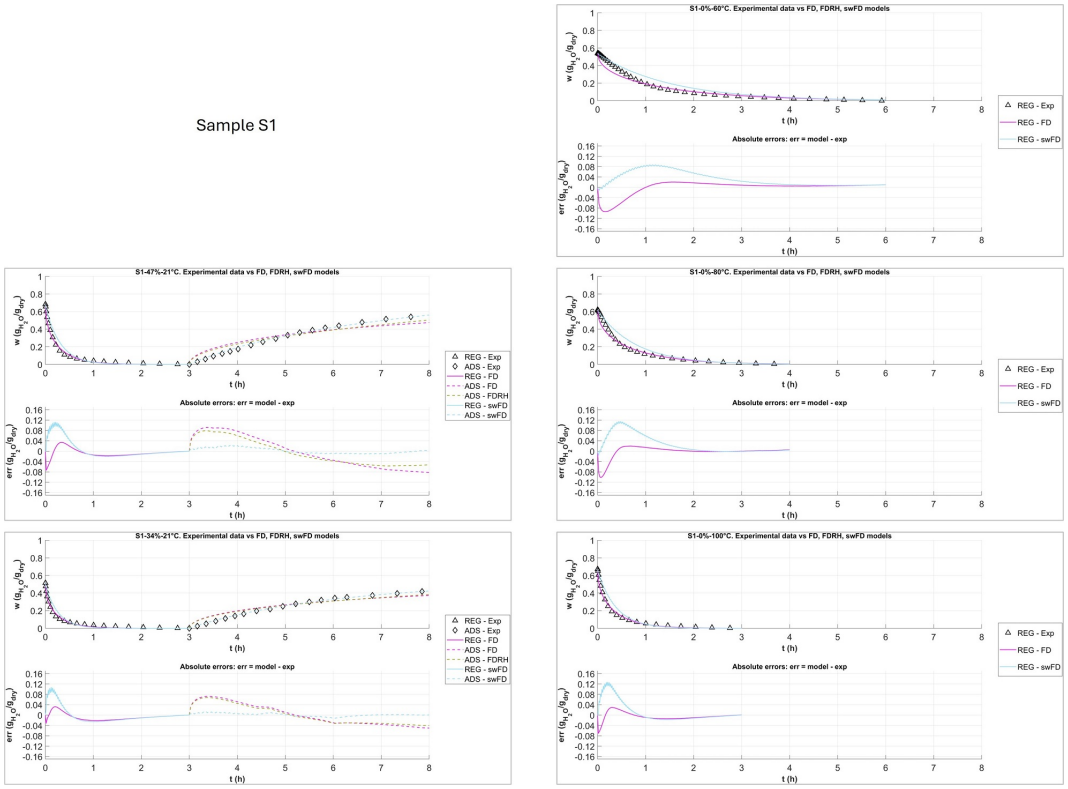

Fig. C.1 FD-based models, best-fittings on sample S1.

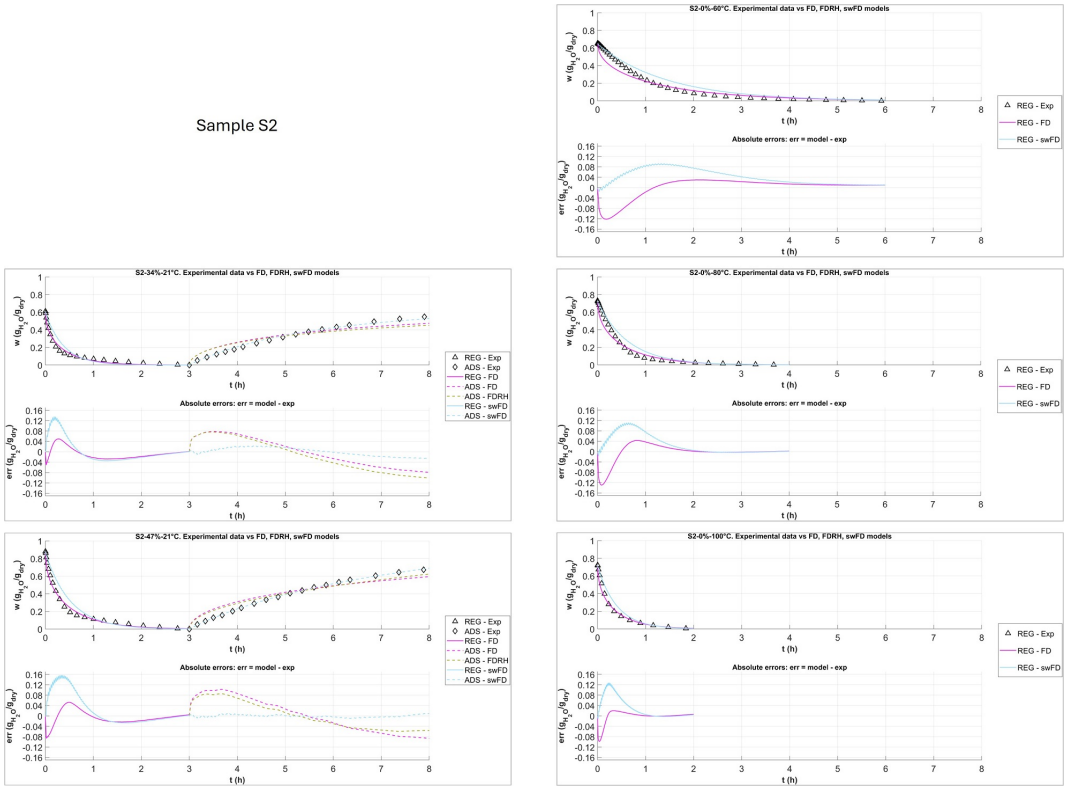

Fig. C.2 FD-based models, best-fittings on sample S2.

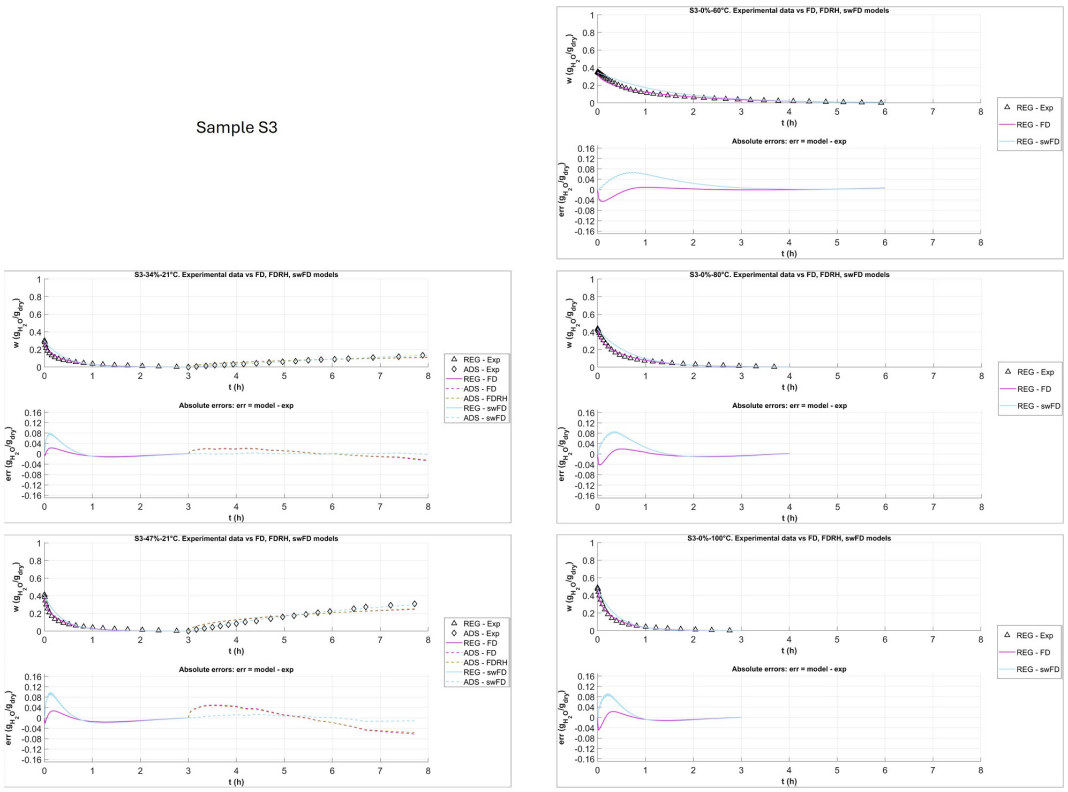

Fig. C.3 FD-based models, best-fittings on sample S3.

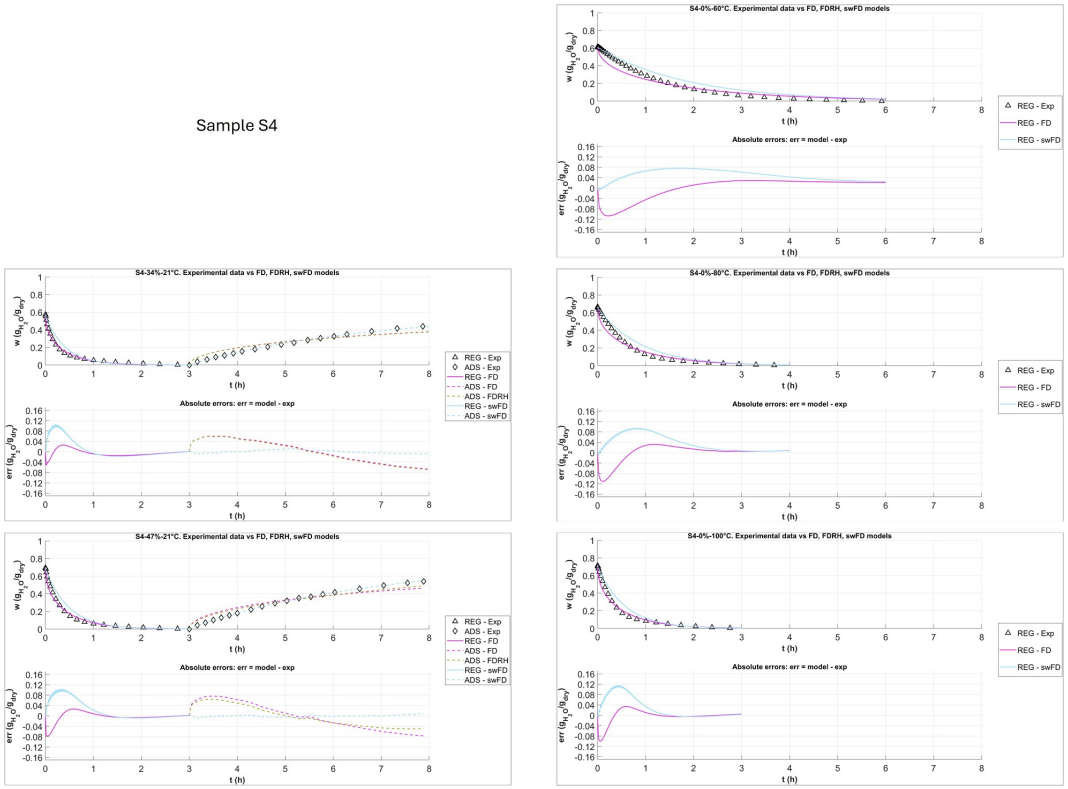

Fig. C.4 FD-based models, best-fittings on sample S4.

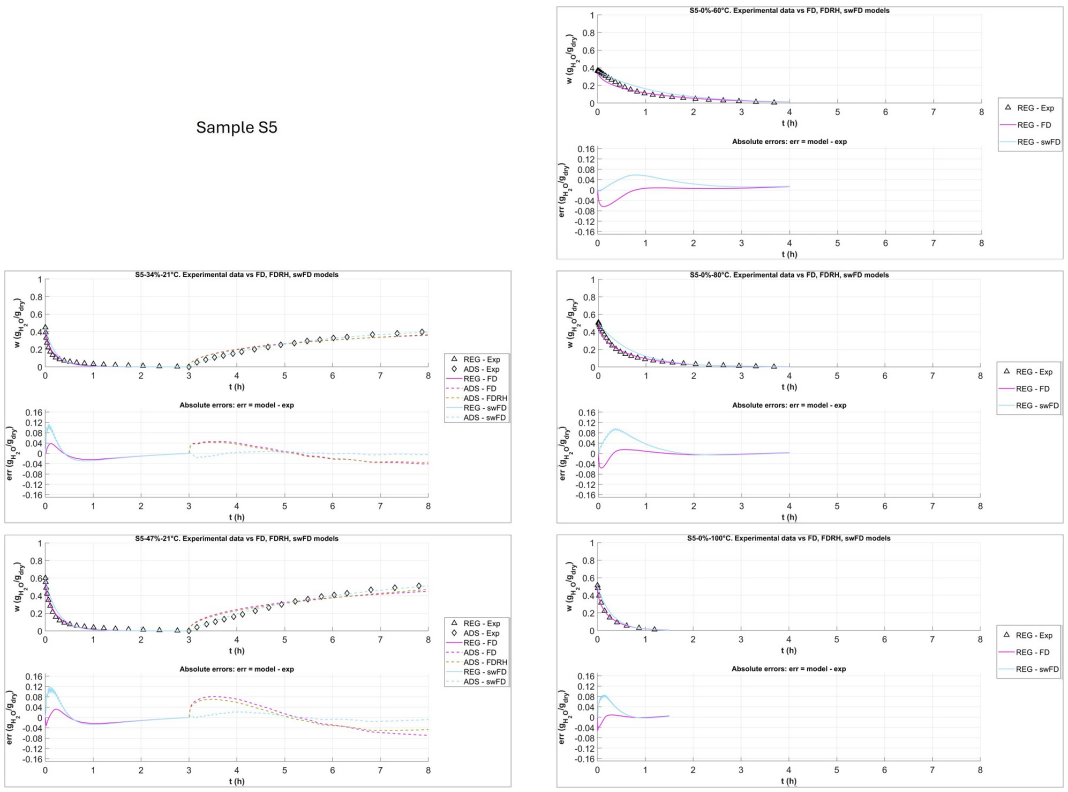

Fig. C.5 FD-based models, best-fittings on sample S5.

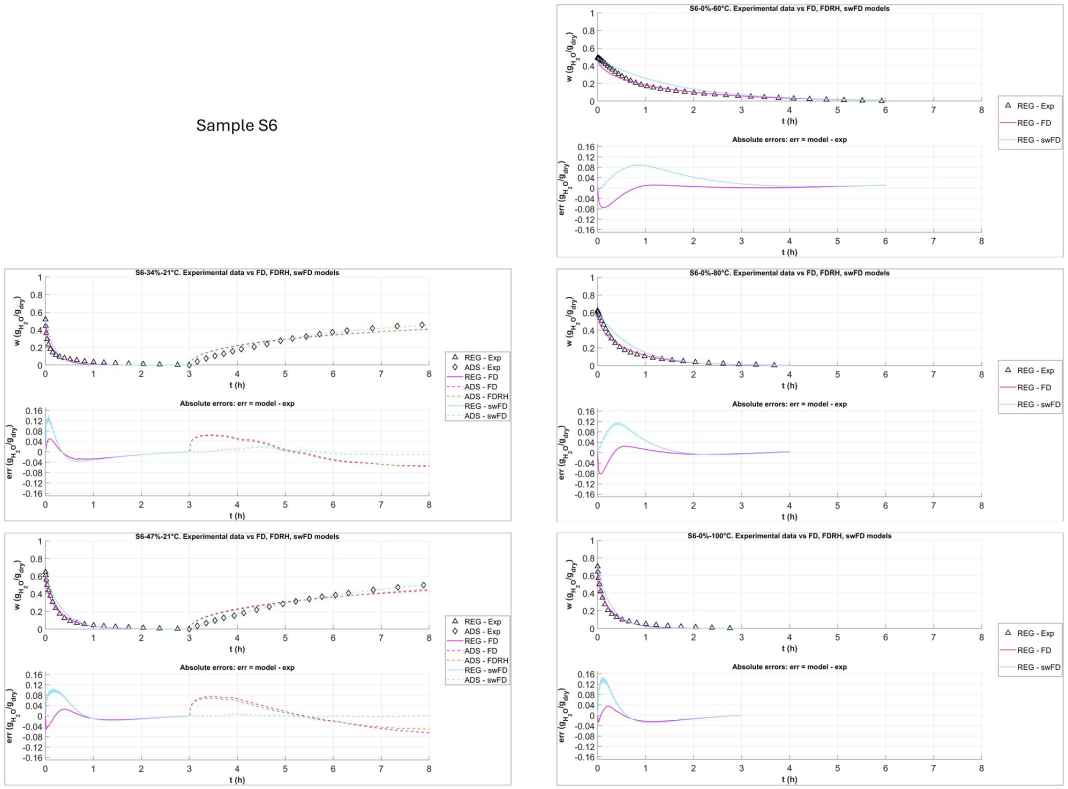

Fig. C.6 FD-based models, best-fittings on sample S6.

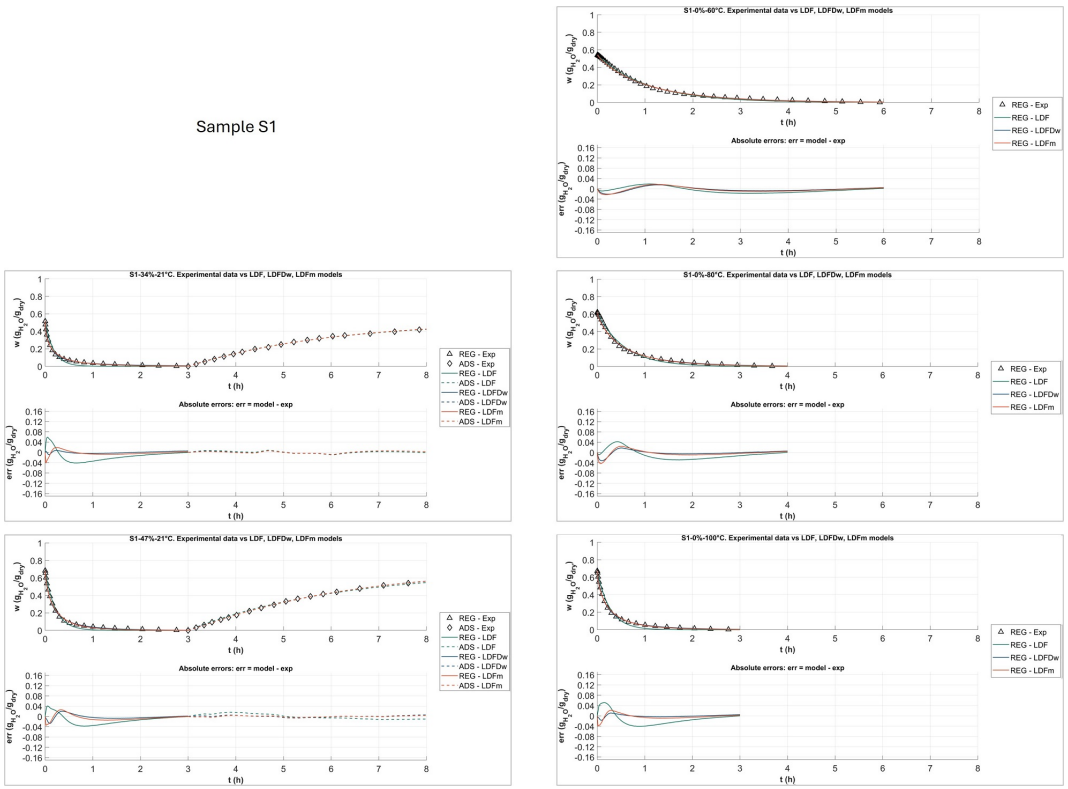

Fig. C.7 LDF-based models, best-fittings on sample S1.

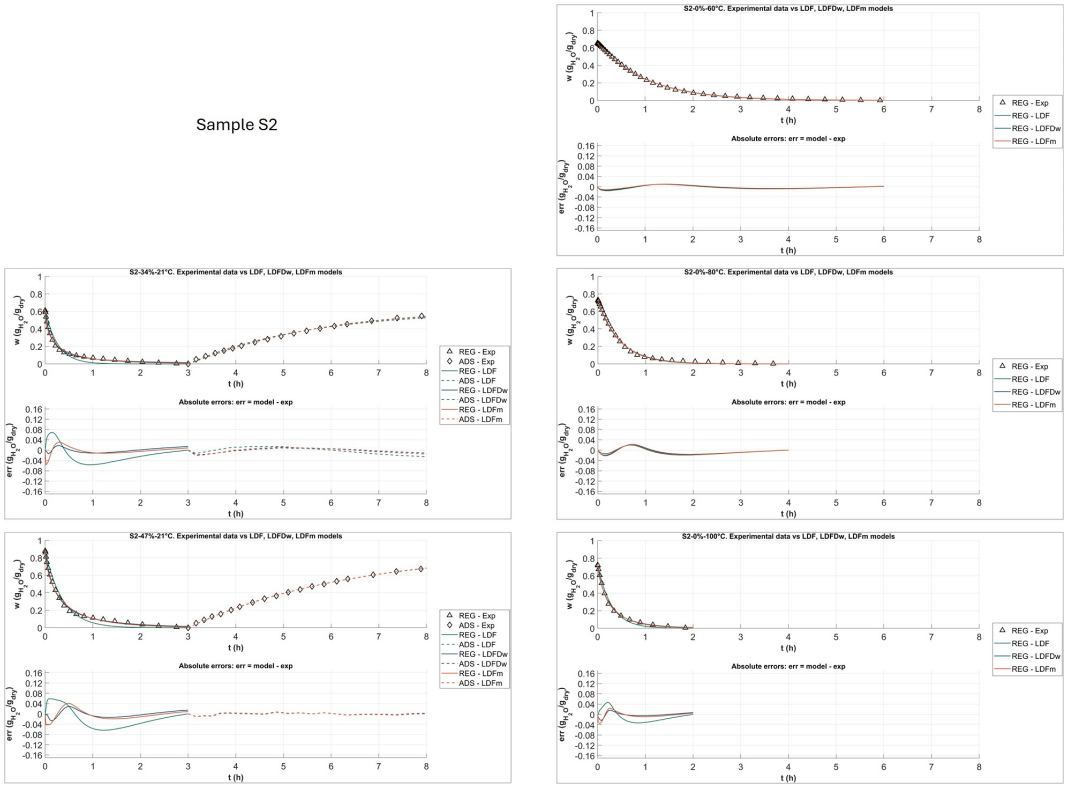

Fig. C.8 LDF-based models, best-fittings on sample S2.

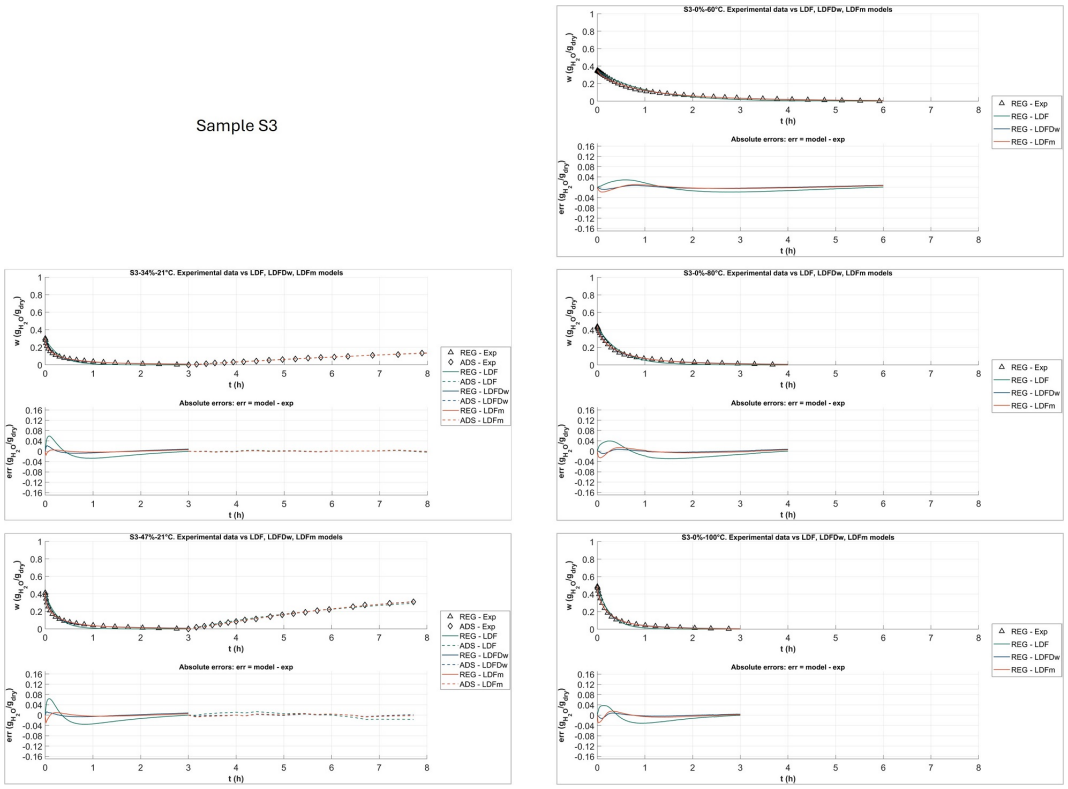

Fig. C.9 LDF-based models, best-fittings on sample S3.

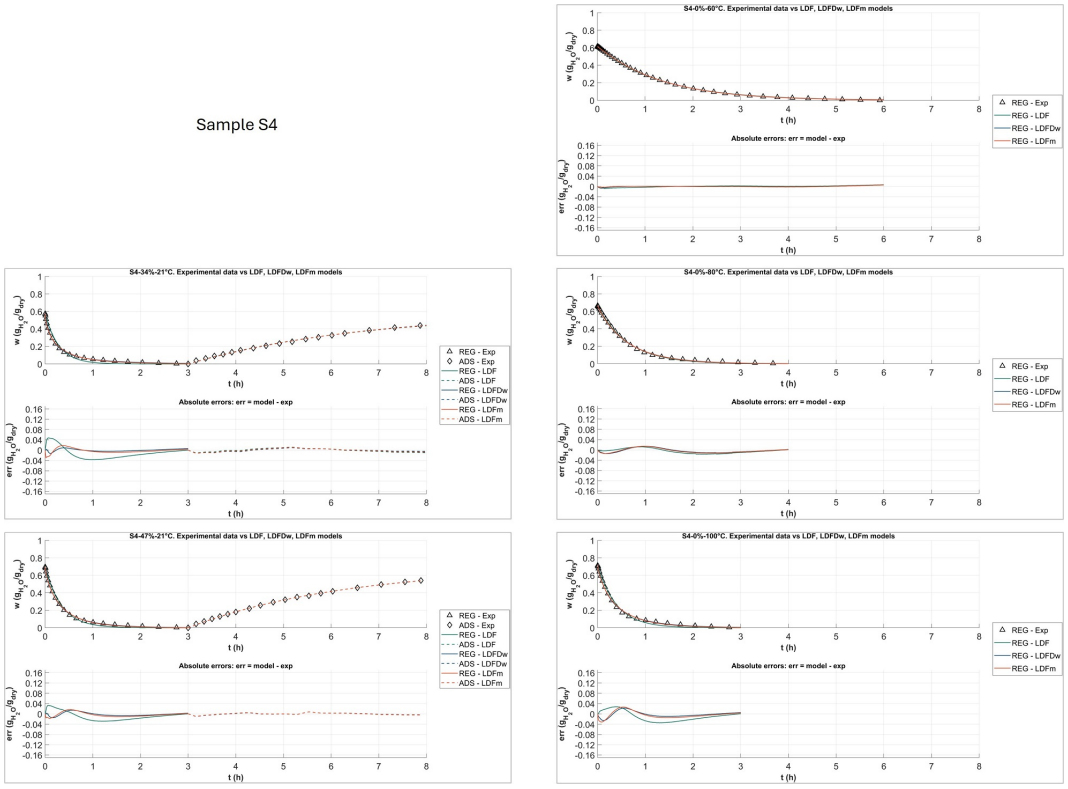

Fig. C.10 LDF-based models, best-fittings on sample S4.

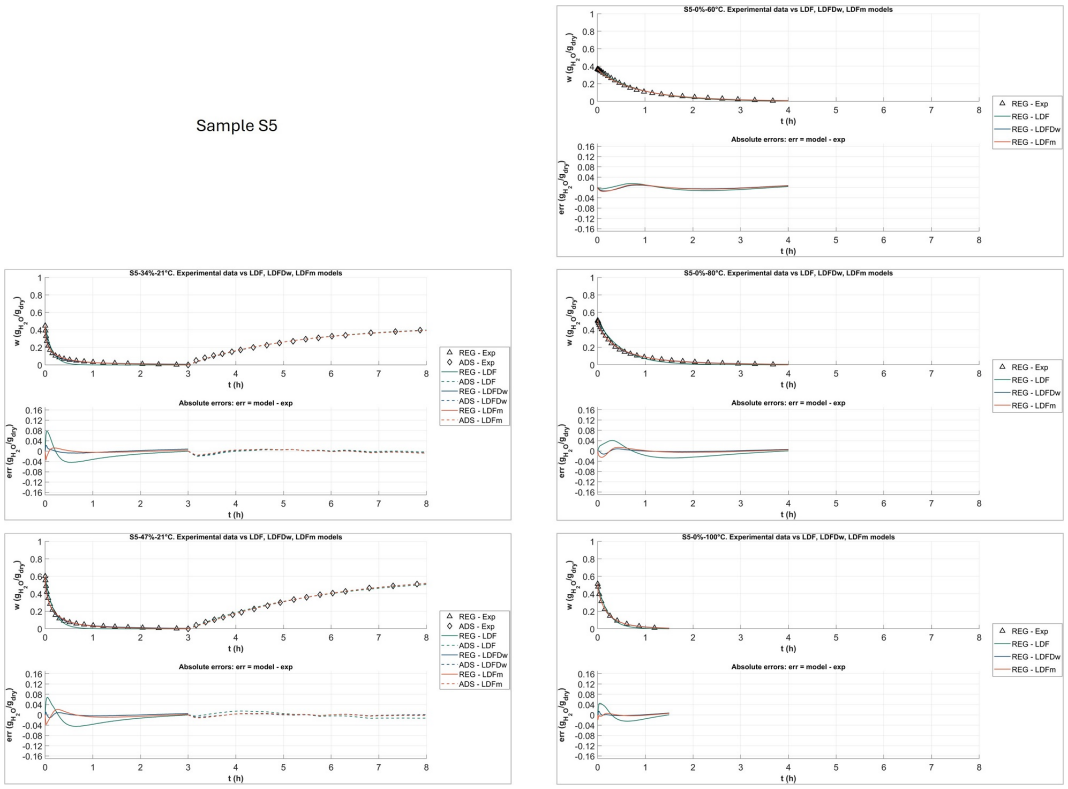

Fig. C.11 LDF-based models, best-fittings on sample S5.

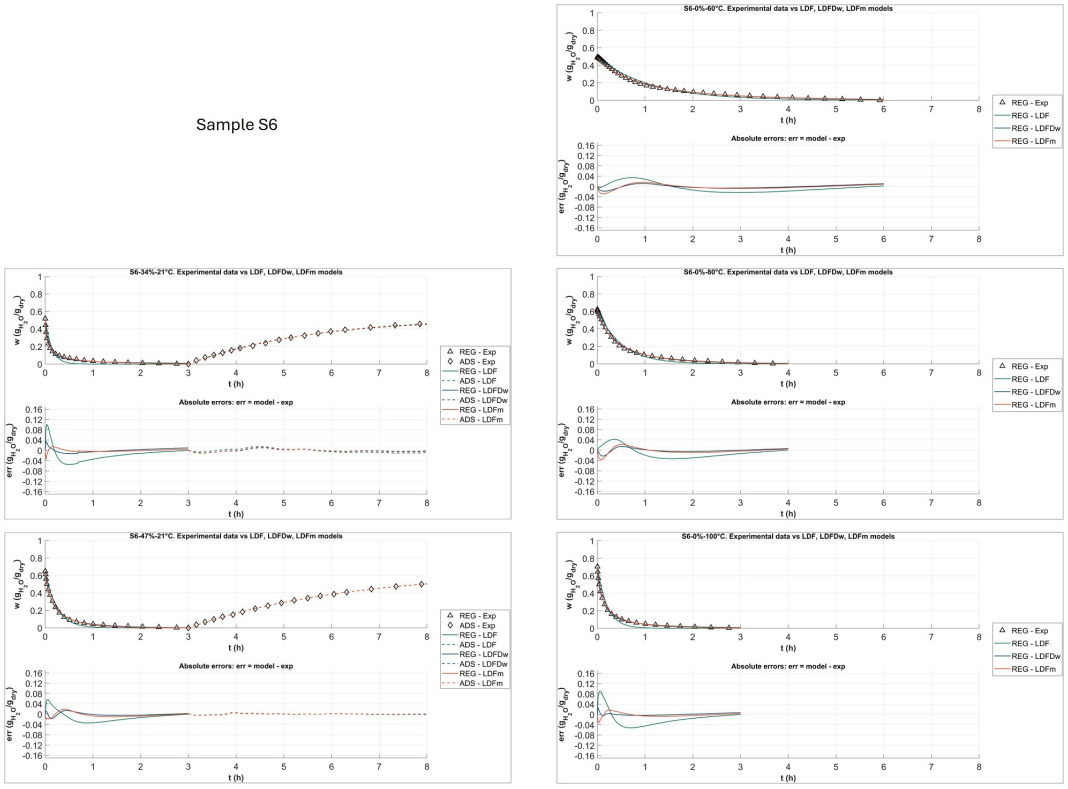

Fig. C.12 LDF-based models, best-fittings on sample S6.

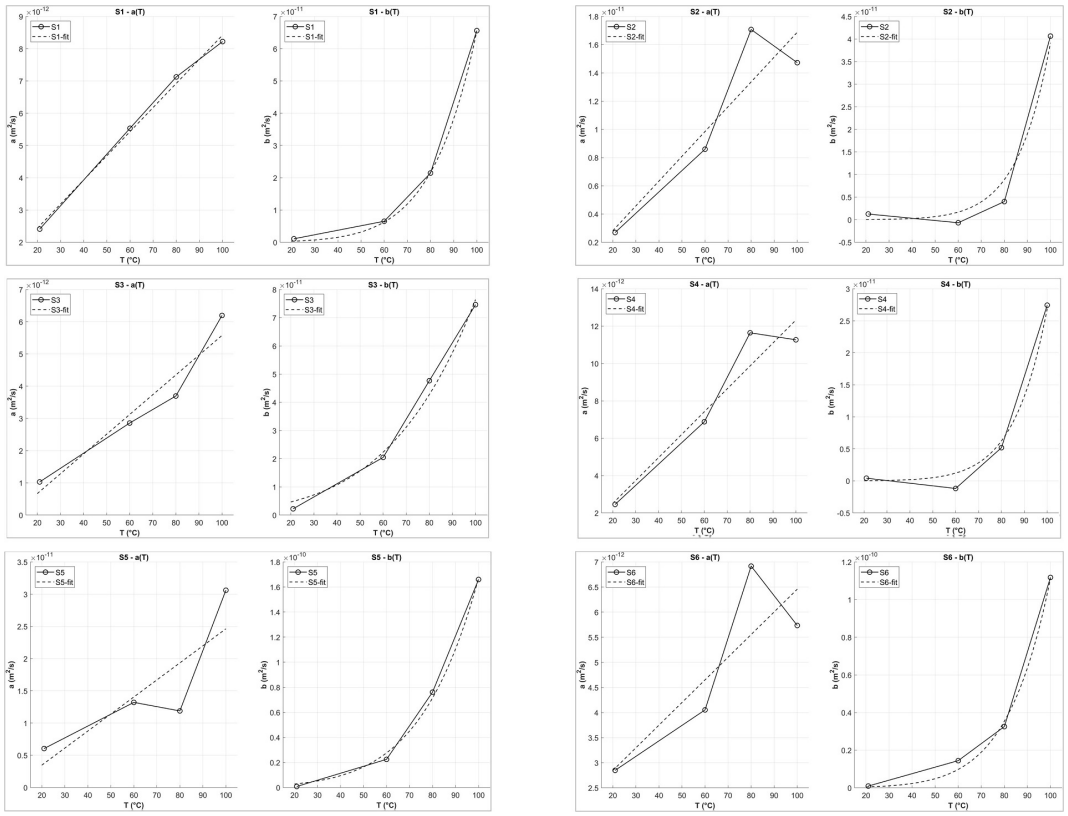

Fig. C.13 LDFDw, parameters a and b with temperature, best-fittings.

Isotherms ramps best-fitting

Isotherm data, best-fittings and errors. Refer to table 4.10.

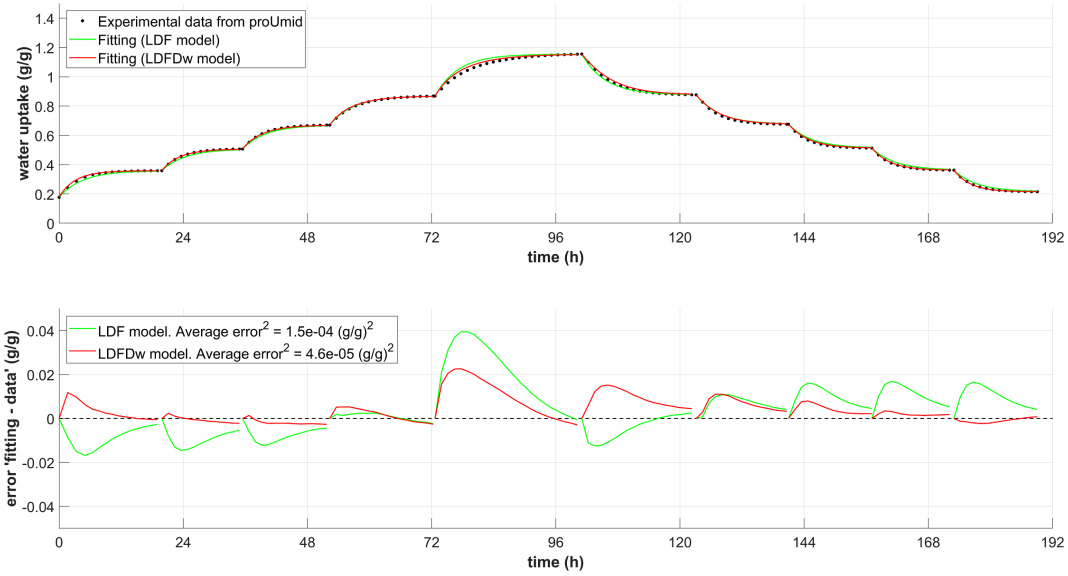

Fig. C.14 Isotherm best-fitting and error, sample 1.

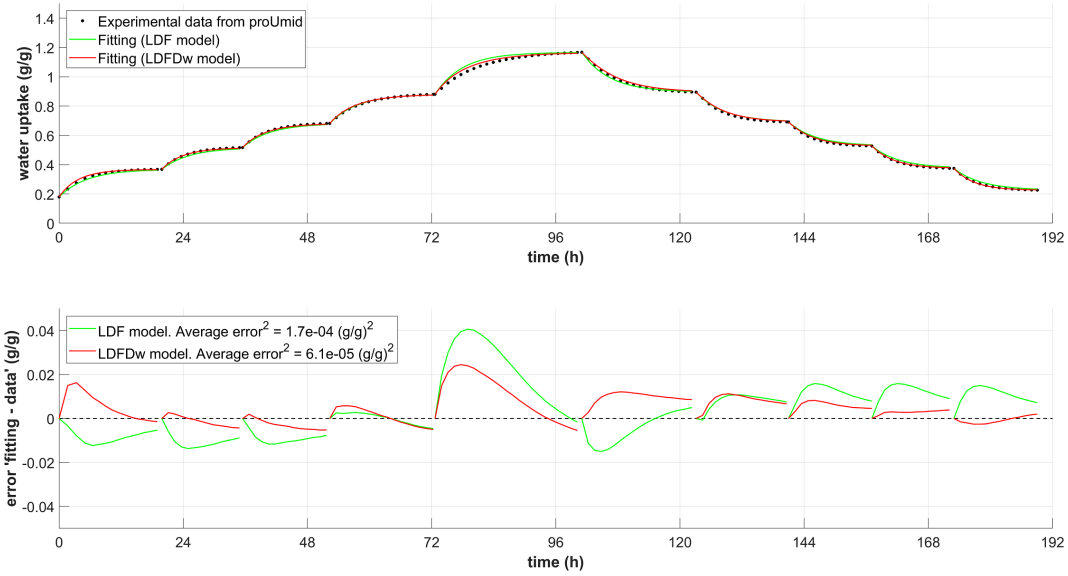

Fig. C.15 Isotherm best-fitting and error, sample 2.

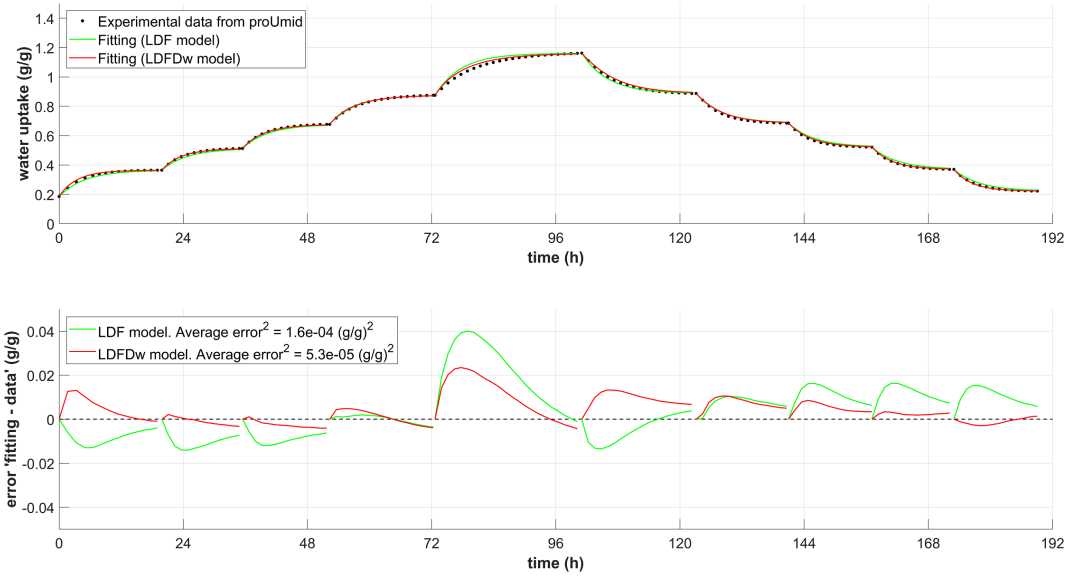

Fig. C.16 Isotherm best-fitting and error, sample 3.

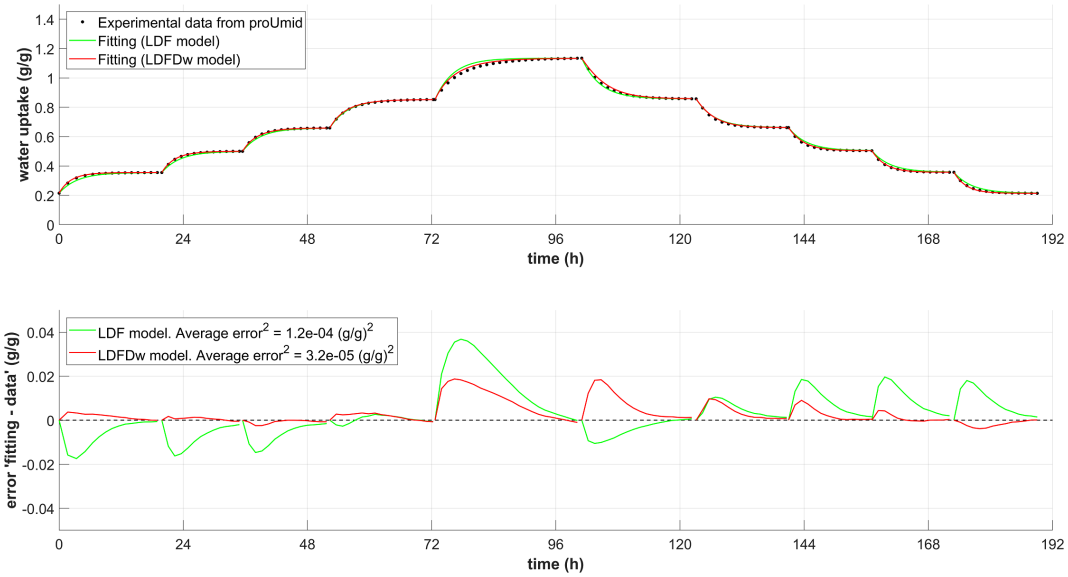

Fig. C.17 Isotherm best-fitting and error, sample 4.

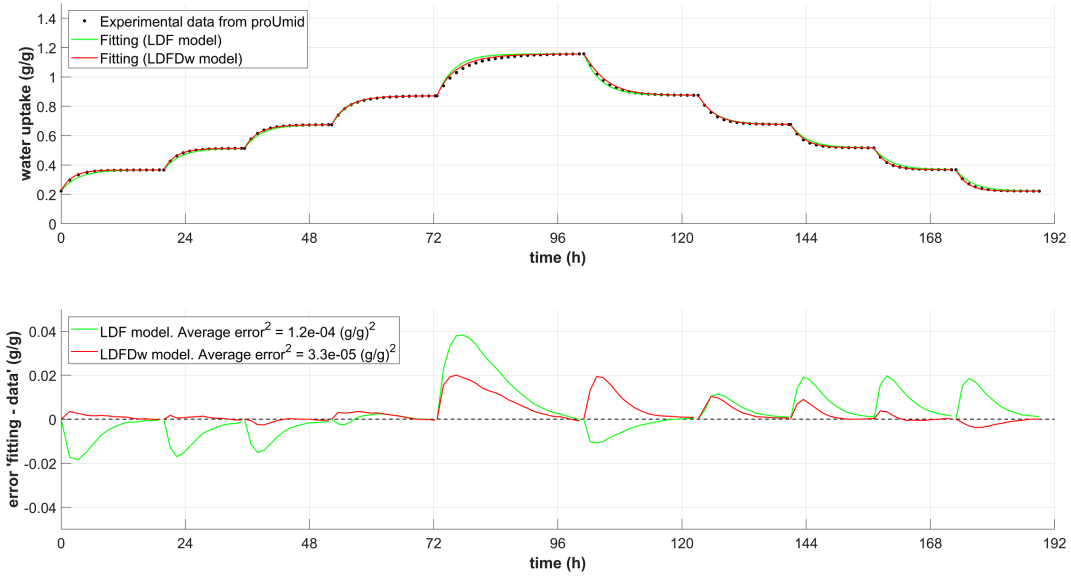

Fig. C.18 Isotherm best-fitting and error, sample 5.

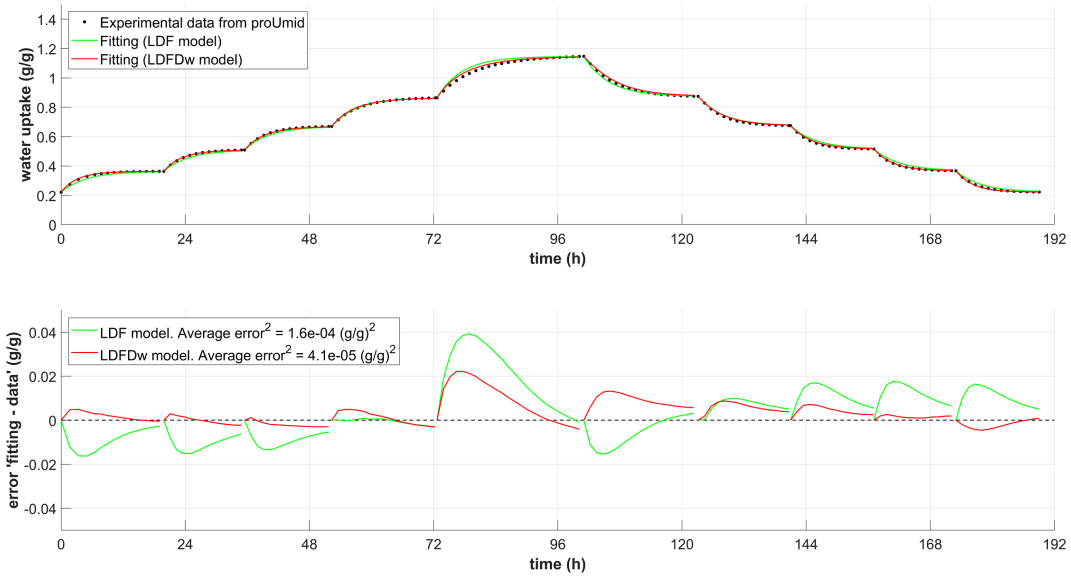

Fig. C.19 Isotherm best-fitting and error, sample 6.

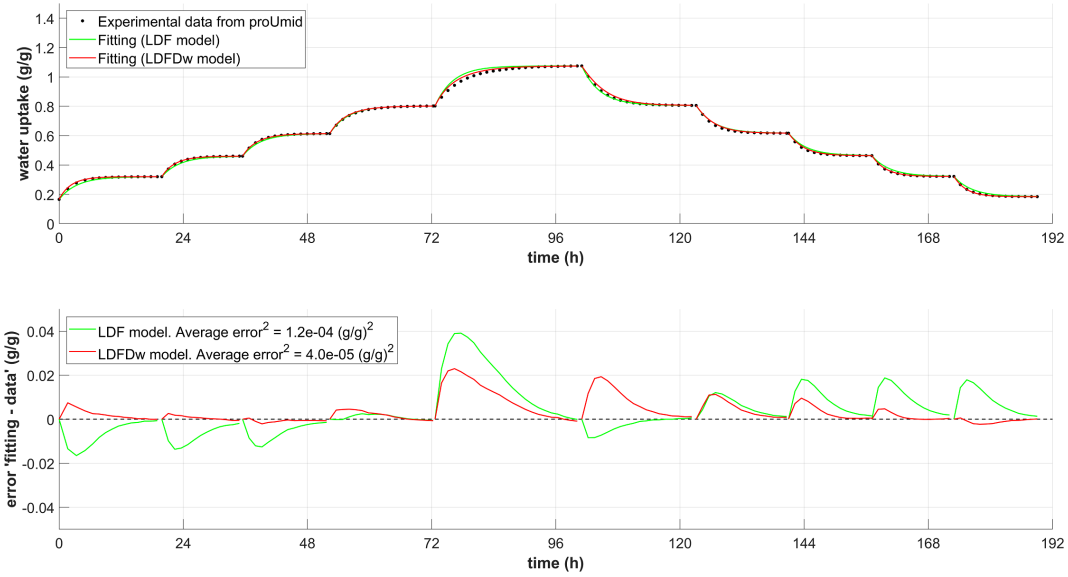

Fig. C.20 Isotherm best-fitting and error, sample 7.

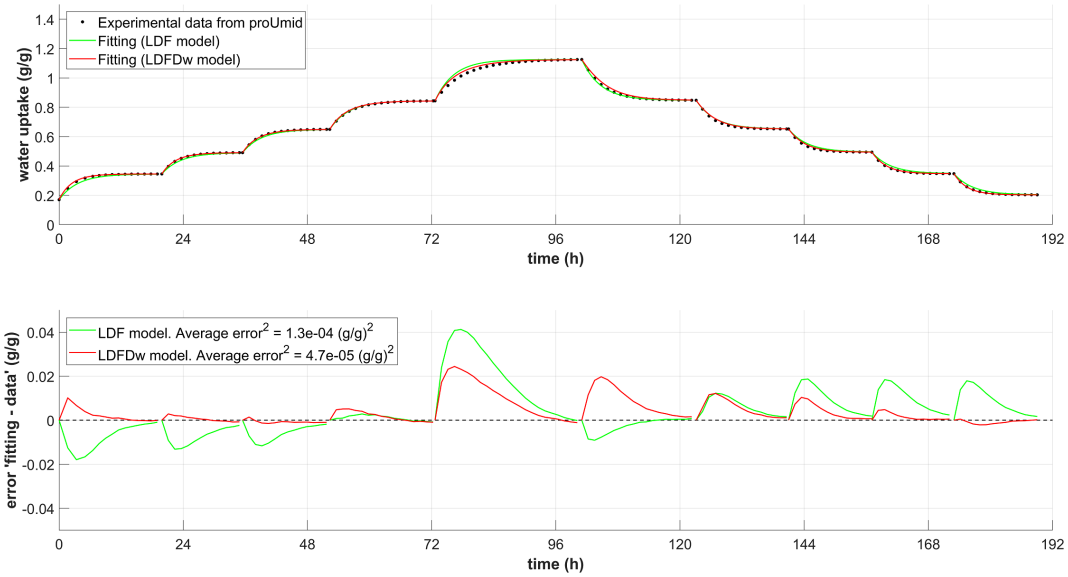

Fig. C.21 Isotherm best-fitting and error, sample 8.

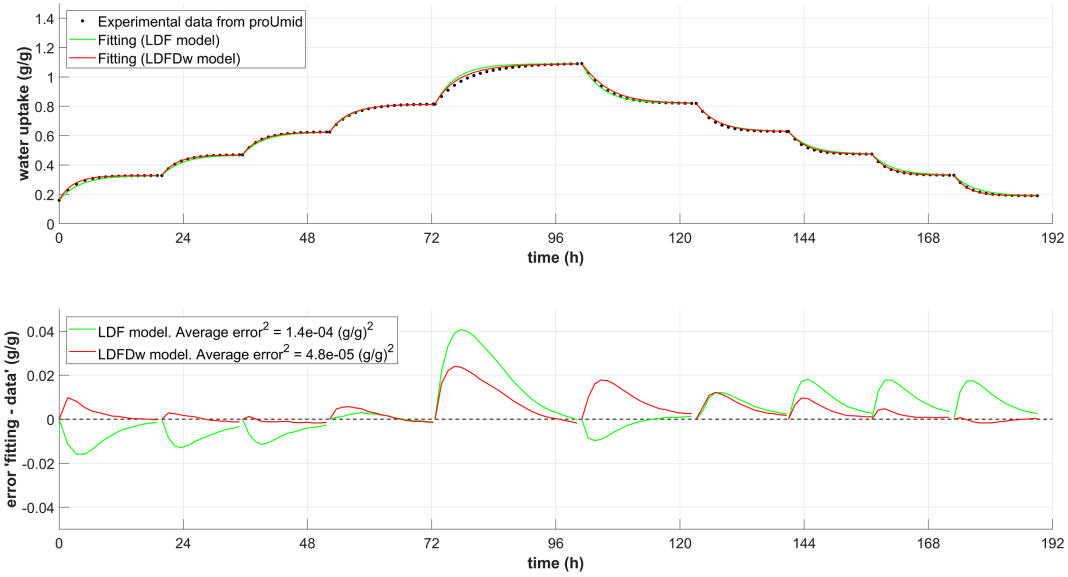

Fig. C.22 Isotherm best-fitting and error, sample 9.

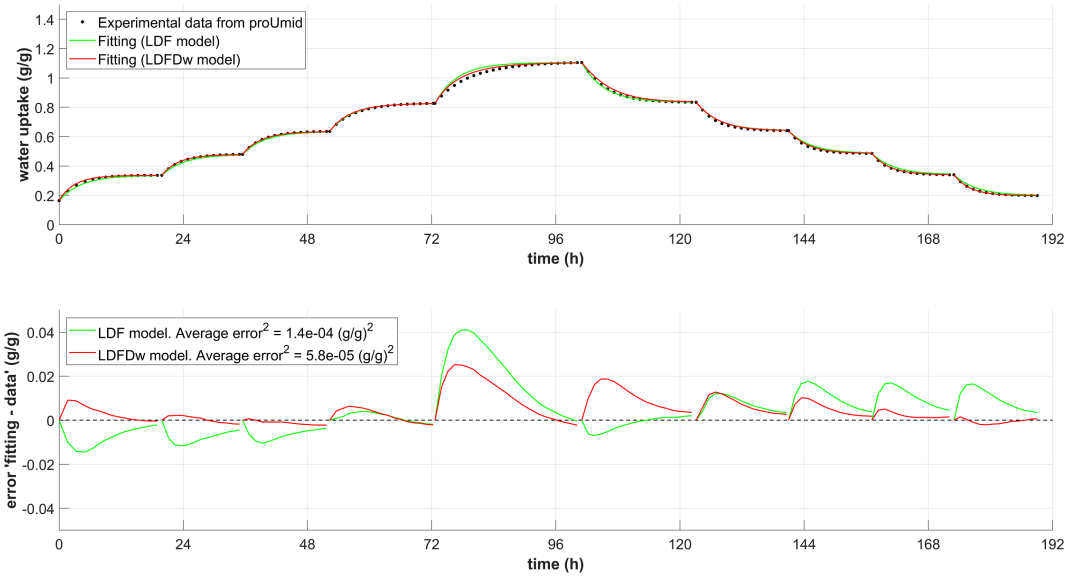

Fig. C.23 Isotherm best-fitting and error, sample 10.

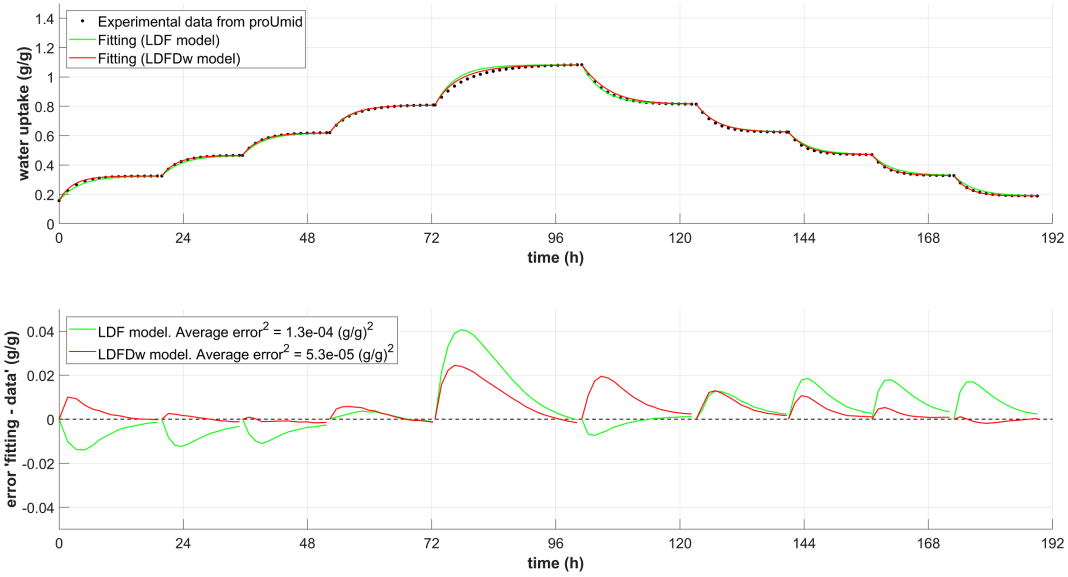

Fig. C.24 Isotherm best-fitting and error, sample 11.

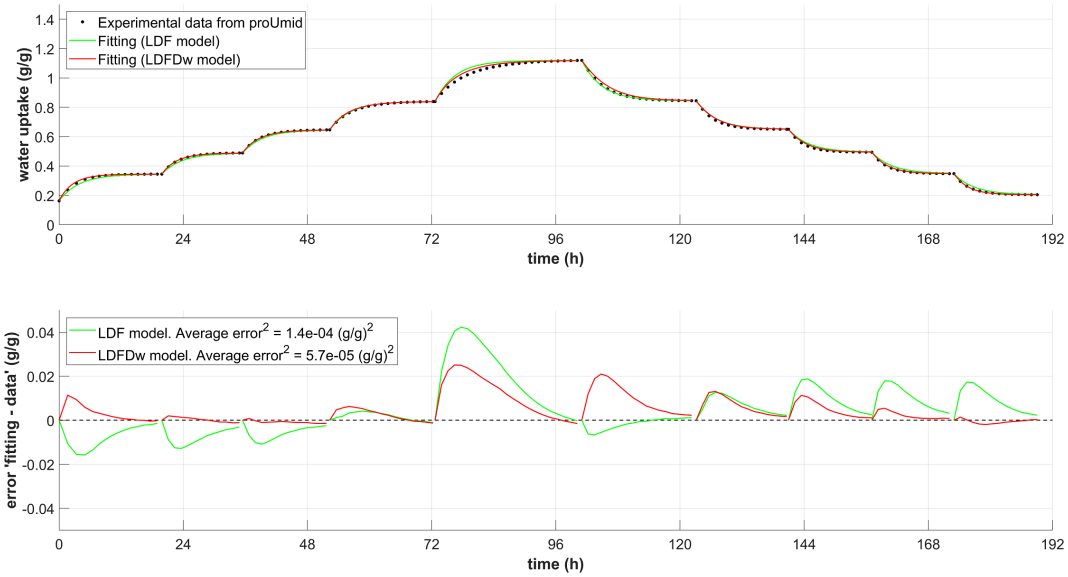

Fig. C.25 Isotherm best-fitting and error, sample 12.

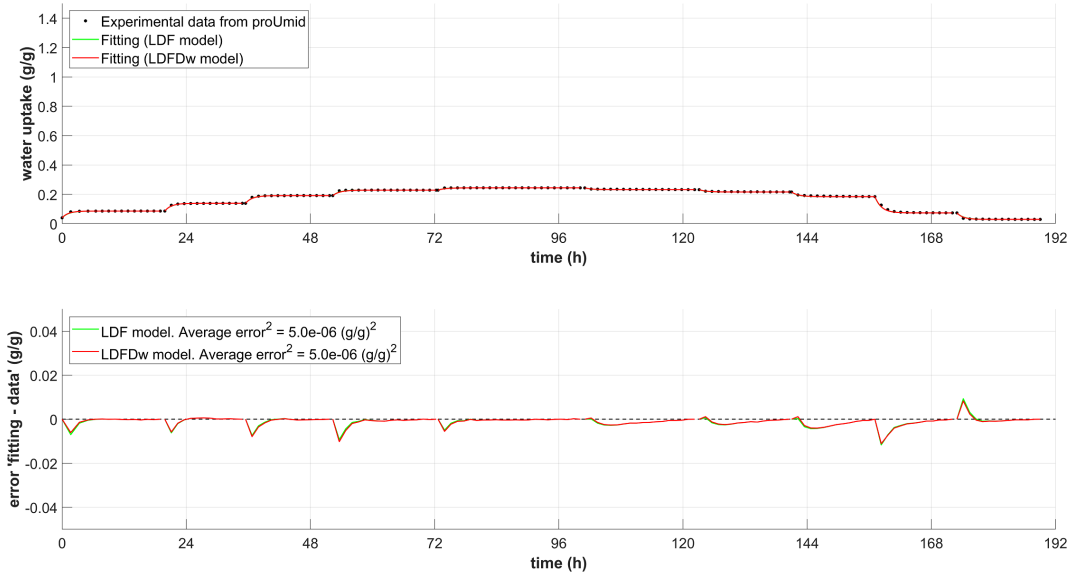

Fig. C.26 Isotherm best-fitting and error, sample 13.

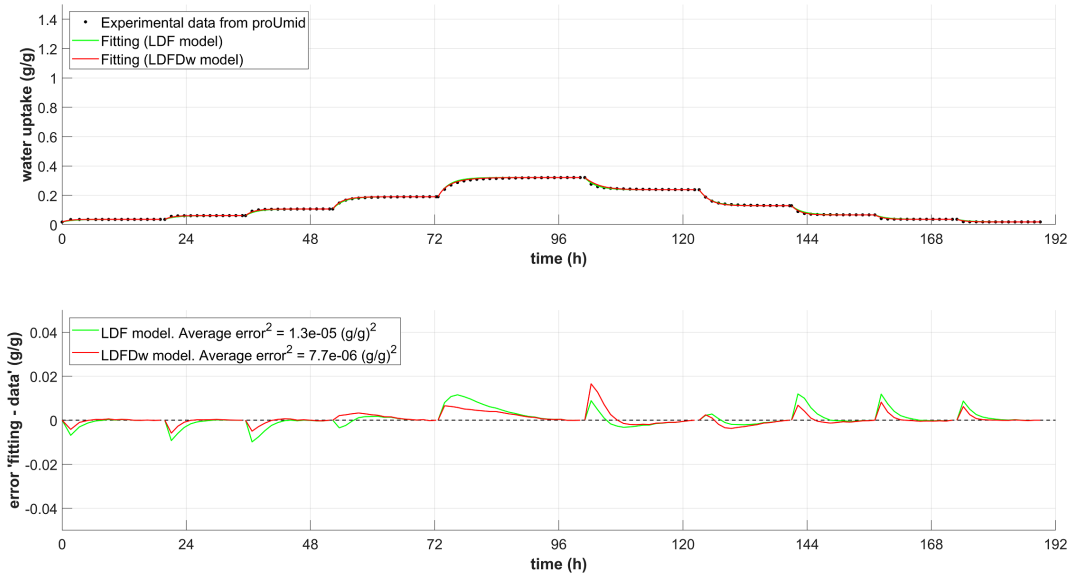

Fig. C.27 Isotherm best-fitting and error, sample 14.

Appendix D

Experimental tests dataset

Tests with AWH unit

In this section, we show the collected data from tests with the AWH unit. See Table 5.2.

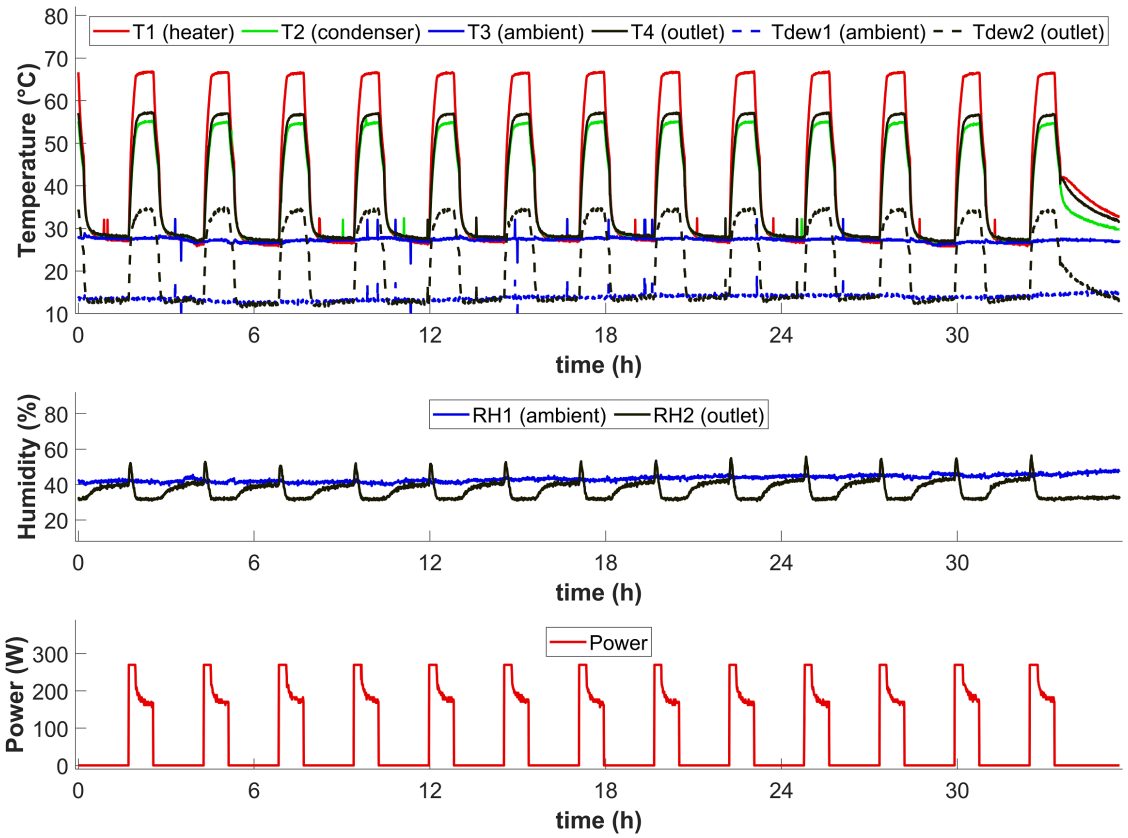

Fig. D.1 Test 1 with AWH unit.

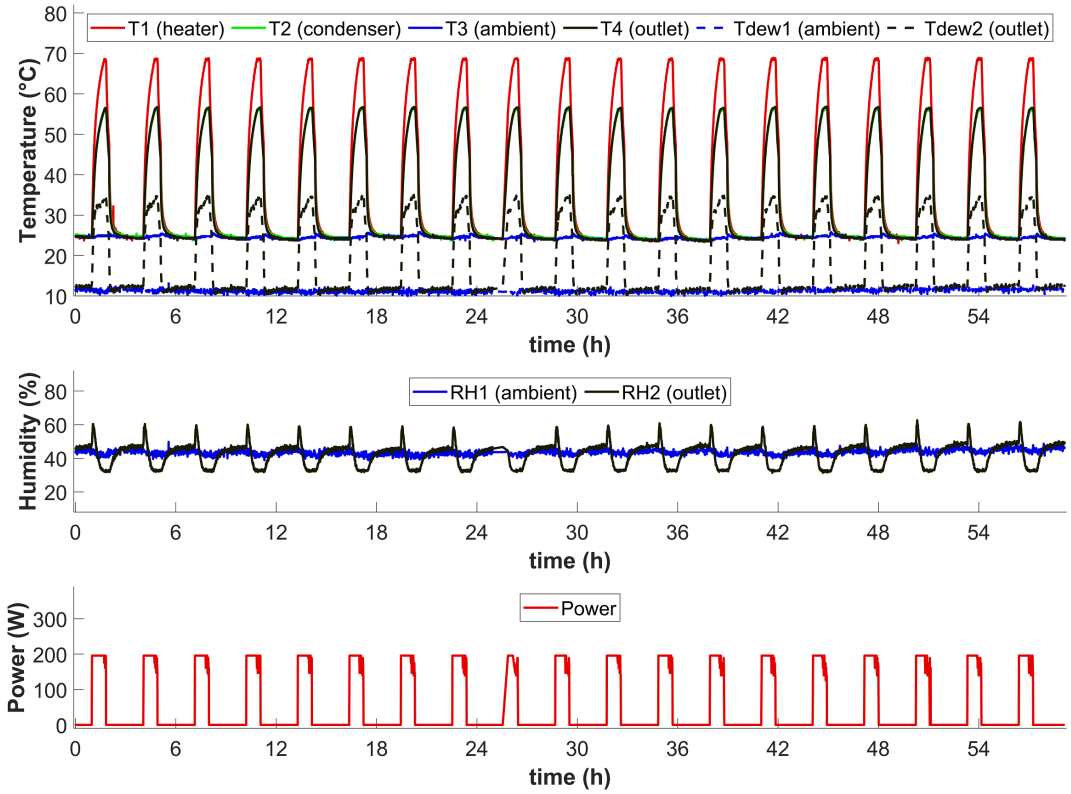

Fig. D.2 Test 2 with AWH unit.

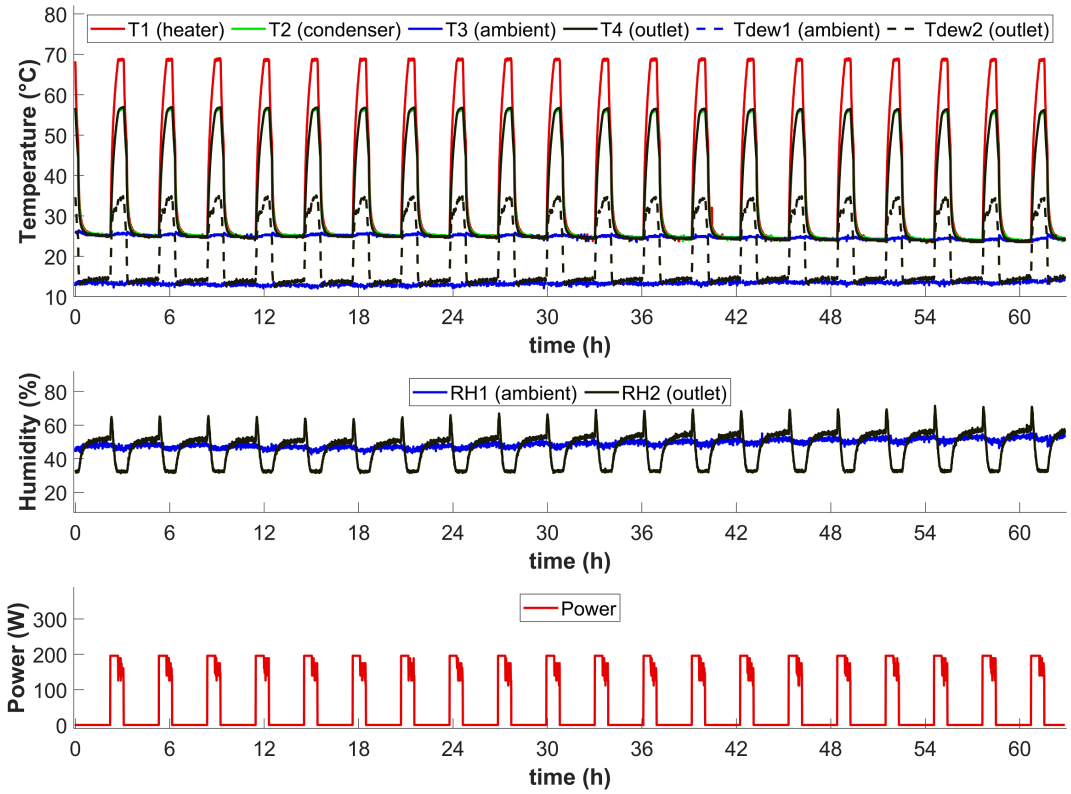

Fig. D.3 Test 3 with AWH unit.

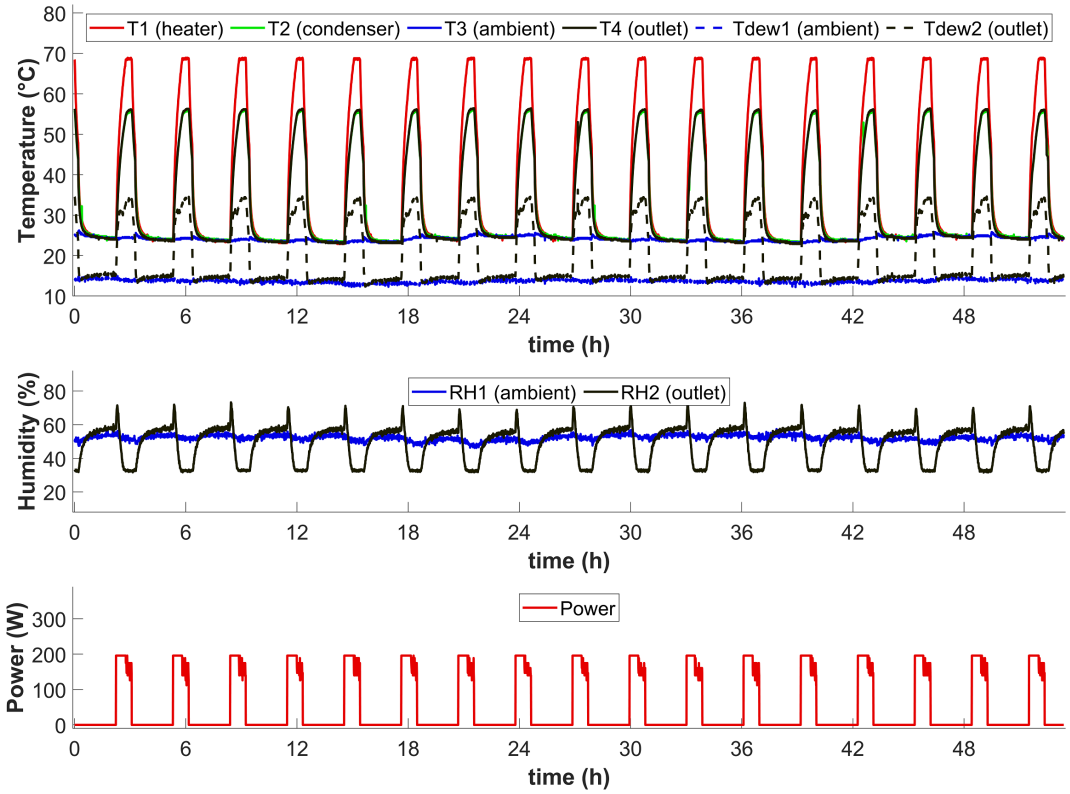

Fig. D.4 Test 4 with AWH unit.

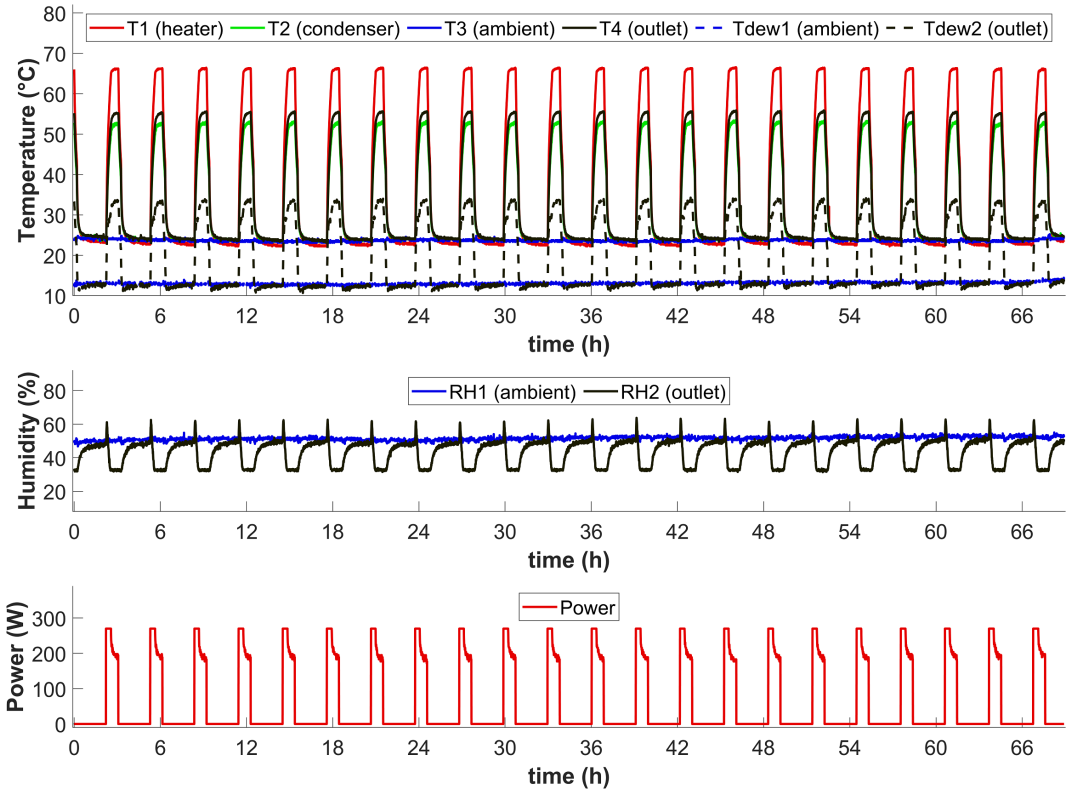

Fig. D.5 Test 5 with AWH unit.

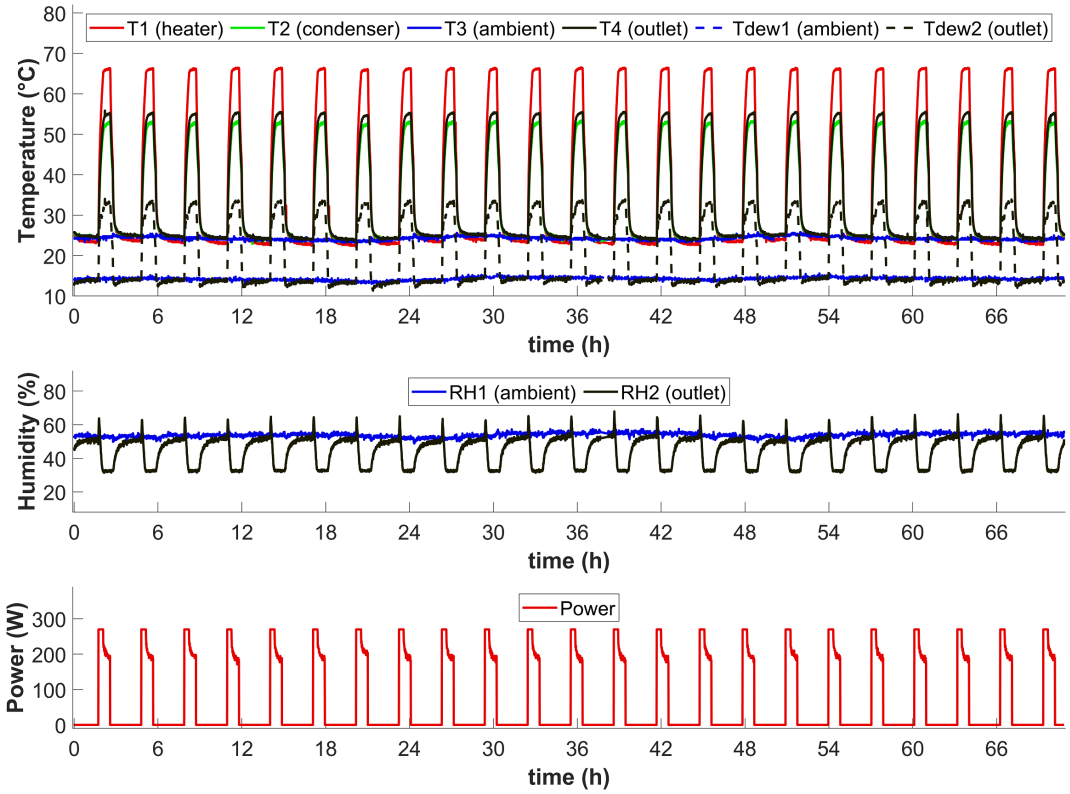

Fig. D.6 Test 6 with AWH unit.

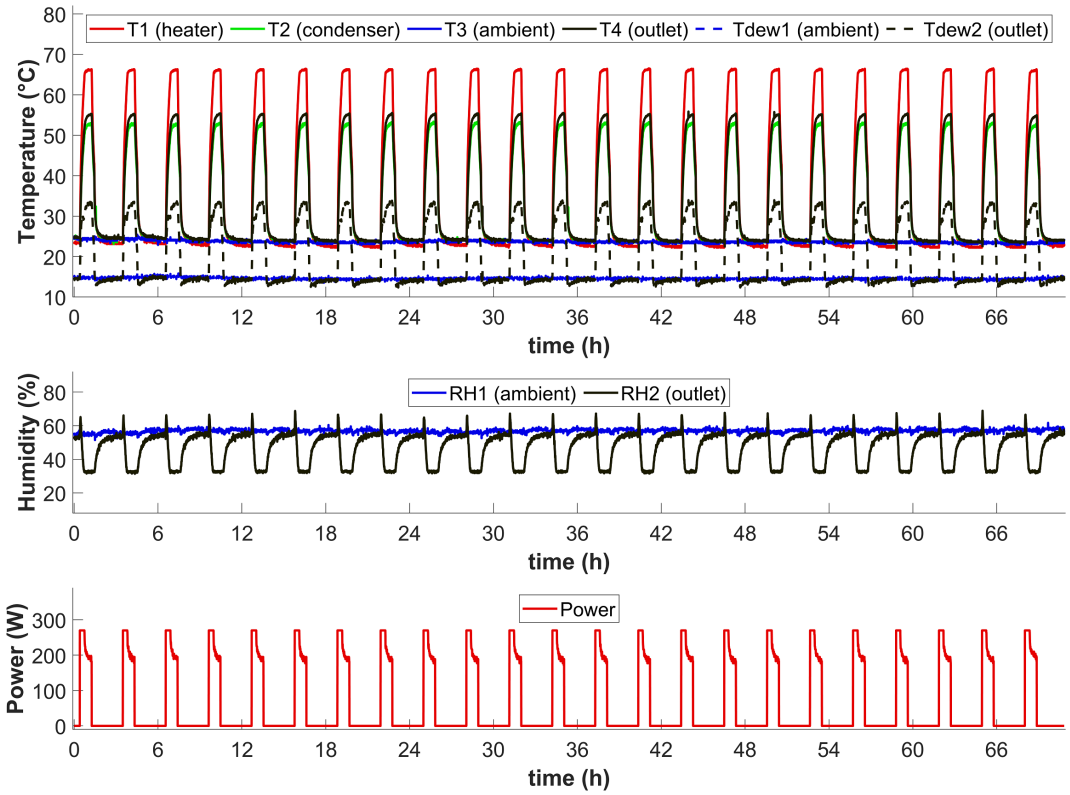

Fig. D.7 Test 7 with AWH unit.

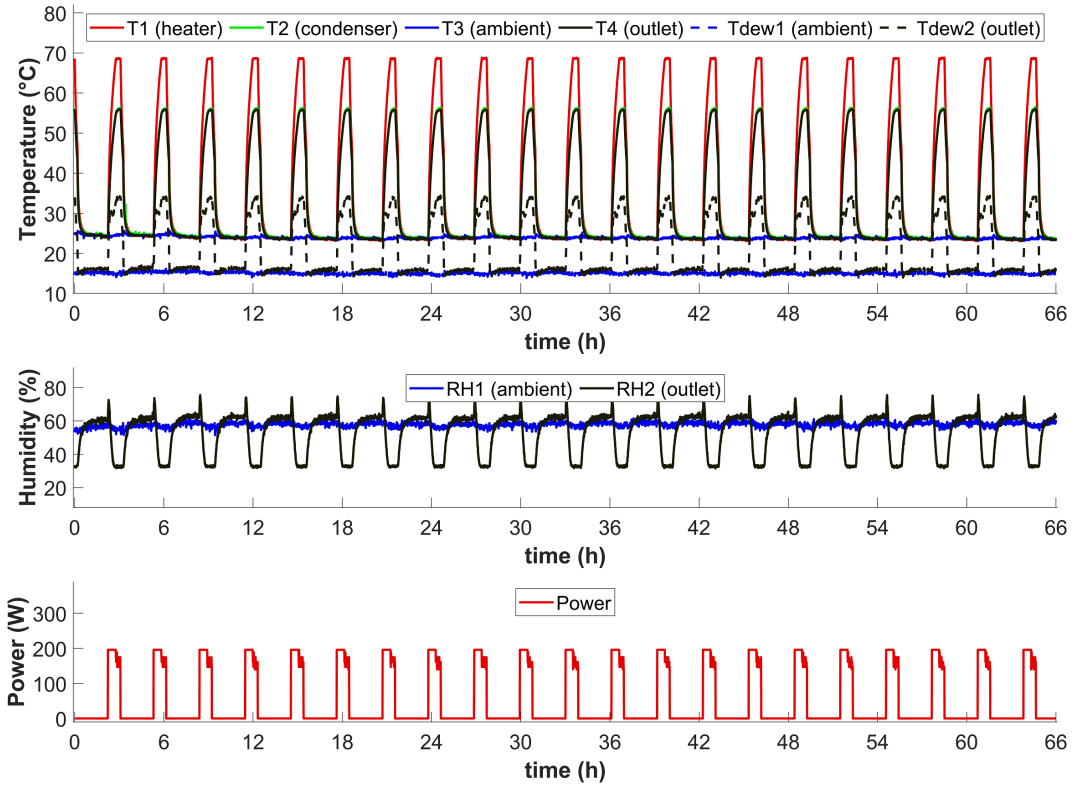

Fig. D.8 Test 8 with AWH unit.

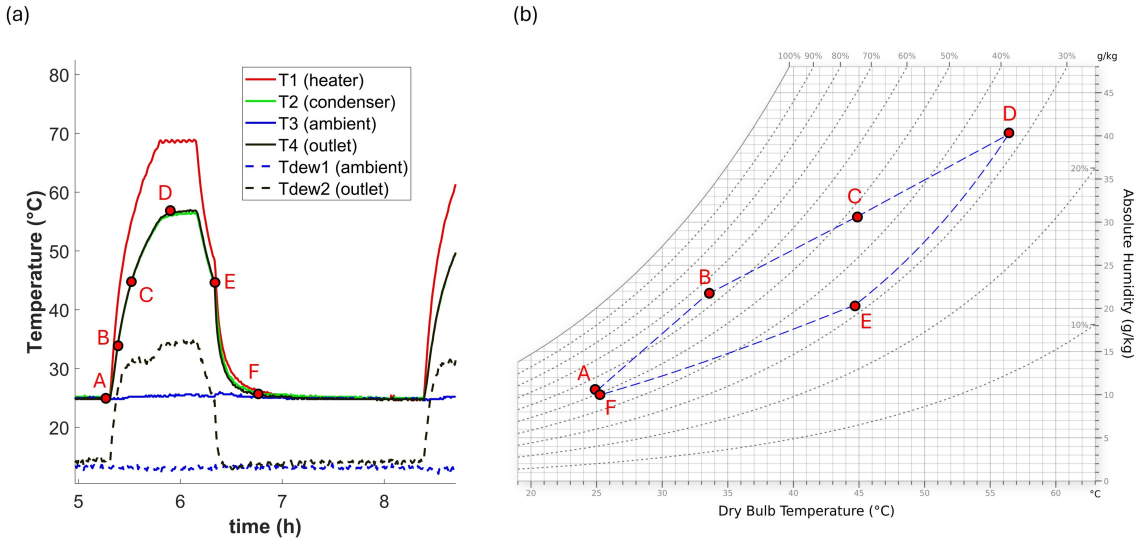

Fig. D.9 Detail of the temperatures in one cycle from test 3 with AWH unit. (a) In the time-temperature diagram. (b) Represented on the psychrometric chart. The reference T and RH used are from the outlet section. Unfortunately, given the sensors position, this is not representative of the actual air behaviour near to the condensation coils (distant from the sensor, and where we expect RH close to 100%), thus the portion D->E->F might not provide valuable information.

Tests with AD unit

In this section, we show the collected data from tests with the AD unit. See Table 5.4.

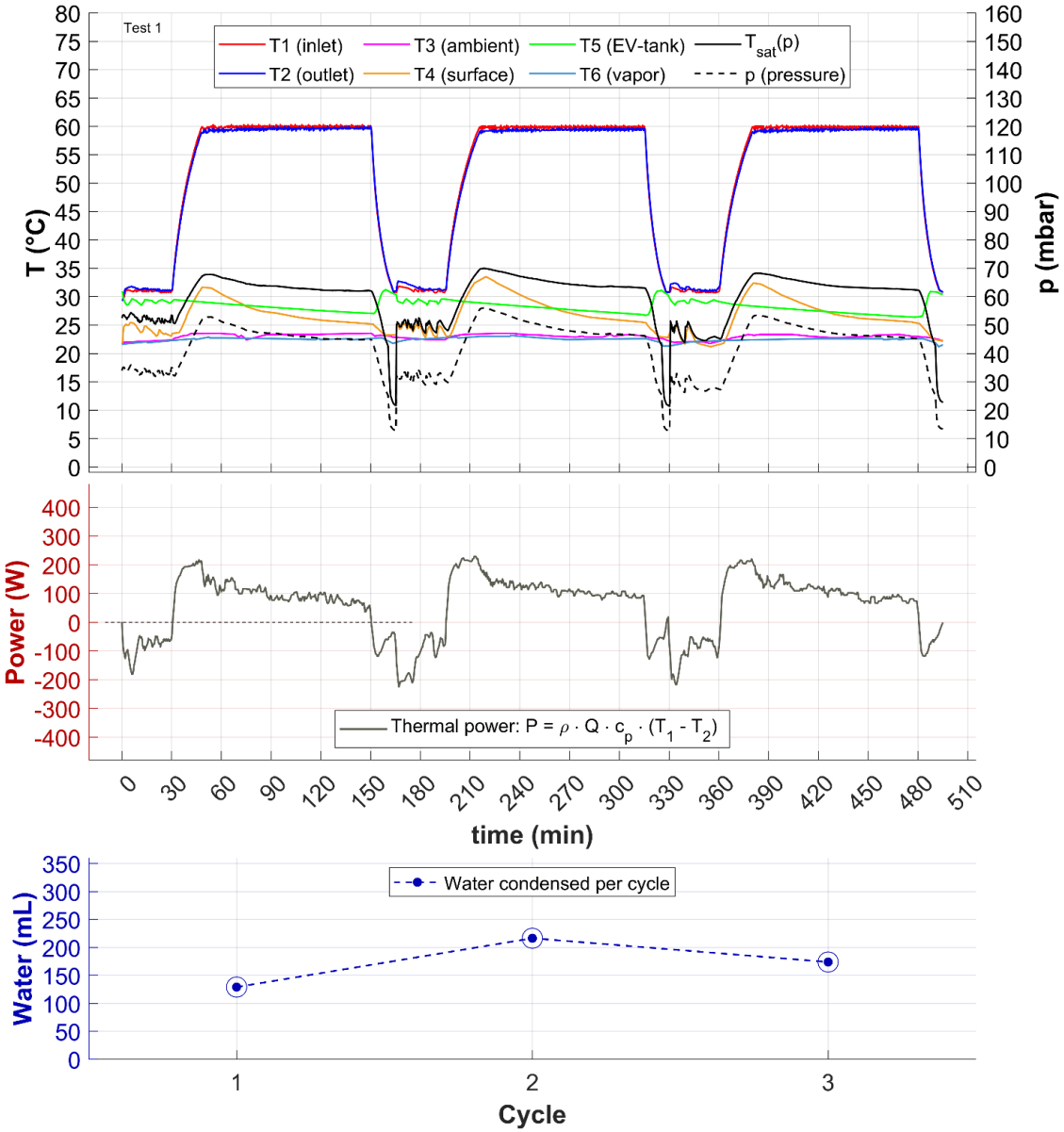

Fig. D.10 Test 1 with AD unit.

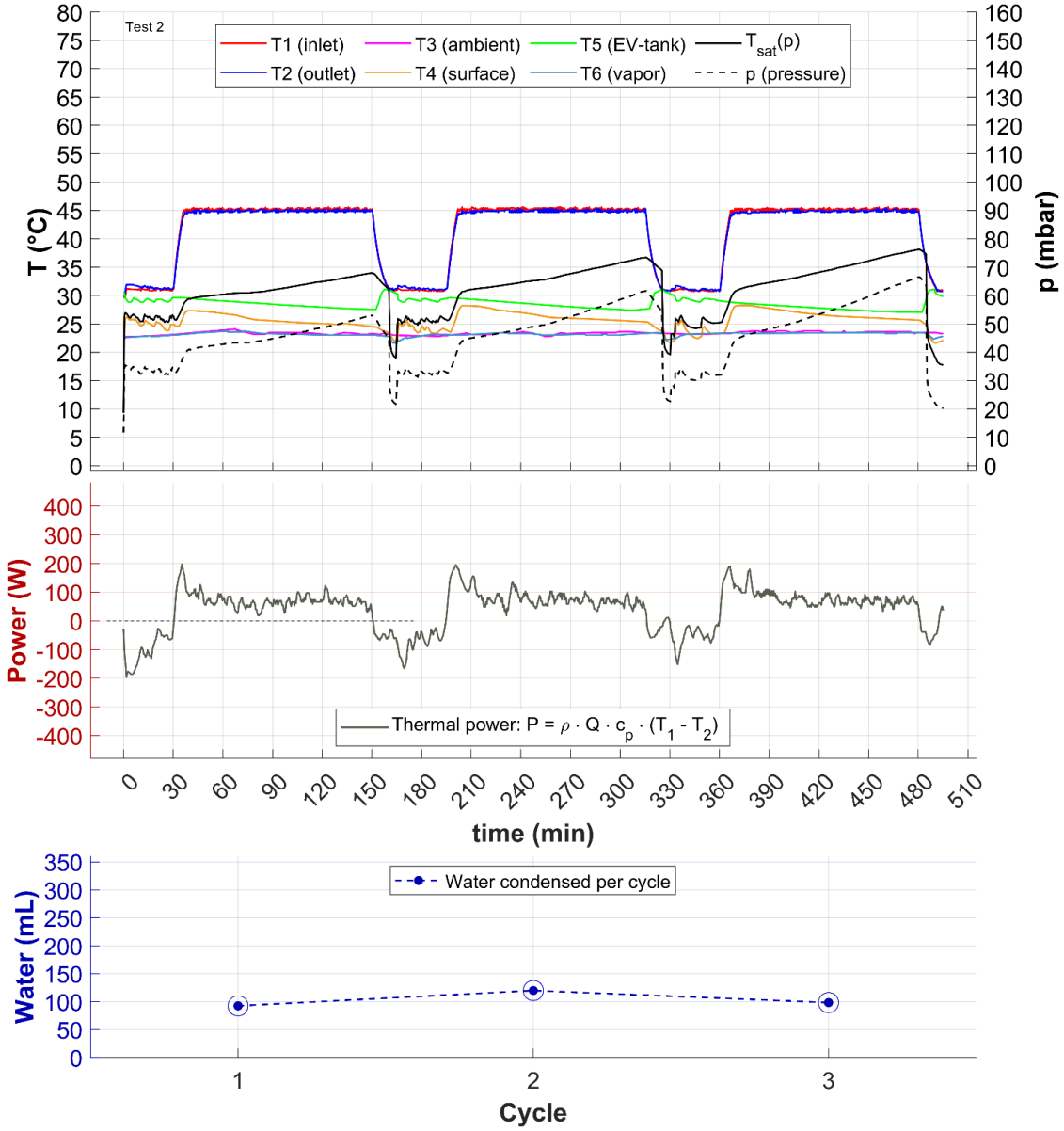

Fig. D.11 Test 2 with AD unit.

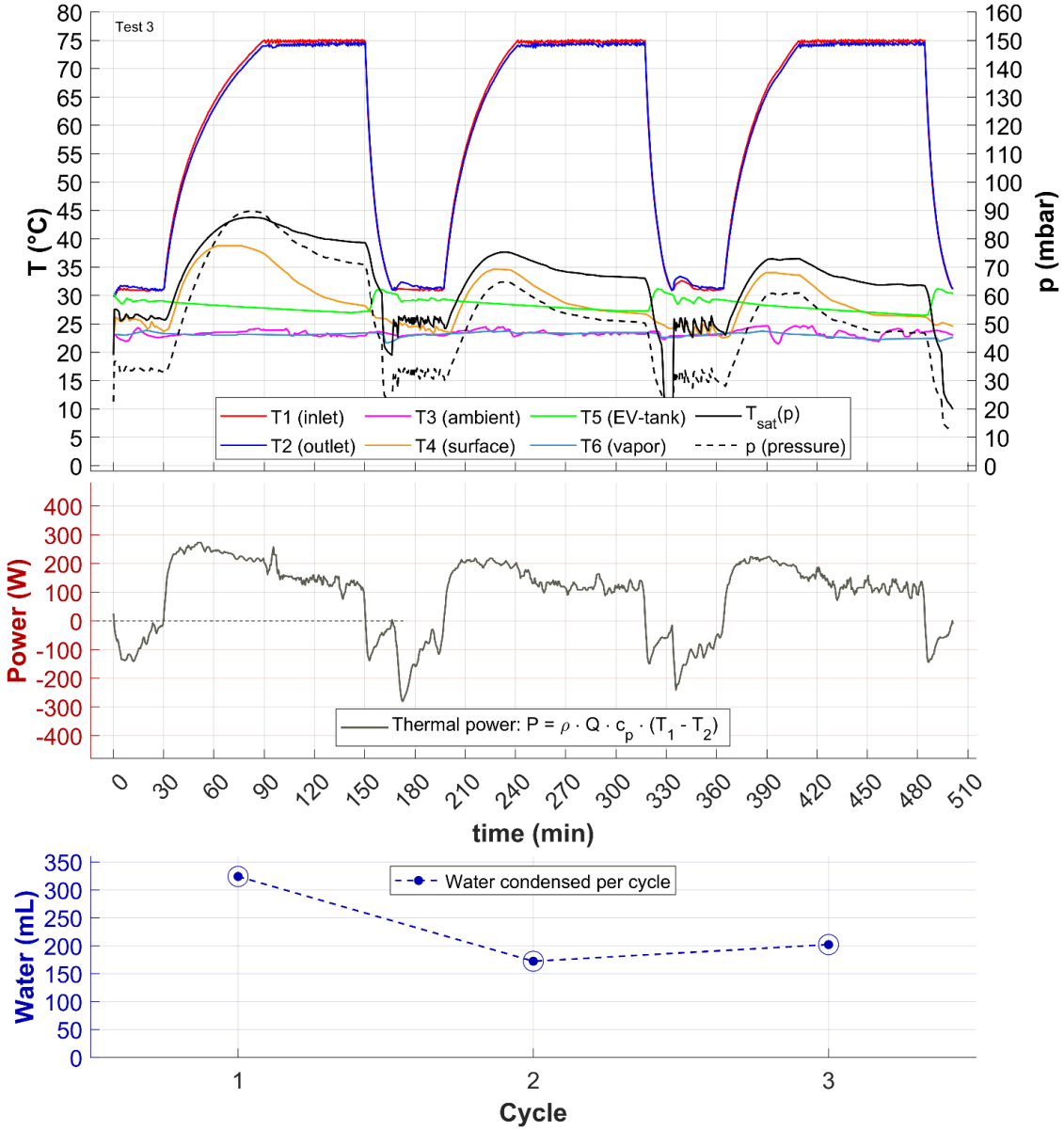

Fig. D.12 Test 3 with AD unit.

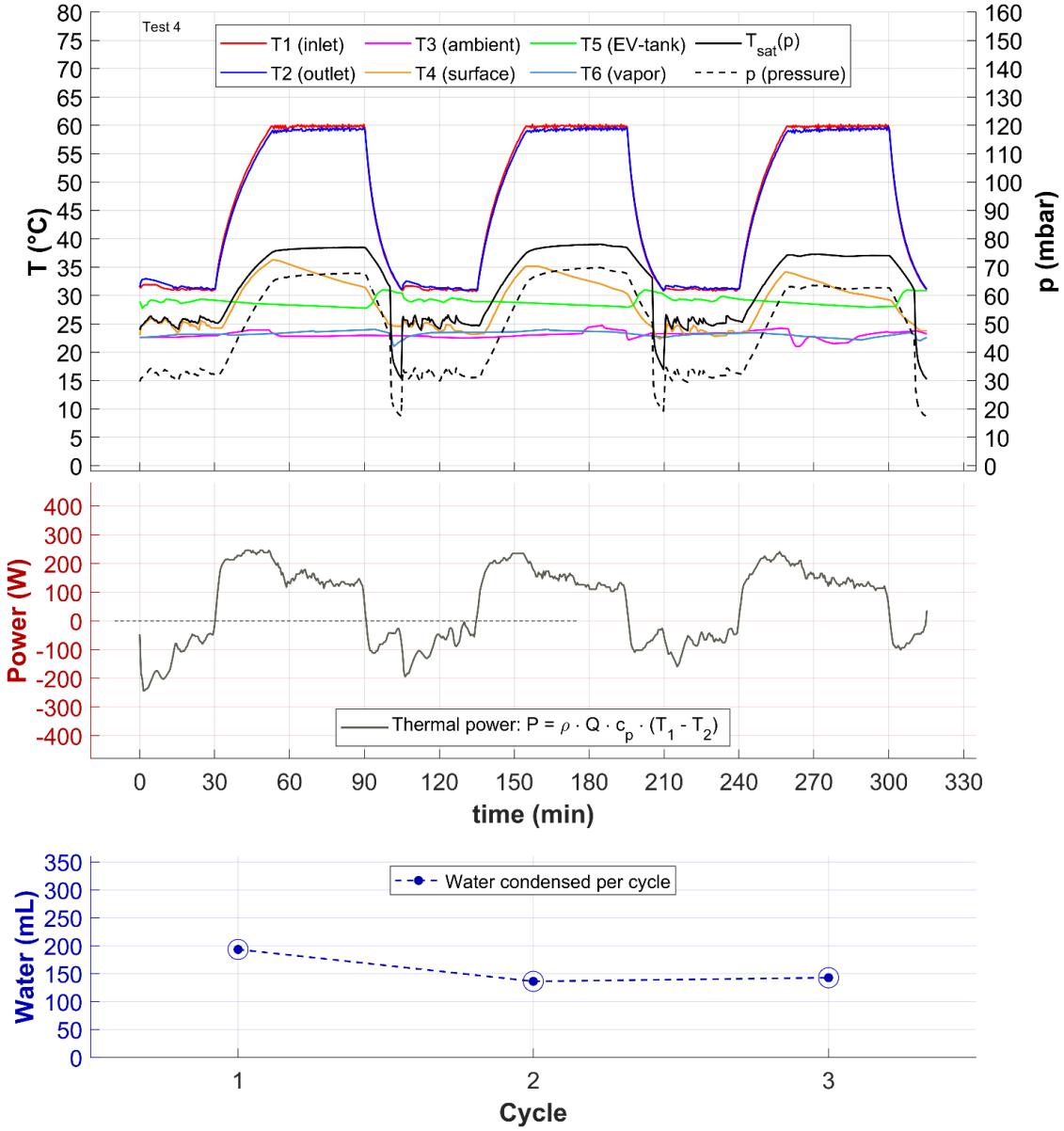

Fig. D.13 Test 4 with AD unit.

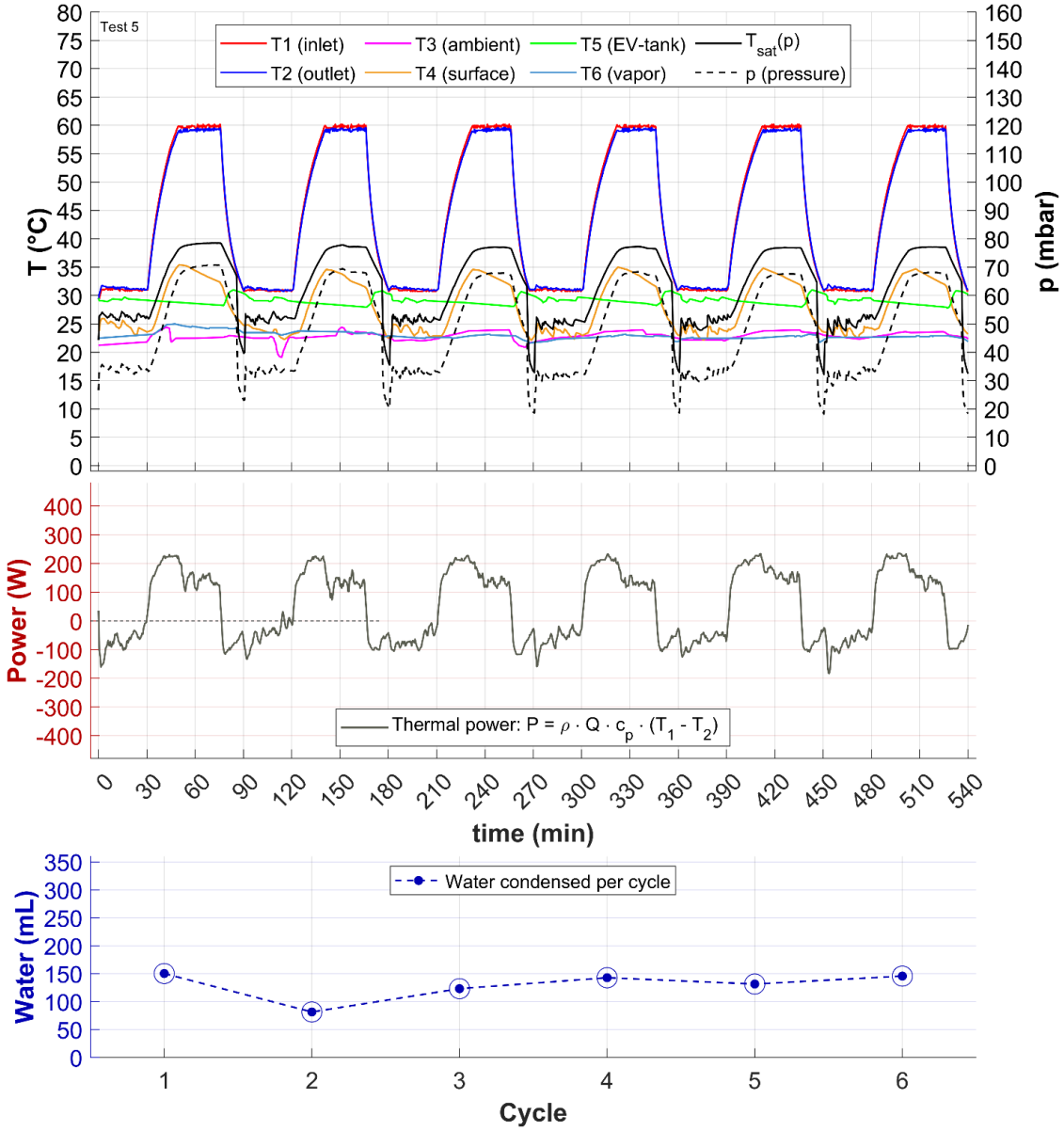

Fig. D.14 Test 5 with AD unit.

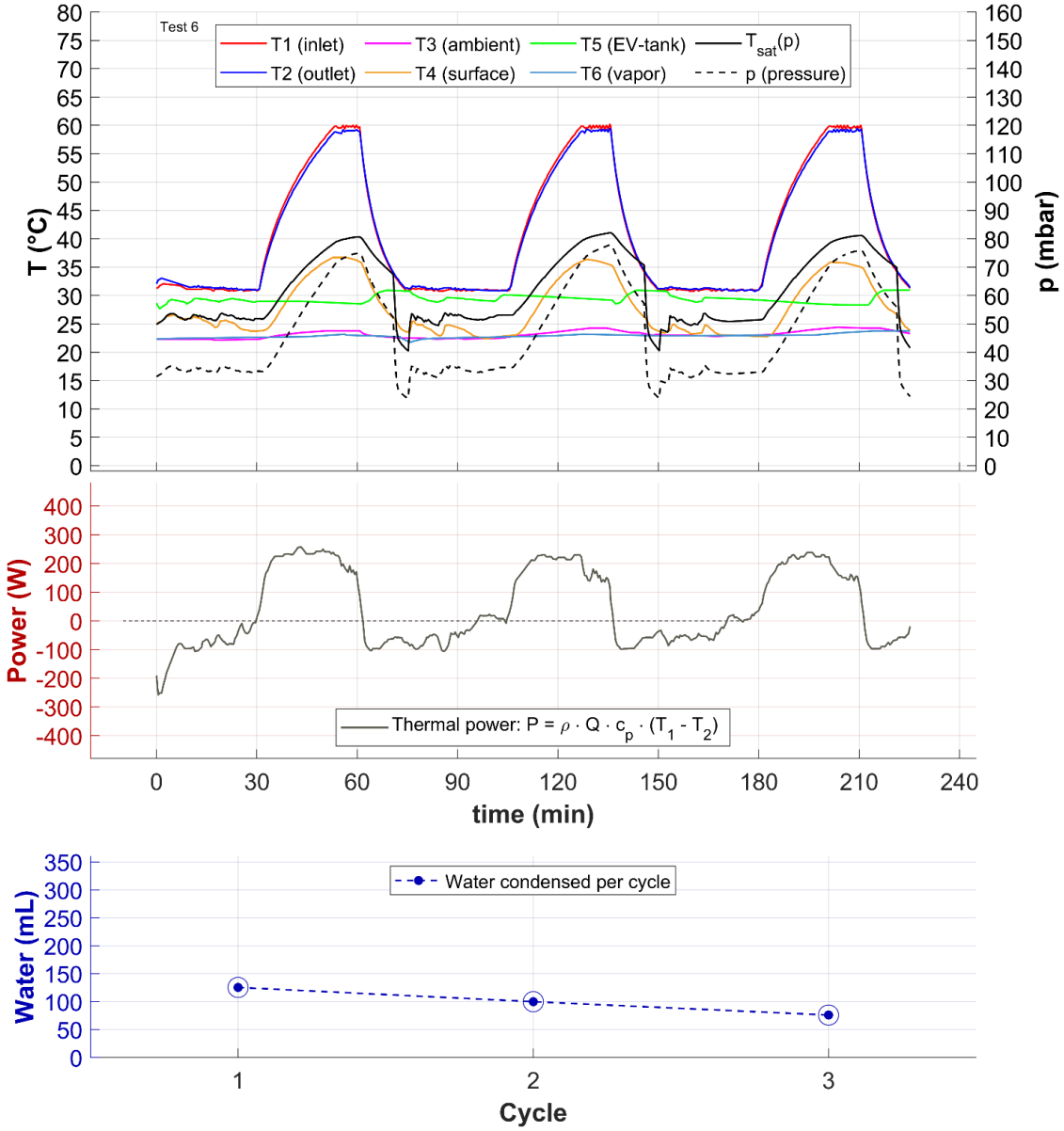

Fig. D.15 Test 6 with AD unit.

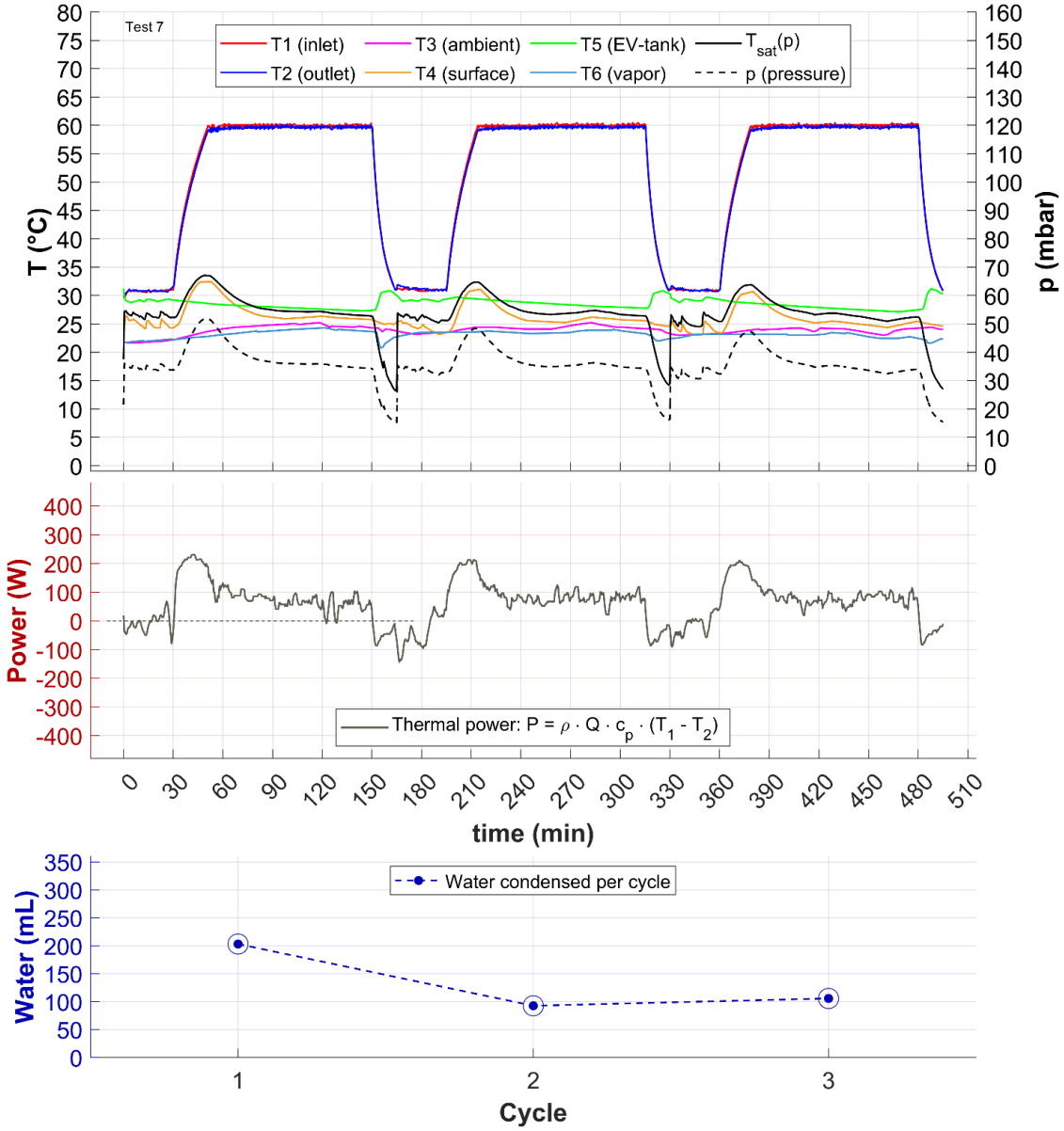

Fig. D.16 Test 7 with AD unit.

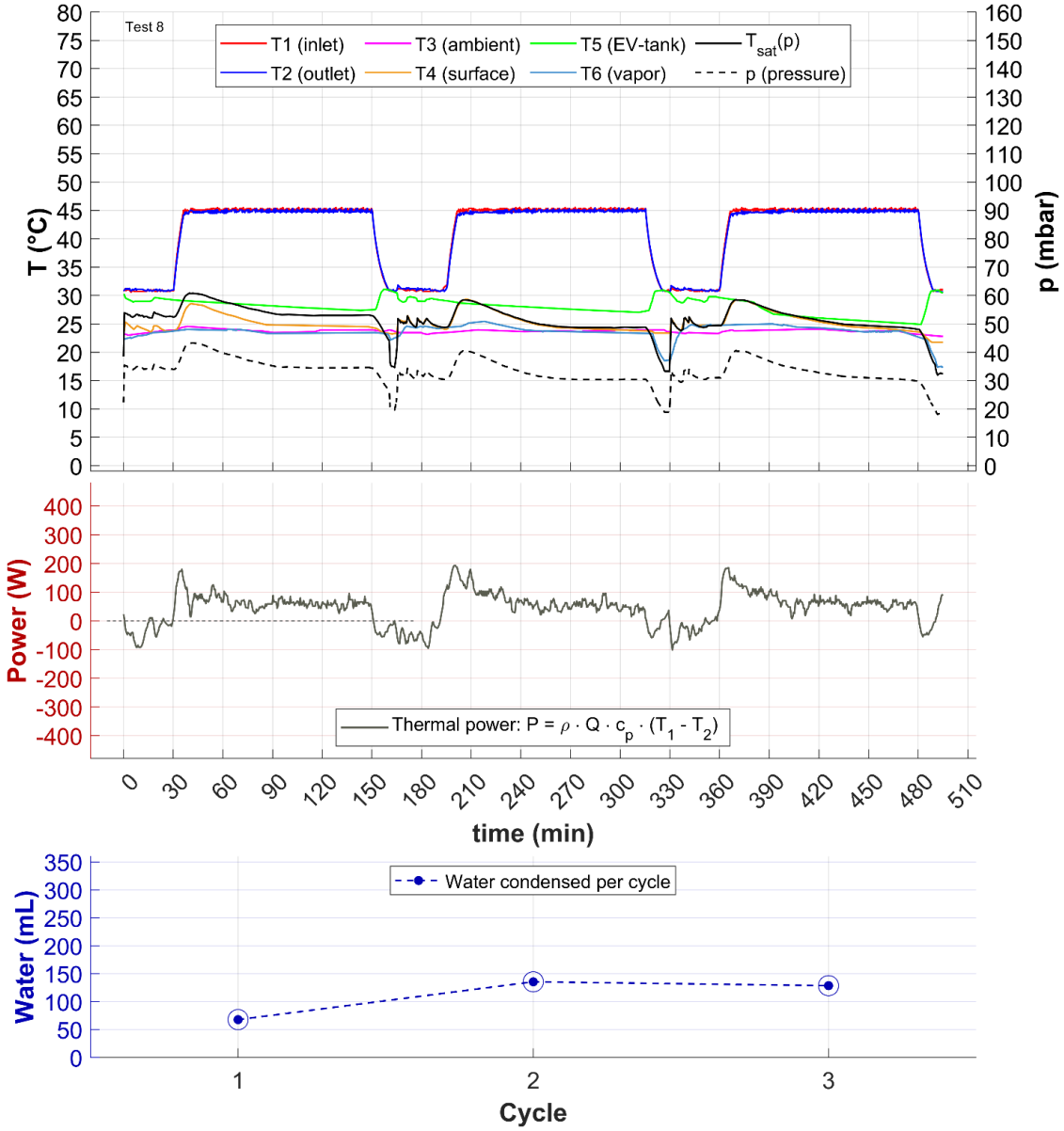

Fig. D.17 Test 8 with AD unit.

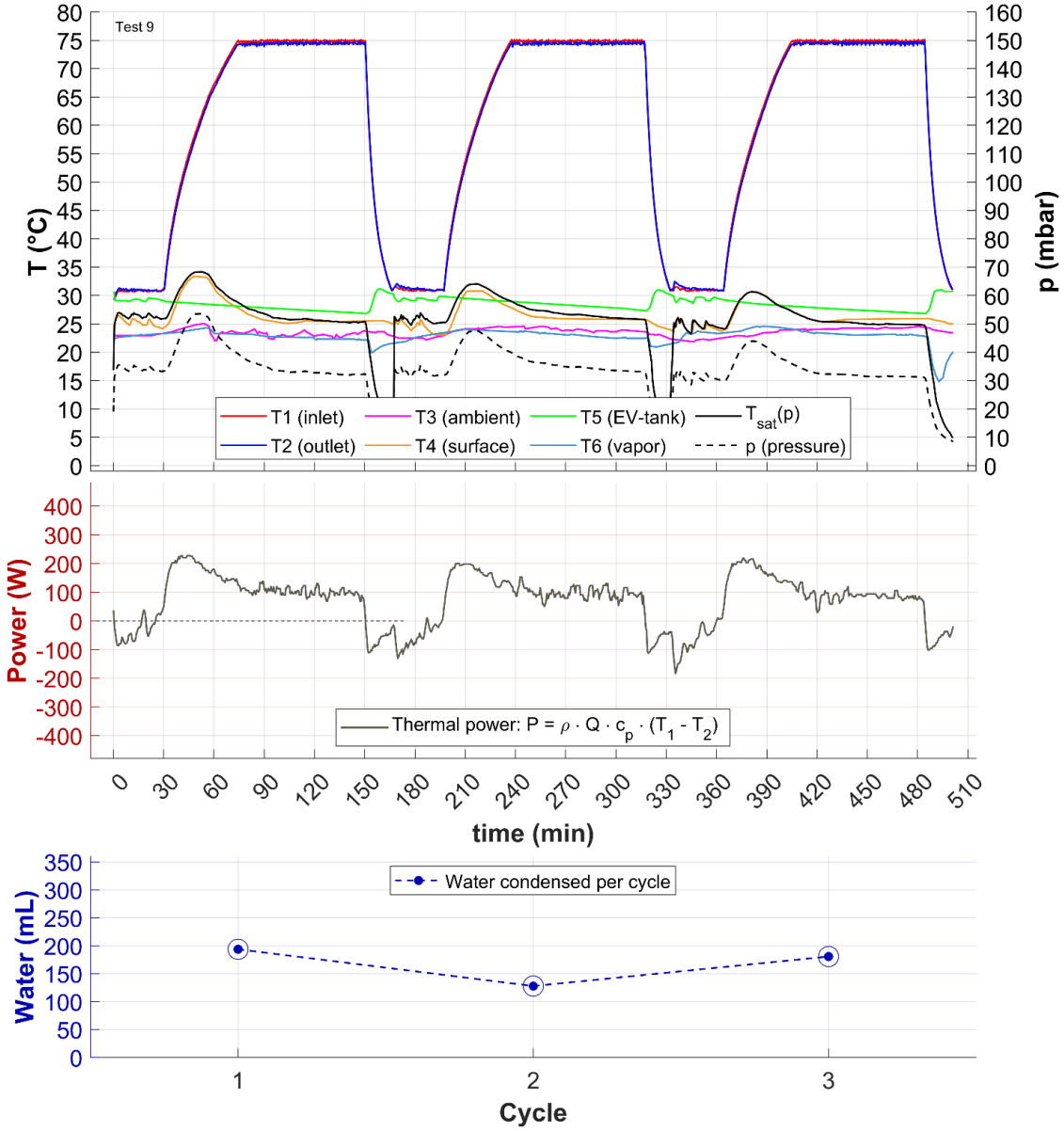

Fig. D.18 Test 9 with AD unit.

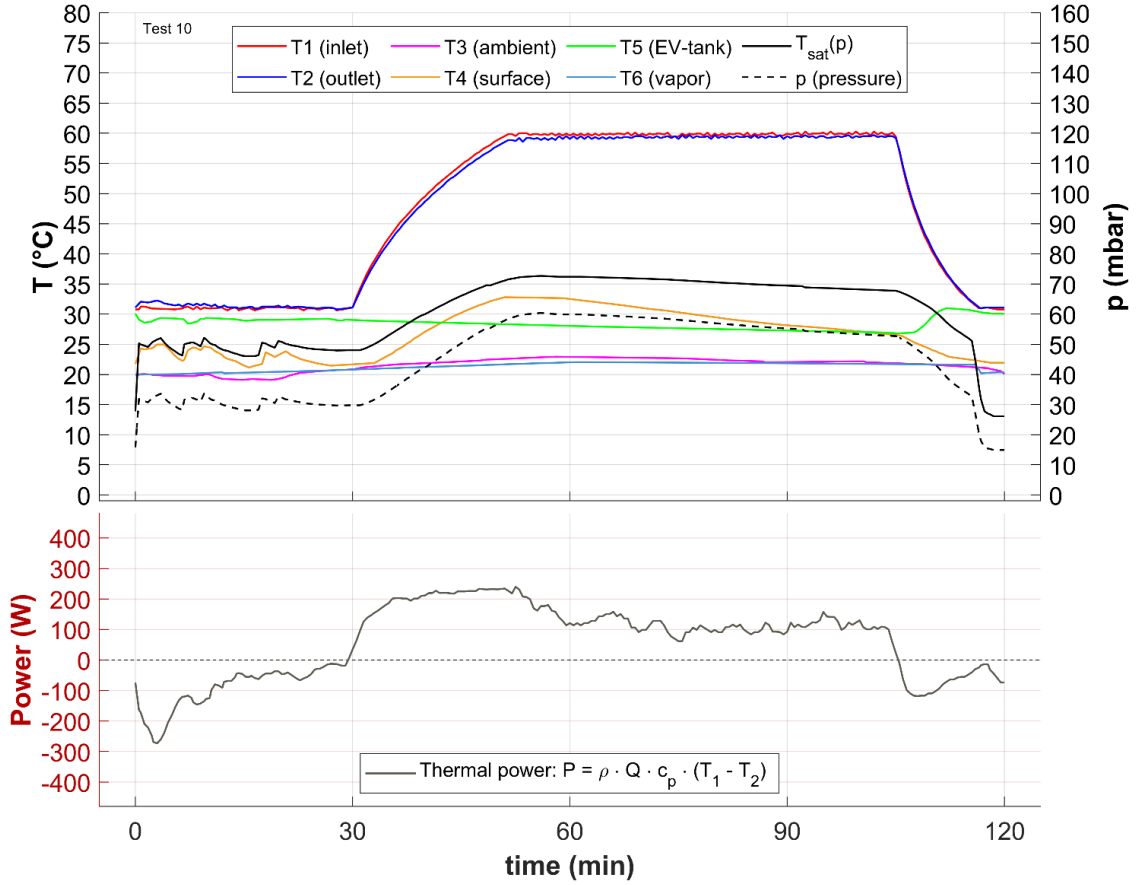

Fig. D.19 Test 10 with AD unit. This test was not included in the main campaign, as it was run with salty feedwater only to assess the desalination capacity of the machine using CaAlg.

Tests with AC unit

In this section, we show the collected data from tests with the AC unit. See Table 6.1.

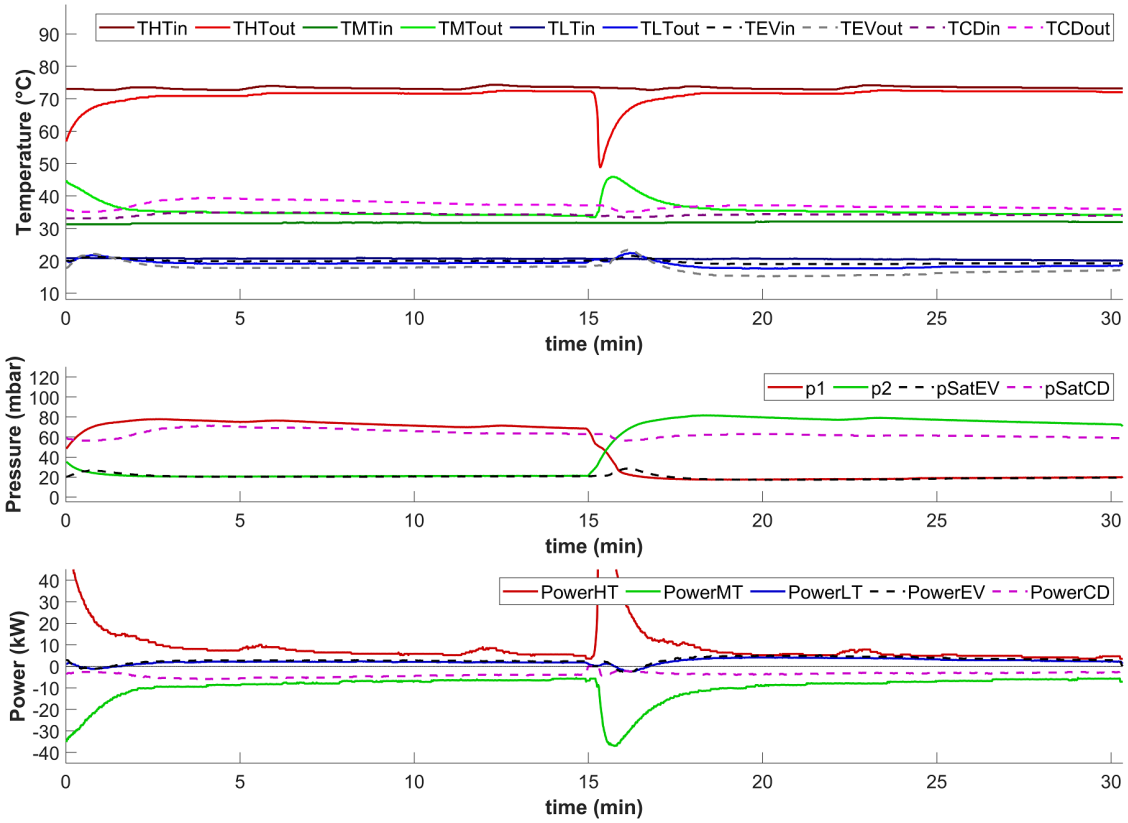

Fig. D.20 Test 1 with AC unit.

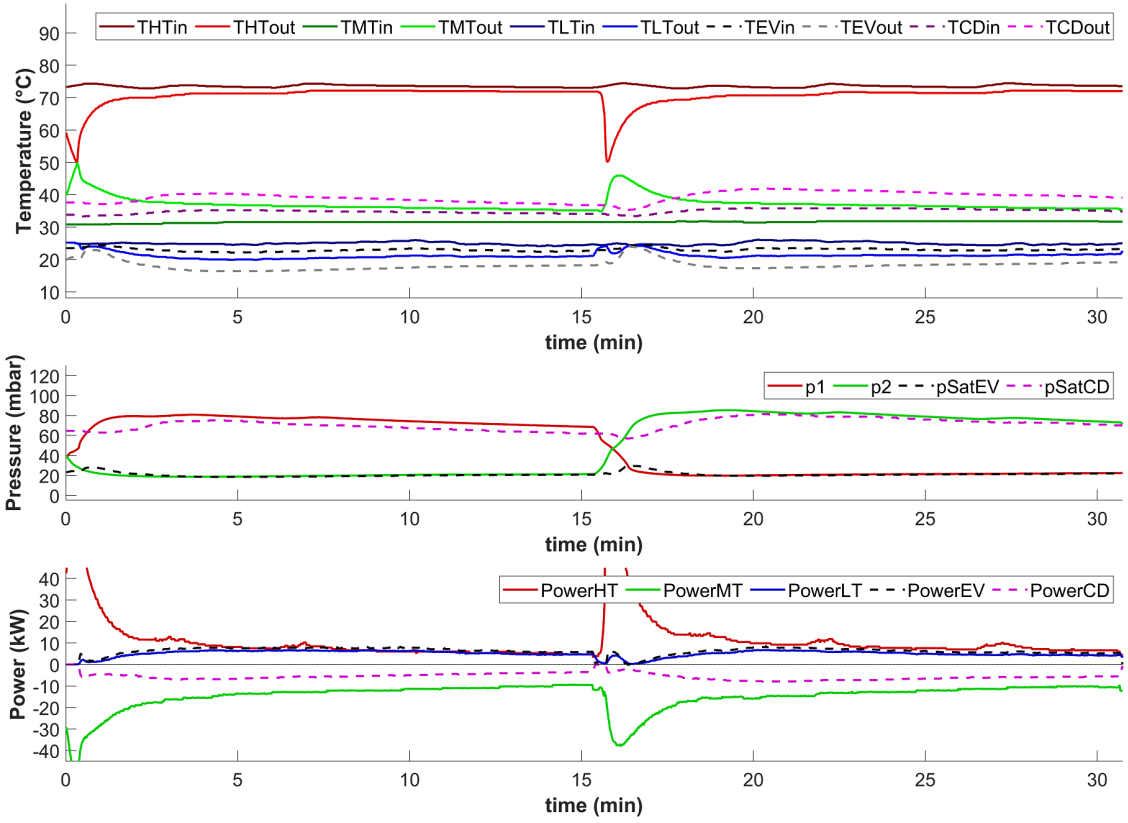

Fig. D.21 Test 2 with AC unit.

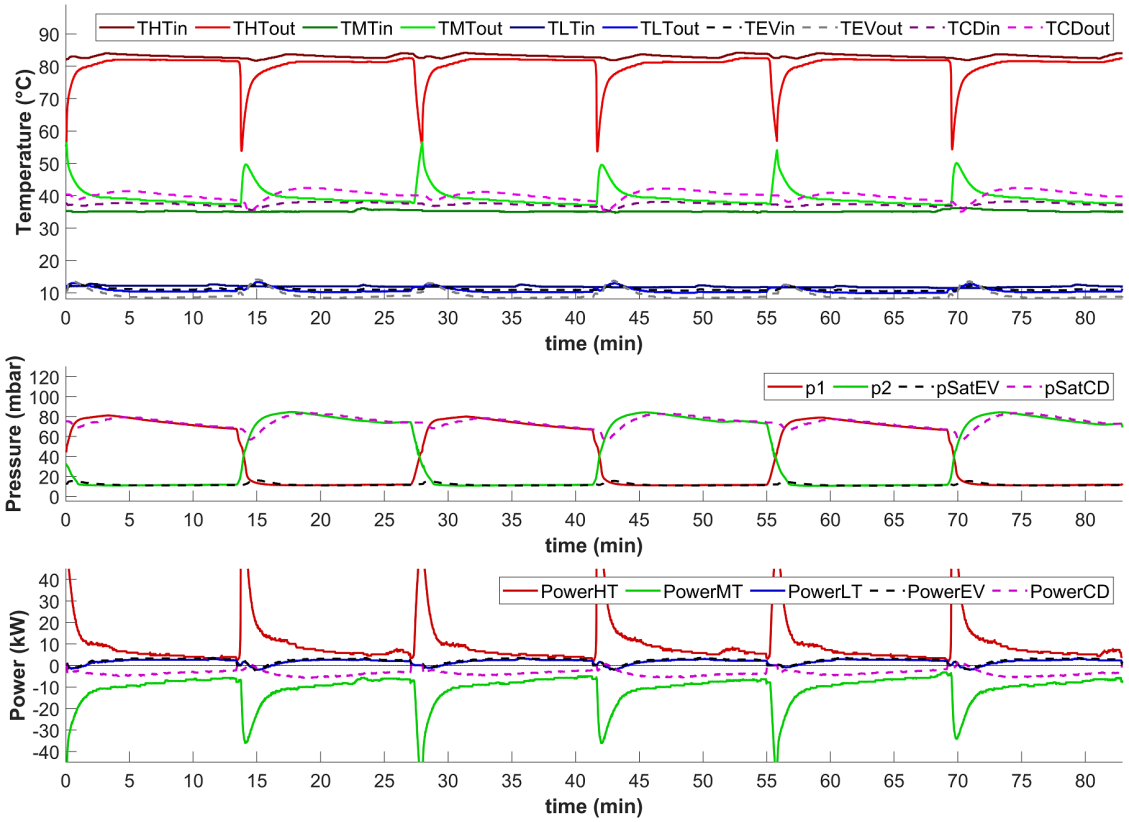

Fig. D.22 Test 3 with AC unit.

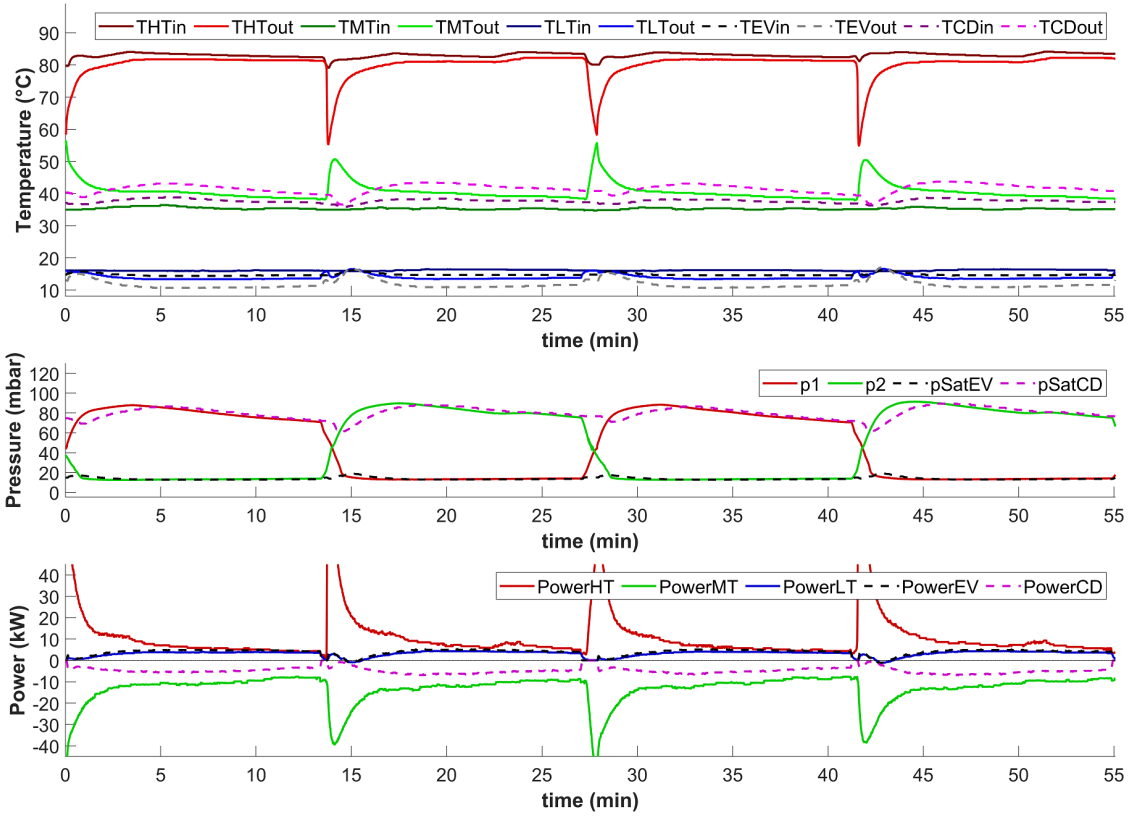

Fig. D.23 Test 4 with AC unit.

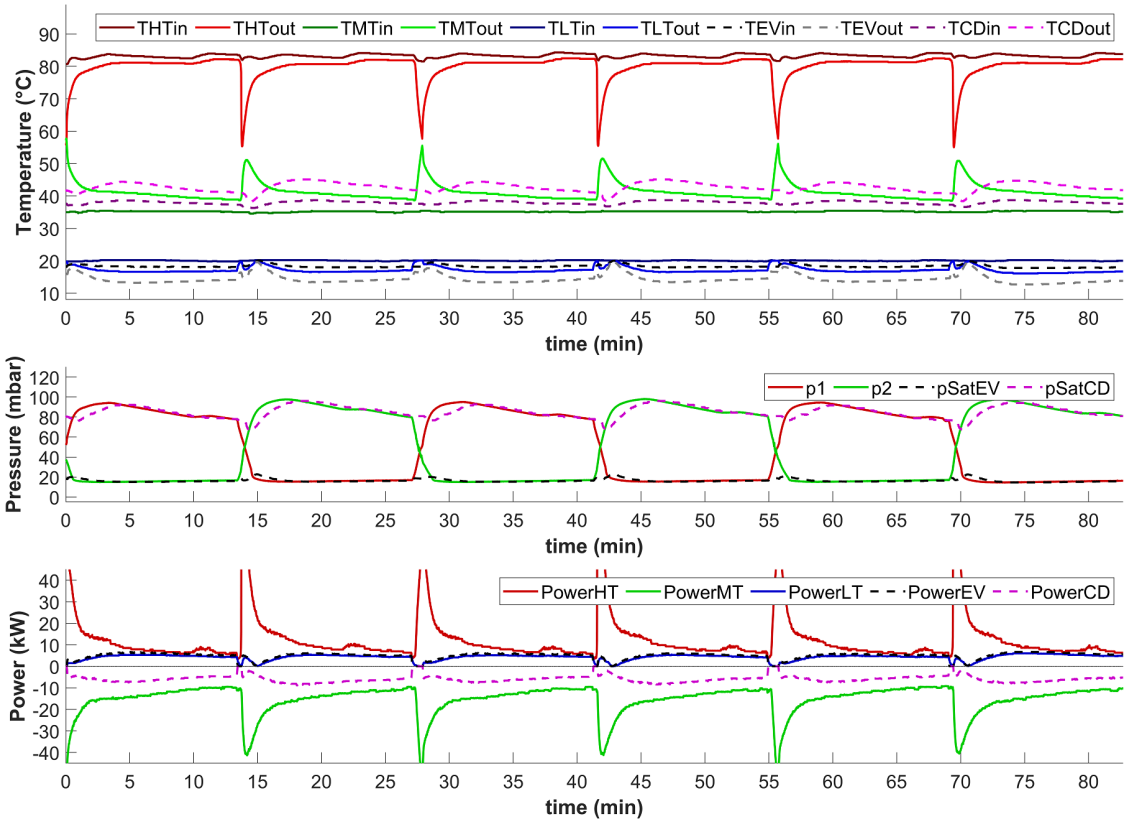

Fig. D.24 Test 5 with AC unit.

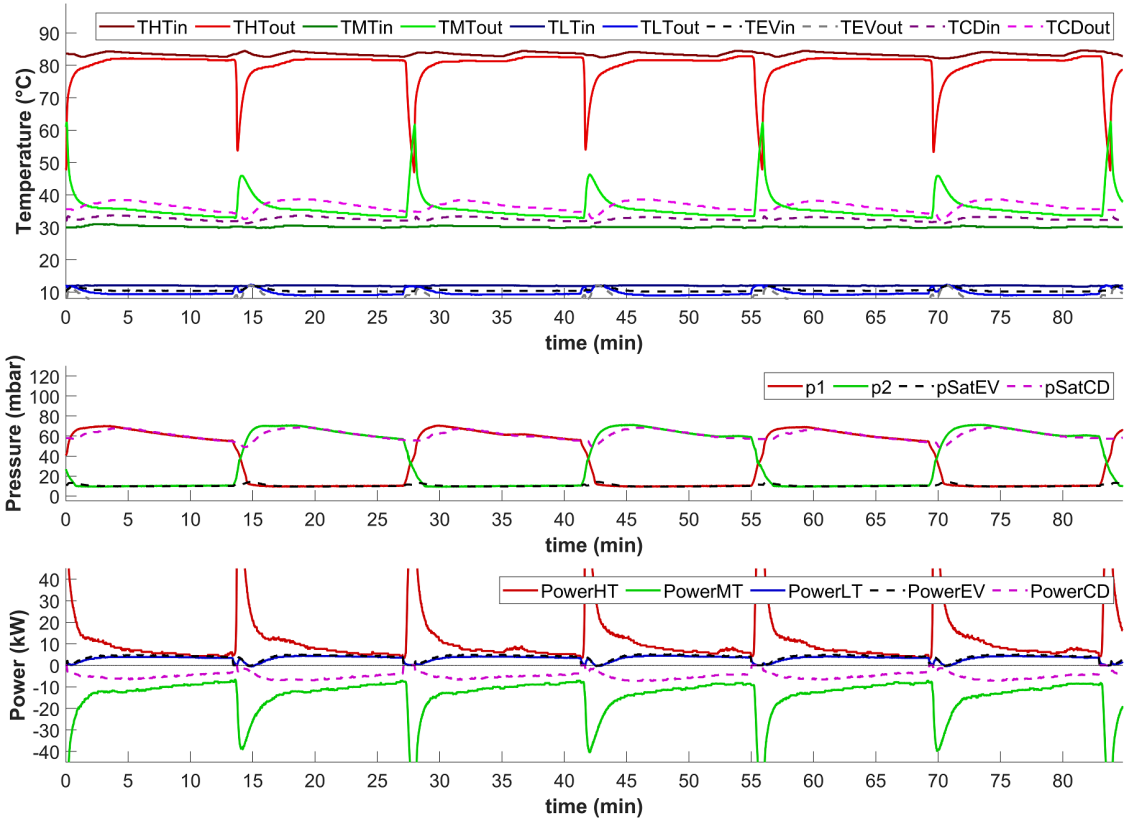

Fig. D.25 Test 6 with AC unit.

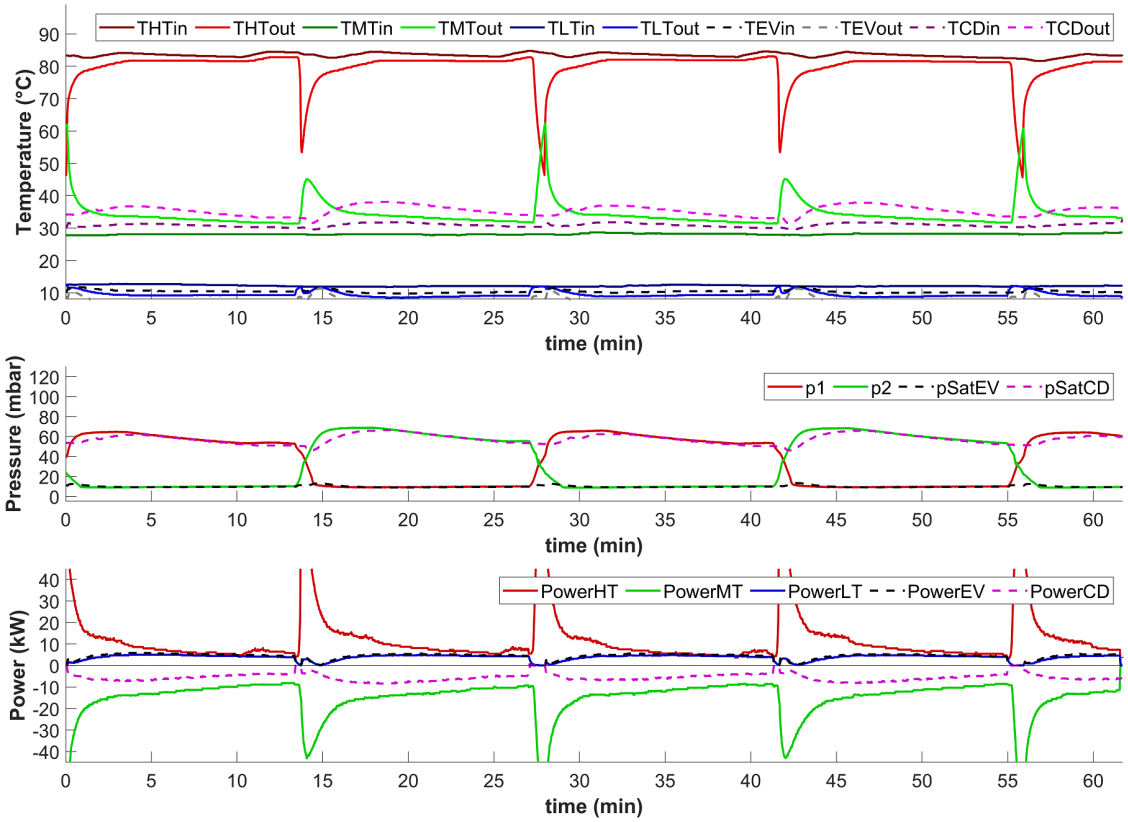

Fig. D.26 Test 7 with AC unit.

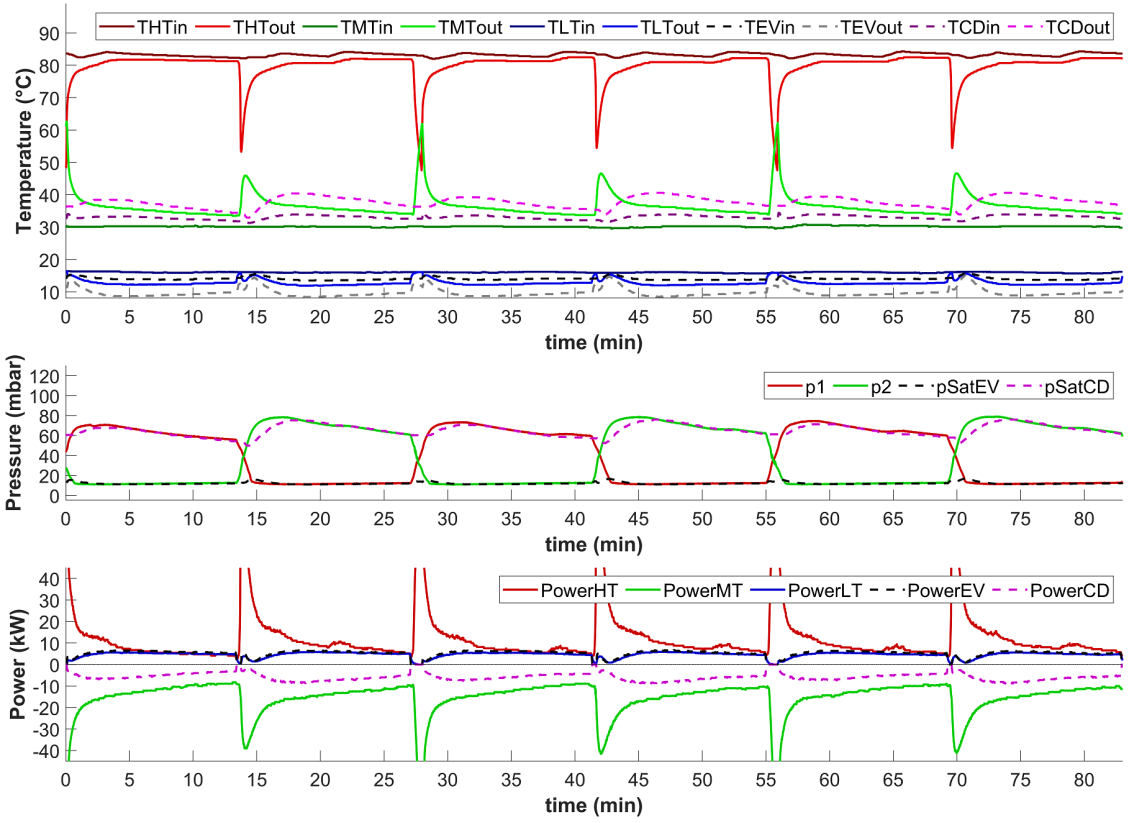

Fig. D.27 Test 8 with AC unit.

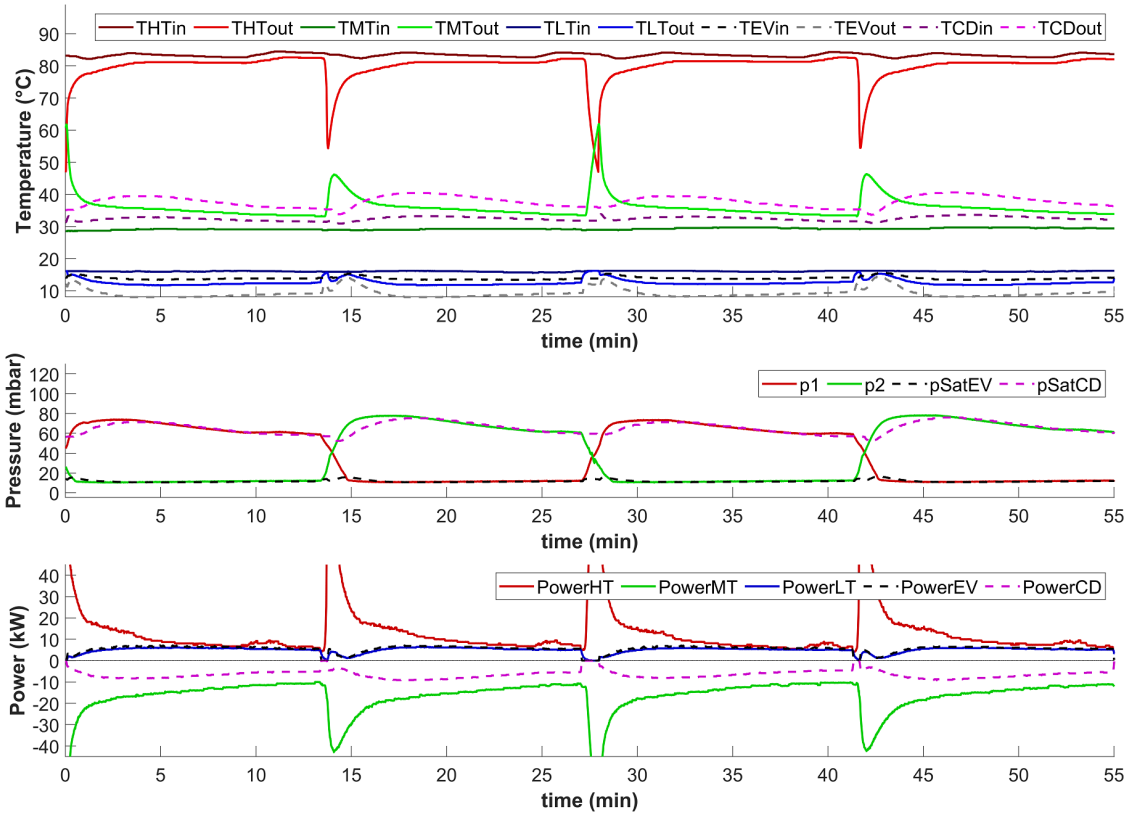

Fig. D.28 Test 9 with AC unit.

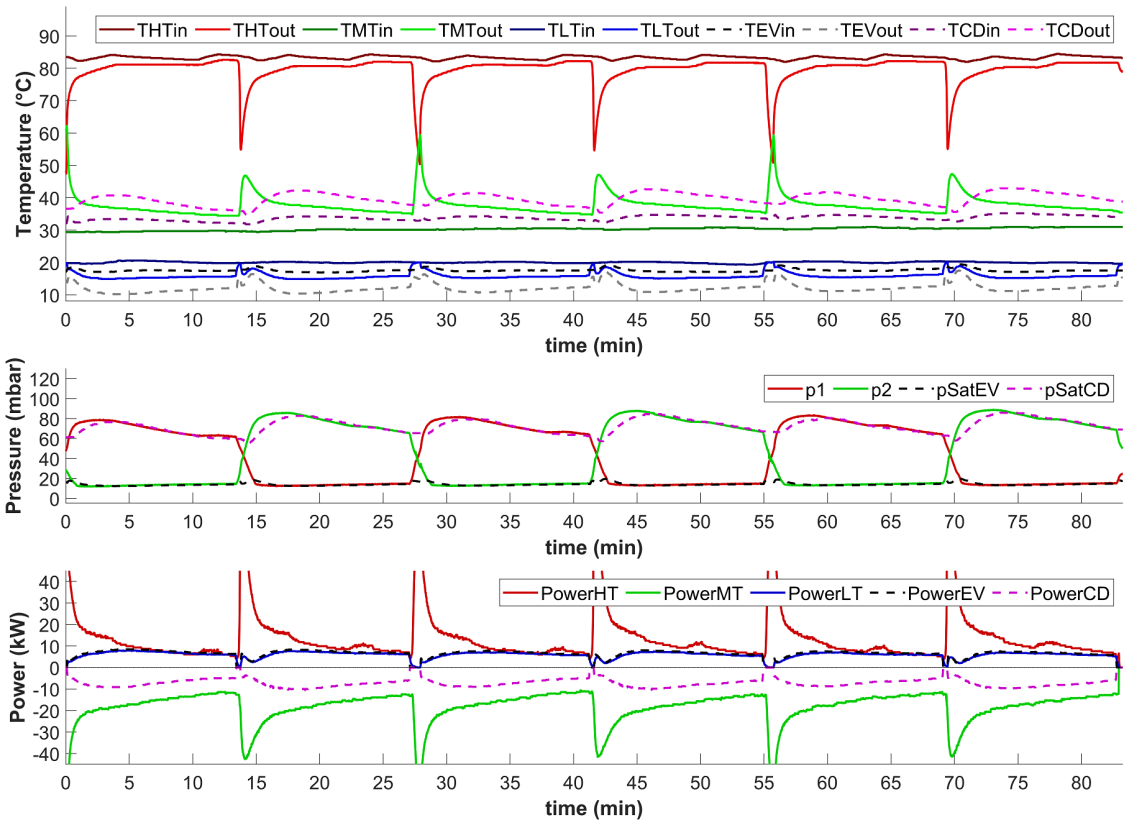

Fig. D.29 Test 10 with AC unit.

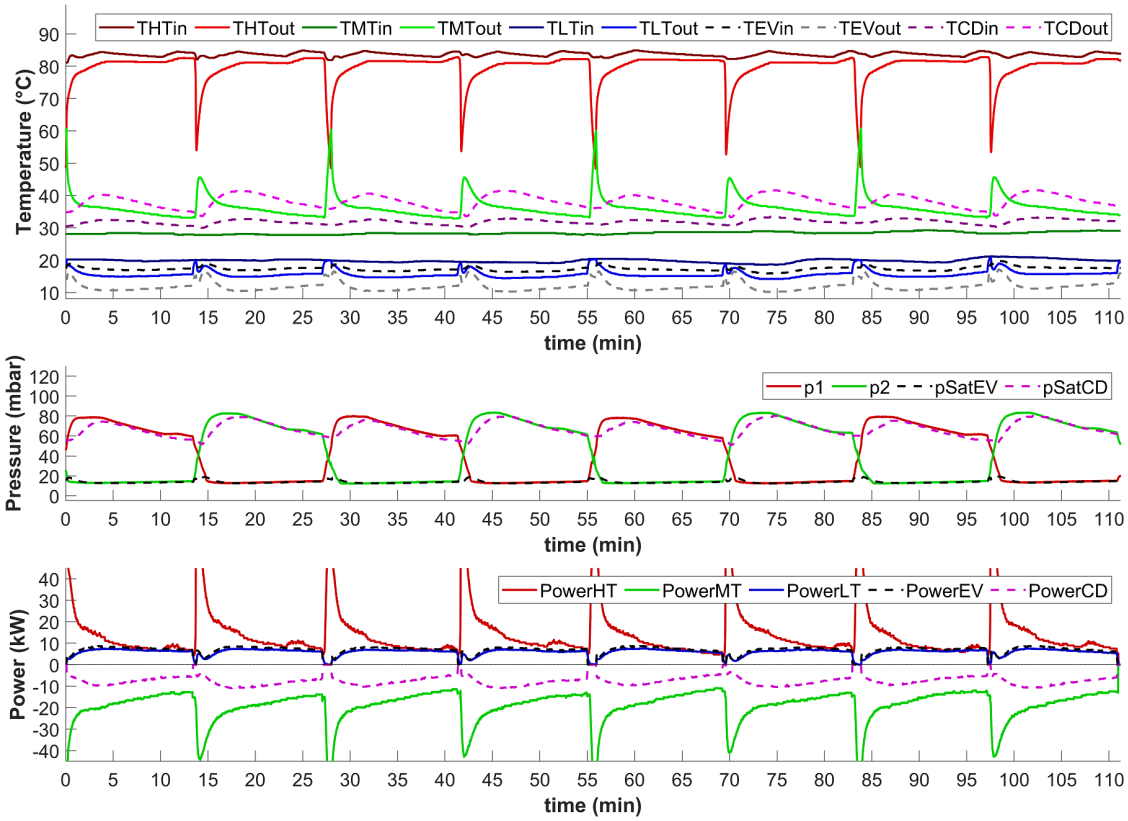

Fig. D.30 Test 11 with AC unit.

Pictures of the sorbents during isotherms construction

In this section, we show the pictures taken with the ProUmid analyser at each equilibrium condition during the construction of the isotherm at T=30°C, RH=10-70%. For the list of samples, refer to table 4.10. We observe that the appearance of CaAlg beads changes with cycling: their surface become more "rough" and the color becomes darker. In some cases, some greenish material appears on the beads, and along with that, some greenish powder was found in the adsorber: this might be explained either with the aluminum fins coating scratching from the heat exchanger fins, or with the insurgence of mould due to organic degradation of the hydrogel. This didn't affect the performances of the material, but further investigation is suggested. Another interesting effect is the change in material volume, due to the polymeric chains rearranging with the collection of vapor. This was discussed in Fig. 4.15 and effectively captured in the time-lapse video at the link https://youtu.be/T1RhqqBuPVg (last visited on 26/10/2025), with the single pictures obtained by performing a dedicated experiment, consisting of a sequence of three transients on CaAlg beads: a desorption at T=40°C, RH=10%, then an adsorption at T=20°C, RH=60%, and finally a desorption at T=40°C, RH=10%. We observe some liquefaction occurring at medium-high RH on CaAlg samples, with some salt lost on the plate surface at the end of the desorption ramps.

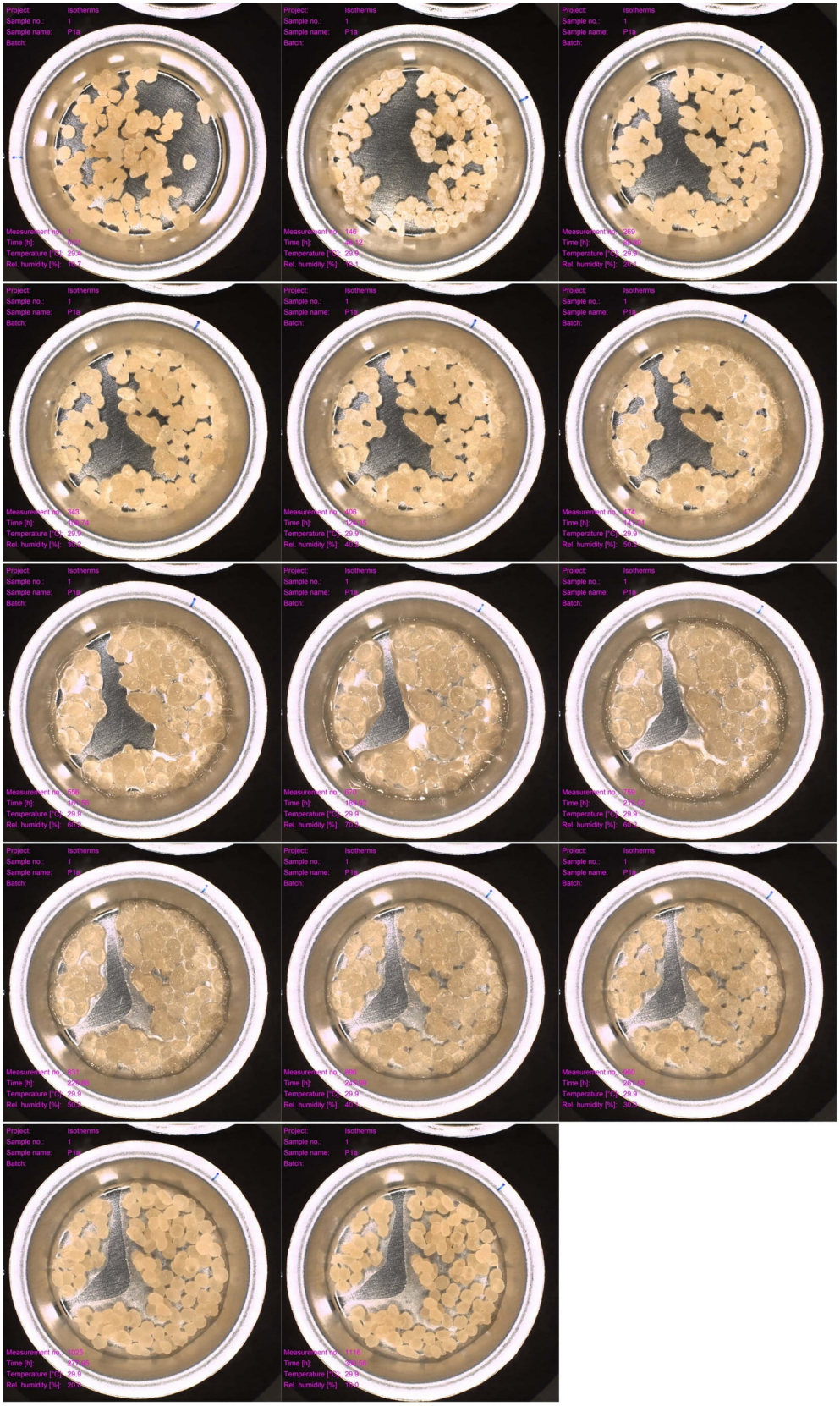

Fig. D.31 Equilibrium pictures on sample 1. Going through rows from top-left to bottom-right, we see RH increasing (10, 20, ..., 70%) and then decreasing (70, 60, ..., 10%). Temperature is always constant and equal to 30°C. The bottom surface of the aluminum dish has a diameter of $\approx$ 21 mm.

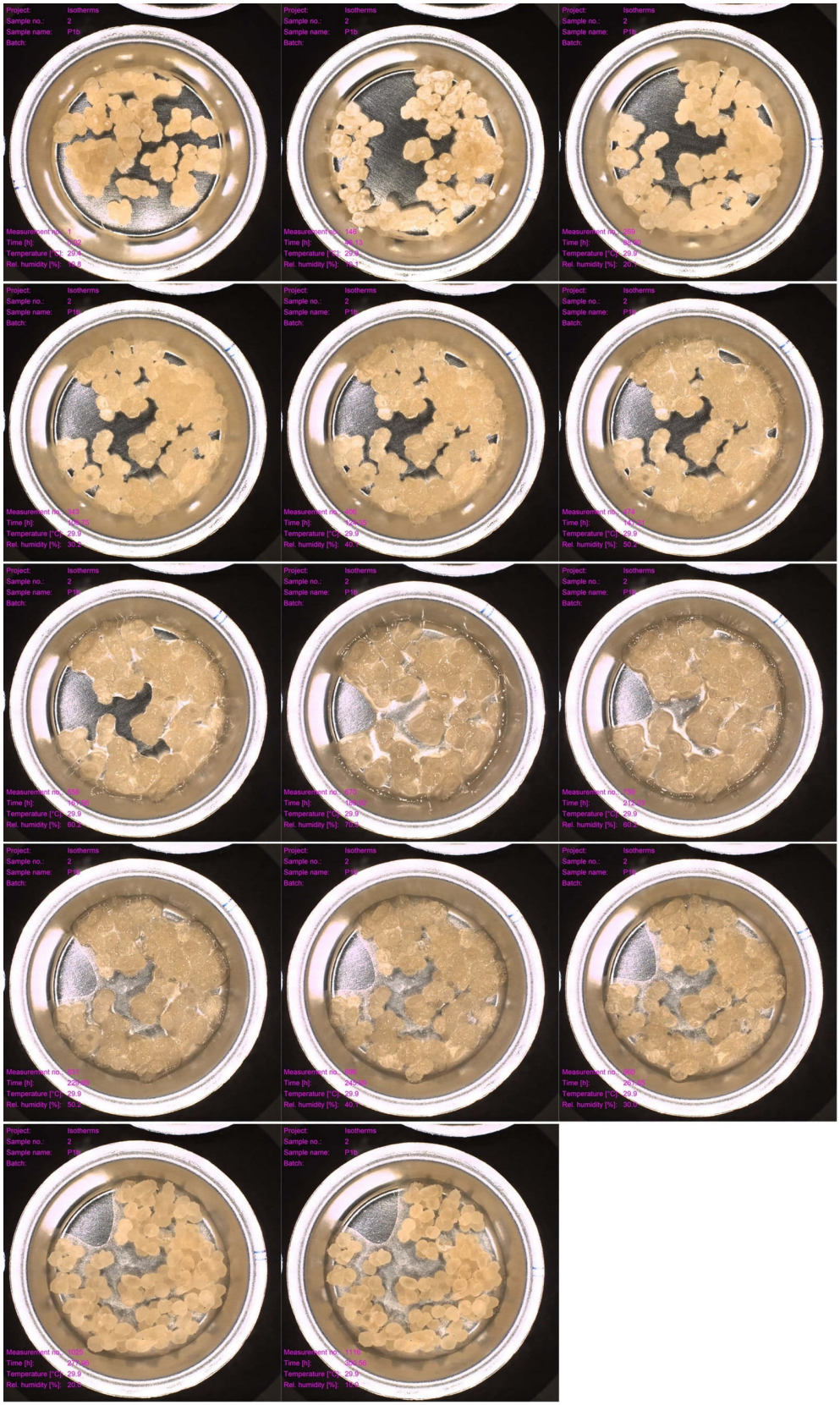

Fig. D.32 Equilibrium pictures on sample 2. Going through rows from top-left to bottom-right, we see RH increasing (10, 20, ..., 70%) and then decreasing (70, 60, ..., 10%). Temperature is always constant and equal to 30°C. The bottom surface of the aluminum dish has a diameter of $\approx$ 21 mm.

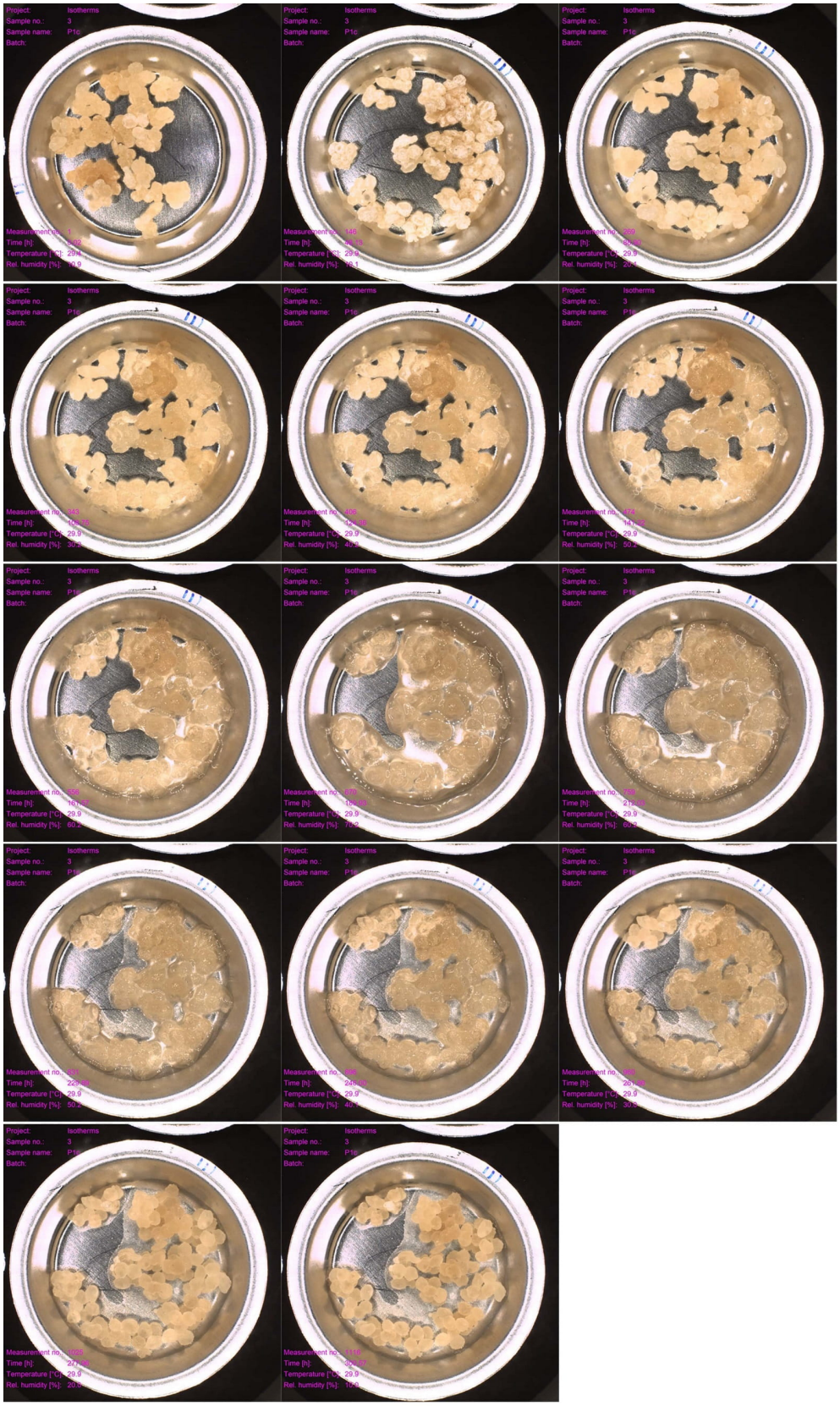

Fig. D.33 Equilibrium pictures on sample 3. Going through rows from top-left to bottom-right, we see RH increasing (10, 20, ..., 70%) and then decreasing (70, 60, ..., 10%). Temperature is always constant and equal to 30°C. The bottom surface of the aluminum dish has a diameter of ≈ 21 mm.

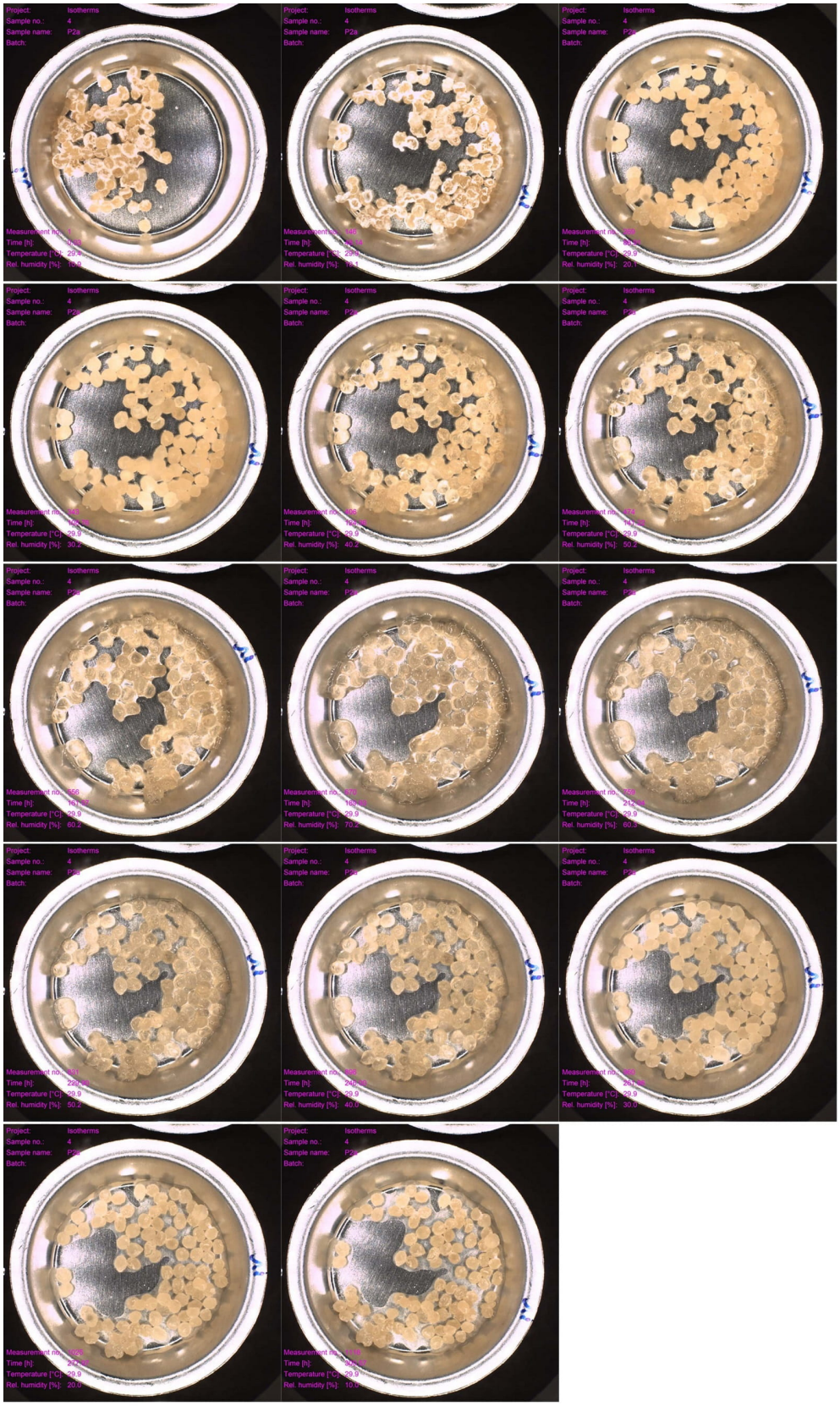

Fig. D.34 Equilibrium pictures on sample 4. Going through rows from top-left to bottom-right, we see RH increasing (10, 20, ..., 70%) and then decreasing (70, 60, ..., 10%). Temperature is always constant and equal to 30°C. The bottom surface of the aluminum dish has a diameter of $\approx$ 21 mm.

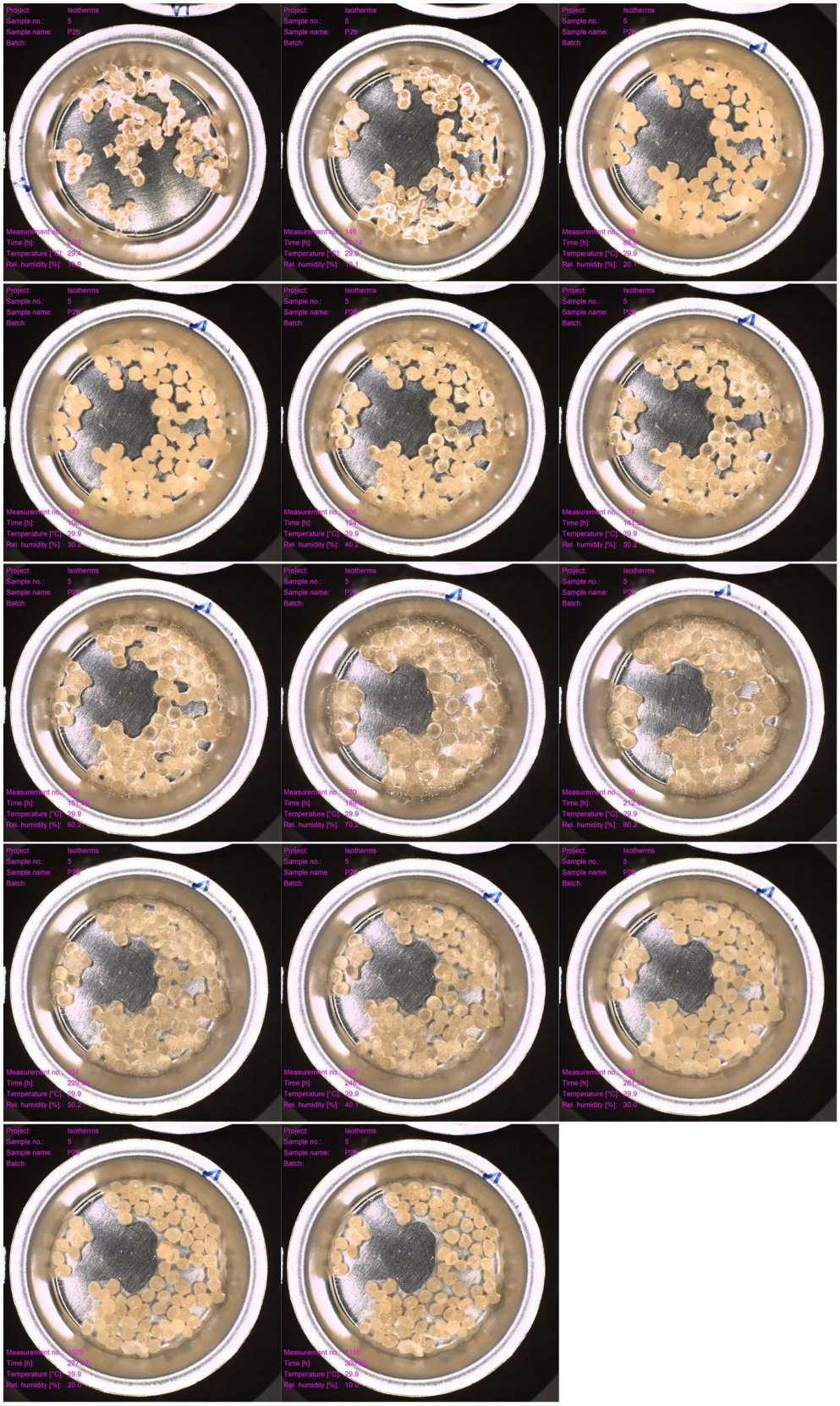

Fig. D.35 Equilibrium pictures on sample 5. Going through rows from top-left to bottom-right, we see RH increasing (10, 20, ..., 70%) and then decreasing (70, 60, ..., 10%). Temperature is always constant and equal to 30°C. The bottom surface of the aluminum dish has a diameter of ≈ 21 mm.

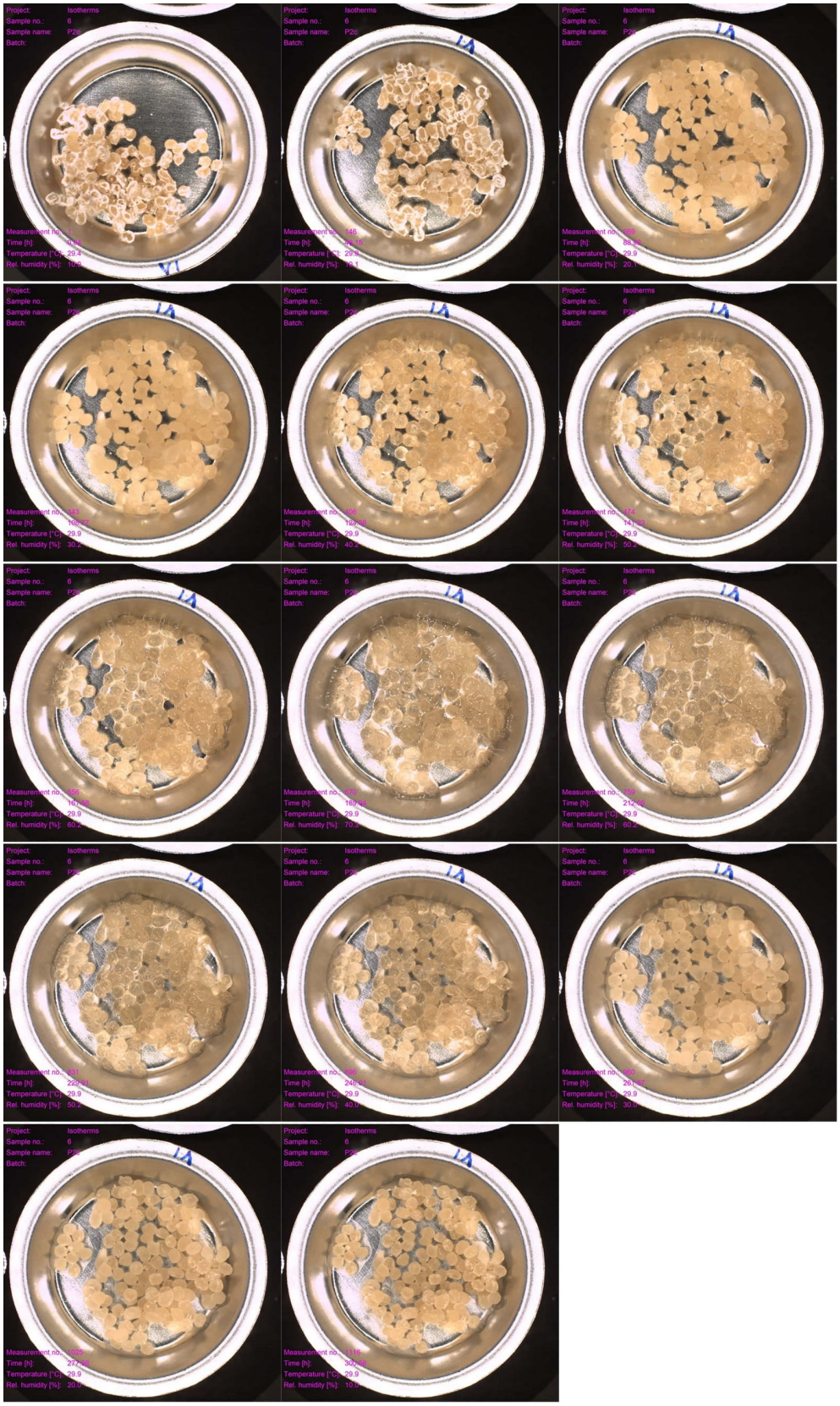

Fig. D.36 Equilibrium pictures on sample 6. Going through rows from top-left to bottom-right, we see RH increasing (10, 20, ..., 70%) and then decreasing (70, 60, ..., 10%). Temperature is always constant and equal to 30°C. The bottom surface of the aluminum dish has a diameter of $\approx$ 21 mm.

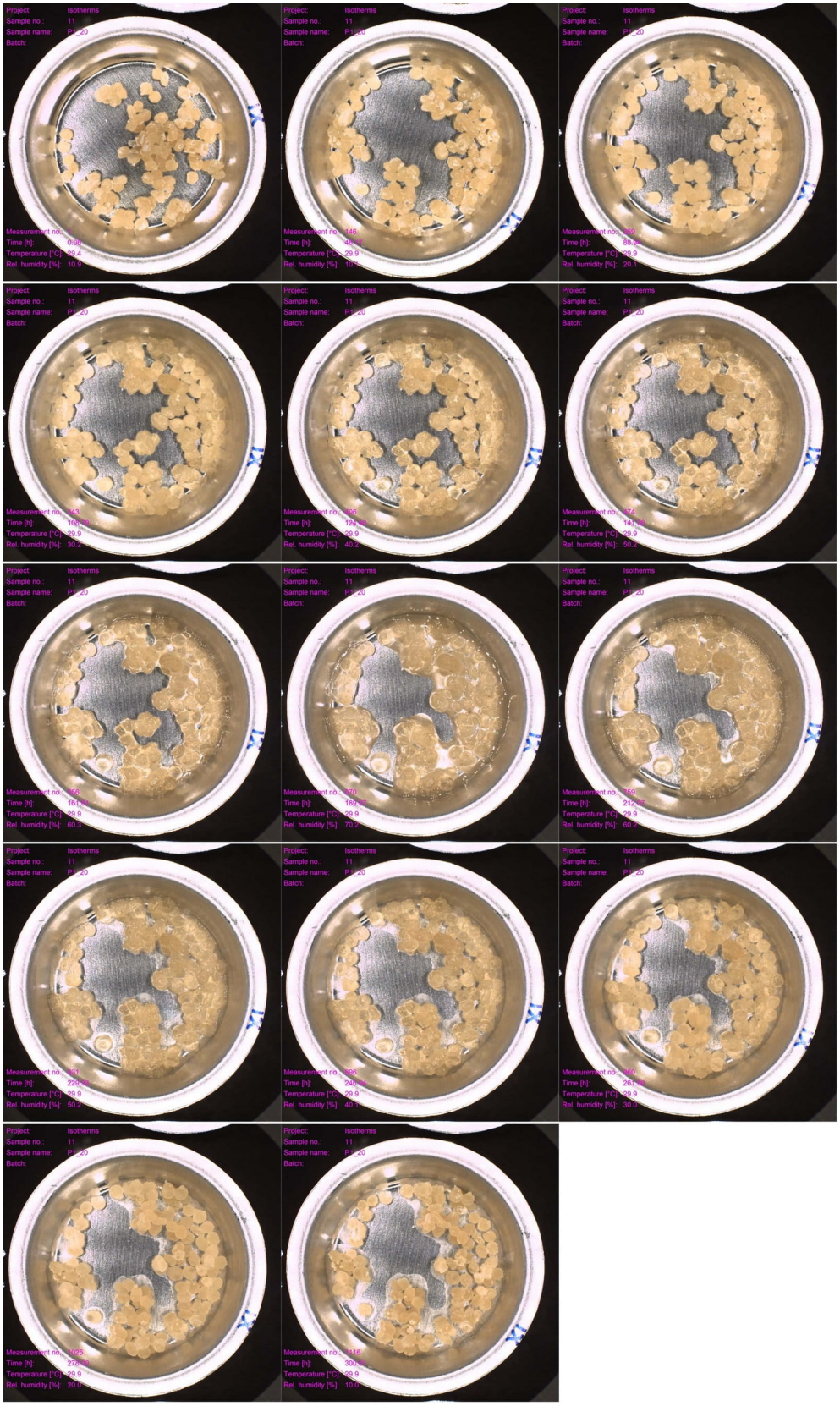

Fig. D.37 Equilibrium pictures on sample 7. Going through rows from top-left to bottom-right, we see RH increasing (10, 20, ..., 70%) and then decreasing (70, 60, ..., 10%). Temperature is always constant and equal to 30°C. The bottom surface of the aluminum dish has a diameter of ≈ 21 mm.

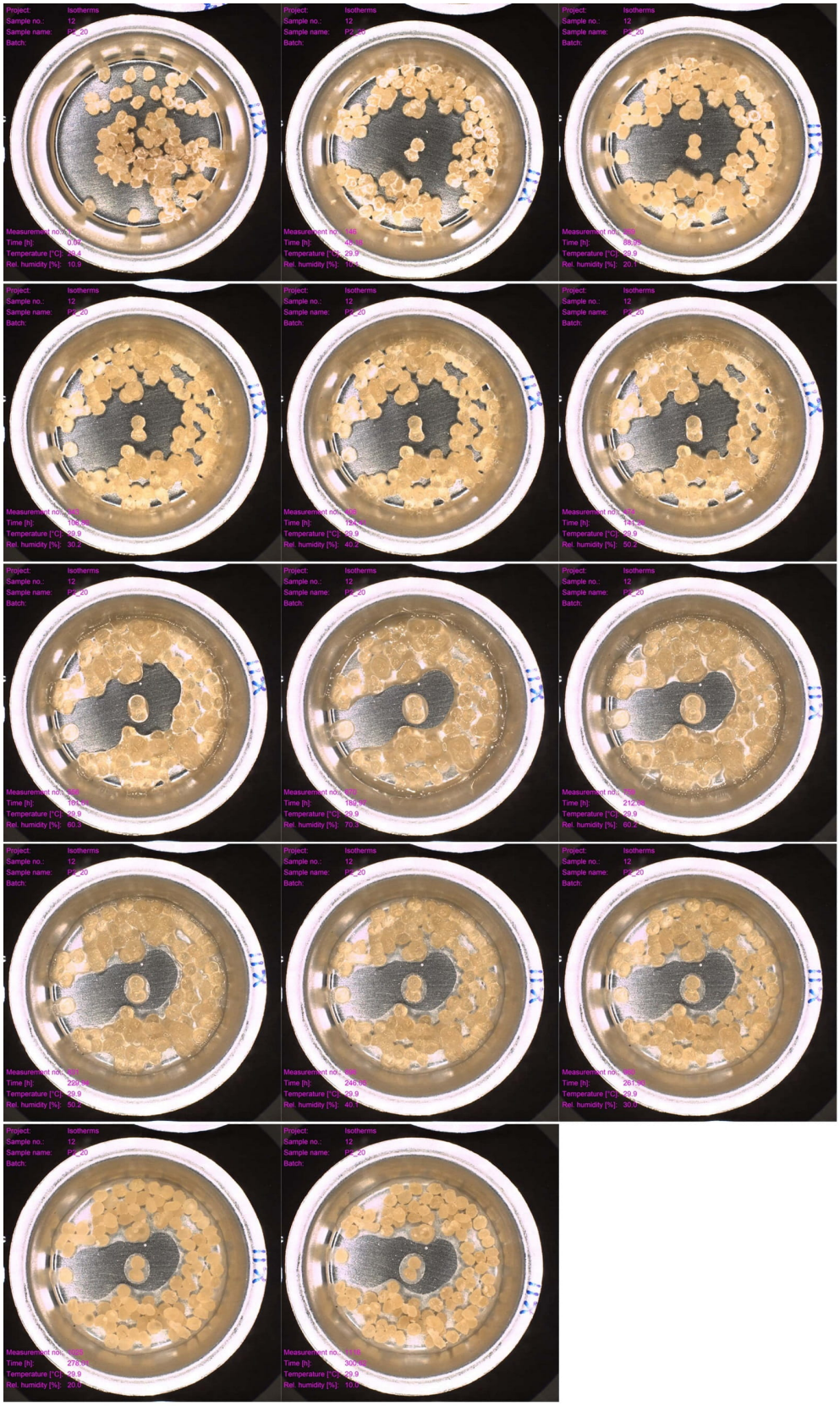

Fig. D.38 Equilibrium pictures on sample 8. Going through rows from top-left to bottom-right, we see RH increasing (10, 20, ..., 70%) and then decreasing (70, 60, ..., 10%). Temperature is always constant and equal to 30°C. The bottom surface of the aluminum dish has a diameter of $\approx$ 21 mm.

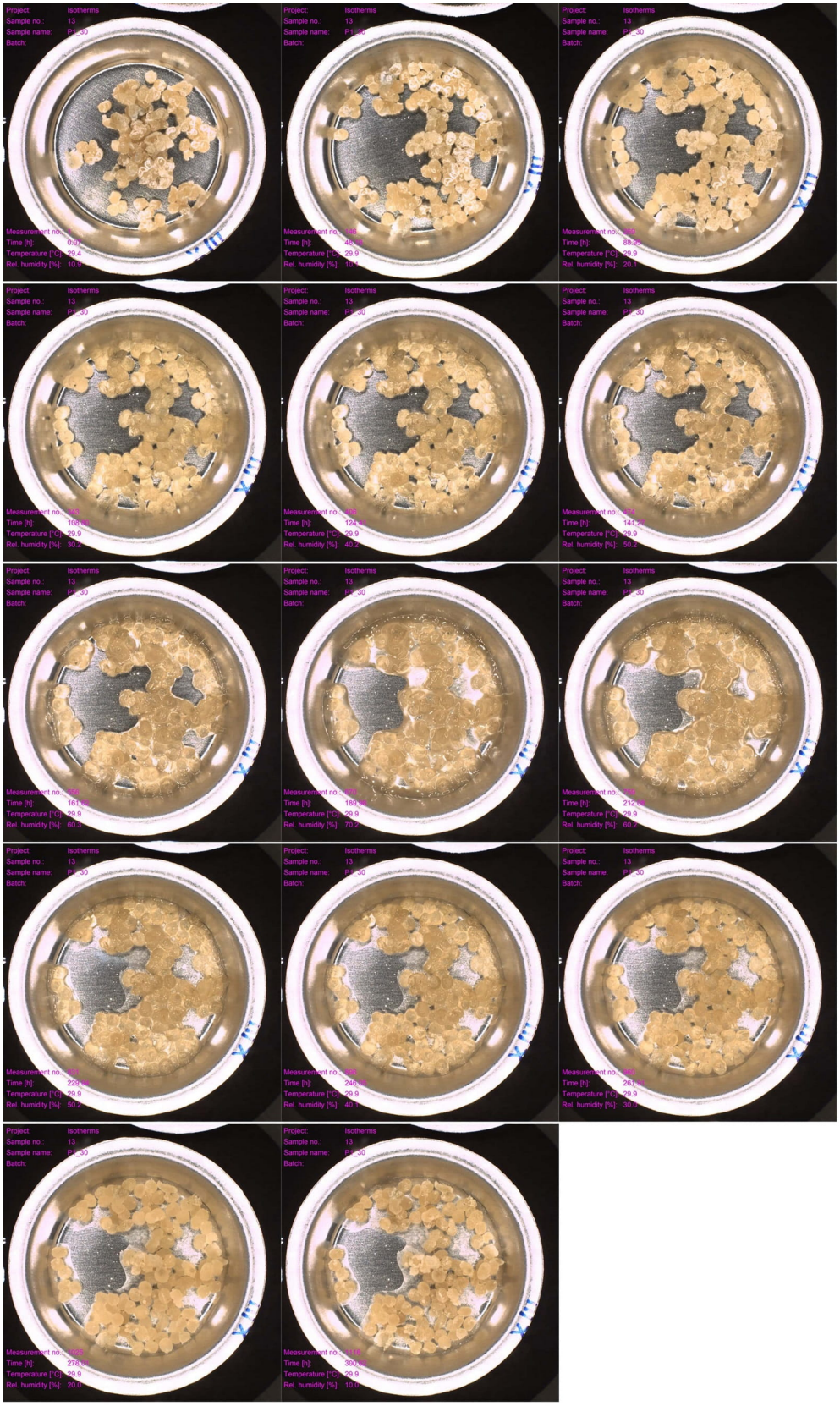

Fig. D.39 Equilibrium pictures on sample 9. Going through rows from top-left to bottom-right, we see RH increasing (10, 20, ..., 70%) and then decreasing (70, 60, ..., 10%). Temperature is always constant and equal to 30°C. The bottom surface of the aluminum dish has a diameter of ≈ 21 mm.

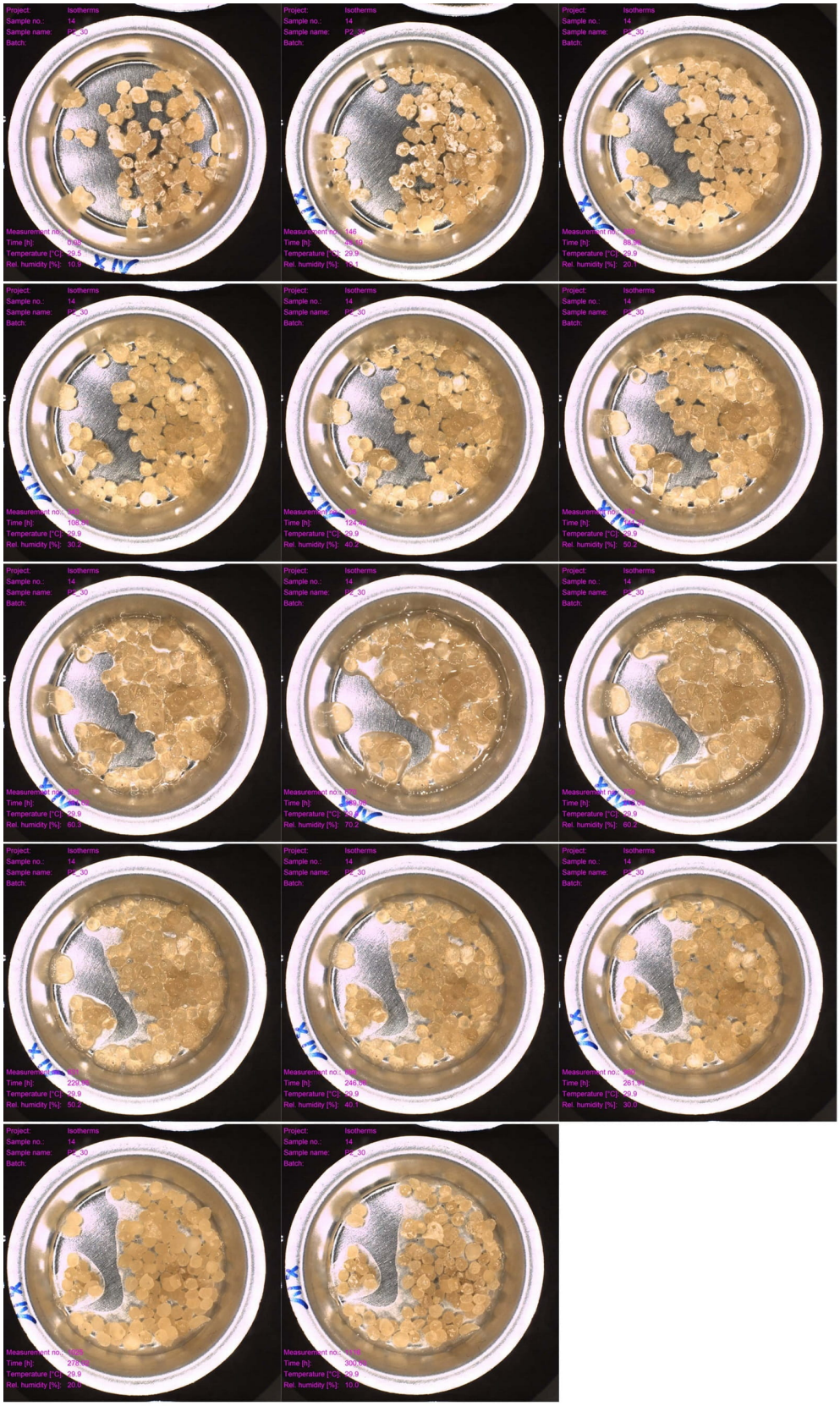

Fig. D.40 Equilibrium pictures on sample 10. Going through rows from top-left to bottom-right, we see RH increasing (10, 20, ..., 70%) and then decreasing (70, 60, ..., 10%). Temperature is always constant and equal to 30°C. The bottom surface of the aluminum dish has a diameter of ≈ 21 mm.

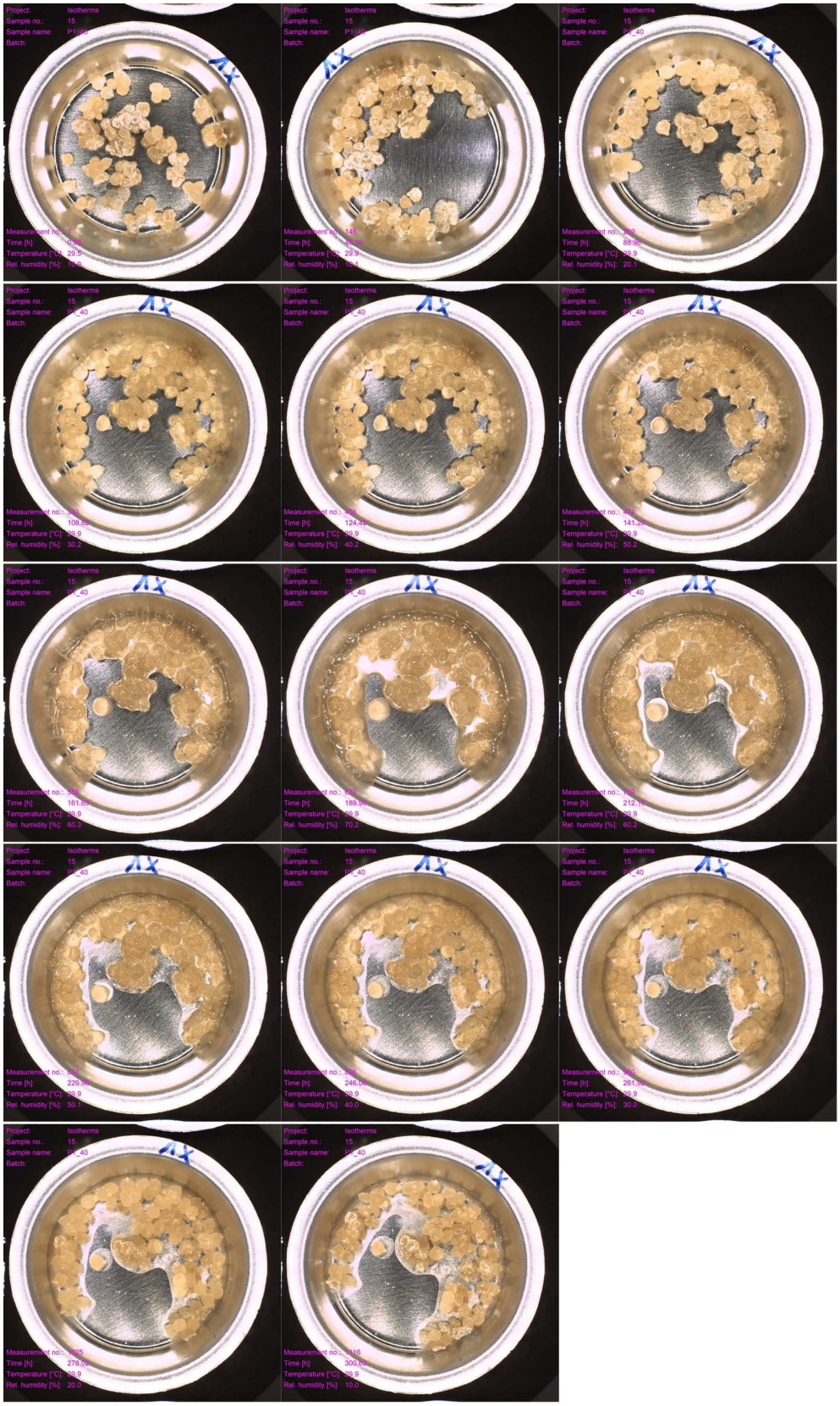

Fig. D.41 Equilibrium pictures on sample 11. Going through rows from top-left to bottom-right, we see RH increasing (10, 20, ..., 70%) and then decreasing (70, 60, ..., 10%). Temperature is always constant and equal to 30°C. The bottom surface of the aluminum dish has a diameter of ≈ 21 mm.

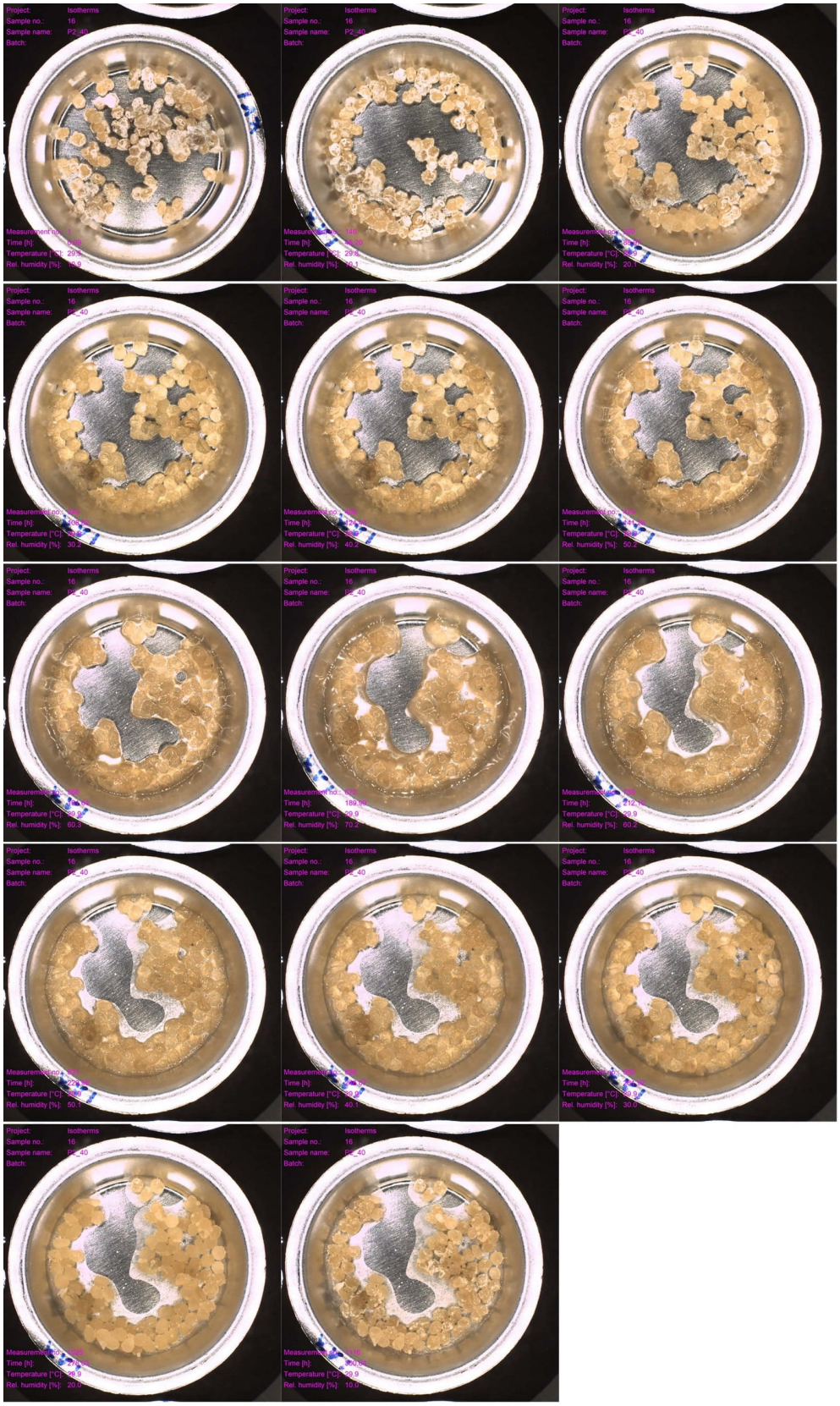

Fig. D.42 Equilibrium pictures on sample 12. Going through rows from top-left to bottom-right, we see RH increasing (10, 20, ..., 70%) and then decreasing (70, 60, ..., 10%). Temperature is always constant and equal to 30°C. The bottom surface of the aluminum dish has a diameter of $\approx$ 21 mm.

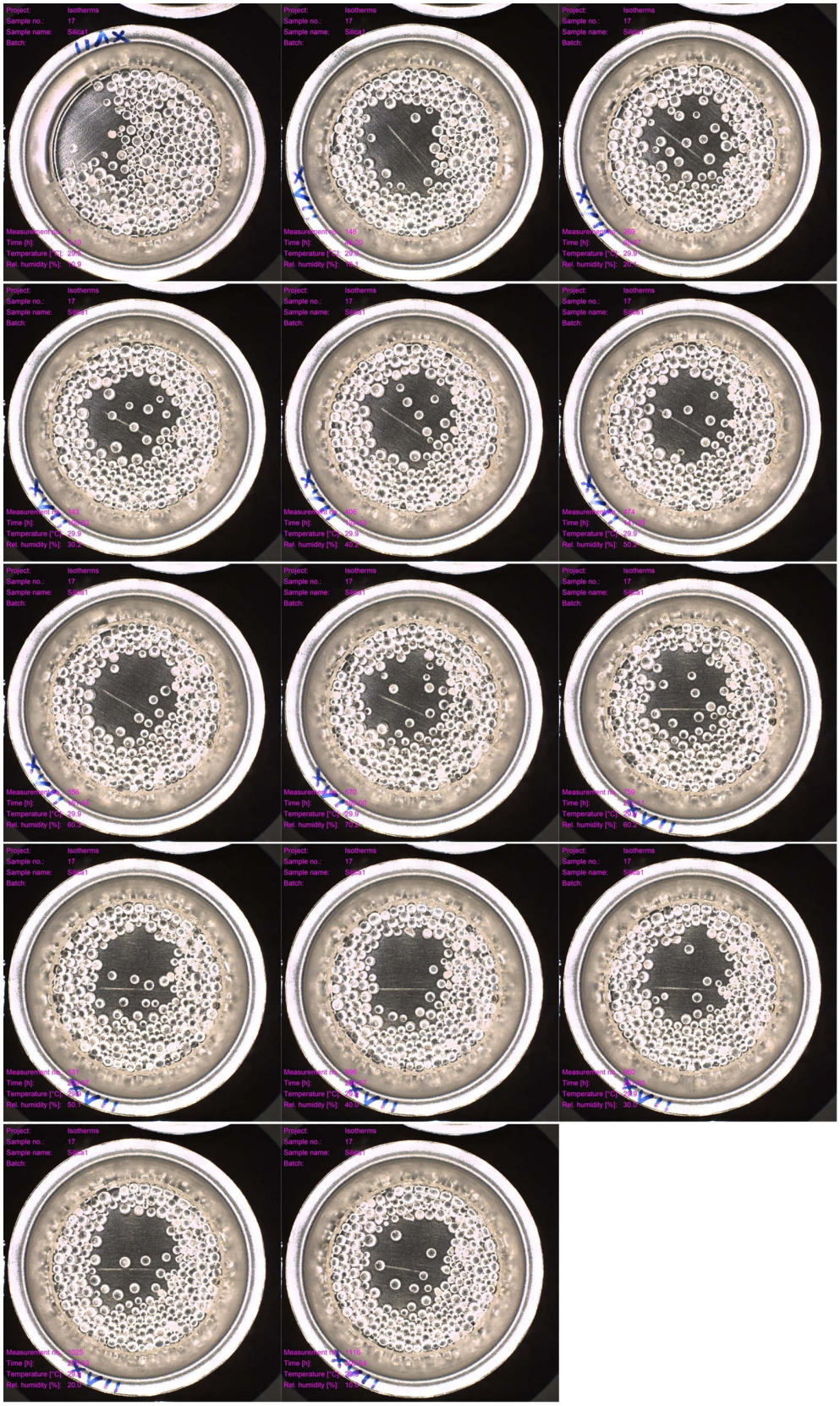

Fig. D.43 Equilibrium pictures on sample 13. Going through rows from top-left to bottom-right, we see RH increasing (10, 20, ..., 70%) and then decreasing (70, 60, ..., 10%). Temperature is always constant and equal to 30°C. The bottom surface of the aluminum dish has a diameter of ≈ 21 mm.

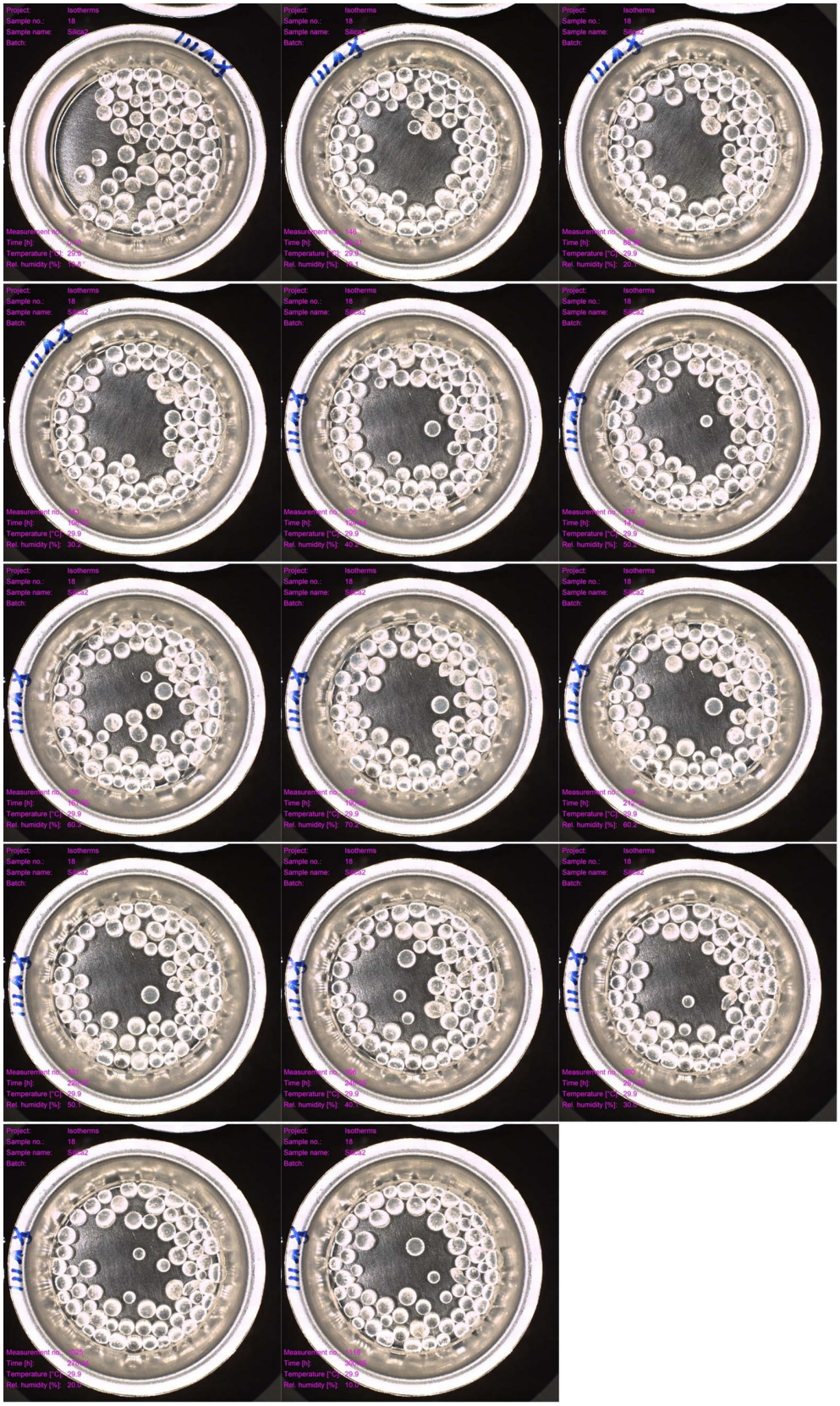

Fig. D.44 Equilibrium pictures on sample 14. Going through rows from top-left to bottom-right, we see RH increasing (10, 20, ..., 70%) and then decreasing (70, 60, ..., 10%). Temperature is always constant and equal to 30°C. The bottom surface of the aluminum dish has a diameter of $\approx$ 21 mm.

Appendix E

Design adjustments on the desalination unit

The initial design of the desalination unit consisted of a symmetric configuration, where a second tank (CD tank) was placed opposite to the EV tank and was meant to collect condensing vapor (see 5.19). This approach had some limitations, though, due to the small passage area between the adsorber and the CD tank (a pipe with 25 mm passage section). When we tried to run experiments we observed the behaviour in fig. E.1:

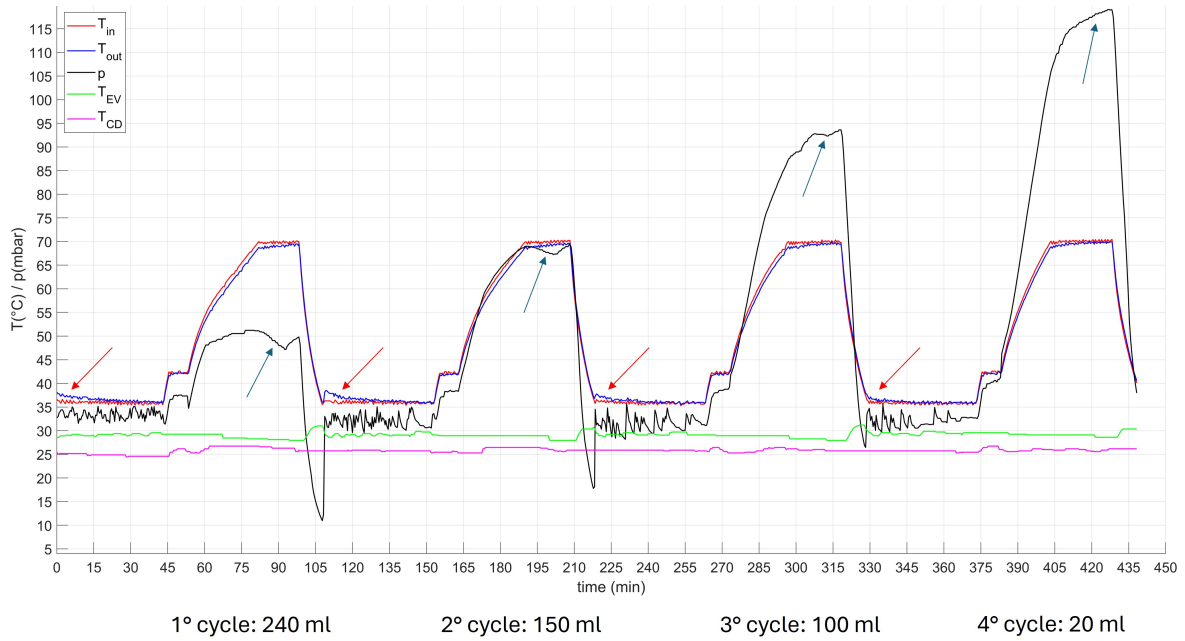

Fig. E.1 Lack of reproducibility in tests with the original design of the AC unit. We show here a test at 70°C, with $t_{Ads} = 45\ min$, $t_{Des} = 55\ min$, $t_{PC} = 10\ min$. Temperatures T_{in} and T_{out} are, respectively, the temperatures at the inlet and outlet of the adsorber. Temperatures T_{EV} and T_{CD} are, respectively, the temperatures of the water in the EV and CD tanks. p is vapor pressure in the adsorber chamber. The water production observed in the CD tank at each cycle is reported below.

It is evident that vapor pressure is not behaving as expected: it keeps increasing with each cycle (blue arrows) and, in parallel, water condensation in the CD tank decreases. A temperature difference $T_{out} - T_{in}$ during adsorption exists, but it keeps decreasing going on along the cycles (red arrows).
We propose the following explanation: during desorption, the chamber saturates with vapor more quickly than vapor travels towards the condenser tank, causing condensation happening in the adsorption vessel rather than in the CD tank. This causes the condensed water to rest inside the vessel and being adsorbed back during the subsequent adsorption phase, reducing the amount of evaporating water (Fig. E.2a,b); but, also, this causes the material to release less vapor, since it meets equilibrium conditions at higher pressures.
To support this hypothesis, we tested the machine under various conditions:

- Connecting a vacuum pump on top of the condensed water tank during desorption, we observed a higher water production. This confirms that the bottleneck in the process was indeed the vapor transport rate between the chambers.
- We heated up the adsorber vessel walls and cooled down the CD tank with colder air. Then, we tried to run slow tests under control of pressure: in particular, we heated up slowly, making sure that the vapor pressure never surpassed saturation pressure at the walls temperature, so to make sure that condensation only happens in the CD tank due to its lower temperature. This allowed to repristinate the correct trend in pressure, but the water production was not measurable.
- Opening the unit immediately after desorption, we observed water condensed allover the internal surface of the adsorber vessel (Fig. E.2c). This is a direct confirmation that condensation was accidentally happening where not supposed.

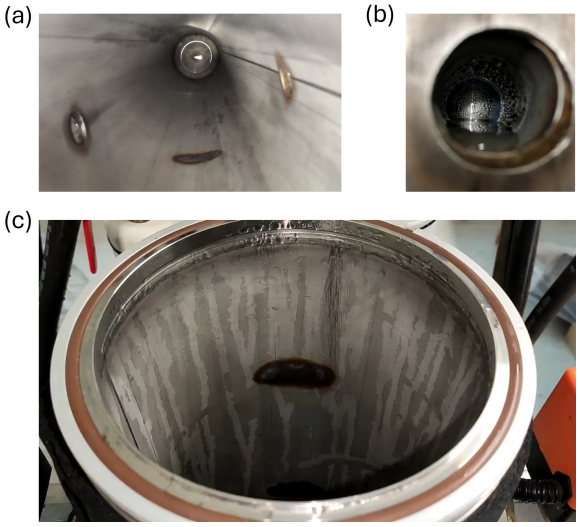

Fig. E.2 Internal surfaces of the AC unit showing unwanted condensation. (a) Bottom of the adsorber vessel at the end of the test. (b) Side channels at the end of the test. (c) Internal surface of the adsorber vessel immediately after desorption.

In order to overcome this limitation, we decided to adapt the machine by isolating the CD tank and deriving a connection at the bottom of the adsorber vessel. This way, the condensing water could be collected directly from the bottom, where it fell by gravity. A flexible pipe (CD pipe) was placed below the adsorber to contain the produced water, and an external fan was added in order to dissipate the heat of condensation from the adsorber vessel walls.

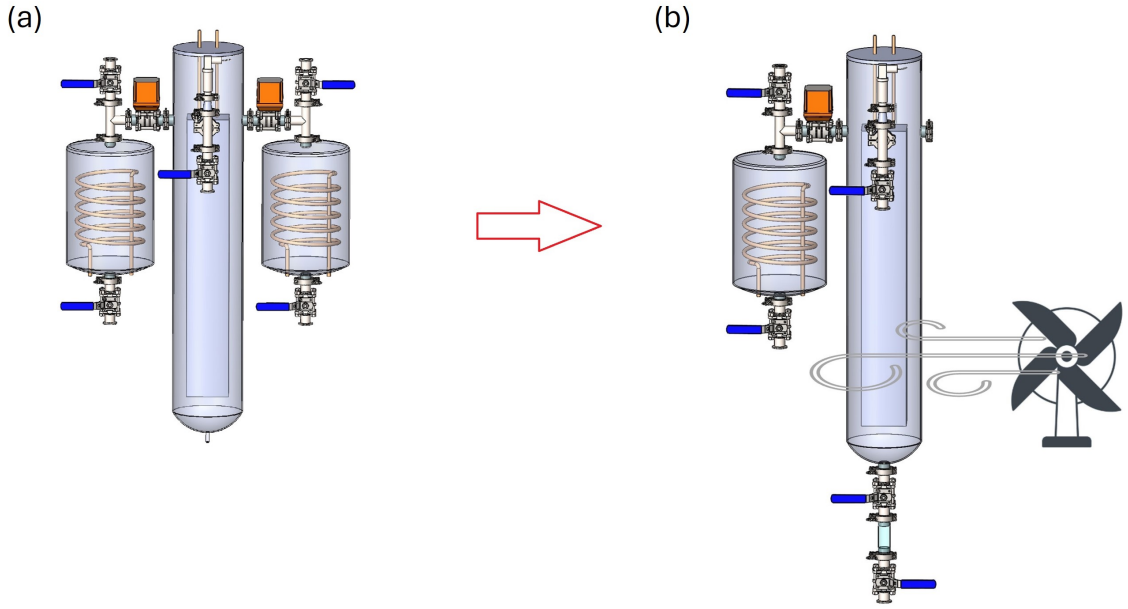

Fig. E.3 Change in the AC unit design. (a) 3D drawing of the desalination unit before the modifications. (b) 3D drawing of the desalination unit after we cut a hole at the bottom of the adsorber and moved the water collection accordingly.

Appendix F

Analytical expression for steady-state SDWP maximization

The Specific Daily Water Production (SDWP) is a useful KPI estimating the performances of adsorption-based desalination machines. The larger the SDWP, the more water is condensed per unit of time and per amount of sorbent material. It strongly depends on the sorbent characteristics (diffusivity, equilibrium water uptakes), but it's also affected by the chosen cycle times: long adsorption and desorption times allow higher absolute water production, but reduce the amount of cycles achievable during a day. For this reason, an optimal SDWP is achieved if using intermediate adsorption and desorption times.
This appendix shows how to derive analytical formulas to estimate the theoretical maximum SDWP achievable starting from the material diffusivities and equilibrium values. The derived formulas also provide what are the optimal adsorption and desorption times. The model used in this derivation is Linear Driving Force (LDF), but the same procedure can be repeated using any other model.

The LDF model

The Linear Driving Force (LDF) model assumes that the rate of increase of water uptake w is proportional to the difference between the instantaneous water uptake and the equilibrium value w_{eq} in the test conditions (i.e., at known temperature T and relative humidity RH, which remain constant during the whole charging or discharging process):

$$\frac{dw(t)}{dt} = -k \cdot \left[w(t) - w_{eq} \right] \tag{F.1}$$

where t is time (s), $w = w(t)$ is water uptake (g/g), $w_{eq} = w_{eq}(T, RH)$ is the equilibrium water uptake (g/g) at temperature T and relative humidity RH and available from the material

isotherm, k is the inverse of the time constant (1/s) of the capacitive sorption phenomenon. The expression of k for spherical beads is provided below:

$$k = \frac{F_0 \cdot D}{R_p^2} \tag{F.2}$$

where F_0 is a shape factor (equal to 15, in case of spherical beads), R_p is the beads radius (m), $D = D(T)$ is the diffusivity (m^2/s), generally dependent on temperature T, but assumed to be constant with water uptake. For the purpose of this work, we will assume that the adsorption conditions (temperature, humidity, diffusivity, equilibrium uptakes) in the application are fixed and constant during the whole transient; the same is true for desorption, even though the conditions during adsorption may differ from the ones during desorption. We will use the pedix A to indicate adsorption-related parameters: $D_A,\ k_A,\ w_{eq,A} \equiv w_A$. We will use the pedix D to indicate desorption-related parameters: $D_D,\ k_D,\ w_{eq,D} \equiv w_D$.
Equation F.1 is a 1^{st} order ODE, satisfied by the following expression:

$$w(t) = w_{eq} + (w_0 - w_{eq}) \cdot e^{-k \cdot (t - t_0)} \tag{F.3}$$

with w_0 being the water uptake at time t_0. The expression is physically significant for times $t \geq t_0$.

Definition of steady-state SDWP

The LDF model allows to simulate adsorption and desorption transients, where the sorbent is respectively charged and discharged with vapor particles. A "cycle" consists of an adsorption followed by a desorption, plus a possible *idle* phase (usually, pre-cooling or pre-heating periods during which the machine is preparing for the next adsorption or desorption phase). We say that a cycle is *complete* if the water uptake at the end of the desorption phase is equal to the one at the beginning of the adsorption phase (meaning that the material is back to its original state).

In order to perform complete cycles, the adsorption and desorption times must be chosen properly: indeed, if the desorption time is too short, the final water uptake would be higher than the initial one since the material didn't have enough time to discharge completely. Nevertheless, even if the initial desorption time is not properly chosen but cycles at fixed times are repeated over time, the capacitive nature of the sorption process allows a self-adjusting mechanism, with the water uptake increasing or decreasing until the chosen cycle times are coherent with the cycle being complete (Fig. 5.23a).

When a sufficient number of cycles are repeated[1], the uptake oscillates indefinitely between the same two values: $w_0 \equiv w_2$ and w_1 (see for instance Fig. 5.18b). We are interested in such regime condition, when the amount $\Delta w = w_1 - w_0$ is potentially[2] convertible in produced water at the end of each cycle of duration Δt. We then define the steady-state SDWP as follows:

$$SDWP = \frac{\Delta w}{\Delta t} = \frac{w_1 - w_0}{t_A + t_D + t_I} \cdot c_t \tag{F.4}$$

where t_A is the adsorption time (s), t_D is the desorption time (s), t_I is the idle time (s). The coefficient $c_t = 86400\ s/day$ is only used to have the KPI use the common unit $ton/ton/day$. Using Eq. F.3, we can evaluate w_1 and w_2:

$$w_1 = w_A + (w_0 - w_A) \cdot e^{-k_A \cdot t_A} \tag{F.5}$$

$$w_2 = w_D + (w_1 - w_D) \cdot e^{-k_D \cdot t_D} \tag{F.6}$$

Replacing Eq. F.5 into F.6 and imposing $w_0 = w_2$ (as it is in regime behaviour), after some algebraic steps we can evaluate the water uptake level w_0 where the oscillations happen:

$$\begin{aligned}
w_2 = w_0 &= w_D + \left(\left[w_A + (w_0 - w_A) \cdot e^{-k_A \cdot t_A} \right] - w_D \right) \cdot e^{-k_D \cdot t_D} \\
w_0 &= w_D + w_A \cdot e^{-k_D t_D} + (w_0 - w_A) \cdot e^{-k_A t_A - k_D t_D} - w_D \cdot e^{-k_D t_D} \\
w_0 \cdot \left(e^{-k_A t_A - k_D t_D} - 1 \right) &= w_A \cdot e^{-k_A t_A - k_D t_D} - w_D - (w_A - w_D) \cdot e^{-k_D t_D} \\
w_0 &= w_A - (w_A - w_D) \cdot \frac{1 - e^{-k_D t_D}}{1 - e^{-k_D t_D - k_A t_A}}
\end{aligned} \tag{F.7}$$

Equation F.7 allows to estimate the lowest state of charge w_0 of the material when cycled with times t_A and t_D. The highest state of charge w_1 is evaluated by replacing F.7 into F.5. These two values are important to know, since some sorbents are subject to deliquescence when used for long time at high states of charge.

The theoretical SDWP can be now evaluated as a function of t_A and t_D only (Fig. F.1), being w_0 a non-free parameter (its expression must be the one in F.7 in order for the cycle to be

[1] The exact number varies according to many parameters, including diffusivities, equilibrium values and initial water uptake (we typically are in the order of 5-20 cycles). For repeatability, in this analysis we will assume that the phenomenon is at steady-state when the difference between initial and final water uptake of a cycle is less than $1 \cdot 10^{-5}$ g/g.

[2] In reality, not all the released vapor is effectively collected due to inefficiencies in the machine (e.g., residual water in the vessel containing the sorbent which is adsorbed back in the next adsorption phase). For this reason, the defined SDWP shall be assumed as an upper-bound of the SDWP achievable during the actual operation of the machine.

complete). In particular:

$$
\begin{aligned}
SDWP &= \frac{\Delta w}{\Delta t} = \frac{w_1 - w_0}{t_A + t_D + t_I} \cdot c_t \\
SDWP &= \frac{\Delta w}{\Delta t} = \frac{w_A + (w_0 - w_A) \cdot e^{-k_A \cdot t_A} - w_0}{t_A + t_D + t_I} \cdot c_t \\
SDWP &= \frac{(w_A - w_0) \cdot \left(1 - e^{-k_A t_A}\right)}{t_A + t_D + t_I} \cdot c_t \\
SDWP &= \frac{(w_A - w_D) \cdot \left[\frac{1 - e^{-k_D t_D}}{1 - e^{-k_D t_D - k_A t_A}}\right] \cdot \left(1 - e^{-k_A t_A}\right)}{t_A + t_D + t_I} \cdot c_t \\
SDWP = SDWP(t_A, t_D) &= \frac{w_A - w_D}{t_A + t_D + t_I} \cdot \frac{(e^{k_A t_A} - 1) \cdot (e^{k_D t_D} - 1)}{e^{k_A t_A + k_D t_D} - 1} \cdot c_t
\end{aligned}
\tag{F.8}
$$

Equation F.8 gives the expression for SDWP that we aim to maximize, in order to achieve the highest possible water daily production. SDWP is here considered only function of t_A and t_D, whose optimal values we need to find. The remaining parameters are instead all known constants, including idle time t_I which is not dependent on the cycle times but is instead a fixed interval needed for the machine preparation (this is true for real applications as well).

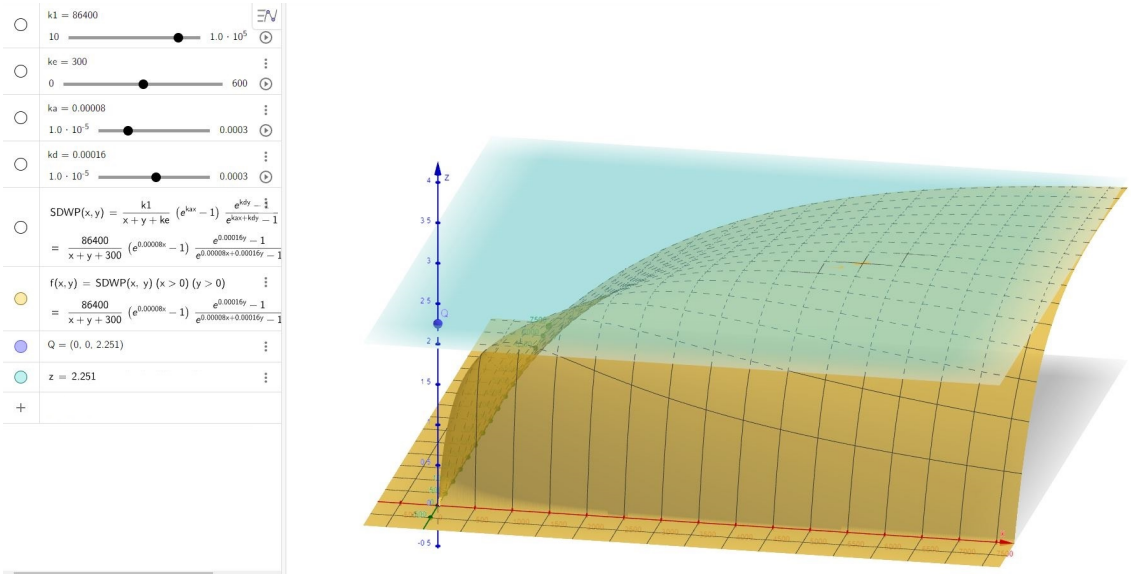

Fig. F.1 3D plot of the analytical expression for SDWP as a function of adsorption and desorption time. The x-axis (red) is adsorption time t_A; the y-axis (green) is desorption time t_D; the z-axis (blue) is SDWP. The graph was made with GeoGebra® [153].

Evaluation of optimal cycle times

Our scope is to find the cycle times t_A and t_D which maximize SDWP in expression F.8. We can easily verify that, both for $t_A \to 0$ and for $t_A \to +\infty$, we get $SDWP \to 0$. The same is true

for t_D, as expected because of the symmetry in F.8.
We can evaluate the partial derivatives of SDWP with respect to t_A and t_D (see below). Given the regularity of the expression and its derivatives, we can expect that, if a maximum exists, that is a local maximum, where the two partial derivatives are both null. In other words, the times t_A and t_D that maximize SDWP are also among the ones which satisfy the follow systems of equations:

$$\begin{cases} \frac{\partial SDWP}{\partial t_A} = 0 \\ \frac{\partial SDWP}{\partial t_D} = 0 \end{cases}$$

$$\begin{cases} c_t \cdot \frac{(1-e^{k_D t_D}) \cdot \left[k_A (t_I+t_A+t_D) \cdot e^{k_A t_A} \cdot (1-e^{k_D t_D}) - e^{k_A t_A + k_D t_D} + e^{2k_A t_A + k_D t_D} - e^{k_A t_A} - 1\right]}{(t_I+t_A+t_D)^2 \cdot (e^{k_A t_A + k_D t_D} - 1)^2} = 0 \\ c_t \cdot \frac{(1-e^{k_A t_A}) \cdot \left[k_D (t_I+t_A+t_D) \cdot e^{k_D t_D} \cdot (1-e^{k_A t_A}) - e^{k_A t_A + k_D t_D} + e^{k_A t_A + 2k_D t_D} - e^{k_D t_D} - 1\right]}{(t_I+t_A+t_D)^2 \cdot (e^{k_A t_A + k_D t_D} - 1)^2} = 0 \end{cases} \tag{F.9}$$

Given that t_A and t_D are strictly greater than 0 (since they are cycle times), the denominators are always different from zero; also, the only way the two expressions are true is that the terms within square brackets are null, that is, after factorization:

$$\begin{cases} k_A (t_I + t_A + t_D) \cdot e^{k_A t_A} \cdot (1 - e^{k_D t_D}) + (1 - e^{k_A t_A + k_D t_D}) \cdot (1 - e^{k_A t_A}) = 0 \\ k_D (t_I + t_A + t_D) \cdot e^{k_D t_D} \cdot (1 - e^{k_A t_A}) + (1 - e^{k_A t_A + k_D t_D}) \cdot (1 - e^{k_D t_D}) = 0 \end{cases} \tag{F.10}$$

We can move the second factors to the right sides and replace the second equation with the term-by-term division between the two equations:

$$\begin{cases} k_A(t_I+t_A+t_D)\cdot e^{k_A t_A}\cdot(1-e^{k_D t_D}) = -(1-e^{k_A t_A+k_D t_D})\cdot(1-e^{k_A t_A}) \\ k_D(t_I+t_A+t_D)\cdot e^{k_D t_D}\cdot(1-e^{k_A t_A}) = -(1-e^{k_A t_A+k_D t_D})\cdot(1-e^{k_D t_D}) \end{cases}$$

$$\begin{cases} k_A(t_I+t_A+t_D)\cdot e^{k_A t_A}\cdot(1-e^{k_D t_D}) = -(1-e^{k_A t_A+k_D t_D})\cdot(1-e^{k_A t_A}) \\ \frac{k_A}{k_D}\cdot\frac{e^{k_A t_A}}{e^{k_D t_D}}\cdot\frac{1-e^{k_D t_D}}{1-e^{k_A t_A}}\cdot\frac{1-e^{k_D t_D}}{1-e^{k_A t_A}} = 1 \end{cases}$$

$$\begin{cases} k_A(t_I+t_A+t_D)\cdot e^{k_A t_A}\cdot(1-e^{k_D t_D}) = -(1-e^{k_A t_A+k_D t_D})\cdot(1-e^{k_A t_A}) \\ \frac{2-(e^{k_D t_D}+e^{-k_D t_D})}{2-(e^{k_A t_A}+e^{-k_A t_A})} = \frac{k_D}{k_A} \end{cases}$$

$$\begin{cases} k_A(t_I+t_A+t_D)\cdot e^{k_A t_A}\cdot(1-e^{k_D t_D}) = -(1-e^{k_A t_A+k_D t_D})\cdot(1-e^{k_A t_A}) \\ \frac{1-\cosh(k_D t_D)}{1-\cosh(k_A t_A)} = \frac{k_D}{k_A} \end{cases} \tag{F.11}$$

And, finally:

$$\begin{cases} k_A(t_I+t_A+t_D)\cdot e^{k_A t_A}\cdot(1-e^{k_D t_D}) + (1-e^{k_A t_A+k_D t_D})\cdot(1-e^{k_A t_A}) = 0 & \text{(F.12a)} \\ t_D = \frac{1}{k_D}\cdot\operatorname{arccosh}\left(1-\frac{k_D}{k_A}\cdot[1-\cosh(k_A t_A)]\right) & \text{(F.12b)} \end{cases}$$

where we recall the definitions: $\cosh(x) = \frac{e^x+e^{-x}}{2}$, $\operatorname{arccosh}(x) = \log(x+\sqrt{x^2-1})$. By replacing Equation F.12b into Equation F.12a, we get one equation with a single unknown variable t_A:

$$\begin{aligned} k_A\left[t_I+\frac{t_A k_A}{k_A}+\frac{1}{k_D}\cdot\operatorname{arccosh}\left(1-\frac{k_D}{k_A}\cdot[1-\cosh(k_A t_A)]\right)\right]\cdot \\ \cdot e^{k_A t_A}\cdot\left(1-e^{\operatorname{arccosh}\left(1-\frac{k_D}{k_A}\cdot[1-\cosh(k_A t_A)]\right)}\right)+ \\ +\left(1-e^{k_A t_A+\operatorname{arccosh}\left(1-\frac{k_D}{k_A}\cdot[1-\cosh(k_A t_A)]\right)}\right)\cdot(1-e^{k_A t_A}) = 0 \end{aligned} \tag{F.13}$$

The expression can be further developed by replacing the definition $\operatorname{arccosh}(x) = \log(x+\sqrt{x^2-1})$ and simplifying some of the exponentials; nevertheless, any attempt of solving explicitly for t_A has been unsuccessful until now, including involving the Lambert W function, since t_A is present inside and outside the argument of the exponentials in non-linear forms. At the current development, Equation F.13 must be solved numerically.

Once the optimal adsorption time t_A is found from F.13, it should be used in Eq. F.12b to analytically derive the optimal t_D. Then, the found optimal t_A and t_D should be replaced in Eq. F.8 to derive the optimal SDWP, and in Eq. F.7 and F.5 to derive the water uptake range between which the material oscillates.
All the calculations until this point are exact and not approximate.

Analytical approximation for optimal t_D/t_A

Equation F.13 is already a significant result, since it reduces the problem of finding the optimal cycle times to solving a 1-variable equation. Nevertheless, it still requires numerical computation.
An explicit analytical formula for approximating the relationship between the optimal t_D and t_A is still achievable under further assumptions. In particular, if the positive product $m = k_A \cdot t_A$ is small enough (as a reference, $m \leq 0.5$), we can approximate $\cosh(X)$, $\operatorname{arccosh}(1+X)$ with their Taylor and Puiseux series expansions centered in 0.
For $x \to 0$, $\cosh(X) \simeq 1 + \frac{X^2}{2}$ and $\operatorname{arccosh}(1+X) \simeq \sqrt{2}\sqrt{X}$. Using these in F.12b and performing some algebraic steps, we get an approximation of the relationship between optimal t_A and optimal t_D:

$$\frac{t_D}{t_A} \simeq \sqrt{\frac{k_A}{k_D}} \tag{F.14}$$

In case the particle radius is not sensibly changing between adsorption and desorption, the ratio of coefficients k_A and k_D is also the ratio of diffusivities D_A and D_D (see Equation F.2), thus:

$$\frac{t_D}{t_A} \simeq \sqrt{\frac{D_A}{D_D}} \tag{F.15}$$

Even if good, the level of approximation of Eq. F.14 is not sufficient to guarantee that all the solutions of Eq. F.12a are not lost. Indeed, by replacing F.14 into F.12a and using $e^X \simeq 1+X$ at $X \to 0$ we can only evaluate the trivial solution $t_A = 0\ s$. In order to estimate the non trivial positive solution, we need to increase the number of terms of the e^x Taylor series to at least the second power, losing the option to invert analytically F.12a. Replacing F.14 into F.8 and deriving with respect to t_A is not useful as well, since the expression does not have any analytical solution.
To reach an exact analytical formula, an idea would be to start all-over again and use a different model from LDF. For instance, LDFDw is an option, but it has a more complex expression, and the resulting equations are difficult to manipulate; on the other hand, we can think to use simpler semi-empirical alternative models (e.g. exponentials) that lead to invertible expressions. This is left to future research.

The approximation in eq. F.15 is simple but still quite precise. For typical values[3] the relative error you get on the value of t_D is below 1%. Furthermore, this approximation not only gives the optimal desorption time after the optimal adsorption time is found (or viceversa), but also gives a good estimation of the best possible desorption time given a sub-optimal adsorption time. For example, with $D_A = 3 \cdot 10^{-12}\ m^2/s$, $D_D = 6 \cdot 10^{-12}\ m^2/s$, $t_A = 30\ min$ we estimate optimal $t_D = 21\ min$, which is exactly what we simulated in case of CaAlg in Chapter 5.

For practical implementations, we suggest the following heuristic strategy: choose the desorption time t_D according to empirical considerations (e.g., in the case on the AD unit in Chapter 5 we observed that desorption time could not go below 20 minutes due to the large thermal inertia); then, choose the adsorption time as:

$$t_A = t_D \cdot \sqrt{\frac{D_D}{D_A}} \tag{F.16}$$

where D_A and D_D are diffusivities during adsorption and desorption, respectively. Since, typically, desorption diffusivity is higher (due to the higher temperature), it is suggested to use a desorption time shorter than the adsorption time (at the limit of constant D, adsorption and desorption time in the optimal case are identical). As a final note: the result in F.16 can also be inverted and used to estimate the unknown diffusivity at a certain temperature, if the diffusivity at another temperature is known and once the optimal ratio between cycle times is experimentally found.

[3] We used $k_a = 8 \cdot 10^{-5}\ 1/s$, $k_d = 1.6 \cdot 10^{-4}\ 1/s$.